Digital multispectral Mueller colposcopy for exploring cervical microstructure in vivo

Junha Park

INSTITUT POLYTECHNIQUE DE PARIS

NNT : 2022IPPAX141

Thèse de doctorat

Digital multispectral Mueller colposcopy for exploring cervical microstructure *in vivo*

Thèse de doctorat de l'Institut Polytechnique de Paris
préparée à École Polytechnique

École doctorale n°626 Ecole Doctorale de l'Institut Polytechnique de Paris (ED IP Paris)
Spécialité de doctorat: Physique

Thèse présentée et soutenue à Palaiseau, 20/12/2022, par

Junha PARK

Composition du Jury :

Guilhem Gallot Directeur de recherche, École polytechnique (LOB)	Président/Examinateur
Arnaud Dubois Professor, Institut d'Optique Graduate School	Rapporteur
Dominique Pagnoux Charge de Recherche, Institut de recherche XLIM	Rapporteur
Xavier Orlik Maître de recherche, Onera (midi-Pyrénées / Toulouse)	Examinateur
Carole Deumié Professeure, École Centrale de Marseille	Examinatrice
Angelo Pierangelo Ingénieur de recherche, École Polytechnique (LPICM)	Directeur de thèse
Razvigor Ossikovski Professeur, École Polytenique (LPICM)	Co-Directeur de thèse
Élodie Debras Practicienne hospitalière, CHU du Kremlin-Bicêtre	Invité

ACKNOWLEDGEMENTS

First of all, I would like to thank my thesis supervisor, Dr. Angelo Pierangelo, who has guided the work of this doctoral thesis over the past four years. Without his enthusiasm, hard work and innovative ideas for this work, this dissertation would not have been possible. In particular, Angelo's positive mindset, constant motivation, and his thoughtful mind made me possible to finish this job like this. I also would like to thank my co-supervisor, Prof. Razvigor Ossikovski, for his valuable discussion on polarimetry and his thoughtful attention. To the examiners and reviewers who take time out of their busy schedule to review this thesis, I would like to thank you for thoroughly reviewing my four-year journey.

Also, thank you to Professor Yvan Bonnassieux, the Director of LPICM, for introducing Angelo and helping me settle down in France and LPICM. And I would like to thank Jean-Charles Vanel, who supported me mentally and helped me whenever I was having a hard time. I didn't say anything, but every question asked if I was doing well was a great comfort in my difficult doctoral life. Though he is not at LPICM now, thanks to Patxi for helping me develop the instrument. Without his contributions, this wonderful piece of equipment would not have come to this world. And, without his sense of humor, I would have had a harder time during the coronavirus pandemic.

A big thank you to Fred for helping us run the data server, which was one of the most important parts of the project. Cyril, Jerome, Jonathan, Marc, Eric, and all Beer staffs, I thank you always to help our research works. Especially Jaqueline, thank you very much for contributing to our team and the clinical trial. I would like to thank the Polarimetry group members, Martin, Tatiana, Enrique, who directly and indirectly helped and discussed this project. I would like to thank Laurance and Gabriela for handling all administrative work related to me since I arrived at LPICM. Thank Denis for always generously providing resources that were lacking for my experiments.

I would like to thank Prof. Hervé Fernandez, Dr. Elodie Debras, Myriam Virlouvet, Waggeh Fatoumata and the entire staffs of the gyneacology department of the Bicêtre hospital for making this clinical project possible. In addition, I would like to tell you that every Tuesday I went to the hospital, Marie, who had been carrying out the clinical trial together for two years, was enjoyable.

Thank you to my former team members Jean, Jérémy and Stan for making a wonderful history for me to be part of this project. Specially, Arvid has spent my tough early PhD together. Much inspired by his genius. Not only that, but his kindness helped me a lot to settle into school life.

My precious former/current office mates (although I didn't go often in the end) were the only reason I went to school even after all the experiments were over. Arvid, Monalisa, Daniel, Bandar, Marta, Guili, Martina, and Ghewa. Thank you for making precious memories over the past 4 years.

My friends who have been with me since the beginning of my study in France, Hyeonseok, Gookbin, and Sangjun. I am also finally completing my PhD :) Thomas and Seonyong, who taught me many things as seniors studying abroad and helped me with countless things without any compensation.

Thank you to my family. To my parents, grandparents, and sister, and to Jihyun, the love of my life, who have always supported me and made me what I am today.

I can't list them all here, but so many people have helped me get this done. I would like to thank to all of them.

TABLE OF CONTENTS

RESUME

La prématurité est la première cause de mortalité périnatale dans le monde, avec un taux estimé à 6 % en France et en Europe et deux fois plus élevé aux États-Unis. La menace d'une naissance prématurée spontanée est la complication la plus importante de la grossesse. Elle survient généralement entre 23 et 37 semaines d'aménorrhée et peut être associée à des modifications de la forme du col utérin, parfois accompagnées par des saignements ou une rupture précoce des membranes.

Dans la pratique clinique actuelle, l'échographie transvaginale pour mesurer la longueur du col utérin est la technique de diagnostic recommandée pour la prématurité. Cependant, en raison de l'incapacité à corréler la longueur mesurée avec le délai d'accouchement, il n'existe pas de directives claires concernant le seuil de la longueur du col utérin pour un diagnostic précis de la prématurité. Malgré les progrès considérables de la technologie médicale moderne, la prédiction des naissances prématurées reste un défi. Par conséquent, une nouvelle approche visant à améliorer le diagnostic des naissances prématurées est nécessaire pour réduire les coûts des soins de santé, prévenir les effets secondaires des hospitalisations inutiles et ouvrir la voie à de nouvelles stratégies de traitement.

Le col utérin est la partie inférieure de l'utérus qui fait saillie dans le vagin. De forme cylindrique, il est traversé sur toute sa longueur par le canal endocervical, qui relie la lumière vaginale à la cavité utérine. L'entrée du canal endocervical du côté du vagin s'appelle l'orifice externe. L'exocol est la partie du col utérin située à l'interface avec la cavité vaginale. Le col utérin joue un rôle crucial pendant la grossesse et l'accouchement. En effet, lors d'une grossesse à terme, il s'assouplit progressivement mais reste fermé pour maintenir le fœtus dans l'utérus pendant la majeure partie de la période de gestation. Après 37 semaines d'aménorrhée, il commence à se raccourcir et à se dilater (maturation cervicale) en vue de l'accouchement, qui a lieu vers 41 semaines d'aménorrhée. En cas de naissance prématurée, la maturation cervicale a lieu avant la 37ème semaine d'aménorrhée.

La modification des propriétés mécaniques du col utérin pendant la grossesse est due au remodelage de sa microstructure. De nombreuses études ont montré que ce remodelage est un processus complexe impliquant majoritairement le collagène, qui est le principal composant microscopique du tissu conjonctif du col utérin. En effet, une augmentation de l'extractibilité et de la solubilité du collagène, ainsi qu'une réduction de sa concentration et de son organisation, ont été observées pendant la grossesse. La caractérisation du remodelage de la microstructure cervicale pendant la gestation à terme est cruciale pour comprendre l'évolution de ce processus dans le cas d'une grossesse à haut risque. A ce jour, de nombreuses techniques d'imagerie (rayons X, IRM, OCT, SHG, etc.) ont été testées à cette fin mais leur application clinique reste très limitée.

Ces dernières années, l'imagerie polarimétrique de Mueller s'est révélée très prometteuse pour les applications biomédicales. La lumière est un champ électromagnétique. La polarisation de la lumière est définie comme la trajectoire spatio-temporelle du champ électrique. Le formalisme de Mueller-Stokes représente la polarisation comme un vecteur quadridimensionnel appelé vecteur de Stokes qui peut être obtenu par

des mesures d'intensité lumineuse. Après interaction avec un échantillon, le vecteur de Stokes de la lumière incidente est modifié. La matrice de Mueller est une matrice réelle à 16 composantes qui relie le vecteur de Stokes à l'entrée au vecteur de Stokes à la sortie de l'échantillon. La mesure de cette matrice permet une caractérisation complète des propriétés d'anisotropie optique et de dépolarisation de l'échantillon.

En particulier, cette technique est bien adaptée à la caractérisation de la structure du collagène dans les tissus biologiques, dont l'anisotropie et les propriétés de diffusion peuvent produire des signatures polarimétriques spécifiques. Elle a donc été largement utilisée pour explorer la microstructure du col utérin riche en collagène. En effet, pour le tissu cervical, une forte anisotropie optique est généralement observée, qui semble être principalement générée par des fibres de collagène bien organisées. D'autre part, la forte dépolarisation de ce type de tissu est la signature du collagène désorganisé et d'autres composants microscopiques. L'avantage le plus significatif de l'imagerie polarimétrique de Mueller est qu'elle peut être mise en œuvre avec un champ de vision macroscopique (plusieurs dizaines de cm^2), tout en fournissant des informations sur la microstructure cervicale à une échelle beaucoup plus petite que la résolution spatiale réelle de l'image.

Une étude de faisabilité menée par les chercheurs du LPICM au CHU Brugman de Bruxelles (Belgique) sur 24 patientes enceintes à terme a montré que la dépolarisation du tissu cervical diminue avec l'avancement de la grossesse. Sur la base de ces résultats préliminaires, le projet de recherche COLPOTERME a été lancé en collaboration avec le CHU du Kremlin-Bicêtre (France) pour tester l'imagerie polarimétrique de Mueller sur un nombre massif de femmes enceintes.

Les travaux décrits dans ce manuscrit de thèse ont conduit au lancement d'un essai clinique pour tester l'imagerie polarimétrique de Mueller in vivo sur une cohorte de patientes enceintes, ce qui constitue une première mondiale. Un nouveau Colposcope polarimétrique de Muller (CPM) multispectral a été conçu et construit dans le cadre de ce travail de thèse. Ce système est capable d'acquérir des images de haute qualité in vivo tout en répondant aux principales exigences d'un essai clinique en termes de rapidité, de convivialité et d'ergonomie.

Le manuscrit de la thèse est structuré comme suit.

Le Chapitre 1 présente les principes de base de la polarimétrie de Mueller.

Le Chapitre 2 se concentre sur la description de l'anatomie et de la structure microscopique du col utérin. De plus, les résultats précédents obtenus au LPICM sur l'utilisation de l'imagerie polarimétrique de Mueller pour sonder le tissu cervical sont décrits.

Le Chapitre 3 présente la conception et le développement d'un nouveau CPM multispectral aux performances inégalées pour l'analyse in vivo du tissu cervical. Le nouveau CPM a été conçu pour acquérir des images polarimétriques à haute résolution en 1 seconde, simultanément à plusieurs longueurs d'onde dans la gamme spectrale visible, avec un champ de vision macroscopique. Les performances et la stabilité du CPM ainsi que l'ergonomie du système sont décrites en détail au Chapitre 4.

Le Chapitre 5 présente les résultats préliminaires de l'étude, qui sont assez spectaculaires. En effet, ces résultats montrent que l'imagerie polarimétrique de Mueller permet de visualiser efficacement les changements microstructuraux de l'exocol pendant la grossesse, qui sont difficiles à observer avec la colposcopie conventionnelle. En général, un épithélium pavimenteux stratifié (épithélium malpighien) tapisse la surface de l'exocol et contribue à protéger le col utérin contre la forte acidité du milieu vaginal. En revanche, une seule couche de cellules muqueuses cylindriques (épithélium glandulaire) tapisse le canal endocervical, qui est caractérisé par une très faible acidité. Le tissu conjonctif sous-tend les deux types d'épithélium. La zone de jonction, c'est-à-dire la limite entre l'épithélium pavimenteux et l'épithélium glandulaire, est généralement située autour de l'orifice externe. Cependant, en raison de changements hormonaux, l'orifice externe peut s'ouvrir, rendant l'épithélium glandulaire visible à la surface de l'exocol (ectropion). Au fil du temps, en raison de la forte acidité du vagin, l'épithélium glandulaire se transforme progressivement en épithélium pavimenteux mieux adapté à cet environnement (métaplasie). Ainsi, des zones d'épithélium pavimenteux, d'ectropion et de transformations métaplasiques peuvent être présentes à la surface de l'exocol au moment de l'acquisition des images polarimétriques.

Les résultats de cette thèse montrent, pour la première fois à notre connaissance, que les transformations métaplasiques de l'exocol impliquent non seulement l'épithélium mais aussi le tissu conjonctif sous-jacent. En effet, l'imagerie polarimétrique de Mueller permet de visualiser efficacement les modifications du tissu conjonctif sous-jacent à l'épithélium recouvrant l'exocol lors des transformations métaplasiques, qui sont très fréquentes dans la vie d'une femme et notamment pendant la grossesse en raison de fortes altérations hormonales. En particulier, les structures fibreuses du tissu conjonctif apparaissent très désorganisées pour l'épithélium glandulaire. Ces structures se réorganisent progressivement avec la progression des transformations métaplasiques jusqu'à devenir complètement organisées (avec une symétrie circulaire autour du canal endocervical) pour l'épithélium pavimenteux.

Sur la base de ces résultats, nous avons identifié les paramètres polarimétriques les plus pertinents qui permettent une segmentation très efficace des images polarimétriques du col utérin afin de distinguer sans ambiguïté les différents types de tissus cervicaux (épithélium pavimenteux, épithélium glandulaire, et différents degrés de métaplasie).

L'étape suivante consistera à développer des algorithmes de machine learning et de deep learning pour produire une segmentation automatique des images polarimétriques. Ces algorithmes seront ensuite utilisés pour étudier l'évolution des propriétés polarimétriques de chaque type de tissu identifié en fonction de la progression de la grossesse pour un grand nombre de patientes.

L'objectif final de cette recherche sera de déterminer une courbe de standardisation basée sur les paramètres polarimétriques les plus pertinents capables de monitorer l'évolution régulière de la grossesse. En effet, la connaissance du comportement typique des propriétés polarimétriques du col utérin au cours d'une grossesse à terme pourrait permettre de détecter des anomalies dans leur évolution et ainsi améliorer le diagnostic des naissances prématurées.

SUMMARY

Prematurity is the leading cause of perinatal mortality worldwide with an estimated rate of 6% in France and Europe and twice as high in the United States. The threat of spontaneous preterm birth is the most important complication of pregnancy. It can occur between 23 and 37 weeks of amenorrhea and is associated with changes in the shape of the cervix and sometimes with bleeding or early rupture of the membranes.

In current clinical practice, transvaginal ultrasound to measure cervical length is the recommended diagnostic technique for prematurity. However, because of the inability to correlate measured length with time to delivery, there is no clear guideline for the threshold of cervical length to accurately diagnose preterm birth. Despite considerable advances in modern medical technology, prediction of preterm birth remains a challenge. Therefore, a new approach for improving the diagnosis of preterm birth is needed to reduce health care costs, prevent the adverse effects of unnecessary hospitalizations, and pave the way for new treatment strategies.

The cervix is the lower part of the uterus that protrudes into the vagina. It is cylindrical in shape and is traversed along its whole length by the endocervical canal, which connects the vaginal lumen to the uterine cavity. The entrance to the endocervical canal on the vaginal side is called the external os. The ectocervix is the part of the cervix at the interface with the vaginal cavity. The cervix plays a crucial role during pregnancy and childbirth. In a full-term pregnancy, it gradually softens but remains closed to hold the fetus in the uterus for most of the gestation period. After 37 weeks of amenorrhea, it begins to shorten and dilate (cervical ripening) in preparation for delivery, which occurs at around 41 weeks of amenorrhea. In the case of premature birth, cervical ripening takes place before the 37th week of amenorrhea.

The change in the mechanical properties of the cervix during pregnancy is due to the remodeling of its microstructure. Numerous studies have shown this remodeling is a complex process mainly involving collagen, which is the principal microscopic component of the connective tissue of the uterine cervix. Indeed, an increase in the extractability and solubility of collagen, as well as a reduction in its concentration and organization, has been observed during pregnancy. The characterization of cervical microstructure remodeling during full-term gestation is crucial to understand the course of this process in a high-risk pregnancy. Many imaging techniques (X-ray, MRI, OCT, SHG, etc.) have been tested for this purpose but their clinical application remains very limited.

In recent years, Mueller polarimetric imaging has shown great promise for biomedical applications. Light is an electromagnetic field. The polarization of light is defined as the space-time trajectory of the electric field. The Mueller-Stokes formalism represents the polarization as a four-dimensional vector called Stokes vector which can be obtained by light intensity measurements. After interaction with a sample, the Stokes vector of the incident light is modified. The Mueller matrix is a 16-component real matrix that relates the Stokes vector at the input to the Stokes vector at the output of the sample. The measurement of this matrix allows a complete characterization of the optical anisotropy and depolarization properties of the sample.

In particular, this technique is well suited to characterize the structure of collagen in biological tissues, whose anisotropy and scattering properties can produce specific polarimetric signatures. Therefore it has been widely used to explore the microstructure of the cervix, rich in collagen. Indeed, for cervical tissue, a strong optical anisotropy is generally observed, which seems to be mainly generated by well-organized collagen fibers. On the other hand, the strong scattering of this type of tissue is the signature of disorganized collagen and other microscopic components. The most significant advantage of Mueller polarimetric imaging is that it can be implemented with a macroscopic field of view (several tens of cm^2), while providing information about the cervical microstructure at a scale much smaller than the actual spatial resolution of the image.

A feasibility study conducted by LPICM researchers at the Brugman University Hospital in Brussels (Belgium) on 24 full-term pregnant women showed that the depolarization of cervical tissue decreases as pregnancy progresses. Based on these preliminary results, the COLPOTERME research project was launched in collaboration with the University Hospital of Kremlin-Bicêtre (France) in order to test Mueller polarimetric imaging on a massive number of pregnant women.

The work described in this thesis manuscript has led to the initiation of a clinical trial (currently still in progress) for testing Mueller polarimetric imaging in vivo on a cohort of patients, which is a world first. A new multispectral Mueller Polarimetric Colposcope (MPC) was designed and built as part of this thesis work. This system is capable of acquiring high quality images in vivo while meeting the main requirements of a clinical trial in terms of speed, usability and ergonomics.

The thesis manuscript is structured as follows.

Chapter 1 presents the basic principles of Mueller polarimetry.

Chapter 2 focuses on the description of the anatomy and microscopic structure of the cervix. In addition, previous results obtained at LPICM on the use of Mueller polarimetric imaging to probe cervical tissue are described.

Chapter 3 presents the design and development of a novel multispectral MPC with unparalleled performance for in vivo analysis of cervical tissue. Indeed, it allows the acquisition of high-resolution polarimetric images in 1 second, simultaneously at multiple wavelengths in the visible spectral range, with a macroscopic field of view. The performance and stability of the MPC, as well as the ergonomics of the system are described in detail in Chapter 4.

Chapter 5 presents the preliminary results of the study. These results show that Mueller polarimetric imaging can effectively visualize microstructural changes of the ectocervix during pregnancy, which are difficult to observe with conventional colposcopy. In general, a stratified squamous epithelium (Malpighian epithelium) lines the surface of the ectocervix and helps to protect the cervix from the high acidity of the vaginal environment. In contrast, a single layer of columnar mucous cells (glandular epithelium) lines the endocervical canal, which is characterized by very low acidity. Connective tissue underlies

both types of epithelium. The junction zone, i.e., the boundary between the squamous and glandular epithelium, is usually located around the external os. However, due to hormonal changes, the external os may open, making the glandular epithelium visible on the surface of the ectocervix (ectropion). Over time, due to the high acidity of the vagina, the glandular epithelium gradually changes into squamous epithelium better adapted to this environment (metaplasia). Thus, areas of squamous epithelium, ectropion and metaplastic transformations may be present on the surface of the ectocervix at the moment of acquisition of polarimetric images.

The results of this thesis show, for the first time to our knowledge, that metaplastic changes in the ectocervix involve not only the epithelium but also the underlying connective tissue. Indeed, Mueller polarimetric imaging allows to efficiently visualize changes in the connective tissue underlying the epithelium covering the ectocervix during metaplastic transformations, which are very frequent in a woman's life and especially during pregnancy due to strong hormonal changes. In particular, the fibrous structures of the connective tissue appear highly disorganized for the glandular epithelium. These structures progressively reorganize with the progression of metaplastic transformations until they become fully organized (with circular symmetry around the endocervical canal) for the squamous epithelium.

Based on these results, we have identified the most relevant polarimetric parameters that allow a very efficient segmentation of polarimetric images of the cervix in order to unambiguously distinguish the different types of cervical tissue (squamous epithelium, glandular epithelium, and various degrees of metaplasia).

The next step will be to develop machine learning and deep learning algorithms to produce automatic segmentation of polarimetric images. These algorithms will then be used to study the evolution of the polarimetric properties of each type of tissue identified as a function of pregnancy progression for a large number of patients.

The final objective of this research will be to determine a standardization curve based on the most relevant polarimetric parameters capable to monitor the steady evolution of the pregnancy. Indeed, knowing the typical behavior of the cervical polarimetric properties during a full-term pregnancy could allow the detection of anomalies in their evolution and thus improve the diagnosis of preterm births.

Chapter 1

Mueller Polarimetry

In this thesis, a preclinical study of a novel medical imaging method based on polarization of light is reported. The polarization of light is a property of propagating electromagnetic waves, defined by the trajectory of an electric field evolving in a plane orthogonal to the direction of propagation. Any polarization state can be represented by a Stoke vector and the Mueller matrix describes the changes of the Stokes vector after an interaction with the medium. Elements of Mueller matrix define the effects of the optical anisotropy and scattering ability of the matter. In biological samples, optical anisotropy is associated with fibrous proteins in connective tissue. Scattering properties are attributed to the large particles in the tissue. Therefore, Mueller polarization imaging technique provides additional information related to the microstructure of the tissue because the naked eye detects only the intensity of light regardless of the polarization of light. In this chapter, the basics of polarization of light and approaches to analyze measured Mueller matrix imaging data are explained to provide methods to analyze and understand the measurement data.

1.1 Polarization ellipse

An electromagnetic wave consists of a space-time varying electric field $\boldsymbol{E}(\boldsymbol{r}, t)$ and magnetic field $\boldsymbol{B}(\boldsymbol{r}, t)$, which are associated each other by Maxwell's equations. In empty space, these fields are orthogonal to each other and oscillate simultaneously in a plane orthogonal to the direction of light propagation. Here, the polarization of light is defined as the trajectory described by the electric field vector in the plane.

We will use a Cartesian coordinate system (x, y, z) to describe an electric field, where $\hat{e}_x$, $\hat{e}_y$, and $\hat{e}_z$ represent the 3 orthogonal unit vectors. In the empty space, a planar electromagnetic plane wave $\boldsymbol{E}(z, t)$ propagating along the z-direction can be written as:

$$\boldsymbol{E}(z, t) = E_x(z, t)\hat{e}_x + E_y(z, t)\hat{e}_y \tag{1-1}$$

In equation (1-1), the z component of $\boldsymbol{E}(z,t)$ is zero because of the transverse nature of the electromagnetic wave in the empty space. The x and y components E_x and E_y can be written as follows:

$$\begin{aligned} E_x(z,t) &= A_x \cos(\omega t - kz + \phi_x) \\ E_y(z,t) &= A_y \cos(\omega t - kz + \phi_y) \end{aligned} \tag{1-2}$$

Where A_x and A_y denote the maximum amplitudes of the electric field along the x and y directions, respectively. ϕ_x and ϕ_y are the phase shifts along x and y directions. ω and k denote the angular frequency and wavenumber.

$$\begin{aligned} \omega &= 2\pi f \\ k &= 2\pi/\lambda \end{aligned} \tag{1-3}$$

f and λ are the frequency and the wavelength of the electromagnetic wave. The term $\omega t - kz$ can be eliminated from equation (1-2). Finally, we can obtain the following ellipse equation[1]:

$$\frac{E_x^2(z,t)}{A_x^2} + \frac{E_y^2(z,t)}{A_y^2} - \frac{2E_x(z,t)E_y(z,t)}{A_x A_y}\cos\delta = \sin^2\delta \tag{1-4}$$

Where $\delta = \phi_x - \phi_y$ denotes the phase shift between the x and y components of the field. Equation (1-4) defines the polarization ellipse in the x-y plane for a fixed value of z. An example of polarization ellipse is shown in Figure 1.1.

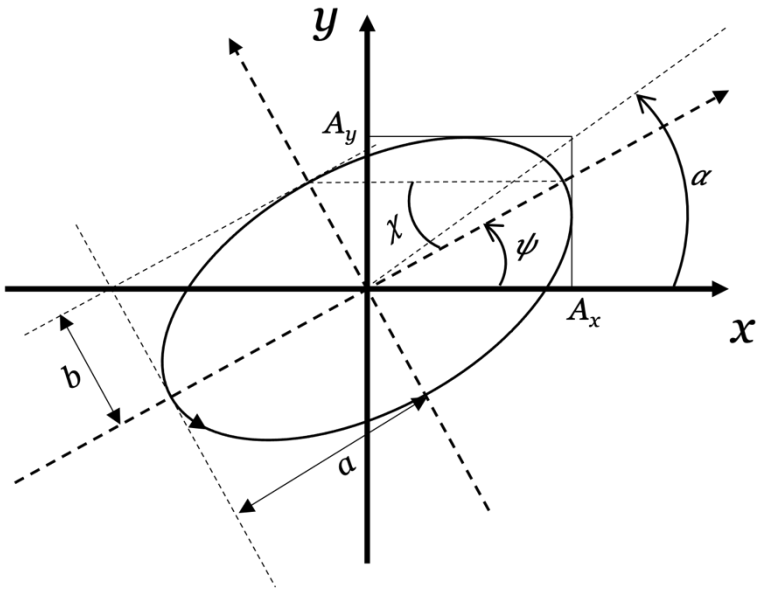

Figure 1.1 An example polarization ellipse expressed by 2 orthogonal components along x and y-axis. The wave is propagating along z-axis. The ellipse can be defined by the ratio between the long and short axis, χ, the orientation of the long axis, ψ, and the max electric field along x- and y- axis, A_x and A_y.

A polarization state can be fully defined by the four parameters of this ellipse. 1) the lengths a and b of the major and minor axis of the ellipse, respectively; 2) the azimuth angle $\psi \in [0, \pi]$, the inclination of the major axis of the ellipse; 3) the ellipticity angle $|\chi| \in [0, \frac{\pi}{4}]$, the arctangent of the ratio between the vertex and co-vertex. 4) the auxiliary angle $\alpha \in [0, \pi/2]$. These parameters are associated with the amplitude of the field A_x and A_y and the phase shift δ by the following trigonometric equations[1]:

$$\begin{aligned} \tan 2\psi &= \frac{2A_xA_y \cos\delta}{A_x^2 - A_y^2} \\ \sin 2\chi &= \frac{2A_xA_y \sin\delta}{A_x^2 + A_y^2} \\ \tan\alpha &= \frac{A_y}{A_x} \end{aligned} \tag{1-5}$$

It is also worthwhile to note the following relations[1].

$$\begin{aligned} \cos 2\chi \cos 2\psi &= \cos\alpha \\ \cos 2\chi \sin 2\psi &= \sin 2\alpha \cos\delta \\ \sin 2\psi &= \sin 2\alpha \sin\delta \\ \tan 2\psi &= \tan 2\alpha \cos\delta \end{aligned} \tag{1-6}$$

In equations (1-5), when δ is in the range $[0, \pi]$ or $[-\pi, 0]$, the light is said to be elliptically polarized. Especially, when δ is positive, the light is said to be right elliptically polarized as the electric field turns clockwise for an observer who sees the wave coming towards him/her. On the contrary, when δ is negative, the light is said left elliptically polarized. If $\delta = 0$ or π the ellipse becomes a straight line, and the light is said to be linearly polarized, as shown in Figure 1.2a. Finally, when $\delta = \pi/2$ or $-\pi/2$ and $A_x = A_y$ the light is said to be circularly polarized since the ellipse is reduced to a circle, as shown in Figure 1.2b. In particular, $\delta = \pi/2$ refers to right circularly polarized light, while $\delta = -\pi/2$ to left circularly polarized light.

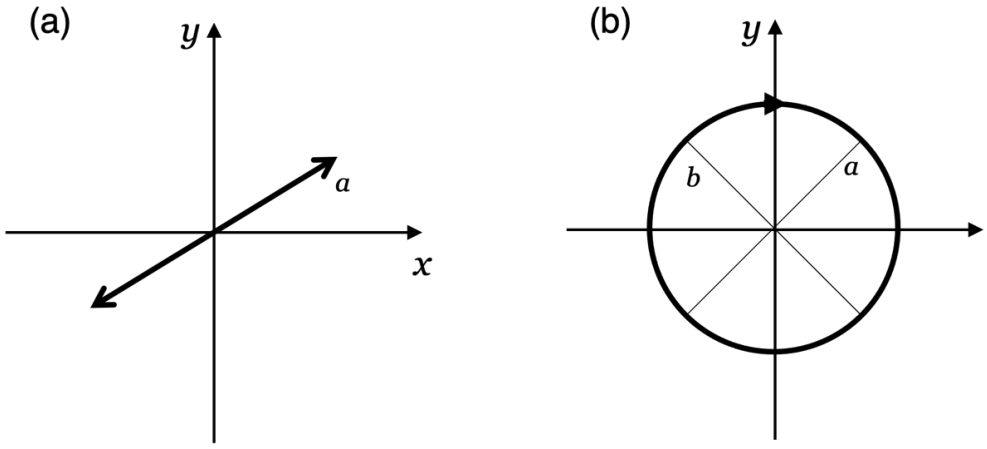

Figure 1.2 (a) Example of linear polarization ($\delta = 0$). (b) Right circular polarization ($\delta = \pi/2$).

1.2 Mueller Stokes formalism

Although the polarization of an electromagnetic wave can be described using the polarization ellipse as described in the previous section, but only for totally polarized light. This is a serious limitation because the polarization of light is often partially or completely depolarized in the real world.

Also, in the visible range, the typical oscillation time of an electric field is in the order of 10^{-15}s. This short time is the time required for the electric field to capture an individual ellipse, circle, or straight line. However, the only physical quantity that can be measured by a photo detector is the intensity of the light, i.e., the square of the electric field, averaged over an integration time.

In this section, the Stokes-Mueller formalism is described. This formalism represents the polarization of light using a four-dimensional real intensity vector $\boldsymbol{S}$ called the Stokes vector. By using this formalism, we can describe the polarization states of partially or totally depolarized light.

1.2.1 Stokes vector

To introduce the Stoke vector, first we set z to 0 in equation (1-4) because the plane wave does not change up to the position z when the field is averaged over an integration time. In the case of an integration time much longer than the oscillation time of light, the polarization ellipse averaged over time can be written:

$$\frac{\langle E_x^2(t)\rangle}{A_x^2}+\frac{\langle E_y^2(t)\rangle}{A_y^2}-\frac{2\langle E_x(t)E_y(t)\rangle}{A_xA_y}\cos\delta=\sin^2\delta \tag{1-7}$$

where <> denotes the time averaging defined as:

$$< E_i(t)E_j(t) >= \frac{1}{T}\int_0^T E_i(t)E_j(t)dt \tag{1-8}$$

Equation (1-7) can be simplified when the integration time T is much greater than the period $1/f$ of the electromagnetic wave and the polarization state is constant over time [1]:

$$\left(A_x^2+A_y^2\right)^2-\left(A_x^2-A_y^2\right)^2-\left(2A_xA_y\cos\delta\right)^2-\left(2A_xA_y\sin\delta\right)^2=0 \tag{1-9}$$

In equation (1-9), the four terms in parentheses correspond to the 4 elements of the Stokes vector $\boldsymbol{S}$ defined as:

$$\boldsymbol{S}=\begin{bmatrix}S_0\\S_1\\S_2\\S_3\end{bmatrix}=\begin{bmatrix}A_x^2+A_y^2\\A_x^2-A_y^2\\2A_xA_y\cos\delta\\2A_xA_y\sin\delta\end{bmatrix}=\begin{bmatrix}I_{0^\circ}+I_{90^\circ}\\I_{0^\circ}-I_{90^\circ}\\I_{45^\circ}-I_{135^\circ}\\I_{\circlearrowleft}-I_{\circlearrowright}\end{bmatrix} \tag{1-10}$$

where the elements S_0, S_1, S_2 and S_3 are called Stokes parameters. The elements S_0, S_1 and S_2 are associated with $I_{0°}$, $I_{90°}$, $I_{45°}$ and $I_{135°}$ which are the intensities of polarized light along the x-axis (0°), the y-axis (90°), and at 45° and 135° (with respect to the x-axis). S_3 can be written in terms of $I_{↺}$ and $I_{↻}$, the intensities of Right Circular (↺) and Left Circular (↻) polarization components, respectively. Then, equation (1-9) can be rewritten using S_0, S_1, S_2 and S_3:

$$S_0 \geq \sqrt{S_1^2 + S_2^2 + S_3^2} \tag{1-11}$$

Where the equality is obtained only for purely polarized light and the inequality is obtained for partially polarized light. For completely depolarized light, $S_1 = S_2 = S_3 = 0$ is satisfied. In this case, equation (1-11) can be rewritten as:

$$S_0^2 = 0 \tag{1-12}$$

In the case of partially polarized light, equation (1-11) can be rewritten as:

$$S_0^2 > 0 \tag{1-13}$$

Based on the inequality (1-11), the degree of polarization (DoP) of a light beam can be defined:

$$DoP = \frac{\sqrt{S_1^2 + S_2^2 + S_3^2}}{S_0} \leq 1 \tag{1-14}$$

According to equation (1-6) and (1-10), the Stokes vector can be rewritten in the normalized form as:

$$\boldsymbol{S} = S_0 \begin{bmatrix} 1 \\ S_1/S_0 \\ S_2/S_0 \\ S_3/S_0 \end{bmatrix} = S_0 \begin{bmatrix} 1 \\ \cos 2\chi \cos 2\psi \\ \cos 2\chi \sin 2\psi \\ \sin 2\chi \end{bmatrix} = S_0 \begin{bmatrix} 1 \\ \cos 2\alpha \\ \sin 2\alpha \cos \phi \\ \sin 2\alpha \sin \phi \end{bmatrix} \tag{1-15}$$

Table 1.1 shows some examples of Stokes vectors with their corresponding shape of polarization.

Table 1.1 Some examples of Stokes vectors. The first row indicates the forms of varios polarizations. From the left: unpolarized, 0° (horizontal), 90°(vertical), 45°, 135°, ↺ (right circular), ↻ (left circular), and an elliptical polarization in general form. The second row shows their Stokes vector.

Stokes vector	Unpolarized	0°	90°	45°	+135°	↺	↻	Elliptical
$\begin{bmatrix} 1 \\ S_1/S_0 \\ S_2/S_0 \\ S_3/S_0 \end{bmatrix}$	$\begin{bmatrix} 1 \\ 0 \\ 0 \\ 0 \end{bmatrix}$	$\begin{bmatrix} 1 \\ 1 \\ 0 \\ 0 \end{bmatrix}$	$\begin{bmatrix} 1 \\ -1 \\ 0 \\ 0 \end{bmatrix}$	$\begin{bmatrix} 1 \\ 0 \\ 1 \\ 0 \end{bmatrix}$	$\begin{bmatrix} 1 \\ 0 \\ -1 \\ 0 \end{bmatrix}$	$\begin{bmatrix} 1 \\ 0 \\ 0 \\ 1 \end{bmatrix}$	$\begin{bmatrix} 1 \\ 0 \\ 0 \\ -1 \end{bmatrix}$	$\begin{bmatrix} 1 \\ \cos 2\chi \cos 2\psi \\ \cos 2\chi \sin 2\psi \\ \sin 2\chi \end{bmatrix}$

1.2.2 Mueller matrix

When light travels a sample, its polarization state can change by light-matter interactions. Herein, let $\boldsymbol{S}_{out}$ be the Stokes vector of light leaving the sample and $\boldsymbol{S}_{in}$ be the Stokes vector of light incident on the sample. Then, the (linear) modifications of the incident Stokes vectors can be expressed as:

$$\boldsymbol{S}_{out} = \boldsymbol{M}\boldsymbol{S}_{in}$$
$$\boldsymbol{M} = \begin{bmatrix} M_{11} & M_{12} & M_{13} & M_{14} \\ M_{21} & M_{22} & M_{23} & M_{24} \\ M_{31} & M_{32} & M_{33} & M_{34} \\ M_{41} & M_{42} & M_{43} & M_{44} \end{bmatrix} \tag{1-16}$$

The linear modification $\boldsymbol{M}$ in equation (1-16) is called the Mueller matrix. It consists of 16 real elements providing a full description about the polarimetric properties of the sample.

For the Mueller matrix, certain physical constraints must be satisfied. First, it has to produce an outgoing Stokes vector satisfying the inequality in (1-11). Second, the elements of the Mueller matrix of a non-fluorescent medium have to satisfy the following condition[2]:

$$\begin{gathered} \mathrm{tr}(\boldsymbol{M}\boldsymbol{M}^T) = \sum_{i=1}^{4} M_{ii}^2 \le 4M_{11}^2, \\ \left|M_{ij}\right| \le M_{11} \\ \forall i,j:\ 1 \le i,j \le 4 \end{gathered} \tag{1-17}$$

Where tr() denotes the trace of a square matrix. In the next section, anisotropic light-matter interactions and depolarizing ability of media are described using the Stokes-Mueller matrix formalism.

1.2.3 Description of the main polarimetric effects

Birefringence

In a birefringent media, 2 refractive indices are defined, the higher and lower index which respectively lead to slower and faster light propagation. Usually, the refractive index along the slow axis is denoted by n_e, the extraordinary index, and the refractive index along

the fast axis is denoted by n_o, the ordinary index. These anisotropic refractive indices cause the optical path different between the 2 orthogonal states, consequently, phase retardation δ occurs.

$$\Delta n = n_e - n_o$$
$$\delta = \frac{2\pi}{\lambda}\Delta n d \tag{1-18}$$

d denotes the propagation length of the beam and λ denotes the wavelength of light. The phase retardance δ is often also referred to as '***retardance***'. Optical filters designed to induce phase retardation are named as retarders or waveplates. In particular, the waveplates causing retardance of quarter wave ($\lambda/4$) and half wave ($\lambda/2$) are called the quarter-waveplate (QWP) and half-waveplate (HWP). The waveplates that have two linear orthogonal axes (eigenstates) are referred to as the linear retarders. It is also worthwhile to note that δ of those waveplates depends on the wavelength due to the dispersion.

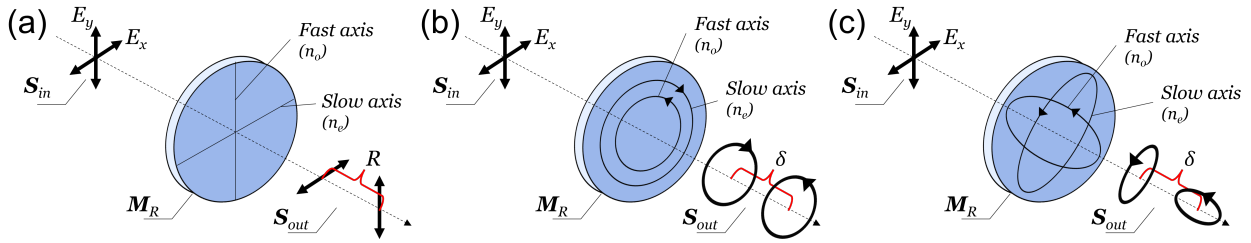

Figure 1.3 A scheme of phase retardation in two electric fields. (a) linear retarder, (b) circular retarder, and (c) elliptical retarder. The retarders have 2 refractive indeices, n_o and n_e, along 2 optical eigenaxes (the fast and slow axes). The anisotropic refractive indices cause a phase retardation δ, which can be denoted by the Mueller matrix of the retarder M_R.

One can notice that by (1-10) the phase retardation can modify the incoming polarization state of the beam. This modification of polarization can be expressed in the form of the Mueller matrix[1]. In particular, a 'linear' phase retarder with the slow axis parallel to the laboratory reference frame can be written:

$$\boldsymbol{M}_R(R) = \begin{bmatrix} 1 & 0 & 0 & 0 \\ 0 & 1 & 0 & 0 \\ 0 & 0 & \cos R & \sin R \\ 0 & 0 & -\sin R & \cos R \end{bmatrix} \tag{1-19}$$

We use the symbol 'R' to indicate 'linear' phase retardance in sample analysis. On the other hand, the in-plane rotation of anisotropic optical components can be obtained by the rotation of the Mueller matrix of the component at axis 0°[1], [3].

$$\boldsymbol{M}_{rot}(\theta) = \begin{bmatrix} 1 & 0 & 0 & 0 \\ 0 & \cos 2\theta & -\sin 2\theta & 0 \\ 0 & \sin 2\theta & \cos 2\theta & 0 \\ 0 & 0 & 0 & 1 \end{bmatrix} \tag{1-20}$$

Where θ denotes the in-plane orientation (positive sign for counterclockwise and negative sign for clockwise). Therefore, the Mueller matrix of a linear retardance oriented in its azimuthal orientation is:

$$\boldsymbol{M}_R(R,\alpha) = \boldsymbol{M}_{rot}(\alpha)\boldsymbol{M}_R(R)\boldsymbol{M}_{rot}(-\alpha)$$
$$= \begin{bmatrix} 1 & 0 & 0 & 0 \\ 0 & \cos^2 2\alpha + \sin^2 2\alpha \cos R & \sin 2\alpha \cos 2\alpha\,(1-\cos R) & -\sin 2\alpha \sin R \\ 0 & \sin 2\alpha \cos 2\alpha\,(1-\cos R) & \sin^2 2\alpha + \cos^2 2\alpha \cos R & \cos 2\alpha \sin R \\ 0 & \sin 2\alpha \sin R & -\cos 2\alpha \sin R & \cos R \end{bmatrix} \quad (1\text{-}21)$$

We specially use the symbol 'α' to indicate the azimuth of linear retarder in sample analysis. There also exist circular and elliptical retarders that have two orthogonal eigen states of circular and elliptical shape; however, these types of retardance are canceled out in the reflective imaging configuration. Therefore, retardance in this thesis denotes the linear retardance R.

The interpretable anisotropic parameters of a retarder such as retardance and orientation can be extracted through the elements of the Mueller matrix of retarder in (1-21) . If a sample is assumed to be a pure retarder, each element of the measured Mueller matrix of the sample has the form (1-21). With simple trigonometry, the linear retardance R can be obtained as[1]:

$$R = \operatorname{acos}\left(\frac{tr(\boldsymbol{M}_R)}{2} - 1\right) \quad (1\text{-}22)$$

Then, the in-plane orientation α of the slow axis can be found[1]:

$$\phi = \frac{1}{2}\operatorname{atan}\left(\frac{M_{24}}{M_{43}}\right), \qquad \phi \in [-45°, 45°] \quad (1\text{-}23)$$

Because of range of equation (1-23) is 90°, an additional conversion to expand the range to be (0°-180°) is needed:

$$\alpha = \begin{cases} \phi, & \forall \frac{M_{24}}{M_{43}} > 0 \; and \; M_{24} > 0 \\ 90° - |\phi|, & \forall \frac{M_{24}}{M_{43}} < 0 \; and \; M_{24} > 0 \\ 90° + \phi, & \forall \frac{M_{24}}{M_{43}} > 0 \; and \; M_{24} < 0 \\ 180° - |\phi|, & \forall \frac{M_{24}}{M_{43}} < 0 \; and \; M_{24} < 0 \end{cases}, \qquad \alpha \in [0°, 180°] \quad (1\text{-}24)$$

The uncertainty in the determination of α using the formula (1-24) becomes large when R is close to zero or if α~0° (for any value of R).

Dichroism

Dichroism denotes the property of materials exhibiting anisotropic light absorption, and more generally diattenuation denotes all types of anisotropic light attenuation including anisotropic absorption and reflection. The cause of dichroism is mainly the anisotropic resonance in the induced dipole-light interaction. By common definition, diattenuation D is defined as the extinction contrast between two orthogonal states:

$$D = \frac{T_{\parallel} - T_{\perp}}{T_{\parallel} + T_{\perp}} \in [0,1] \; where \; T_{\parallel} > T_{\perp}$$
$$T = \frac{I_{after}}{I_{before}} \in [0,1] \tag{1-25}$$

Where T denotes the ratio of light intensity before/after interaction. The most representative diattenuating optical component might be a polarizer. There are two common types of polarizers: a dichroic polarizer that polarizes light through an anisotropic absorption process and a wire-grid polarizer that polarizes light through an anisotropic reflection process. In the case of polarizers, the more transmissive axis is often referred to as the transmission axis $T_{\parallel}$, and the attenuating axis is referred to as $T_{\perp}$. A polarizer with D=1 is called the perfect polarizer, and most of polarizers have a diattenuation close to 1. Conversely, D=0 corresponds to an isotropic neutral density filter.

The most common form of diattenuation might be linear diattenuation. Linear diattenuation has two orthogonal linear states, as shown in Figure 1.4a. There can also exist circular diattenuation that has two orthogonal circular eigenstates, left- and right-hand polarizations, as shown in Figure 1.4b. The most general form of polarizers is an elliptical polarizer as shown in Figure 1.4c.

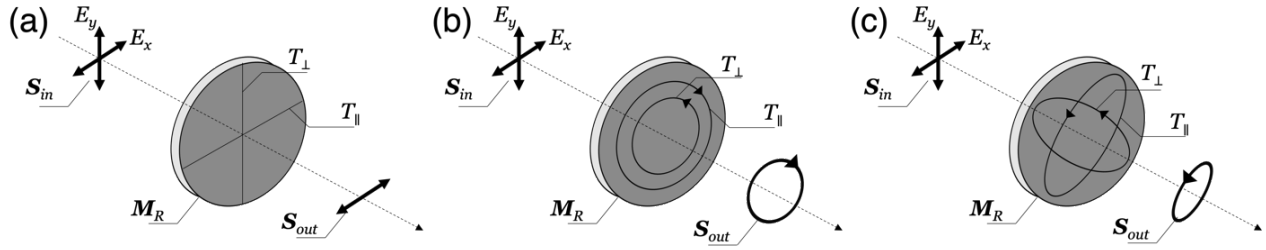

Figure 1.4 A scheme of three types of diattenuators. It can be illustrated by 2 different optical transmittances $T_{\perp}$ and $T_{\parallel}$ along 2 orthogonal eigenstates. (a) linear, (b) circular, (c) elliptical. The diattenuating behavior of a material can be expressed by a Mueller matrix of a linear diattenuator M_D.

The Mueller matrix of a linear diattenuator rotated by an angle θ is defined by[1]:

$$q_1 = (T_{\parallel} + T_{\perp}), q_2 = (T_{\parallel} - T_{\perp}), q_3 = 2\sqrt{T_{\parallel} T_{\perp}}$$
$$\boldsymbol{M}_{\mathrm{D}}(D,\theta) = \boldsymbol{M}_{rot}(\theta)\boldsymbol{M}_{\mathrm{D}}(D)\boldsymbol{M}_{rot}(-\theta)$$
$$= \frac{1}{2}\begin{bmatrix} q_1 & q_2\cos 2\theta & q_2 \sin 2\theta & 0 \\ q_2\cos 2\theta & q_1\cos^2 2\theta + q_3 \sin^2 2\theta & (q_1 - q_3)\cos 2\theta \sin 2\theta & 0 \\ q_3 \sin 2\theta & (q_1 - q_3)\cos 2\theta \sin\theta & q_1 \sin^2 2\theta + q_3 \cos^2 2\theta & 0 \\ 0 & 0 & 0 & q_3 \end{bmatrix} \tag{1-26}$$

The general form of the Mueller matrix of a diattenuator can be written based on the ellipse geometry in Figure 1.1[1]:

$$T_0 = \frac{T_\parallel + T_\perp}{2}, \qquad \overline{D} = \sqrt{1 - D^2}$$
$$a = \cos 2\chi \cos 2\psi\,, \qquad b = \cos 2\chi \sin 2\psi\,, \qquad c = \sin 2\chi$$
$$\boldsymbol{M}_{\mathrm{D}} = T_0 \begin{bmatrix} 1 & aD & bD & cD \\ aD & \overline{D} + (1-\overline{D})a^2 & ab(1-\overline{D}) & ac(1-\overline{D}) \\ bD & ab(1-\overline{D}) & \overline{D} + (1-\overline{D})b^2 & bc(1-\overline{D}) \\ cD & ac(1-\overline{D}) & bc(1-\overline{D}) & \overline{D} + (1-\overline{D})c^2 \end{bmatrix} \tag{1-27}$$

By the geometric definition of the elliptical polarization in Figure 1.1 and (1-10), diattenuation along three polarization axes can be extracted.

$$\begin{aligned} D_{0^\circ} &= \frac{T_{0^\circ} - T_{90^\circ}}{T_{0^\circ} + T_{90^\circ}} = \frac{M_{21}}{M_{11}} \\ D_{45^\circ} &= \frac{T_{45^\circ} - T_{135^\circ}}{T_{45^\circ} + T_{135^\circ}} = \frac{M_{31}}{M_{11}} \\ D_{\circlearrowleft} &= \frac{T_{\circlearrowleft} - T_{\circlearrowright}}{T_{\circlearrowleft} + T_{\circlearrowright}} = \frac{M_{41}}{M_{11}} \\ D &= \sqrt{D_{0^\circ}^2 + D_{45^\circ}^2 + D_{\circlearrowleft^\circ}^2} \end{aligned} \tag{1-28}$$

Where D_{0°, D_{45°, and $D_{\circlearrowleft}$ are the diattenuation along the 0°, 45°, and right-handed circular axes with respect to the laboratory frame. However, since the origin of diattenuation in cervical tissue is only the surface condition, the diattenuation effect is negligible in cervical tissues[4].

Depolarization

Based on the DoP in (1-14), one more polarimetric property can be defined in the Stokes-Mueller formalism. That is, depolarization. The depolarizer is a generic term indicating an optical component that reduces the DoP of incoming polarizations. As mentioned earlier, the decrease in DoP results from the incoherent sum of Stokes vectors of the integrated light. The incoherent sum of Stokes vectors can be written[5]:

$$\begin{gathered} \boldsymbol{S}_{\mathrm{out}} = \sum_n \boldsymbol{S}_{\mathrm{out,i}} = \left(\sum_n p_i \boldsymbol{M}_i \right) \boldsymbol{S}_{in} = \boldsymbol{M}\boldsymbol{S}_{in} \\ \sum_i p_i = 1, p_i \geq 0 \end{gathered} \tag{1-29}$$

Where $\boldsymbol{M_i}$ denotes the non-depolarizing Mueller matrix along the *i-th* optical path, and p_i denotes the intensity ratio or probability of passing the *i-th* path. The depolarizing process is illustrated in Figure 1.5. The pure incoming state $\boldsymbol{S_{in}}$ is divided into various states by the spatial heterogeneity of the medium. This heterogenous interface is often referred to as scattering media[5]. Arbitrary interfaces formed by heterogenous systems result in the splitting of the incoming state. When these outcoming polarizations are detected by a single

detector, the signal is determined by the intensity ratio between the divided states. Consequently, the incoherent sum of the integrated Mueller matrices is detected[5].

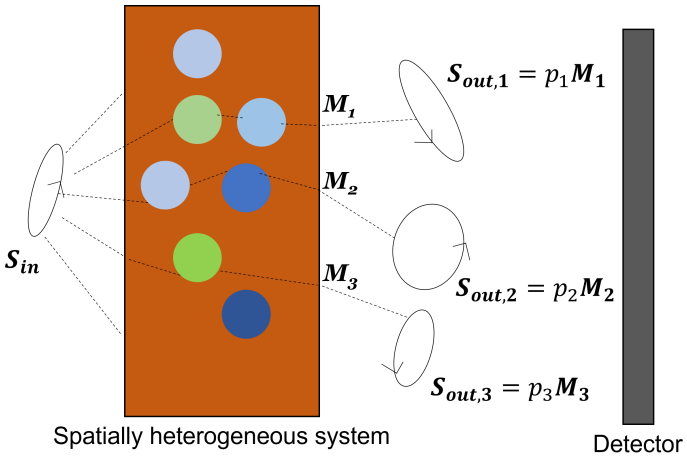

Figure 1.5 A scheme of depolarization effects in Mueller polarimetry. Each path propagating in a spatially heterogeneous medium forms diverged polarization states. The detector integrates these states as incoherent sum as expressed in (1-29).

Similarly, temporal randomness of detected state during the integration time can also cause depolarization. If the probability p_i is uniform, i.e., the paths are equiprobable, the medium is said to be completely depolarizing and leads to DoP=0 [5]. The depolarization effect of the incoherent sum can be written in the forms of some canonical matrices of the depolarizer[6]. The most commonly used depolarizer might be the diagonal depolarizer.

$$\boldsymbol{M}_{\Delta}(a,b,c) = \begin{bmatrix} 1 & 0 & 0 & 0 \\ 0 & a & 0 & 0 \\ 0 & 0 & b & 0 \\ 0 & 0 & 0 & c \end{bmatrix} \qquad (1\text{-}30)$$
$$a, b, c \in [-1,1]$$

a, b, and c represent the depolarizing factors for S_2, S_3, and S_4 of the Stokes vector, respectively. The matrix multiplication of $\boldsymbol{M}_{\boldsymbol{\Delta}}$ lead to a decrease of DoP of the Stoke vector. Total depolarizing power of a diagonal depolarizer is then defined as:

$$\boldsymbol{\Delta} = 1 - \frac{tr(|\boldsymbol{M}_{\boldsymbol{\Delta}}|) - 1}{3} \qquad (1\text{-}31)$$

1.3 Implementation of Mueller polarimetry

Measuring the Mueller matrix $\boldsymbol{M}$ of a sample allows the characterization of all main polarimetric properties, including optical anisotropy and scattering. This section describes the implementation of Mueller polarimetry for the measurement of the Mueller matrix $\boldsymbol{M}$ of a sample.

The Mueller matrix is about how a medium transforms the incoming polarizations. One can easily reach to the simple idea of the measurement of the Mueller matrix: " Then, let's try illuminating some polarization states on the target and see how the medium transforms the illuminated states." The actual practice is not far from this idea. The

measurement of the Mueller matrix can be performed using a Mueller polarimeter which consists of the following basic components: 1) a light illumination system, 2) a polarization state generator (PSG), 3) a polarization state analyzer (PSA), and 4) a photodetector.

The combination of the illumination system and the PSG play the role of the illumination of polarized light. The PSG functions to generate polarized light from the unpolarized light of the illumination system. In other words, the PSG is a type of polarizing filters, i.e., a polarizer. What is different from ordinary polarizers is that the PSG is designed to dynamically generate "four" polarization states.

On the other hand, the combination of the photodetector and the PSA plays the role of detecting the transformed states. The photodetector simply measures the time-averaged light intensity rather than the polarization state of light. The PSA encodes polarization states into different intensities of light. Therefore, the PSA enables the photodetector to be sensitive to polarization states. Like the PSG, the PSA can encode (or analyze) an incoming state into "four" different intensities. One might notice that the four states in the illumination and the four states in the detection result in 16 combinations of intensity which correspond to the dimensionality of the Mueller matrix – 16 elements.

The most widespread are the time-sequential Mueller polarimeters which perform 16 intensity measurements one after the other. In particular, during this thesis work, we worked with a sequential Mueller polarimeter based on Ferroelectrics Liquid Crystals (FLCs) which can be promisingly used for different types of applications ranging from microelectronics to biomedical diagnostics as discussed in detail in Chapter 3[7].

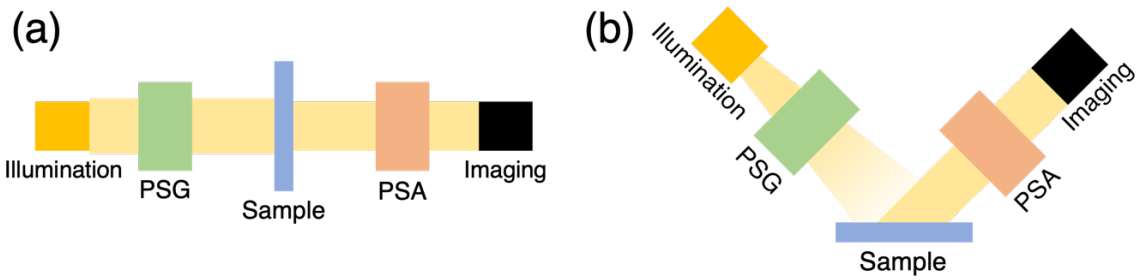

Figure 1.6 Two imaging configurations combined with the Mueller polarimetric system. (a) Transmission configuration. (b) Reflection configuration.

For a sequential Mueller polarimeter, the PSG illuminates four different polarizations of light by consecutively generating four independent, probing polarization states. Each of four states is described by a Stokes vector $\boldsymbol{S_{Wi}}$ (i = 1 to 4). These four Stokes vectors produced by the PSG can be horizontally concatenated as the columns of a modulation matrix named $\boldsymbol{W}$.

$$\boldsymbol{W} = [\boldsymbol{S_{W1}} \quad \boldsymbol{S_{W2}} \quad \boldsymbol{S_{W3}} \quad \boldsymbol{S_{W4}}] \tag{1-32}$$

The light re-emitted from the sample passes through the PSA located in front of the detector as shown in Figure 1.6. Each of the four polarization states that illuminated the sample through the consecutive modulation of the PSG is analyzed through four consecutive

polarization configurations of the PSA after interacting with the sample. Each of the four polarization configurations of the PSA is described by a Stokes vector $\mathbf{S_{Ai}}$ (i = 1 to 4). These four Stokes vectors produced by the PSA can be vertically concatenated as the rows of an analysis matrix named $\boldsymbol{A}$.

$$\boldsymbol{A} = [\boldsymbol{S_{A1}} \quad \boldsymbol{S_{A2}} \quad \boldsymbol{S_{A3}} \quad \boldsymbol{S_{A4}}]^{\top} \tag{1-33}$$

In this way, at least 16 intensity measurements are sequentially performed and regrouped into a 4×4 real matrix B which can be expressed as:

$$\boldsymbol{B} = \boldsymbol{AMW} = \begin{bmatrix} b_{11} & b_{12} & b_{13} & b_{14} \\ b_{21} & b_{22} & b_{23} & b_{24} \\ b_{31} & b_{32} & b_{33} & b_{34} \\ b_{41} & b_{42} & b_{43} & b_{44} \end{bmatrix} \tag{1-34}$$

Then, the Mueller matrix $\boldsymbol{M}$ of the sample can be obtained through inverse of the matrices $\boldsymbol{A}$ and $\boldsymbol{W}$.

$$\boldsymbol{M} = \boldsymbol{A^{-1}BW^{-1}} \tag{1-35}$$

However, $\boldsymbol{W}$ and $\boldsymbol{A}$ matrices need to be precisely determined through a calibration procedure. The Eigenvalue Calibration Method (ECM) was used to calibrate the polarimetric system used in this thesis work. Applying the ECM enables us to determine the $\boldsymbol{W}$ and $\boldsymbol{A}$ matrices without detailed modeling of the PSG and the PSA. However, the optimization of $\boldsymbol{W}$ and $\boldsymbol{A}$ matrices is priorly needed for the precise extraction of $\boldsymbol{M}$ from equation (1-35), as the inverse of matrix can amplify fluctuation in $\boldsymbol{B}$ dependent on the condition number of $\boldsymbol{W}$ and $\boldsymbol{A}$ matrices. The optimization of a polarimeter concerning the condition number, as well as its calibration via the ECM will be described in detail below.

1.3.1 Optimization of a Mueller polarimeter

Optimization of Mueller polarimeters is very important for building systems that can perform highly precise measurements. This optimization is more important specially when measuring complex biotic samples under non-ideal measurement conditions. This is the case with Mueller polarimeters configured to perform in vivo biomedical diagnostics. Here, measurements are made in a hospital setting on a moving sample (patient) under critical lighting and sensing conditions. Various optimization criteria for Mueller polarimeters exist in literature[8], [9]. In this thesis, we focus on the optimization of the condition number of $\boldsymbol{W}$ and $\boldsymbol{A}$ matrices.

Generally, the condition number of a matrix is a scalar value that indicates how well it can be inverted. To mathematically introduce the importance of the condition number, we consider a general linear system given by:

$$\boldsymbol{Ax} = \boldsymbol{b} \tag{1-36}$$

where $\boldsymbol{A}$ is a known $n\times n$ matrix, $\boldsymbol{b}$ is the n-dimensional measured vector and $\boldsymbol{x}$ is the n-dimensional vector to be found. The vector $\boldsymbol{x}$ can be obtained from (1-36) by inverting the matrix $\boldsymbol{A}$ as follows[10]:

$$\boldsymbol{x} = \mathbf{A}^{-1}\boldsymbol{b}. \tag{1-37}$$

In practice, the vector $\boldsymbol{b}$ can be affected by both the experimental noise obtained from the measurement and the numerical noise generated when rounding the components. If $\Delta\boldsymbol{b}$ is the error vector associated with $\boldsymbol{b}$, the inversion of the matrix $\boldsymbol{A}$ will generate a numerical error in the determination of $\boldsymbol{x}$ which will be indicated as $\Delta\boldsymbol{x}$. The supremum of the noise of $\boldsymbol{x}$ in a noisy system is[11]:

$$\frac{\|\Delta\boldsymbol{x}\|}{\|\boldsymbol{x}\|} \leq \|\mathbf{A}^{-1}\|\|\mathbf{A}\|\frac{\|\Delta\boldsymbol{b}\|}{\|\boldsymbol{b}\|} = \kappa(\mathbf{A})\frac{\|\Delta\boldsymbol{b}\|}{\|\boldsymbol{b}\|}. \tag{1-38}$$

$\|\quad\|$ denotes the l-2 norm. Herein, the condition number κ of a matrix is defined.

$$\kappa(\boldsymbol{A}) = \|\boldsymbol{A}\|\left\|\boldsymbol{A}^{-1}\right\| \tag{1-39}$$

Thus, the noise of $\boldsymbol{x}$ is proportional to $\kappa(\boldsymbol{A})$ and the noise of $\boldsymbol{A}$ and $\boldsymbol{b}$. This error propagation in a linear system can be applied on the Mueller polarimetric system (1-35). Equation (1-35) can be written in the $\boldsymbol{Ax}=\boldsymbol{b}$ form through the vectorization using the Kronecker product [12]:

$$\vec{\boldsymbol{M}} = ((\boldsymbol{W}^{-1})^{\top}\otimes\boldsymbol{A}^{-1})\vec{\boldsymbol{B}} \tag{1-40}$$

The symbol $\otimes$ denotes the Kronecker product. $\vec{\boldsymbol{M}}$ and $\vec{\boldsymbol{B}}$ are the 16-dimensional vector transformed from the Mueller matrix $\boldsymbol{M}$ and intensity matrix $\boldsymbol{B}$. Using the properties of the Kronecker product [12], as well as the switching property of the inverse and the transpose of a square matrix[13], it is possible to rewrite equation (1-40) as:

$$\vec{\boldsymbol{M}} = (\boldsymbol{W}^{\top}\otimes\boldsymbol{A})^{-1}\vec{\boldsymbol{B}} = \boldsymbol{O}^{-1}\vec{\boldsymbol{B}} \tag{1-41}$$

Where $\boldsymbol{O} = \boldsymbol{W}^{t}\otimes\boldsymbol{A}$ is a 16×16 real matrix. Thus, the condition number of the polarimetric system can be obtained [14]:

$$\kappa(\boldsymbol{O}) = \|\boldsymbol{O}^{-1}\|\|\boldsymbol{O}\| \tag{1-42}$$

Finally, using the properties of the Kronecker product, $\kappa(\mathbf{O})$ can be written as:

$$\kappa(\boldsymbol{O}) = \kappa(\boldsymbol{W})\kappa(\boldsymbol{A}) \tag{1-43}$$

It is important to minimize the respective condition number of the PSG and PSA. Because $\boldsymbol{W}$ and $\boldsymbol{A}$ are resulted from concatenations of four Stokes vectors, the infimum of the condition number is constrained by the physical condition (1-12)[15].

$$\kappa^{-1}(\boldsymbol{W}) \geq \sqrt{3}$$
$$\kappa^{-1}(\boldsymbol{A}) \geq \sqrt{3} \quad (1\text{-}44)$$

In other to determine the orientations of the polarimetric elements of the PSG and PSA, this optimization procedure has to be carried out in order to maximize $\kappa^{-1}(\mathbf{W})$ and $\kappa^{-1}(\mathbf{A})$. One of the major limitations of FLCs is their spectral dispersion, which makes it difficult to use them to build devices optimized at multiple wavelengths simultaneously [16], [17]**.** In this case, optimizing the condition number at one wavelength can significantly degrade performance for the rest of the spectral range of interest. Finally, especially if the properties of FLC are not properly evaluated, the actual experimental values obtained for the condition number compared to the theoretical values expected at all wavelengths can be significantly degraded [18].

Each component's optimal orientation maximizing the condition number has to be found. The LPICM has already developed an integrated numerical-experimental approach to fabricate high-performance Mueller polarimeters using FLCs[14]. This approach allows the design and construction of Mueller polarimeters that are optimized in the spectral range from 450 to 700 nm. The Mueller polarimeter developed in this thesis work was also optimized by the same approach. The optimization result will be presented in Chapter 3.

1.3.2 Calibration of a Mueller polarimetric system

Calibrating a Mueller polarimeter system consists in determining the **W** and **A** matrices[10], [19]. The eigenvalue calibration method (ECM) is a very powerful approach because it allows for accurate determination of the **W** and **A** matrices without detailed modeling of the PSG and PSA.

The ECM is suitable for calibration of a Mueller polarimeter operating in transmission or reflection. For a transmitting Mueller polarimeter, shown in Figure 1.6a, there is air between the PSG and the PSA, which has no impact on the polarization. In a reflective system, a sandblasted metallic plate is placed at the position of sample illustrated in Figure 1.6b so that it lies between the PSG and the PSA. The metallic plate is characterized by a Mueller matrix equal to the identity matrix and has no significant effect on the polarization.

The ECM requires that 16 intensity images, corresponding to all possible permutations of the PSG and the PSA, are initially acquired in sequence without any sample and in the presence of air only in transmission or a sandblasted metallic plate in reflection.

These images are stacked in a 4×4 real matrix $\boldsymbol{B_0}$ given by:

$$\boldsymbol{B_0} = \boldsymbol{AW} \quad (1\text{-}45)$$

In a second step, several reference components with well-known polarimetric properties are placed consecutively between the PSG and the PSA in order to perform new measurements. These components are: i) a first linear polarizer, whose transmission axis is oriented at 0° with respect to the laboratory reference frame (indicated as P0); ii) a second linear polarizer, whose transmission axis is oriented at 90° with respect to the transmission axis of P0 (indicated as P90); iii) a phase retarder, whose fast axis is oriented at 30° with respect to the transmission axis of P0 (indicated as L30).

The Mueller matrix of each of these reference components is indicated as $\boldsymbol{M}_i$ (i = P0, P90, L30). In a compact manner, $\boldsymbol{M}_i$ can be represented as a Mueller matrix containing both the linear phase retardance and the dichroism, which can be expressed as:

$$\boldsymbol{M}_i = \tau_{\mathrm{i}} \boldsymbol{M}_{rot}(\theta_i) \begin{bmatrix} 1 & -\cos 2\Psi_{\mathrm{i}} & 0 & 0 \\ -\cos 2\Psi_{\mathrm{i}} & 1 & 0 & 0 \\ 0 & 0 & \sin 2\Psi_{\mathrm{i}} \cos R_{li} & \sin 2\Psi_{\mathrm{i}} \sin R_{li} \\ 0 & 0 & -\sin 2\Psi_{\mathrm{i}} \sin R_{li} & \sin 2\Psi_{\mathrm{i}} \cos R_{li} \end{bmatrix} \boldsymbol{M}_{rot}(\theta_i) \quad (1\text{-}46)$$

In equation (1-40), for each reference component we have that:

- τ_i is the transmission coefficent for totally unpolarized light;
- Ψ_{i} is the angle of dichroism. In our specific case $\Psi_{\mathrm{i}} = \pi/2$, 0, and $\pi/4$ respectively for P0, P90 and L30;
- R_{li} is the linear phase retardance;
- θ_i is the orientation angle for the transmission axis of a linear polarizer and the slow axis of a linear retarder. The axis azimuth of P90 and L30 are referred to the transmission axis of P0. In this way, we obtain that θ_{P0}=0°, θ_{P90}=90° and θ_{L30}=30°;
- $\boldsymbol{M}_{rot}(\theta_i)$ is the rotation matrix described by Equation (1-20).

For each reference component, 16 intensity images are sequentially acquired and stacked in a 4×4 real-valued matrix $\boldsymbol{B}_i$ given by:

$$\boldsymbol{B}_i = \boldsymbol{A}\boldsymbol{M}_i\boldsymbol{W} \quad (1\text{-}47)$$

By multiplying the inverse of equation (1-45) on the left for equation (1-47) it can be obtained that:

$$\boldsymbol{C}_i = \boldsymbol{B}_0^{-1}\boldsymbol{B}_i \sim \boldsymbol{W}^{-1}\boldsymbol{M}_i\boldsymbol{W} \quad (1\text{-}48)$$

$\boldsymbol{C}_i$ and $\mathbf{M_i}$ are similar matrices, which are characterized by the same eigenvalues. Thus, it is possible to obtain the eigenvalues of $\boldsymbol{M}_i$ by calculating the eigenvalues of $\boldsymbol{C}_i$. From equation (1-46), these eigenvalues can be expressed as:

$$\begin{aligned} \sigma_{r1} &= 2\tau_i \sin^2 \Psi_i \\ \sigma_{r2} &= 2\tau_i \cos^2 \Psi_i \\ \sigma_{c1} &= 2\tau_i \sin^2 \Psi_i \exp(i\delta_{li}) \\ \sigma_{c2} &= 2\tau_i \sin^2 \Psi_i \exp(-i\delta_{li}) \end{aligned} \quad (1\text{-}49)$$

where σ_{r1} and σ_{r2} are two real eigenvalues, as well as σ_{c1} and σ_{c2} are two complex eigenvalues. They are directly calculated from $\boldsymbol{C_i}$. It is then possible to partially reconstruct the matrix $\boldsymbol{M}_i$ by calculating the parameters τ_i, δ_{li} and Ψ_i from equations in (1-49) as:

$$\begin{aligned} \tau_i &= 0.5(\sigma_{r1} + \sigma_{r2}) \\ \delta_{li} &= 0.5 \arg(\sigma_{c1}/\sigma_{c2}) \\ \Psi_i &= \arctan\sqrt{\sigma_{r1}/\sigma_{r2}} \end{aligned} \tag{1-50}$$

Only the parameter θ_i cannot be determined directly by these calculations. Then, we can rewrite the equation (1-48) as:

$$\boldsymbol{M}_i\boldsymbol{W} - \boldsymbol{W}\boldsymbol{C}_i = \boldsymbol{0} \tag{1-51}$$

where $\boldsymbol{0}$ is a 4×4 zero matrix. The equation (1-51) is a special case of the Sylvester equation whose solution is $\boldsymbol{W}$ [19], [20]. Inserting a 4××4 identity matrix into equation (1-51) it can be obtained that:

$$\boldsymbol{M}_i\boldsymbol{W}\boldsymbol{I} - \boldsymbol{I}\boldsymbol{W}\boldsymbol{C}_i = \boldsymbol{0} \tag{1-52}$$

Equation (1-52) can be easily vectorized as[21]:

$$(\boldsymbol{I} \otimes \boldsymbol{M}_i)\overrightarrow{\boldsymbol{W}} - (\boldsymbol{C}_i^{\top} \otimes \boldsymbol{I})\overrightarrow{\boldsymbol{W}} = \vec{\boldsymbol{0}} \tag{1-53}$$

Equation (1-53) can be rewritten as:

$$\boldsymbol{H}_i\overrightarrow{\boldsymbol{W}} = \vec{\boldsymbol{0}} \tag{1-54}$$

where $\boldsymbol{H_i} = (I \otimes \boldsymbol{M}_i) - (\boldsymbol{C}_i^{\top} \otimes \boldsymbol{I})$ is a 16×16 real matrix, $\overrightarrow{\mathbf{W}}$ is a 16x1 real vector and $\vec{\mathbf{0}}$ is a 16×1 zero vector. The objective is now to obtain $\overrightarrow{\boldsymbol{W}}$ in the eigenspace of $\mathbf{H}_i$ that satisfies equation (1-54). For this purpose, the matrix $\boldsymbol{H}_i$ is multiplied on the left by its transposed matrix $\boldsymbol{H}_i^{\top}$ to obtain:

$$\boldsymbol{H}_i^{\top}\boldsymbol{H}_i\overrightarrow{\boldsymbol{W}} = \vec{\boldsymbol{0}} \tag{1-55}$$

The matrix $\boldsymbol{H}_i^{\top}\boldsymbol{H}_i$ is a positive-semidefinite symmetric matrix which is diagonalized on a base of orthonormal vectors that restricts the solutions of the equation (1-55) to only real values. $\overrightarrow{\boldsymbol{W}}$ can now be determined in the 16-dimensional eigenspace of $\boldsymbol{H}_i^{\top}\boldsymbol{H}_i$. In order to sufficiently restrict the space of the solutions to only one solution for $\overrightarrow{\boldsymbol{W}}$ we consider the following expression[10], [22]:

$$(\boldsymbol{H}_{\boldsymbol{P0}}^{t}\boldsymbol{H}_{\boldsymbol{P0}} + \boldsymbol{H}_{\boldsymbol{P90}}^{\top}\boldsymbol{H}_{\boldsymbol{P90}} + \boldsymbol{H}_{\boldsymbol{L30}}^{\top}\boldsymbol{H}_{\boldsymbol{L30}})\overrightarrow{\boldsymbol{W}} = \vec{\boldsymbol{0}} \tag{1-56}$$

which can be rewritten as:

$$\boldsymbol{K}\overrightarrow{\boldsymbol{W}} = \mathbf{0} \tag{1-57}$$

with $\boldsymbol{K} = \boldsymbol{H}_{\boldsymbol{P0}}^{\top}\boldsymbol{H}_{\boldsymbol{P0}} + \boldsymbol{H}_{\boldsymbol{P90}}^{\top}\boldsymbol{H}_{\boldsymbol{P90}} + \boldsymbol{H}_{\boldsymbol{L30}}^{\top}\boldsymbol{H}_{\boldsymbol{L30}}$, $\boldsymbol{K}$ is a symmetric and positive-semidefinite matrix that can be diagonalized through an orthogonal passage matrix $\boldsymbol{P}$, grouping on its columns the eigenvectors $\vec{\mathbf{p}}_{\mathbf{i}}$ $(i = 1, 2 \ldots 16)$ of the matrix $\boldsymbol{K}$**.** The diagonalization of this positive-semidefinite symmetric matrix is identical to its singular value decomposition and allows writing $\boldsymbol{K}$ as:

$$\mathbf{K} = \mathbf{P}\boldsymbol{\Lambda}\mathbf{P}^{-1} = \mathbf{P}\boldsymbol{\Lambda}\mathbf{P}^{\top} \tag{1-58}$$

where $\boldsymbol{\Lambda}$ is a diagonal matrix containing the 16 eigenvalues λ_i $(i = 1, 2 \ldots 16)$ of $\mathbf{K}$ on its diagonal, with $\lambda_1 \geq \lambda_2 \geq \cdots \lambda_{16}$. In explicit form, the equation (1-58) can be written as:

$$\boldsymbol{K} = [\vec{\boldsymbol{p}}_{\boldsymbol{1}} \quad \vec{\boldsymbol{p}}_{\boldsymbol{2}} \quad \cdots \quad \vec{\boldsymbol{p}}_{\boldsymbol{16}}] \begin{bmatrix} \lambda_1 & 0 & \cdots & 0 \\ 0 & \lambda_2 & \cdots & 0 \\ \vdots & \vdots & \ddots & \vdots \\ 0 & 0 & \cdots & \lambda_{16} \end{bmatrix} \begin{bmatrix} \vec{\boldsymbol{p}}_{\boldsymbol{1}}^{\boldsymbol{t}} \\ \vec{\boldsymbol{p}}_{\boldsymbol{2}}^{\boldsymbol{t}} \\ \vdots \\ \vec{\boldsymbol{p}}_{\boldsymbol{16}}^{\boldsymbol{t}} \end{bmatrix} \tag{1-59}$$

If the matrices $\boldsymbol{M}_i$ (i=P0, P90 and L30) are reconstructed with the real values of τ_i, Ψ_{i}, δ_{li} and θ_i, then the matrix $\boldsymbol{K}$ has 15 non-zero eigenvalues and only one zero eigenvalue. Therefore, only one solution exists for $\overrightarrow{\mathbf{W}}$ that can satisfy equation (1-57). This solution corresponds to the eigenvector of $\boldsymbol{K}$ associated with the zero eigenvalue. The diagonalization operation of the matrix $\boldsymbol{K}$ is therefore repeated until to determine the value of θ_i (i = P0, P90, L30) which minimizes the λ_{16}. If $\boldsymbol{K}$ is computed with incorrect values of θ_{P0}, θ_{P90}, and $\theta_{\mathrm{L30}^{\circ}}$, then the eigenvalues of $\boldsymbol{K}$ are all strictly positive and far from 0. In this case equation (1-57) does not have a solution. On the contrary, if $\boldsymbol{K}$ is computed with accurate values of θ_{P0}, θ_{P90}, and θ_{L30}, then its first 15 eigenvalues are strictly positive and λ_{16} is close to zero. In practice, λ_{16} can be very small but not exactly zero since $\boldsymbol{K}$ is perturbed by experimental fluctuations. For this reason, the described procedure is executed by minimizing the parameter given by:

$$e(\theta_{\mathrm{P0}}, \theta_{\mathrm{P90}}, \theta_{\mathrm{L30}}) = \lambda_{16}/\lambda_{15} \tag{1-60}$$

Generally, the transmission axis of P0 is considered as the reference axis. Therefore θ_{P0} is fixed while θ_{P90} and $\theta_{\mathrm{L30}}$are varied with respect to it. Therefore, the inputs angles θ_{P90} and θ_{L30} are varied until to determine the values that minimize equation (1-60). As a starting point, $\boldsymbol{K}$ is calculated with theoretical values $\theta_{\mathrm{P90}} = 90°$ and $\theta_{\mathrm{L30}} = 30°$. The orientations of P90 and L30 are optimized around these theoretical values by using a sequential quadratic programming algorithm implemented in Matlab's Fmincon in order to determine the true values $\tilde{\theta}_{\mathrm{P90}}$ and $\tilde{\theta}_{\mathrm{L30}}$ able to minimize equation (1-60). These values should be close to 90° and 30° for P90 and L30, respectively, if the samples have been correctly aligned beforehand, as shown in Figure 1.7.

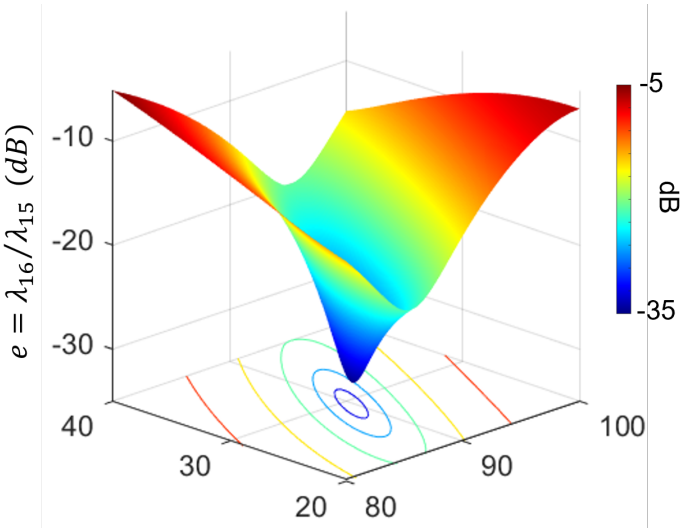

Figure 1.7 The Curve of the parameter e in equation (1-60) as a function of θ_{P90} and θ_{L30} obtained from a Mueller polarimeter developed by the LPICM. The minimum of the parameter e corresponds to $\theta_{P90} = 89.7$ and $\theta_{L30} = 29.1$.

When Equation (1-60) is minimized, the eigenvector $\vec{p}_{16}$ associated with λ_{16} is the vector $\overrightarrow{W}$. Then, the matrix $\boldsymbol{W}$ is obtained by reshaping the vector $\overrightarrow{W}$ in a 4×4 matrix. Finally, the matrix $\boldsymbol{A}$ is extracted by Equation (1-45) as:

$$\boldsymbol{A} = \boldsymbol{B}_0 \boldsymbol{W}^{-1} \tag{1-61}$$

This procedure enables to accurately determine $\boldsymbol{W}$ and $\boldsymbol{A}$ matrices.

1.3.3 Interpretation of Mueller matrices

In the previous section I have described 3 canonical polarimetric components, the retarder, diattenuator, and depolarizer. They are effortlessly interpretable through their standard matrices (1-21), (1-27), and (1-30), if they are respectively measured; however, most of Mueller matrices of biotic samples are the result of complex light-matter interactions attributed to the complicated composition and structure of biotic tissue. These interactions result in complex linear combinations of the 3 polarimetric components, and this mixture is hardly interpretable, i.e., the mixture no longer satisfies the models of (1-21), (1-27), and (1-30). Therefore, one needs to decompose the measured matrix using the 3 canonical forms. Because it is not possible to infer the actual structure and interactions of biotic tissue, a generalized implication of the tissue structure and statistical nature of the coherency matrix are applied to decomposition processes. This section introduces some representative decomposition methods.

Serial decomposition

First, one can consider sequential linear modifications of an incoming Stokes vector. A polarized light that propagates into a stratified structure is sequentially modified by each layer[23]. This process is equivalent to matrix multiplication.

$$\boldsymbol{S}_{\text{out}} = \boldsymbol{M}_n \dots \boldsymbol{M}_2 \boldsymbol{M}_1 \boldsymbol{S}_{\text{in}} = \boldsymbol{M}\boldsymbol{S}_{\text{in}} \tag{1-62}$$

Decomposition of a matrix resulting from sequential interactions is referred to as the serial decomposition. Each layer can be modeled as one of the canonical components, diattenuator, retarder, and depolarizer. The most used parallel decomposition might be the Lu-Chipman decomposition illustrated in Figure 1.8[24]. The Lu-Chipman decomposition assumes that the measured matrix is resulted from a sequential interaction of the 3 canonical components in the following order:

$$\begin{gathered} \boldsymbol{M}_n \dots \boldsymbol{M}_2 \boldsymbol{M}_1 \boldsymbol{S}_{\text{in}} \equiv \boldsymbol{M}_\Delta \boldsymbol{M}_{\text{R}} \boldsymbol{M}_D \boldsymbol{S}_{\text{in}} \\ \boldsymbol{M} \equiv \boldsymbol{M}_\Delta \boldsymbol{M}_{\text{R}} \boldsymbol{M}_D \end{gathered} \tag{1-63}$$

It is reasonable since what the incident light encounters at first is diattenuation by reflection at the surface (interface). Then, the retarder and depolarizer correspond to simple modifications – rotation and scaling of the Stoke vector[24], [25].

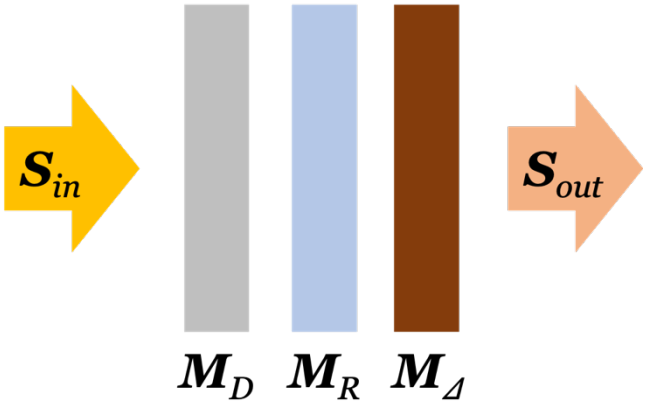

Figure 1.8 Lu-Chipman decomposition assumes complex interactions by a medium to be 3 canonical components, diattenuator, retarder, and depolarizer in the serial combination.

The multiplication $\boldsymbol{M}_\Delta \boldsymbol{M}_{\text{R}} \boldsymbol{M}_D$ results in:

$$\begin{gathered} \boldsymbol{P}, \boldsymbol{D} \in \mathbb{R}^4, \boldsymbol{m} \in \mathbb{R}^{3\times 3} \\ \boldsymbol{M}_\Delta \boldsymbol{M}_{\text{R}} \boldsymbol{M}_D = \begin{bmatrix} M_{11} & M_{12} & M_{13} & M_{14} \\ M_{21} & M_{22} & M_{23} & M_{24} \\ M_{31} & M_{32} & M_{33} & M_{34} \\ M_{41} & M_{42} & M_{43} & M_{44} \end{bmatrix} = M_{11} \begin{bmatrix} 1 & \boldsymbol{D}^{\mathsf{T}} \\ \boldsymbol{P} & \boldsymbol{m} \end{bmatrix} \end{gathered} \tag{1-64}$$

Where $\boldsymbol{P}$ and $\boldsymbol{D}$ are called the polarizance and diattenuation vector, respectively[23], [24]. The parameter of the diattenuator is given in the first row and column. From the diattenuation vector $\boldsymbol{D}$, the equivalent diattenuator can be found[24]

$$\begin{gathered} \widehat{\boldsymbol{D}} = \frac{\boldsymbol{D}}{\sqrt{\|\boldsymbol{D}\|}}, \qquad \boldsymbol{I}_3 = \begin{bmatrix} 1 & 0 & 0 \\ 0 & 1 & 0 \\ 0 & 0 & 1 \end{bmatrix} \\ \boldsymbol{M}_{\text{D}} = \boldsymbol{I}_3 \sqrt{1 - |\boldsymbol{D}|^2} \left(1 - \sqrt{1 - |\boldsymbol{D}|^2}\right) \widehat{\boldsymbol{D}} \widehat{\boldsymbol{D}}^{\mathsf{T}} \end{gathered} \tag{1-65}$$

$\|\boldsymbol{D}\|$ denotes the l-2 norm of the vector $\boldsymbol{D}$. Then, $\boldsymbol{M}_\Delta \boldsymbol{M}_{\text{R}}$ is obtained by inverse of $\boldsymbol{M}_{\text{D}}$.

$$\boldsymbol{M}\boldsymbol{M}_{\mathrm{D}}^{-1} \equiv \boldsymbol{M}_{\Delta}\boldsymbol{M}_{\mathrm{R}} = \begin{bmatrix} 1 & \boldsymbol{0}^{\top} \\ \boldsymbol{P}_{\Delta} & \boldsymbol{m_R} \end{bmatrix}, \qquad \forall \det(\boldsymbol{M}_{\mathrm{D}}) \neq 0 \tag{1-66}$$

Here, the singular value decomposition is applied[24] to decompose $\boldsymbol{M}_{\Delta}\boldsymbol{M}_{\mathrm{R}}$ because $\boldsymbol{m}'$ is often singular due to low retardance and high depolarization of biotic samples:

$$\begin{aligned} \boldsymbol{m}' &= \boldsymbol{U}\boldsymbol{\Sigma}\boldsymbol{V}^{\top} \\ \boldsymbol{m_R} &= \pm\boldsymbol{U}\boldsymbol{V}^{\top} \\ \boldsymbol{m}_{\Delta} &= \pm\boldsymbol{V}\boldsymbol{\Sigma}\boldsymbol{V}^{\top} \end{aligned} \tag{1-67}$$

$\boldsymbol{U}$ and $\boldsymbol{V}$ are 3×3 real orthogonal matrices and $\boldsymbol{\Sigma}$ is the 3×3 diagonal matrix of the singular values of $\boldsymbol{m}'$. Where $\boldsymbol{m}_{\mathrm{R}}$ and $\boldsymbol{m}_{\Delta}$ is the 3×3 submatrix of the retarder and depolarizer obtained by removing the first row and the first column of $\boldsymbol{M}_{\mathrm{R}}$ and $\boldsymbol{M}_{\Delta}$. The sign is determined by the determinant of $\boldsymbol{m}'$[24]. Then, $\boldsymbol{M}_{\mathrm{R}}$ and $\boldsymbol{M}_{\Delta}$:

$$\begin{aligned} \boldsymbol{M}_{R} &= \begin{bmatrix} 1 & \boldsymbol{0}^{\top} \\ \boldsymbol{0} & \boldsymbol{m_R} \end{bmatrix} \\ \boldsymbol{M}_{\Delta} &= \begin{bmatrix} 1 & \boldsymbol{0}^{\top} \\ \boldsymbol{P}_{\Delta} & \boldsymbol{m}_{\Delta} \end{bmatrix} \end{aligned} \tag{1-68}$$

$\boldsymbol{P}_{\Delta}$ is the polarizance of the depolarizer. The depolarizer from the Lu-Chipman decomposition is not the same to the standard diagonal depolarizer of (1-30). It represents a depolarizer with polarizance[24], and this type of depolarizers takes into account the effect of direct propagation. This can make significant difference when a system involves an asymmetric series arrangement of diattenuation and depolarization[5].

Consequently, polarimetric properties, such as retardance and depolarization of a target medium can be extracted from elements of the matrices $\boldsymbol{M}_{\mathrm{D}}$, $\boldsymbol{M}_{\mathrm{R}}$, and $\boldsymbol{M}_{\Delta}$.

Parallel decomposition

As shown in Figure 1.5, a measured Mueller matrix can result from an incoherent sum of multiple Mueller matrices. This process is equivalent to a sum of Mueller matrices as shown in (1-29). In this case, the equivalent linear combination is not uniquely determined. Herein, the statistical nature of positive semidefinite Hermitian matrix, the coherency matrix $\boldsymbol{H}$, is employed [5]:

$$\begin{aligned} \boldsymbol{E}_{ij} &= \boldsymbol{\sigma}_i \otimes \boldsymbol{\sigma}_j, i, j \in [1,4] \subset \mathbb{N} \\ \boldsymbol{H} &= \frac{1}{4}\sum_{i,j=1}^{4} M_{ij}\boldsymbol{E}_{ij} \end{aligned} \tag{1-69}$$

Where $\boldsymbol{\sigma}_i$ is the group of the Pauli matrices + the identity matrix. M_{ij} corresponds to the *ij-th* element of the Mueller matrix. $\otimes$ denotes the Kronecker product. Because the coherency matrix is a positive semidefinite Hermitian matrix, it can be diagonalized by the unitary transformation.

$$\boldsymbol{H} = \boldsymbol{U}\boldsymbol{\Sigma}\boldsymbol{U}^{\dagger} \tag{1-70}$$

Where $\boldsymbol{\Sigma}$ represents the diagonal non-negative eigenvalue matrix ordered so that $0 \leq \lambda_4 \leq \lambda_3 \leq \lambda_2 \leq \lambda_1$. $\boldsymbol{U}$ is a 4×4 unitary matrix whose columns are the unitary orthogonal eigenvectors. Then, the coherency matrix can be expressed as a linear sum of:

$$\begin{aligned} \boldsymbol{H}^{(n)} &= tr(\boldsymbol{H})(\boldsymbol{u}_n \otimes \boldsymbol{u}_n^{\dagger}) \\ \boldsymbol{H} &= \sum_{n=1}^{4} \frac{\lambda_n}{\mathrm{tr}(\boldsymbol{H})} \boldsymbol{H}^{(n)} \end{aligned} \tag{1-71}$$

Where $\boldsymbol{u}_n$ represents the n-th column of $\boldsymbol{U}$. This linear expansion of $\boldsymbol{H}$ is called Cloude decomposition or spectral decomposition[5]. It shows that a depolarized Mueller matrix can be expressed equivalently to a parallel combination of four pure linear systems weighted by the eigenvalues of $\boldsymbol{H}$. Each term of (1-71) can be converted to the equivalent Mueller matrix, and they correspond to four pure Mueller matrices. The n-th pure Mueller matrix is[5], [23]:

$$\boldsymbol{M}^{(n)} = \left(M_{ij}^{(\mathrm{n})}\right) = \left(\mathrm{tr}\left(\boldsymbol{E}_{ij}\boldsymbol{H}^{(n)}\right)\right) \in \mathbb{R}^{4\times4}, \qquad 1 \leq n \leq 4 \tag{1-72}$$

1.3.4 Mueller polarimeters based on ferroelectric liquid crystals

Mueller polarimetric imaging can be implemented using a wide variety of polarization modulators and analyzers based on rotating waveplates (WPs) [26], liquid crystal variable retarders (LCVRs) [27], [28], photoelastic modulators (PEMs) [29], [30], or ferroelectric liquid crystals (FLCs) [16], [17], [31]. Each type of polarization modulators has advantages and disadvantages. Mechanically rotating WPs are accurate, but require rotation time, which greatly increases measurement time. LCVR-based polarimeters, on the other hand, can generate or analyze all polarization states by applying a specific voltage. LCVRs have a response in the millisecond range, but are strongly affected by changes in ambient temperature. In the case of PEMs, they enable very sensitive and fast Mueller polarimeters, but PEM-based polarimeters are difficult to miniaturize because they require cumbersome piezoelectric motors.

Among all these possible solutions, FLCs are well adapted to the exploration of biological tissues in vivo. FLCs are electronically controlled, which allows a fast modulation (in the microsecond range) without moving mechanical parts. Moreover, FLCs can be fixed in a compact way to obtain miniaturized systems. Finally, they are well suited for wide field imaging (up to several cm²).

In particular, the Mueller polarimeters designed and built in our laboratory make use of PSG and PGA based on bistable V-shaped FLCs on Smectic C phase which behave like WP with fixed linear phase retardance. The orientation of the two eigenaxes of the FLC (fast and slow axes orthogonal to each other) can be varied in a plane orthogonal to the direction of light propagation between two different positions corresponding to the application of a

positive or negative voltage. The angle (less than 90°) between these two positions around the fast (or slow) axis is defined as the switching angle.

The PSG is composed of the following optical elements along the direction of beam propagation: i) a linear polarizer oriented at 0° with respect to the laboratory frame (denoted as HP), ii) a quarter-wave FLC1 (denoted as QFLC), iii) a quarter-waveplate (denoted as QWP) and iv) half-wave FLC2 (denoted as HFLC). The PSA consists of the same optical elements as the PSG, but is placed in the reverse order with respect to the PSG.

According to equation (1-26), the Mueller matrix of the HP can be written as:

$$\mathrm{M_{HP}} = \frac{1}{2}\begin{bmatrix} 1 & 1 & 0 & 0 \\ 1 & 1 & 0 & 0 \\ 0 & 0 & 0 & 0 \\ 0 & 0 & 0 & 0 \end{bmatrix} \tag{1-73}$$

The general form of the Mueller matrix of a linear retarder $\boldsymbol{M}_R$ with the slow axis oriented at an angle θ (also called azimuth) with respect to a reference axis (in this case the transmission axis of the HP), is described as:

$$\mathbf{M}_{\mathrm{R}}(\delta,\theta) = \begin{bmatrix} 1 & 0 & 0 & 0 \\ 0 & \cos^2 2\theta + \sin^2 2\theta \cos\ \delta & \sin 2\theta \cos 2\theta\,(1-\cos\delta) & -\sin 2\theta \sin\delta \\ 0 & \sin 2\theta \cos 2\theta\,(1-\cos\delta) & \sin^2 2\theta + \cos^2 2\theta \cos\ \delta & \cos 2\theta \sin\delta \\ 0 & \sin 2\theta \sin\delta & -\cos 2\theta \sin\delta & \cos\delta \end{bmatrix} \tag{1-74}$$

where δ is the linear phase retardance in radians defined as:

$$\delta(\lambda) = \frac{2\pi L \Delta n(\lambda)}{\lambda} \tag{1-75}$$

where $\Delta n(\lambda)$ is the birefringence of the linear retarder (depending on the wavelength λ) and L is the thickness. The sign of the angle θ is considered positive (or negative) if measured counterclockwise (or clockwise) along the direction of light propagation.

For FLCi ($i = 1, 2$), the phase retardance is indicated as δ_{FLCi}. Moreover, the orientation of the fast axis is indicated as θ_{FLCi} for a negative applied voltage and as $\theta_{\mathrm{FLCi}} + \theta_{\mathrm{SWi}}$ for a positive applied voltage, θ_{SWi} being the switch angle. For WP, the phase retardance and the orientation of the fast axis are indicated with δ_{WP} and θ_{WP}, respectively.

The Mueller matrix of the PSG can be written as:

$$\begin{aligned} &\boldsymbol{M_{PSG}}\left(\delta_{\mathrm{HFLC}}, \theta_{\mathrm{HSW}}, \theta_{\mathrm{HFLC}}, \delta_{\mathrm{QWP}}, \theta_{\mathrm{QWP}}, \delta_{\mathrm{QFLC}}, \theta_{\mathrm{QSW}}, \theta_{\mathrm{QFLC}}\right) \\ &= \boldsymbol{M_{HFLC}} \boldsymbol{M_{QWP}} \boldsymbol{M_{QFLC}} \boldsymbol{M_{HP}} \end{aligned} \tag{1-76}$$

where $\boldsymbol{M_{QFLC}}$ and $\boldsymbol{M_{HFLC}}$ are the Mueller matrices of QFLC and HFLC respectively, $\boldsymbol{M_{QWP}}$ is the Mueller matrix of QWP and $\boldsymbol{M_{HP}}$ is the Mueller matrix of HP. When a synchronized square wave signal is applied to the QFLC and HFLC of the PSG (the signal applied to HFLC having a frequency twice than the signal applied to QFLC), it is possible to generate four Stokes vectors regrouped as the columns of the matrix $\boldsymbol{W}$ as follows:

$$
\begin{aligned}
S_{W1} &= M_{PSG}(\theta_{HFLC}, \theta_{QFLC})S_{in}, \\
S_{W2} &= M_{PSG}(\theta_{HFLC} + \theta_{HSW}, \theta_{QFLC})S_{in}, \\
S_{W3} &= M_{PSG}(\theta_{HFLC}, \theta_{QFLC} + \theta_{QSW})S_{in}, \\
S_{W3} &= M_{PSG}(\theta_{HFLC} + \theta_{HSW}, \theta_{QFLC} + \theta_{QSW})S_{in}
\end{aligned}
\tag{1-77}
$$

where $S_{in} = [1,0,0,0]^T$ is the Stokes vector representing the completely depolarized polarization state of the light produced by the light source.

In Figure 4 we indicated as $\theta_{FLC1}^{W(A)}$, $\theta_{WP}^{W(A)}$ and $\theta_{FLC2}^{W(A)}$ the orientations of the fast axes for FLC1, WP, and FLC2 respectively, referred to the transmission axis of HP. Otherwise, $\theta_{SW1}^{W(A)}$ and $\theta_{SW2}^{W(A)}$ indicate the switch angles for FLC1 and FLC2 respectively.

The relative orientation between the optical elements composing the PSG (PSA) determines the properties of the modulation (analysis) matrix W (A). An optimization procedure has to be used to find the best values for $\theta_{FLC1}^{W(A)}$, $\theta_{WP}^{W(A)}$ and $\theta_{FLC2}^{W(A)}$ in order to maximize $\kappa^{-1}(W)$ and $\kappa^{-1}(A)$.

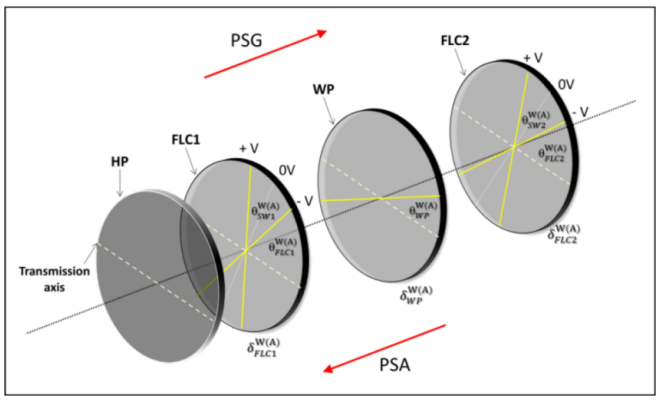

Figure 1.9. Schematic of PSG and PSA based on the use of ferroelectric liquid crystals.

1.4 Biomedical applications of Mueller polarimetry

Polarimetric imaging certainly forms significantly different contrast from the conventional intensity and color imaging. In other word, polarimetric images contains additional information about a target in term of optical anisotropy than simple reflection and absorption. Even polarimetric imaging is scalable and simply realizable by modifying conventional intensity-base imaging systems. It also does not cause any harmful radiations or does not require any strict conditions. Some researchers noticed these fruitful characters of polarimetric imaging and tried to exploit it for assessing biotic media, i.e., tissues. Specially, the qualifications of polarimetric imaging above more accord with biomedical applications. Indeed, biotic tissues are plentiful of anisotropic proteins such as collagen, elastin, actin, and intermediate filaments.

The first attempt on biomedical imaging using Mueller polarimetry was carried out in ophthalmology in 1999 by J.M. Bueno et al. [32] They acquired polarimetric images of in-vivo human eyes using a LC-base Mueller polarimetric system. Depolarization of retina and fovea was investigated in term of degree of polarization. Retardance was investigated in their

second attempt[33]. However, their data cannot be considered correct due to low SNR and depolarization by intraocular diffusion.

Another attempt in dermatology was performed in 2000 as a diagnostic tool for benign and malignant moles[34]. Afterward, a lot of studies on dermatologic pathology have been reported. Mueller polarimetry has exhibited significant potential in diagnostic applications of precancerous lesions[35]–[42]. Development of neoplasia and dysplasia is strongly related to tissue organizations because cancer phenotypes often lead disordered connective tissues[43]. Considering the connective tissue is predominated by collagen, one can easily conclude that Mueller polarimetry would be sensible to the changes of collagen organization. Specially, a lot of diagnostic applications for cervical pathology have been actively being studied in LPICM[4], [39], [40], [42], [44].

Mueller polarimetry have also showed its considerable performance in other fiber-related pathology such as fibrosis not only precancerous lesions. M. Dubreuil et al.[45] and Y. Wang el al.[46] reported a diagnostics of liver fibrosis using Mueller polarimetry. P. Schucht et al. recently reported a study about neural fibers of gray matter of human brains[47].

On the top of these studies, we have developed a novel obstetric diagnostic application using Mueller polarimetry for estimation/prediction of spontaneous preterm birth. Spontaneous preterm birth is acknowledged to be fatal pregnancy complication that leads developmental disorder, morbidity, impaired growth, and mortality of babies. In the next chapter, the physiology of the human uterine cervix and cervical dynamics during pregnancy will be described for interconnection of the 2 different disciplinaries, polarimetry–gynecology and obstetrics.

1.5 Conclusions

In this chapter, we presented the basic concepts of polarimetry. First, we introduced the polarization ellipse, which is used to describe fully polarized light. Then we introduced the more general Stokes-Mueller formalism, which is used to represent partially polarized or fully depolarized light as well. We then explained the algebraic concept of the Mueller matrix and the different algebraic methods to analyze it (decompositions). We described in detail the structure of a Mueller polarimeter, its optimization and calibration using Eigenvalue Calibration Method. Finally, we presented the Mueller polarimeters based on ferroelectric liquid crystals which are the basis of all the technology we develop at LPICM and in particular of the multispectral Mueller polarimetric colposcope designed and fabricated during this thesis work.

Chapter 2

Mueller polarimetric imaging of the cervix

The microstructure of the cervix undergoes significant alterations throughout a woman's life and especially during pregnancy due to strong hormonal changes. The objective of this thesis work is to determine whether Mueller polarimetric imaging is a suitable technique for monitoring the steady remodeling of the microstructure of cervical tissue during pregnancy, thus providing new criteria to improve the diagnosis of prematurity, the leading cause of perinatal mortality worldwide.

In this chapter, the very complex structure of the cervix will be described in detail, first from an anatomical point of view and then from a microscopic point of view in relation to its physiological changes. Understanding these concepts is crucial to interpret the different polarimetric signatures that can be observed on the cervical tissue. We will therefore introduce the colposcope, i.e., the optical system that is currently used for in vivo inspection of the cervix in routine medical practice, especially for early cancer detection. Finally, we will describe previous studies performed at LPICM on the use of Mueller polarimetric imaging for cervical analysis, in particular for two different medical problems, namely the early detection of cancer and the diagnosis of prematurity.

2.1 The uterine cervix

2.1.1 Anatomy and role

The cervix is the lower part of the uterus protruding into the vagina, as shown in Figure 1.1. It is characterized by a cylindrical shape and is about 4 centimeters long. The endocervical canal, also named the endocervix, connect the lumen of the vagina to the uterine cavity along the length of the cervix. The entrance to the endocervical canal on the vaginal side is called the "external os". The other end of the endocervical canal on the side of the uterus is called the "internal os". The portion of the cervix at the interface with the vaginal cavity is called the ectocervix.

The boundary between the vagina and the cervix is called the fornix, as shown in the inset of Figure 2.1. The diameter of the cervix (corresponding to the line that joins two points of the fornix placed in diametrically opposite positions with respect to the ectocervix) is about 3 centimeters.

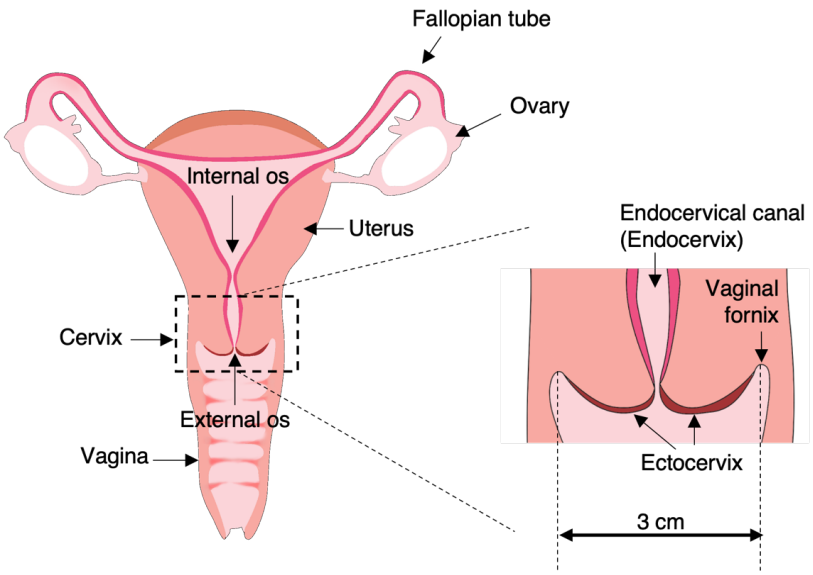

Figure 2.1 Anatomy of the female reproductive system. The cervix is the passageway between the uterus and the vagina.

The cervix allows different types of fluids to flow from the inside to the outside of the uterus (and vice versa). For example, it produces mucus during the most fertile phase of the menstrual cycle to help sperm move from the vagina to the uterus. It also opens slightly to allow blood to flow out of the uterus during menstruation. The most significant role of the cervix as a reproductive organ occurs during pregnancy. Indeed, it must remain closed during most of the gestation period so that the fetus is well protected in the uterus, while it shortens and opens at the end of pregnancy to allow delivery. The mechanical properties of the cervix are strictly related to its microscopic structure, which will be described in more detail in the next section.

2.1.2 Description of cervical microstructure

Figure 2.2 shows a typical image of cervix acquired in vivo. The ectocervix is lined by the stratified squamous epithelium (SSE) that extends from the vaginal wall. It helps to protect the cervix from external agents and the high acidity of the vaginal environment. In contrast, a single layer of columnar epithelium (CE) lines the endocervical canal characterized by lower acidity. The connective tissue underlying both epithelia represents the main mechanical support of the cervix. The SSE and CE meet at a line called the squamocolumnar junction (SCJ). The different components of the cervix mentioned in this paragraph will be described in detail in the next sections.

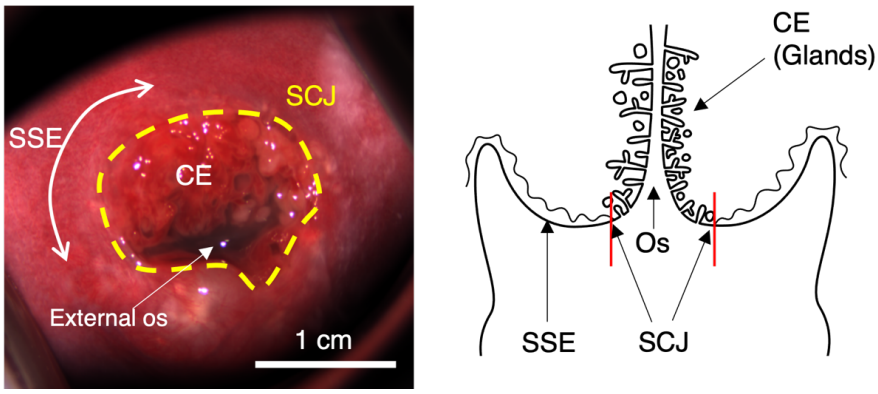

Figure 2.2 Typical image of the cervix in colposcopy (Left). An illustration of the coronal section of the cervix (Right). Grape-like villi covered with the CE are found near the external os, while a pinkish smooth surface lined with the SSE surrounds the glandular part. The boundary between the two epithelial types (the yellow dotted line) corresponds to the SCJ.

Stratified squamous epithelium (SSE)

The SSE is a multilayered epithelial tissue of about 300 microns thick. It is composed of more than 10 layers of large flat cells arranged in a very compact way, which gives it a great mechanical resistance. This type of epithelial tissue lines the entire vaginal wall and the ectocervix from the fornix to the SCJ, i.e., all the parts of the female reproductive system that are most exposed to mechanical damage caused for instance by sexual intercourse [48]. In addition, this type of epithelium is essential to protect the cervix from the high acidity of the vaginal environment.

The SSE exhibits a smooth surface morphology in visual inspection and is often characterized by pinkish color. However, a more reddish hue can be observed during pregnancy due to a general increase in the vascularity of the cervix. In general, hairpin terminal vessels or fine reticular network vessels are predominantly observed on the surface of healthy SSE [49]. Figure 2.3a and b show the images of a cervix at different magnifications with the ectocervix completely covered by the SSE. Figure 2.3c shows a typical histological section of the SSE.

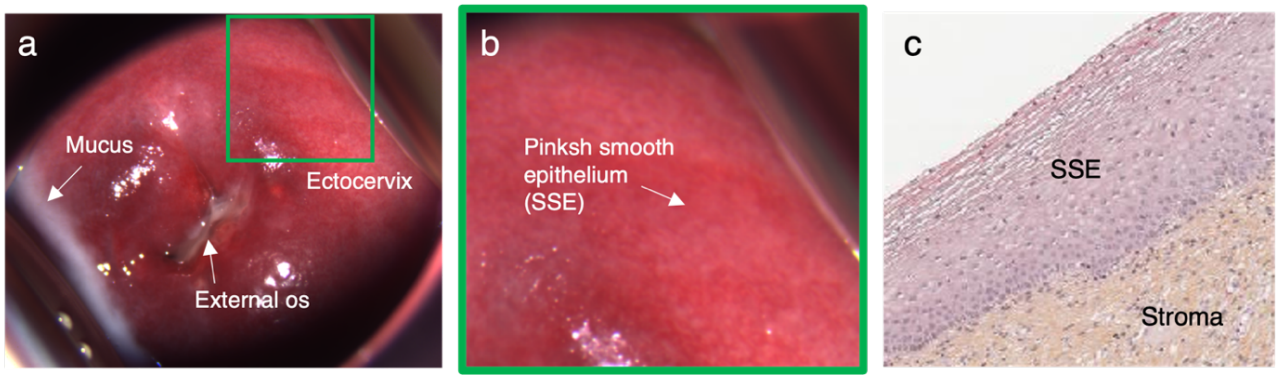

Figure 2.3 (a) Typical image of the cervix in which the SSE is predominantly observed in the ectocervix. (b) Cropped image of the green rectangle. A pinkish surface with reticular network blood vessels is observed. (c) Typical histological image of the SSE.

Columnar epithelium (CE)

A single layer of columnar mucosal cells, about 5-10 microns thick, forms the glandular epithelium also referred to as the columnar epithelium (CE), which covers the internal surface of the endocervical canal. Its main function is to secrete vaginal mucus.

The CE has a grape-like aspect and appears as composed by clearly separated villi. The spaces between the villi are also called the crypts. Reddish microcapillaries are present in the connective tissue composing the villi beneath the CE covering their surface. For this reason, the CE usually appears more reddish than the SSE to visual inspection because of its much thinner thickness, which allows microcapillaries in the connective tissue to be seen in transparency. Figure 2.4a and b show the image of a cervix at different magnifications where the CE is visible around the cervical OS. Figure 2.4c shows a typical histological section of the CE. The SCJ is also clearly visible in these images.

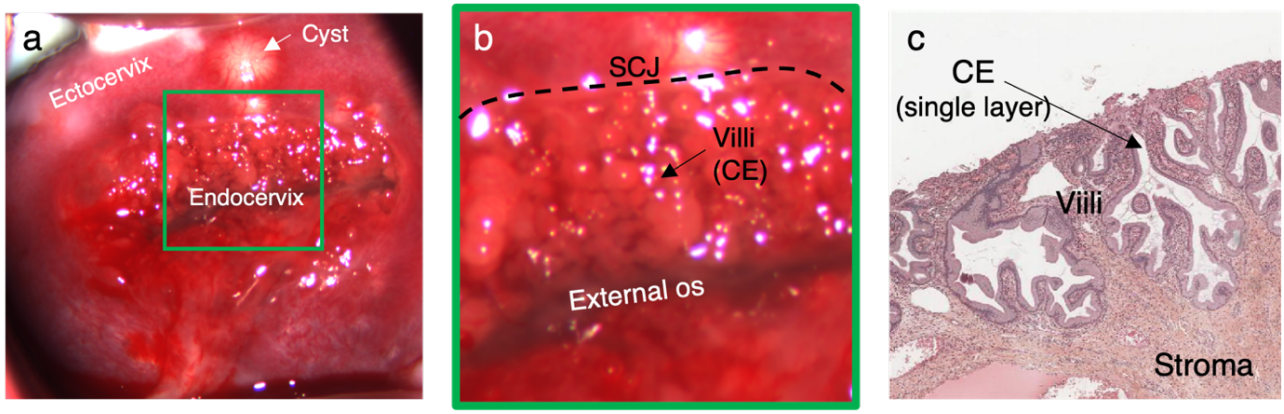

Figure 2.4 (a) Typical image of the cervix with villi observed in the endocervix. (b) Cropped image of the green rectangle. A grape-like surface with villi is observed. (c) Typical histological image of the CE.

Metaplastic Squamous Epithelium (MSE)

As explained earlier, the SCJ is the boundary between the SSE and the CE. It is usually found near the cervical os. Due to an increase in estrogen during adolescence or pregnancy, the external os may open, generating a displacement of the SCJ that makes the CE visible on the surface of the cervix. This particular structure of the ectocervix is called ectopy or

ectropion [50]. The SSE and CE form a well-defined SCJ in the frontal view of the cervix for postnatal or prepubertal women [50]. The CE exposed to the high acidity of the vagina, gradually transforms over time into the SSE better adapted to this type of environment. The gradual transition between the two epithelia is called metaplasia. Other factors can activate this process such as sex hormones [51], [52] or vitamin A deficiency [53].

Metaplastic transformation is usually found in a region around the SCJ, called the Transformation Zone (TZ). The goal of the metaplastic maturation is the reconstitution of the SSE in the area previously occupied by the CE, creating a new SCJ near the cervical os. Figure 2.5a and b show the image of a cervix at different magnifications where a metaplastic transformation is visible around the cervical os. Figure 2.5c shows a typical histological section of metaplasia.

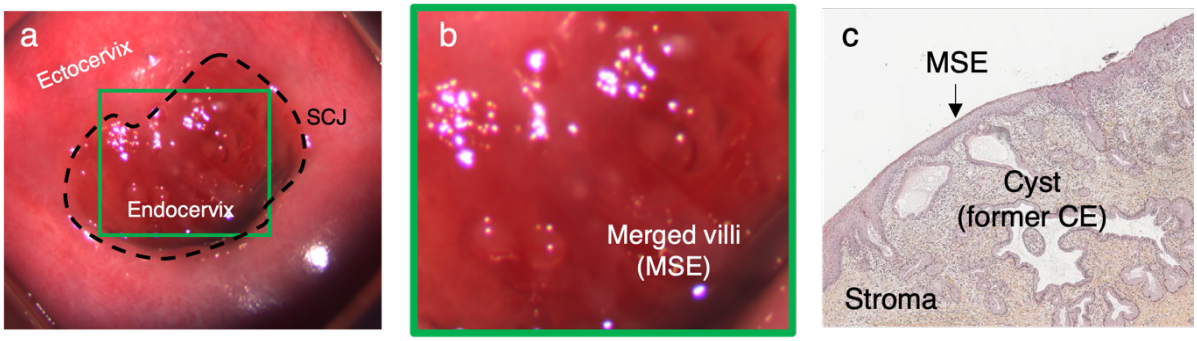

Figure 2.5(a) Typical image of the cervix with merged villi observed in the endocervix (the TZ). (b) Cropped image of the green rectangle. Villi are merged and form a relatively smooth surface. (c) Typical histological image of the MSE.

The whole metaplastic process in cervical epithelia is sketched in Figure 2.6. In general, on the uterine cervix, a metaplastic transformation or metaplasia refers to the transition from the CE to the SSE. Cervical metaplasia is thought to be triggered by the influence of the acidic vaginal environment. Therefore, the early stage of metaplastic transition is often found in the tips of the CE villi [54], which are the most exposed parts to the acidic vaginal environment, as shown in Figure 2.6a and e. At this stage, the metaplasia is not significantly distinguishable from the CE in the visual inspection, as illustrated in the front view of Figure 2.6a (the red areas). As a histological landmark of the metaplastic transition, discontinuities of the basement membrane underlying the active metaplasia can be found, especially at the tips of villi [54].

In other words, cleavage of the basement membrane is often associated with the proliferation of reserve cells. This proliferation thickens the epithelium and form a new stratified epithelium, as shown in Figure 2.6b and f. At this stage, transitional epithelia can be found near the SCJ as shown in the front view of Figure 2.6b (the green areas). Due to the epithelial thickening, the separated villi and cleft-like spaces are merged and filled, resulting in flattening of the cervical surface.

Finally, the villi disappear in a mature Metaplastic Squamous Epithelium (MSE), that exhibits a smooth morphology similar to that of the SSE, as illustrated in Figure 2.6c and g. Indeed, the mature MSE has a very similar appearance to the SSE on visual inspection, and a new SCJ may appear near the external os, as illustrated by the dotted outline in Figure

2.6g. However, the two types of epithelia have slightly different histological features in terms of basement cell alignment and stromal organization [55].

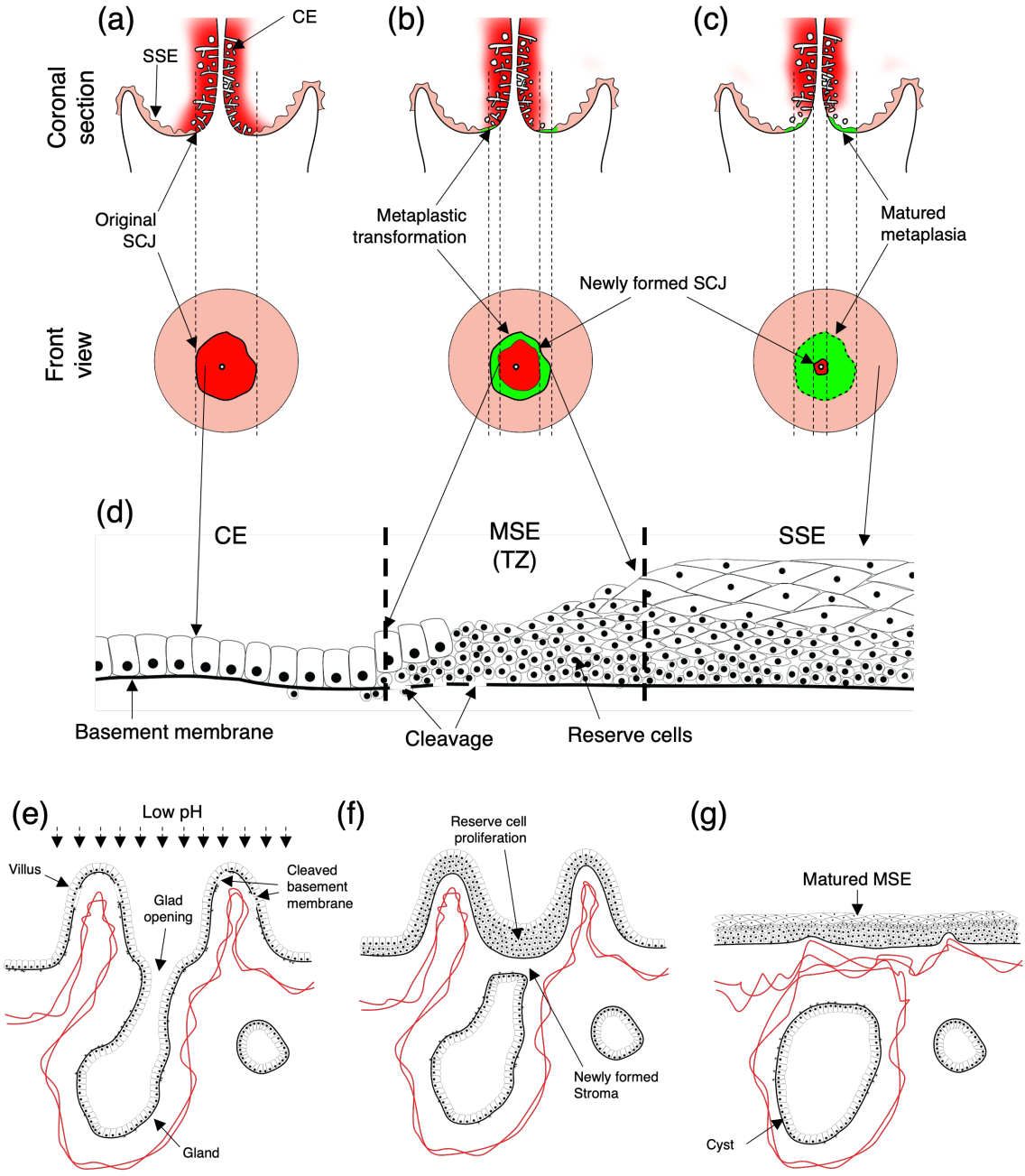

Figure 2.6 (a) Illustration of a coronal section and front view of the cervix before metaplastic transitions. The red and pink areas correspond to the CE and SSE, respectively. (b) Gradual progression of metaplasia (the green area). The MSE starts to replace the CE within the SCJ. (c) Maturation of metaplasia forms a new SCJ near the external os. (d) Illustration of the transition between the two epithelial types, the SSE and CE. (e) Illustration of metaplasia in tissue level. Discontinuities of the basement membrane can be found in the early stage. (f) Villi and glandular systems start to merge by proliferation of metaplastic reserve cells. (g) Matured MSE exhibits the smooth surface similar to the SSE.

In addition to the transition from the CE and the SSE, active angiogenesis is also observed during metaplastic transformation [50], [56]. In particular, long parallel vessels are often present in areas of immature metaplasia covering fused villi, whereas the SSE is usually characterized by the presence of hairpin terminal vessels or fine reticular vessels [50].

In general, the structure of the epithelia overlying the ectocervix and endocervix is very complex. In particular, distinguishing the different stages of MSE is not straightforward in actual practice. The correct classification of metaplastic transition is almost impossible in some cases on visual examination, even for an experienced practitioner.

Although the observation of a gradual progression of the metaplasia is rarely feasible in clinics in the case of mature women, it can appear more frequently during pregnancy due to strong hormonal changes [57].

Cervical connective tissue

Cervical connective tissue or stroma underlying the epithelia accounts for more than 95% of the cervical volume. It is composed of 80% collagen (70% type I and 30% type II), related basic substances, 15% smooth muscle tissue, and 0.9% to 1.6% elastin [58]. Collagen is the main protein that constitutes the extracellular matrix of cervical connective tissue and determines its mechanical properties. Type I collagen, for instance, also called linearized collagen, is rigid and can withstand high tensile stresses.

A collagen molecule (procollagen and tropocollagen) is approximately 300 nm long and is presented as a chain of 3 polypeptides twisted to form a triple helix. The aggregation of numerous collagen molecules by intermolecular cross-links results in the formation of a collagen fibril. The bundles of these fibrils form the collagen fibers. The diameter of collagen fibers varies dependent on their required mechanical property. Collagen fibrils are 100-200 nm in diameter, while collagen fibers can reach 50-100 μm [59]. The uniaxial aggregation of collagen fibers results in a non-centrosymmetric permittivity that produces a strong optical anisotropy. In contrast, other structures of the cervix, such as the basement membrane, a thin layer of collagen IV separating the epithelium from the underlying connective tissue, may appear completely isotropic, depending on the observation scale.

Many imaging techniques have been used to characterize the microscopic structure of cervical connective tissue. Analysis of *ex vivo* cervices obtained from total hysterectomy of non-pregnant women using X-ray diffraction showed that collagen fibers are circularly distributed around the cervical canal in the medial area [60]. Meanwhile, as illustrated in Figure 2.7, collagen fibers in the outermost region and near the longitudinal axis of the endocervical canal are mainly oriented parallel to the canal with predominantly disordered organization[61], [62].

This overall distribution of collagen fibers in cervical stroma appears to be preserved even during pregnancy before delivery, as evidenced by analyses of *ex vivo* cervices performed by optical coherent tomography (OCT) [63]. This collagen orientation is thought to determine the ability of the cervix to resist the forces it faces during pregnancy. The longitudinally oriented fibers should resist the tension associated with cervical effacement [63], whereas circumferentially distributed fibers should prevent cervical dilation [60].

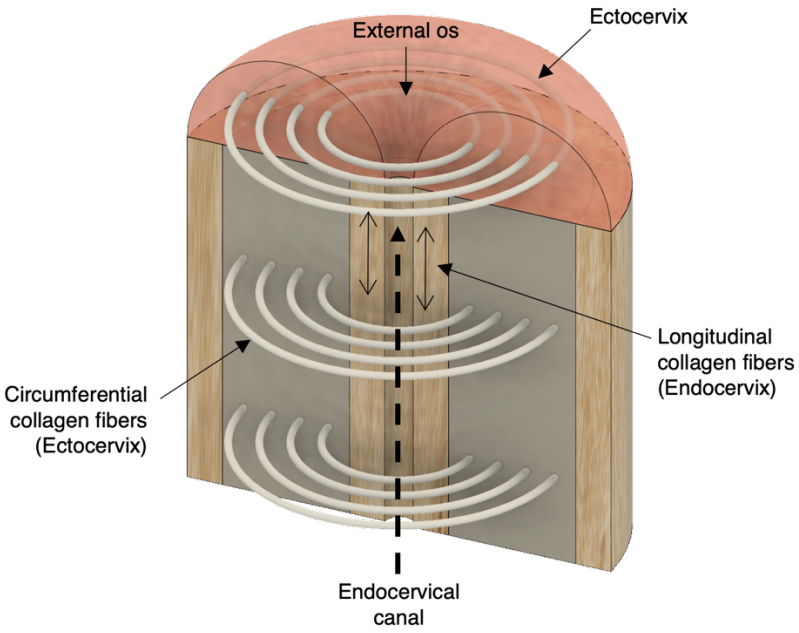

Figure 2.7 Distribution of the collagen fiber in the cervical stroma. Collagen fibers in the medial stroma are oriented circumferentially with respect to the canal, whereas collagen fibers near the endocevical canal are oriented along the longitudinal axis of the canal.

In an early study of metaplasia, it was considered as a type of healing process. A histological study reported distinct stromal patterns underlying native and regenerated (metaplastic) squamous epithelia [55], [64]. It implies that metaplasia produces active connective tissue remodeling. Breaking of basement membrane, often observed in the early stage of metaplasia [65], and angiogenesis during transition [50], [56] are also signs of stromal remodeling.

However, the dynamics of these alterations are hardly observed in *in vitro* or *ex vivo* experiments, as they require complex signaling, enzymes, and cell-cell/cell-stroma interactions [52], [66], [67]. A suitable technique for monitoring the metaplastic transition *in vivo* at the tissue level has not been found yet. Conventional medical imaging methods, such as MRI and CT-scan, are not able to visualize these microscopic modifications in metaplastic tissues. Endomicroscopy allows to capture images of tissues in vivo with high resolution. However, the evolution of a metaplastic transformation on a microscopic scale using this technique is not feasible in vivo due to the movement of objects.

2.2 Inspection of cervix using a colposcope

The colposcope is a medical imaging device with an optical and ergonomic design that allows for a cervicovaginal examination in a clinical setting. It consists of a binocular stereoscopic microscope with low magnification (between 4× and 6×) used during gynecological consultations or surgical procedures, usually for the early detection and removal of precancerous lesions of the cervix.

2.2.1 Optical specifications of the colposcope Olympus OCS-500

For the work described in this manuscript, we used a commercial colposcope Olympus OCS-500 shown in Figure 2.8a. The colposcope head, illustrated in Figure 2.8b, allows the

cervix to be illuminated and imaged effectively at different distances and magnifications. It is equipped with an optimized optical system to obtain a sharp image of the cervix at a working distance (WD) of 220 to 350 millimeters. The WD is defined as the distance between the front of the colposcope head and the cervix to be imaged as shown in Figure 2.8b. For a specific WD, a zoom system allows the magnification of the image to be changed. The field of view (FOV) can vary, for instance, between Ø73.1 millimeters and Ø11.6 millimeters for a WD of 300 millimeters. It is possible to optimize the image sharpness by means of a focusing optical system.

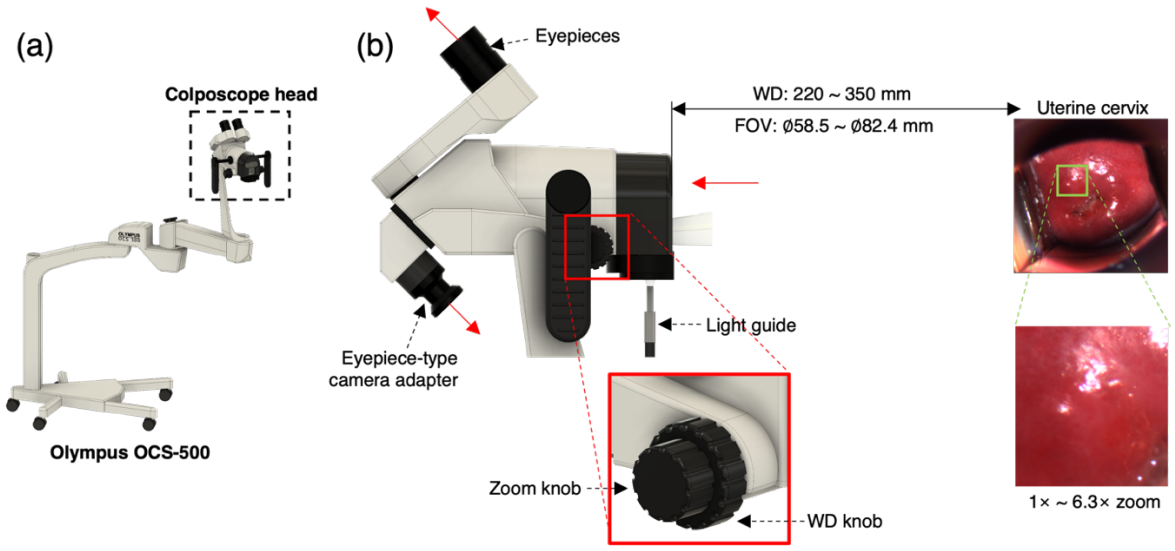

Figure 2.8 (a) Overall appearance of the colposcope OCS-500. (b) Detailed configuration of the colposcope head. The light beam from the light guide illuminates the cervix at a working distance of 220 ~ 350 millimeters. The colposcope then captures an image of the cervix at the working distance. The cervical image can be captured with both binocular eyepieces and digital cameras simulteanously.

During a medical procedure, the magnification and image sharpness for a fixed WD can be easily adjusted by the practitioner using knobs positioned on the colposcope head, as shown in the inset (the red square) in Figure 2.8b. Therefore, the practitioner can directly visualize the cervix with the desired magnification thanks to the binocular system that allows a stereoscopic view, as shown in Figure 2.9a and b. In addition, a digital camera can be connected to the colposcope head, as shown in Figure 2.9c. In this way, the practitioner has the possibility to view the image of the cervix directly on a computer screen, which also allows the recording of photos or videos.

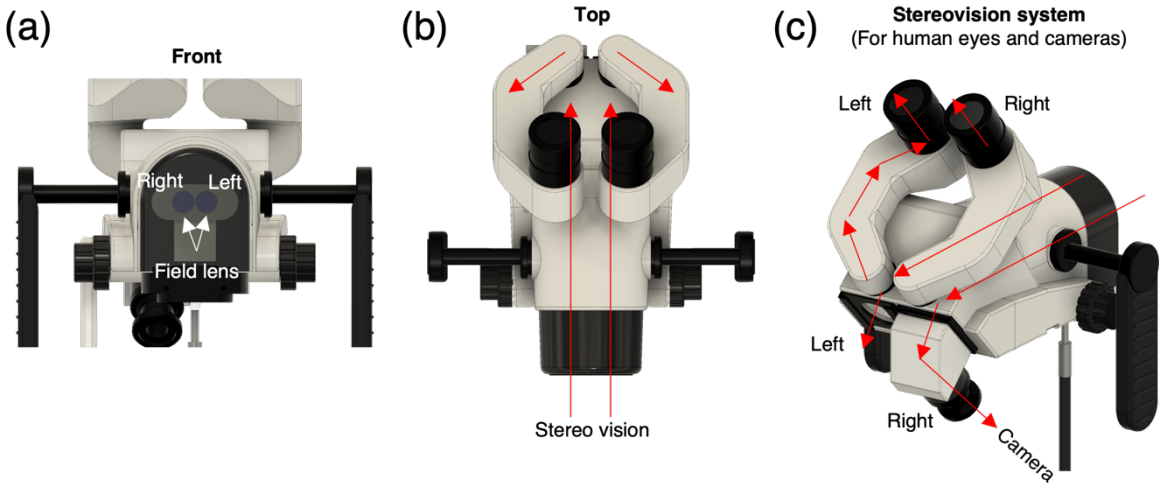

Figure 2.9 (a) The front view of the colposcope head. The colposcope has two field lenses for the right and left eyes form stereoscopic vision. (b) and (c) The top and side views of the colposcope head. The red arrows represent the beam path of the imaging system.

Figure 2.10 describes the illumination system for the colposcope head. Unpolarized light is provided by a halogen source and carried to the colposcope head by a silica fiber bundle. A collimator at the output end of the light guide produces a beam with a spot size of about 6.5 centimeters at a working distance of 30 centimeters from the colposcope head. A right-angle prism changes the beam path from vertical to horizontal. The prism is tilted of about 4° (with respect to the horizontal direction) to guide the beam upwards and compensate for the offset with the axis of the imaging system. With this opto-mechanical system, the beam is perfectly centered on the axis of the imaging system at a WD of 300 millimeters from the colposcope head, as shown in Figure 2.10.

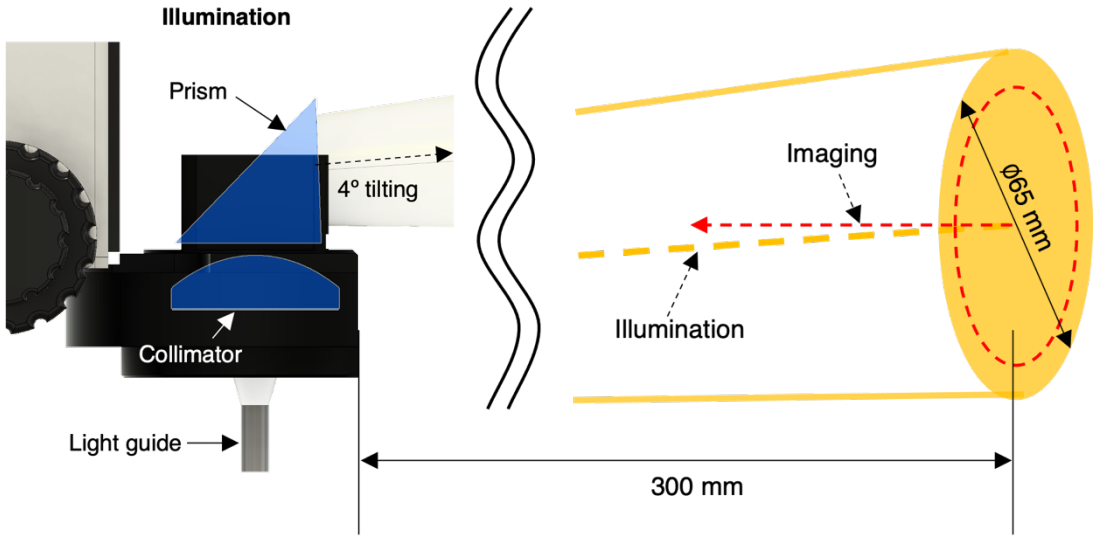

Figure 2.10 The scheme of the illumination system of the colposcope.

The technical specifications concerning the optics of the colposcope Olympus OCS-500 are charted in Table 2.1.

Table 2.1 Optical specification of the colposcope Olympus OCS-500.

Eyepiece	Magnification	10×
	Field number	22
Zooming	Zoom ratio	1:6.3
Focusing	Focus range	220 – 350 mm
Illumination	System	Light guide
Magnifications	WD220	3.7 – 23.4×
	WD300	3.0 – 18.8×
	WD350	2.7 – 16.9×
Field of view	WD220	58.5 – 9.3 mm
	WD300	73.1 – 11.6 mm
	WD350	82.4 – 13.1 mm
Photography	Digital camera	Connectable using a camera adapter

2.2.2 Mechanical specifications of the colposcope Olympus OCS-500

The colposcope head is attached to a spring-loaded mechanical arm capable of freely changing its height, as well as translating and rotating its position in the horizontal plane. These ergonomic features allow practitioners to handle the colposcope efficiently in a sedentary or standing position.

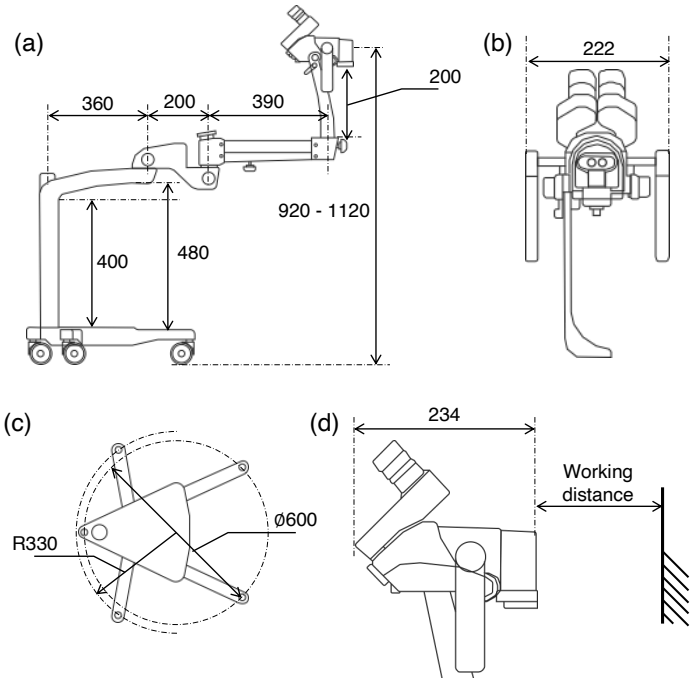

Figure 2.11 The actual size of OCS-500 in millimeters. (a) The side view of OCS-500. The colposcope head is suspended on a 390-millimeter spring arm. The height of the head is adjustable from 920 to 1120 millimeters, which corresponds to the seat height of an adult. (b) The front view of the colposcope head. (c) The floor plan of the floor stand. (d) The side view of the head. The working distance is measured from the front of the head.

In the colposcopic visual inspection, a vaginal speculum is used to dilate the vaginal walls and allow the practitioner to visualize the cervix using the colposcope, as shown in Figure 2.12.

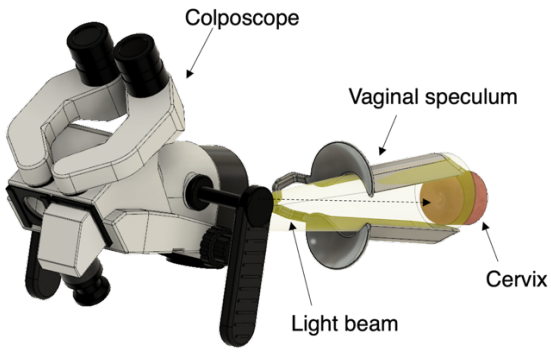

Figure 2.12 An illustration of a typical colposcopic examination with a vaginal speculum. The cervix is captured through the opening of the vaginal speculum.

2.3 Mueller polarimetric analysis of cervix

Polarimetric imaging has been demonstrated to be relevant for the characterization of highly scattering [68]–[71] or anisotropic [72]–[74] media. In recent years, this technique has shown great promise for biomedical diagnostic technology [75]–[77]. Indeed, it has been widely used for investigating biotic tissues, optically very complex systems in which scattering and anisotropic effects exist simultaneously. As described in the previous chapter, polarimetric imaging uses the polarization of light, which has proven to be highly sensitive to pathological changes in the microstructure of biotic tissues. In fact, it can detect alterations in cellular structure and density, as well as the organization and size of fibers that make up the extracellular matrix [78]–[81]. In particular, this technique is well suited for exploring the structure of collagen, whose optical anisotropic and scattering properties can produce specific polarimetric responses [81]–[83].

The LPICM (Laboratoire de Physique des Interfaces et des Couches Minces) is a laboratory of the Ecole Polytechnique (France) acknowledged as one of the leaders in the field of Mueller polarimetry. The use of this technique for biomedical applications is currently a major research activity at the LPICM.

It commenced since 2005 with the ANR RNTS "Polarimetry" contract aimed to develop an application of Mueller polarimetric imaging for early diagnosis of cervical cancer.

The ANR IMULE contract was established in 2011 in collaboration with the Xlim laboratory of Limoges (France) for the development of the first Mueller polarimetric endomicroscope for exploring the internal cavities of the human body. The "PAIR Gynéco" project, funded by the French National Cancer Institute, was established in 2012. This project aimed to statistically evaluate the diagnostic performance for detection of precancerous cervical lesions in ex vivo Mueller polarimetric imaging. In this project, the first prototype of a Mueller polarimetric colposcope was made and tested in vivo in a hospital setting on human patients for a feasibility study.

The ANR DigitMC-PB project has been approved for funding in 2019. This project aimed to design and fabricate a novel Mueller polarimetric colposcope for *in vivo* analysis of cervical microstructure to improve the detection of prematurity. This thesis work was developed as part of this project which is still ongoing.

Finally, the HORAO project funded by the Swiss National Science Foundation was awarded in April 2022 and focuses on the use of Mueller polarimetry for improving brain cancer surgery.

The exploration of the microstructural properties of the cervix using Mueller polarimetric imaging is one of the principal research topics developed at LPICM, especially for two applications: the early detection of cancer and the preterm birth.

2.3.1 Early detection of cervical cancer

Every year there are approximately 500,000 new cases of cervical cancer worldwide, and about half of that, 260,000 women, die from it. The standard diagnostic method currently implemented in developed countries is regular screening with a Papanicolaou (Pap) smear test, and if necessary, visual examination using colposcopy is also performed. This method has reduced the incidence rate of cervical cancer in developed countries. However, due to its high incidence in low- and middle-income countries where resources and infrastructure for regular and high-quality screening are scarce [84], it is still the second most common cancer and the major cause of death in women worldwide.

The main cause (95-98% of cases) of cervical cancer is chronic infection with various types of human papillomavirus (HPV), especially HPV-16 and HPV-18 [68], that invade cervical tissue through the TZ. This infection is widespread and can cause dysplasia or cervical intraepithelial neoplasia (CIN), which are the proliferation of abnormal cells in the squamous epithelium. Cervical lesions are histologically classified as CIN1 (mild dysplasia) or CIN2 (moderate dysplasia), respectively, if the deformity affects one-third or two-thirds of the thickness of the SSE. And, if the entire thickness of the SSE is affected, it is classified as CIN3 or precancerous lesion (severe dysplasia). Finally, the disease can progress from CIN3 to invasive cancer if the malignant cells spread into the connective tissue beneath the SSE. Each stage of dysplasia is illustrated in detail in Figure 2.13.

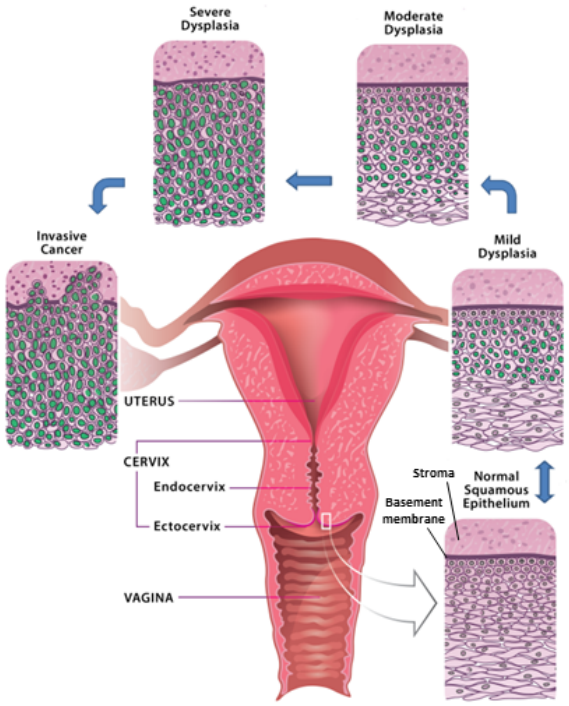

Figure 2.13 Illustration showing the progress of cervical cancer. Reproduced with permission from [69]**.**

Although the HPV vaccine was introduced in 2006 [68], this is unlikely to change this situation in the short term. Moreover, they are not curative and can be used for prophylactic purposes but are not 100% effective [70]. In addition, there is strong psychological resistance to its use in some developed countries [71]. Finally, due to the high cost of these vaccines and, in some cases, political or logistical obstacles, they are not widely used in low-resource developing countries [72]. For all these reasons, no matter how developed a country is, cervical cancer will remain a important health issue for many years to come. Therefore, it is important to improve the detection and treatment of cervical cancer in both developed and low-resource countries.

As mentioned above, the first step in cervical cancer screening is the Pap smear test, which collects epithelial cells from the surface of the cervix and examines them under a microscope. Patients with an abnormal smear are referred for colposcopy. Here, 3% acetic acid and iodine are applied as contrast agents and the cervix is visually inspected with a colposcopy. Suspected areas, usually whitened by applying acetic acid and iodine negative, are biopsied to confirm the presence of malignant tissue by histological analysis. Finally, the abnormal areas are surgically removed by conization, which is an excision of a conical piece of tissue (~2 cm in diameter) usually guided by the colposcope. Conization is sufficient to prevent recurrence of the disease.

Unfortunately, colposcopy is highly operator-dependent with a sensitivity of 60-70% and a specificity of 50% for detection of CIN 2-3 and moderate inter-operator reproducibility [80], [81], [83]. This results in difficulties for practitioners in accurately locating biopsy sites and determining the boundaries of surgical resection. The poor performance of colposcopy is attributed to the difficulty in distinguishing the CIN 3 from the various degrees of metaplasia, which are whitened similarly after the application of acetic acid.

It is also important to define precise surgical boundaries. This is because the size of the conization must be as small as possible to ensure healthy margins of the resected tissue and to minimize the risk of complications in future pregnancies [85], [86]. Moreover, the current screening programs take several weeks to diagnose and treat [87]. These programs are expensive and need highly skilled medical practitioners and tissue analysis laboratories, making them impossible in low-resource countries. Therefore, there is a need for a new, effective and inexpensive approach that:

- improves the accuracy of colposcopy to significantly reduce the cost and time for diagnosis and patient management in developed countries;
- designs and fabricates a new low-cost technology that could be part of an affordable "screen and treat" approach in low-resource countries.

Ex vivo Mueller polarimetric imaging of the uterine cervix: proof of principle

The proof-of-principle for the relevance of Mueller polarimetric imaging for the detection of precancerous lesions of the cervix was performed on a dozen *ex vivo* conization specimens. For this purpose, a full field multispectral Mueller polarimetric imaging system was built at the LPICM and installed in the Department of Pathology of the Institut Mutualiste Montsouris (France).

This system enabled the exploration of *ex vivo* cervical samples at multiple wavelengths between 500 and 700 nm in 50 nm steps using 40 nm band color filters. Figure 2.14 shows an example of the polarimetric response of a conization specimen at 550 nm. The polarimetric images were obtained from a measured Mueller matrix image and the Lu-Chipman decomposition [24].

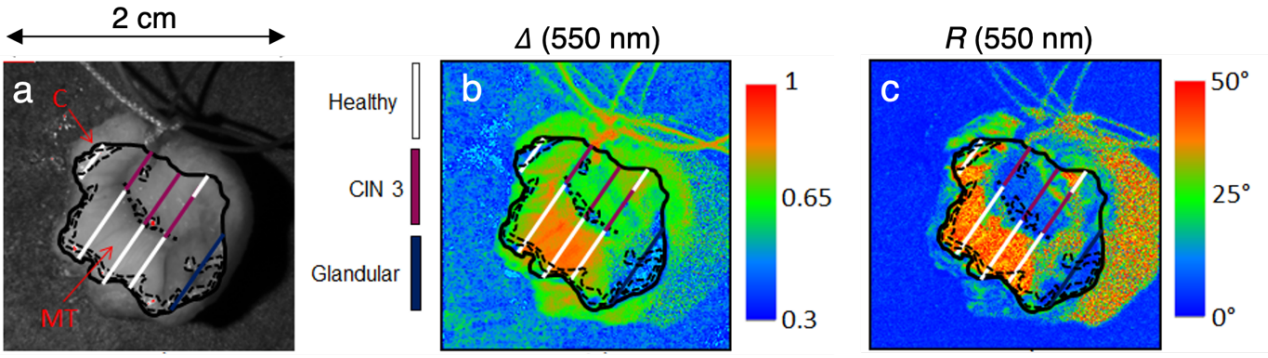

Figure 2.14 A conization specimen exhibiting healthy squamous epithelium (white lines), CIN3 (purple lines) and glandular epithelium (blue line). The 3 images correspond to (a) the conventional unpolarized intensity image, (b) depolarization (*Δ*), and (c) retardance (*R*) at 550 nm, respectively. MT in (a) indicates the SSE and C the underlying connective tissue (also named chorion). Polarimetric images in (b) and (c) were obtained by the Lu-Chipman decomposition.

The polarimetric images in Figure 2.14b and c exhibit contrast not seen in the conventional unpolarized intensity image in Figure 2.14a. Histological analysis of this specimen showed that it contained a large portion of healthy SSE, a CIN3 lesion, and glandular epithelium (CE). We observed a strong birefringence in the regions corresponding to healthy SSE (between 30° and 70° *R*), which decreases sharply in the CIN3 and glandular

parts (< 10° R). Δ increases from the glandular epithelium (approximately 0.3) to CIN 3 (approximately 0.7) and to the healthy SSE (approximately 0.9). By combining the R image with the Δ image, it was possible to detect the presence of a precancerous lesion (CIN3). This example clearly shows that nearly two thirds of conization was unnecessarily excised [42].

Understanding the preliminary experimental results

To better understand the polarimetric contrasts described above, histological slides of cervix, mainly healthy samples, were analyzed using a Mueller polarimetric microscope built at LPICM. This study revealed that the strong anisotropy that characterizes the healthy areas originates from the connective tissue beneath the SSE. In particular, the polarimetric images of connective tissue were compared with images obtained with second harmonic generation (SHG) microscopy. This comparison clearly showed that the azimuth of the linear retardance (α) is related to the orientation of collagen fibers [88]. The strong anisotropy that characterizes the healthy SSE of the cervix is predominantly due to the presence of a well-ordered and structured collagen layer in the adjacent connective tissue. Furthermore, the first model describing the interaction between polarized light and isotropic complex media was developed to explain the strong depolarization that characterizes healthy areas of various tissues (cervix, rectum, colon, etc.) [41], [89]. The observed depolarization is mainly due to scattering by the cells and intracellular particles that make up the SSE and connective tissue, as well as small structures (compared to the wavelength of light) identified as unorganized collagen fibers in the connective tissue below the epithelium.

To account for the polarimetric contrasts observed on the cervix, development of a more realistic anisotropic model that can simultaneously account for tissue anisotropy and diffusion effects is underway in the LPICM.

First *ex vivo* statistical evaluation

In the "PAIR Gynéco" project, an extensive series of measurements on *ex vivo* conization specimens were carried out at three hospitals in Paris (Kremlin Bicêtre University Hospital, Gustave Roussy Institute, and Mutualiste Montsouris Institute). The samples were analyzed at multiple wavelengths from 450 to 700 nm in 50 nm steps using 40 nm band color filters. The polarimetric images of the conization specimens were compared with the "gold standard" provided by histopathological analysis. Optimized classification performance of ~84% and ~82% at 450 nm and 550 nm, respectively, for sensitivity and specificity were obtained to classify CIN3 lesions from healthy SSE using only linear retardance as a discriminating parameter [40].

Preliminary *in vivo* results

The first prototype of a monochromatic Mueller polarimetric colposcope (MPC) was fabricated by "grafting" a miniaturized Mueller polarimeter onto a conventional colposcope Olympus OSC-500 [4]. A miniaturized Mueller polarimetric system, framed in a 30×50×100 mm^3 metal box, is placed in front of the colposcope, as shown in Figure 2.15a.

Unpolarized light is supplied by a halogen source and delivered to the colposcope head through a liquid light guide (Thorlabs LLG0528-6), as shown in Figure 2.15b. A collimator

positioned at the exit end of the liquid light guide is capable of producing a beam with a spot size of 6.5 centimeters at a work distance of 30 centimeters from the colposcope head (approximately equivalent to the location of the cervix to be analyzed).

As explained in the previous chapter, the light from the collimator passes through a Polarization State Generator (PSG) before illuminating the cervix. The light backscattered from the tissue is analyzed by a Polarization State Analyzer (PSA) before being collected by the detector. The miniaturized PSG and PSA, embedded in the polarimetric box, are built by using bistable V-shaped ferroelectric liquid crystals (FLCs) in smectic C phase [14], [90]. The FLCs operate as a wave plate with fixed linear retardance and a variable azimuth of the fast (or slow) axis. Taking into account the light propagation, the PSG is composed in the order of a linear polarizer, a quarter-wave FLC (QFLC), a waveplate (WP) and a half-wave FLC (HFLC). The PSA is a the mirror symmetry of the PSG. The PSA actually consists of the same optical elements as the PSG but placed in the reverse order. An illustration of all components of the polarimetric box is shown in Figure 2.15c. The MPC was equipped with a monochromatic CCD camera, Allied Prosilica GT1920, shown in Figure 2.15d, capturing 800 × 600 pixel images (in the 2×2 binning mode) with 25 frames per second (FPS). Thus, with the MPC. reliable Mueller polarimetric images can be obtained in 1.6 s at 550 nm in with a field of view of 4×3 cm² and an actual measured spatial resolution of about 150 μm/pixel.

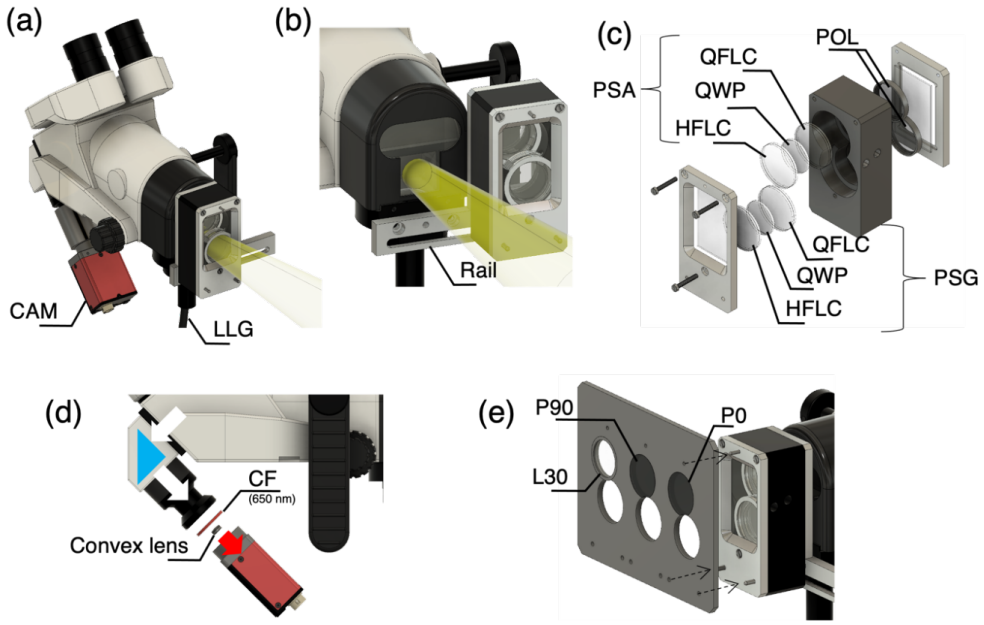

Figure 2.15 (a) The polarimetric system in the "ON" position. In this position, the PSG and PSA are aligned to the optical axis of the colposcope. (b) The box in the "OFF" position. The box is removed from the optical axis of the colposcope. (c) The assembly of the polarimetric elements of the PSG and PSA. (d) The configuration of the digital imaging system. (e) The metal plate for calibration of the polarimetric system. QFLC: quarter waveplate FLC, HFLC: half waveplate FLC, QWP: Quarter waveplate, POL: linear polarize, CAM: camera, LLG: liquid light guide, CF: color filter, P0: polarizer at 0°, P90: Polarizer at 90°, and L30: linear retarder at 30°.

More specifically, the polarimetric box is attached to a rail fixed to the colposcope head and can be slid into either the "OFF" position as shown in Figure 2.15b for conventional colposcopy or the "ON" position as shown in Figure 2.15a for polarimetric measurement. On the other hand, placing the polarimetric head in the "ON" position disables the use of one of

the colposcope's eyepieces, which is a practical limitation of this system as it prevents the practitioner from operating the MPC like a conventional colposcope.

For the calibration of the MPC, we used the eigenvalue calibration method (ECM) described in detail in Chapter 1. The ECM consists of acquiring the 16-element intensity matrix $\boldsymbol{B}$ consecutively for the three optical reference elements, namely the first polarizer whose transmission axis is oriented at 0° to the laboratory reference (P0), the second polarizer whose transmission axis is oriented at 90° to the first polarizer (P90), and a waveplate whose slow axis is oriented at 30° to the first polarizer (L30).

For this first MPC prototype, the reference elements for calibration were mounted on a metal holder that can be connected directly to the polarimetric box, as shown in Figure 2.15e. To calibrate the system, the operator has to move the metal holder by hand to position each reference element in front of the PSG or PSA. A sandblasted aluminum plate serving as a reflector for calibration can be attached to the rail of the polarimetric box, as shown in Figure 2.16. It is centered with respect to the light beam at a working distance of 30 centimeters.

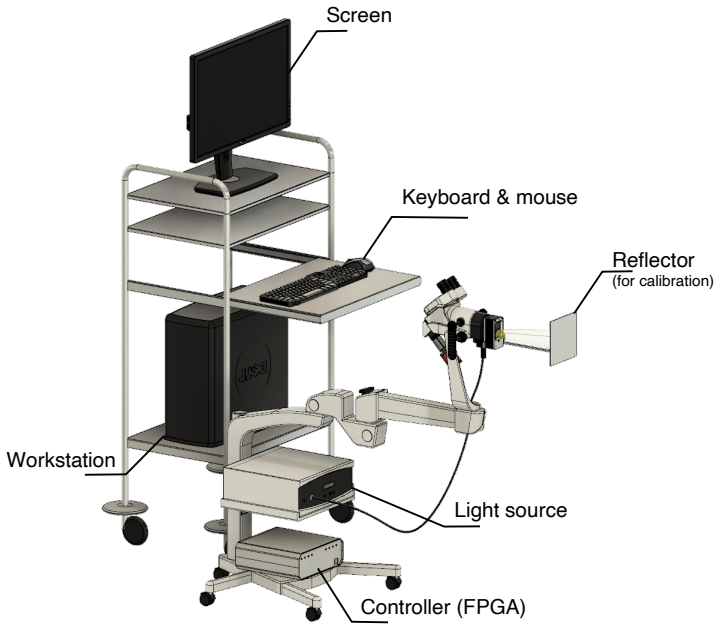

Figure 2.16 The full appearance of the first prototype. The cables has been omitted for better visualization. The workstation is mounted on a bulky medical trolley. This bulky system with the trolley compromises ergonomics and mobility of the system.

Figure 2.16 shows the appearance of the first MPC prototype. The FPGA that synchronizes the polarimeter and the camera, as well as the light source are mounted on the colposcope. The workstation including the monitor, keyboard and mouse to operate the image acquisition and processing is placed on a separate medical cart. Image acquisitions are controlled by a Graphical User Interface (GUI) program written in LabVIEW while MATLAB scripts are used to process the acquired Mueller polarimetric images.

This first prototype of MPC was used for an *in vivo* feasibility study conducted at the University Hospital of Kremlin-Bicêtre on a few patients [4]. It allowed the measurement

of a Mueller matrix in about 2 s, which considerably reduces (but does not completely eliminate) artifacts of patient's movement during image acquisition.

Figure 2.17 shows a typical polarimetric response obtained on the *in vivo* cervix, without dye application. We observed strong linear retardance (*R*) in the areas corresponding to healthy SSE while it strongly decreases to very low values in the CIN3 and glandular parts. Moreover, depolarization (Δ) increases from the glandular part to the CIN3 and then to the healthy SSE. This feasibility study clearly confirmed the trend previously described and observed *ex vivo* described above [42].

The combination of these two main polarimetric parameters allows the detection of the presence of precancerous lesions that are likely to be indistinguishable in conventional colposcopy even after the application of acetic acid and iodine, as shown in Figure 2.17. The implementation of *in vivo* Mueller polarimetric imaging can provide very useful contrasts to significantly improve cervical cancer screening.

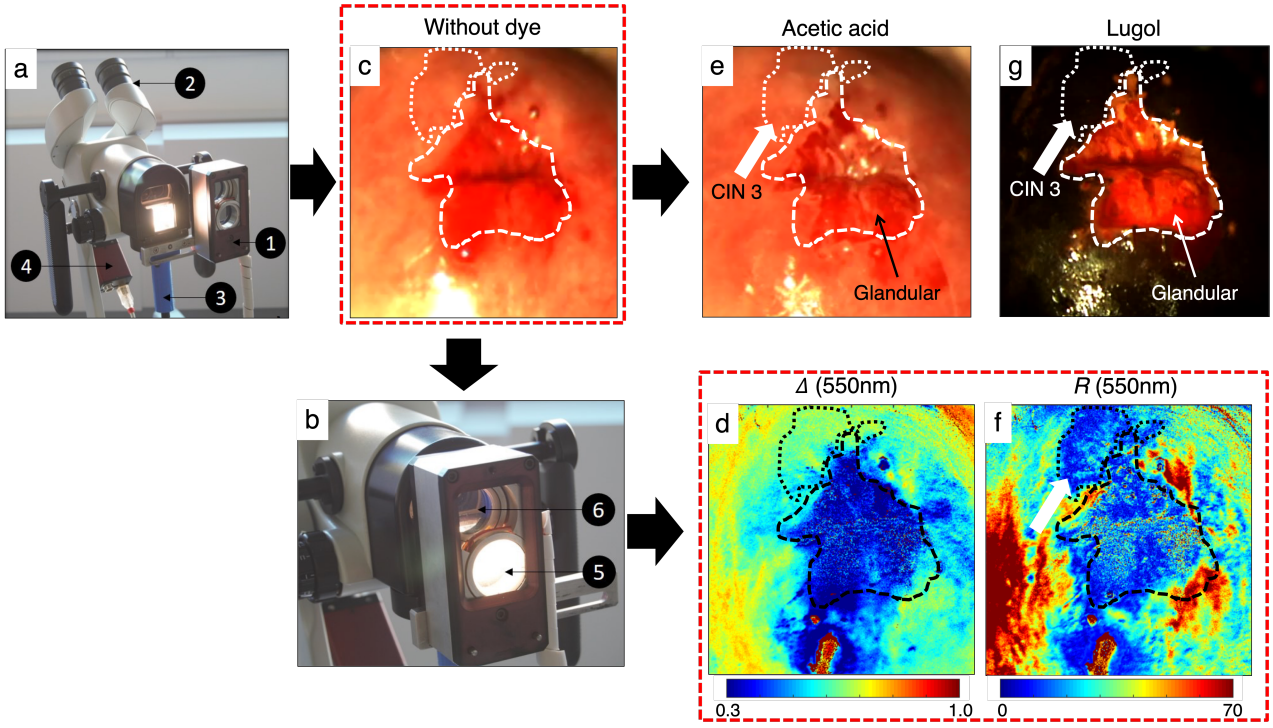

Figure 2.17 (a, b) Photos of the MPC system. 1: Polarimetric head, 2: Binoculars for stereoscopic vision of the uterine cervix, 3: Liquid light guide, 4: CCD Camera, 5: Polarization States Generator (PSG), 6: Polarization States Analyzer (PSA). The polarimetric head in the "OFF" position in (a) allows the practitioner to perform classical colposcopic examinations. The polarimetric system can be moved to the "ON" position to allow the acquisition of Mueller polarimetric images shown in (d) and (f). (c, e, g) RGB unpolarized intensity images, acquired with conventional colposcopy, without dye, after the application of acetic acid and after the application of Lugol respectively. (d, f) depolarization (Δ), retardance (R) images respectively at 550 nm. Polarimetric images were acquired for uterine cervix without colorant. White arrow in (e), (g), and (f) indicate the zone of CIN3. This zone is clearly detected by polarimetric images while it is invisible to the conventional colposcopy.

2.3.2 Monitoring the cervical microstructure remodeling during pregnancy

As explained in this chapter, spontaneous preterm birth (SPTB) is a birth less than 37 weeks of amenorrhea and is the leading cause of perinatal death worldwide. Its rate is estimated at 6% in France and Europe and twice as high in the United States 1. The threat of SPTB is the most important complication during pregnancy. It occurs between 23 and 37 weeks of amenorrhea and related symptoms include contractions of the uterus associated with changes in the shape of the cervix, and sometimes bleeding or premature membrane rupture. Pregnant women diagnosed with SPTB are hospitalized and given tocolytic treatments to reduce contractions and suppress SPTB [91]. However, assessing the severity of SPTB to accurately predict the risk of preterm birth remains a challenge in current medical practice [92].

The recommended technique is transvaginal ultrasound imaging for measurement of cervical length, sometimes supplemented by biomarker detection [93], [94]. Pregnant women with a cervical length of less than 20 millimeters at less than 37 weeks of amenorrhea are considered at risk of preterm delivery. However, because of the impossibility to correlate measured length with time to delivery, there is no clear recommended threshold for cervical length that would reliably detect prematurity [95]. As a result, preterm delivery only occurs in less than 50% of women diagnosed with SPTB. Thus, a large percentage of women are hospitalized unnecessarily, which is costly [96] and may lead to complications from side effects of tocolytic treatments [97] and thromboembolic risks associated with bed rest [98]. A new method to improve the diagnosis of SPTB is needed to reduce medical health care costs, prevent side effects associated with unnecessary hospitalizations, and lay the groundwork for new therapeutic strategies to lower the preterm birth rate.

The uterine cervix plays an important role in maintaining pregnancy and delivery [99], [100]. The mechanical properties of the cervix change noticeably as gestation progresses. For a full-term pregnancy, this process progresses slowly until approximately 37 weeks of amenorrhea. During this phase, the cervix is gradually softened without any noticeable changes in anatomy (cervical softening) so that the growing fetus can be well protected in the uterus. After 37 weeks of amenorrhea, the cervix shortens and dilates (cervical ripening) in preparation for labor, which occurs at approximately 40 weeks of amenorrhea. Changes in the mechanical properties of the cervix during pregnancy are attributed to remodeling of its microstructure. This process mainly involves its connective tissue, which accounts for more than 95% of the cervical volume and, is predominantly composed of collagen as explained above.

Numerous studies have shown that connective tissue remodeling during pregnancy is a complex process involving an increase in collagen extractability and solubility and a decrease in collagen concentration [101]–[105]. In addition, increases in collagenolytic activity and hydration of cervical tissue are observed [104], [105]. Thus, characterization of cervical microstructural remodeling during term gestation is important to understand how this process unfolds in a high-risk pregnancy.

Various imaging techniques, such as x-ray diffraction[60], optical coherence tomography (OCT) [63], magnetic resonance imaging [106], and second harmonic

generation (SHG) microscopy [107], have been used to investigate this remodeling process. However, applying these techniques to medical diagnosis during pregnancy is still difficult. For example, X-rays can be potentially hazard for the mother and fetus. OCT and SHG microscopy can examine cervical tissue with micrometer resolution but the maximum depth is less than one millimeter. In addition, these techniques are slow and not suitable for *in vivo* use as they require a scanning system to image a large area.

A feasibility study was conducted by the LPICM in collaboration with the Brugmann University Hospital in Brussels to figure out whether Mueller polarimetric imaging is capable of characterizing microstructural changes of the cervix during pregnancy. In this study, A group of full-term pregnant women with various gestational ages was analyzed. This allowed us to monitor the regular course of pregnancy in order to identify the potentially most relevant polarimetric parameters [108].

For the feasibility study, a dual-wavelength MPC was built as an improved version of the first monochromatic prototype described above. This new MPC prototype was equipped with a detection system allowing the simultaneous acquisition of images at 550 nm and 650 nm, as shown in Figure 2.18a. This system consists of a dichroic beam splitter (Thorlabs DMLP605) that splits the upper and lower parts of the optical spectrum above 605 nm into two orthogonal beams. In addition, a color filter was placed in front of each camera. This optical system allows the measurement of Mueller polarimetric images at 650 nm for camera 1 (Thorlabs FB650-40, 40 nm FWHM) and at 550 nm for camera 2 (Thorlabs FB550-40, 40 nm FWHM). The camera used for each wavelength is always an Allied Prosilica GT1920 providing 800 × 600 pixel images (in 2×2 binning mode) with a rate of 25 FPS. The dual-wavelength MPC is able to perform accurate polarimetric measurements simultaneously at 550 nm and 650 nm in 2 s with a field of view of 4×3 cm² and a spatial resolution of about 150 µm/pixel for both wavelengths. Finally, a third color camera was added as shown in Figure 2.18b for the acquisition of reference RGB images of the cervix.

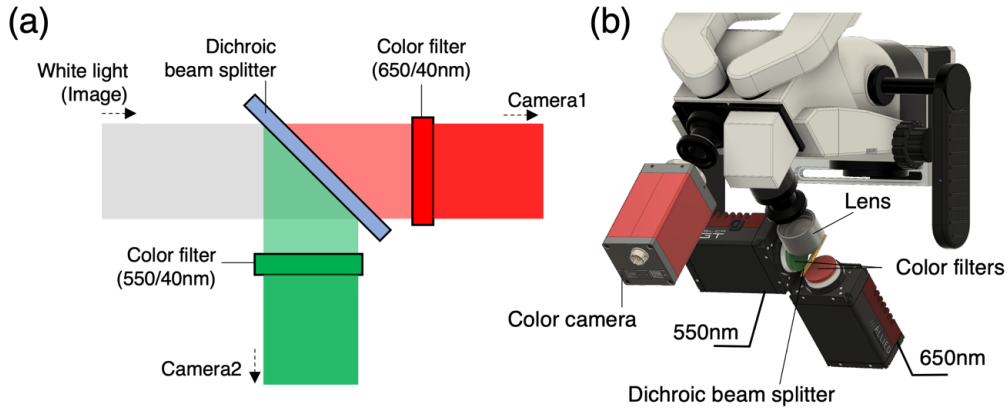

Figure 2.18 The bi-chromatic imaging system based on a dichroic beam splitter. (a) The optical scheme. (b) The actual configuration on the colposcope head.

The dual-wavelength MPC was used to examine the cervix of 24 full-term pregnant women of different gestational ages. This study was offered to patients older than 14 weeks of amenorrhea without any exclusion criteria other than gestational age, resulting in a very heterogeneous population. The main objective of this study was to determine the most relevant polarimetric parameters for monitoring the steady remodeling of cervical

microstructure during pregnancy. For comparison, cervical length was also measured for each patient by transvaginal ultrasound (conventional procedure) after polarimetric imaging.

The evolution of cervical polarimetric properties as a function of gestational age was investigated. For each patient, the mean value of the depolarization Δ, denoted as $\mu(\Delta)$, was calculated at 650 nm for all pixels contained in a ROI corresponding to the ectocervix. Overall, $\mu(\Delta)$ decreases linearly with pregnancy progression for both wavelengths, suggesting that the depolarization Δ may be a well-suited polarimetric parameter for monitoring the cervical microstructure remodeling during full-term gestation. However, the correlation between $\mu(\Delta)$ and the gestational age is high at 650 nm while it is relatively moderate at 550 nm. This difference may be due to the smaller within-population variability (up to 5%) for this parameter at 650 nm, whereas it may increase significantly (up to 30%) at 550 nm, as shown in Figure 2.19.

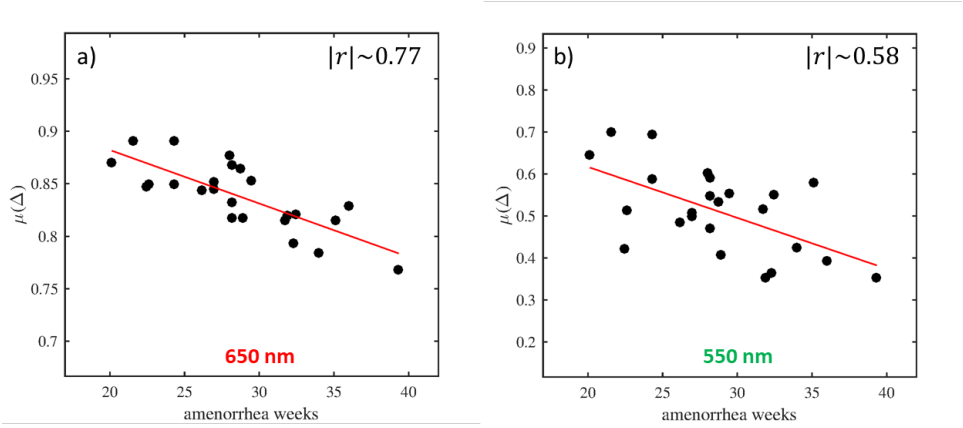

Figure 2.19 (a) and (b) Scatter plots describing gradual changes in $\mu(\Delta)$ with the gestational age at 650 nm and 550 nm, respectively. A negative linear correlation is observed between $\mu(\Delta)$ and gestational age at both wavelengths. This correlation is higher at 650 nm ($|r|\sim 0.77$) than at 550 nm ($|r|\sim 0.58$).

The biological origin of the decrease in $\mu(\Delta)$ for both wavelengths can be attributed mainly to decreased volume scattering power of the cervix due to decreased collagen density and increased connective tissue hydration at different depths [101]–[105]. In contrast, cervical length measured by transvaginal ultrasound is not correlated with gestational age, as shown in Figure 2.20.

This feasibility study demonstrates that depolarization imaging, particularly for red light, is a promising tool for probing cervical microstructure during gestation and determine a standardization curve able to monitor the steady progression of pregnancy.

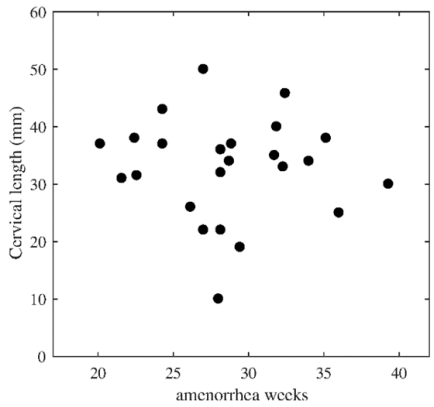

Figure 2.20 The scatter plot of the cervical length measured by transvaginal ultrasound (standard procedure) with patients' gestational age. No correlation is found between cervical length and gestational age.

However, the number of patients analyzed in this study remains very limited to draw conclusions on the relevance of Mueller polarimetric imaging to probe the cervical microstructure during pregnancy. On the other hand, thanks to these very promising preliminary results, the LPICM has received funding from the French National Research Agency (ANR) for the Digit MC-PB project aimed at testing multispectral Mueller polarimetric imaging on a massive number of patients in a clinical study. This thesis work was developed within the framework of the Digit MC-PB project renamed COLPOTERME.

2.4 Conclusions

The microstructure of the cervix undergoes significant changes throughout a woman's life and especially during pregnancy due to strong hormonal variations. In recent years, Mueller polarimetry, whose mathematical formalism was presented in Chapter 1, has shown great potential for the analysis of biological tissues. The objective of this thesis is to verify the ability of Mueller polarimetric imaging to monitor the remodeling of the cervical microstructure during pregnancy.

In this chapter, we first introduced the cervix from an anatomical perspective, clarifying its crucial role as a female reproductive organ. We then described the microstructure of the cervix in relation to its physiology. In particular, we described in detail the microscopic structure and physiology of the epithelial tissues (glandular epithelium, squamous epithelium and metaplastic epithelium) that cover the surface of the cervix, as well as the different types of modifications that they may undergo throughout a woman's life and especially during pregnancy due to hormonal changes. Thus, we described the structure of the connective tissue underlying the epithelium and its modifications during pregnancy.

In addition, we presented the colposcope, the optical system used in medical practice to explore the surface of the cervix to detect precancerous lesions. Finally, we summarized the main previous research conducted at LPICM on the use of Mueller polarimetry to explore the microstructure of the cervix for two main applications, namely the early detection of cancer and the improvement of prematurity diagnosis.

Chapter 3

Development of the advanced MPC

The main objective of this thesis work was to initiate, for the first time to our knowledge, a clinical trial to examine the cervix of a massive number of pregnant women in vivo using Mueller polarimetric imaging in order to evaluate the ability of this technique to monitor the cervical microstructure remodeling during pregnancy.

For this purpose, we first designed and developed a novel Mueller polarimetric imaging system well suited for use in a clinical trial. In general, a medical device must be used by healthcare professionals in a hospital setting on many patients according to well-established clinical protocols. Moreover, the subject of clinical research is a living human subject. Various studies have shown that many factors such as hostility towards clinical trials can strongly influence the degree of patient recruitment [109].

For these reasons, in addition to being able to perform high-quality repeatable measurements in a very short time interval, a medical device must also have strong ergonomics and usability. Moreover, it requires relatively simple and robust software as well as an intuitive and user-friendly graphical interface. The development of a medical device for use in a clinical trial is a real instrumental challenge.

This chapter describes the key steps we took in designing and building a novel multispectral Mueller polarimetric colposcope (MPC) capable of acquiring high-quality in vivo images while meeting the key clinical trial requirements in terms of speed and usability.

3.1 Project COLPOTERME

In collaboration with the Department of Obstetrics and Gynecology of the University Hospital of Kremlin-Bicêtre (France), the ANR project Digit MC-PB ("Digital Mueller Polarimetric Colposcopy for the Prediction of Preterm Birth"), renamed COLPOTERME, has been launched to test Mueller polarimetric imaging as a new tool for the diagnosis of spontaneous preterm birth.

In the COLPOTERME project, the new multispectral MPC prototype is being used to analyze the cervix of 650 pregnant women, 400 with full-term delivery and 250 at high risk of preterm delivery, over a 36-month period. Each woman is analyzed 1 to 5 times (average of 3 times) during pregnancy depending on her gestational age at the time of the recruitment.

The main objective of the COLPOTERME project is to determine the best "polarimetric biomarkers" to define an optimal "Polarimetric Score" reflecting the state of the microscopic structure (in particular collagen) of the cervix throughout its remodeling process due to pregnancy in a population at low risk of preterm birth. This "polarimetric score" should make it possible to define a standardization curve capable to monitor the steady evolution of a pregnancy.

The secondary objective of this study is to define a second optimal "polarimetric score" for a population at high risk of preterm delivery. This second score should make it possible to determine the time remaining before delivery and help to predict prematurity.

3.1.1 Requirements for setting up a clinical trial

After setting the main objectives of the study, it is essential to define the minimum requirements to achieve them. These requirements are listed below.

- The MPC must be able to perform the planned examinations in the allotted time.
- The acquired images must be of high quality to allow detailed inspection of the cervical tissue.
- The performance of the MPC must be consistent throughout the 36-month study period to ensure the repeatability and reproducibility of measurements.
- The MPC must be ergonomic and easy to use by a practitioner. In addition, relatively simple and robust software with an intuitive and user-friendly graphical interface is required.
- Medical practice should be respected as much as possible. For this purpose, the MPC must have a mode of operation very close to that of a classical colposcope.
- The database has to provide an efficient environment for users to easily read and exploit 36 months of accumulated data.
- The quality of care must be very satisfactory for the patients in order to encourage their repeated participation in the study (analysis of each patient's cervix several times during the study) and also to maximize the number of inclusions.
- This thesis work has focused on the instrumental development of a new MPC prototype. At the same time, considerable work has also been done on the development of user-friendly software and the implementation of a relational database to manage a large amount of data. However, only the part concerning the instrumental development will be discussed in detail in this manuscript. Information about the software and the database can be found in the Appendix (Chapter 6.8-11).

3.1.2 Drawbacks and limitations of the dual-wavelength MPC prototypes

A feasibility study of 24 patients *in vivo* at Brugmann University Hospital (Brussels) was performed using the dual-wavelength MPC developed at the LPICM and described in detail in Chapter 2. Although this study yielded very promising results, it also revealed significant limitations of the dual-wavelength MPC that preclude its use on a massive number of patients in a clinical trial. The limitations of this system are summarized in Table 3.1.

Table 3.1 Drawbacks of the dual-wavelength MPC.

Component	Category	Limitation	Effect
Imaging system	Mechanics	Unstable camera connection.	Misalignment between the 2 cameras. Images at the two used wavelengths (550 nm and 650 nm) not perfectly superimposable.
	Color imaging	Parallax between color and polarimetric images. Size of color image different from that of the polarimetric images.	Color image not superimposable to polarimetric images.
	Acquisition speed	Slow image acquisition rate. Maximum acquisition of 25 FPS. No averaging of images to increase the signal to noise ratio.	High motion blur in polarimetric images. Low signal to noise ratio. Noisy images.
	Optics	A single lens camera objective.	Strong optical aberrations. Non-uniform sharpness (field curvature). Loss of image resolution.
Polarimetric system	Opto-mechanics	Poorly adapted geometry.	Disabling one ocular by the polarimetric box. Activate/deactivate the polarimetric imaging modality by manually moving the polarimetric box. Strong change in medical practice.
	Manual calibration	Reference calibration samples manually exchanged by the user during calibration process.	Long calibration time. Calibration not feasible by a practitioner. Strong change in medical practice.
Usability	Software and user-interface.	Complex and unstable software. Complex and non-intuitive user interface.	Difficult handling and high training cost.
	Ergonomics	Voluminous system (2 monochromatic CCD cameras + 1 reference color CCD camera).	Uncomfortable in practice. Impossible to use for long-term studies involving massive number of patients.
	Database	Based on the use of text-files.	Difficulty in data management and browsing. Impossible to use for a massive amount of data.

Additional details on the described drawbacks of the dual-wavelength MPC are given in the Appendix (Chapter 6.2).

3.1.3 The points of development

The new MPC must acquire, within a maximum of one second, high-quality polarimetric images simultaneously at three different wavelengths in the blue, green and red part of the visible spectral range, as well as a reference color image of the examined cervix. A necessary condition is that the polarimetric images are superimposable pixel by pixel with each other and with the color image. In addition, this new prototype has to be able to function as both a conventional and a polarimetric colposcope without any mechanical movement and must have a rapid and automated calibration system.

Moreover, it has to be equipped with robust software and an intuitive user interface that can be easily operated by a practitioner to perform the necessary calculations to quickly verify the quality of polarimetric images within a few seconds after their acquisition and to calibrate the machine right after each medical procedure on a patient. Finally, the new MPC must be characterized by a certain ergonomics that allows it to be used like a conventional colposcope, with minimal modification of established medical practice.

The significant improvement of the old MPC was necessary to obtain a system that can be used in a clinical study. The imaging system and the lighting system have been improved for a better quality of the acquired images. The physical ergonomics has been completely modified to obtain a more practical and compact configuration. A relational database has also been implemented to facilitate the management of a large amount of data. In the following section, the improvements to the MPC hardware are described.

3.2 Hardware

During this thesis work, we developed a novel MPC to probe the cervical microstructure *in vivo* at different depths. The MPC was designed and built by modifying a conventional colposcope to make minimal change to established medical practice. For this end, a Mueller polarimetric imaging system was “grafted” onto the head of a conventional colposcope. Specifically, we used the Olympus OCS-500 colposcope described in Chapter 2.

The Mueller polarimetric imaging system is composed of three main parts: *i)* a miniaturized polarimetric box, *ii)* an imaging system, and *iii)* an illumination system. Each of these components will be described in detail below.

3.2.1 Polarimetric system design

The polarimetric box, consisting of a miniaturized Polarization State Generator (PSG) and Polarization State Analyzer (PSA), as described in Chapter 1, has been designed to be attached to the front of the colposcope head (patient side), as shown in Figure 3.1a. With this configuration, the modulation and analysis of light polarization takes place entirely outside the colposcope head. In this way, polarimetric distortions by the optics that make up the colposcope head don’t need to be characterized and taken into account in the

determination of the Mueller matrix of tissue being analyzed. More precisely, the PSG is placed on the illumination optical axis.

On the other hand, the PSA is placed on the detection optical axis which corresponds to the axis of one of the two colposcope eyepieces, precisely the right one (with respect to the operator) at the end of whose optical path the 3-CMOS camera is placed, as shown in Chapter 2. They are based on the use of bistable V-shaped ferroelectric liquid crystals (FLCs) in smectic C phase [90]. The FLCs operate as waveplates with fixed phase retardance and a variable azimuth of the fast (or slow) axis.

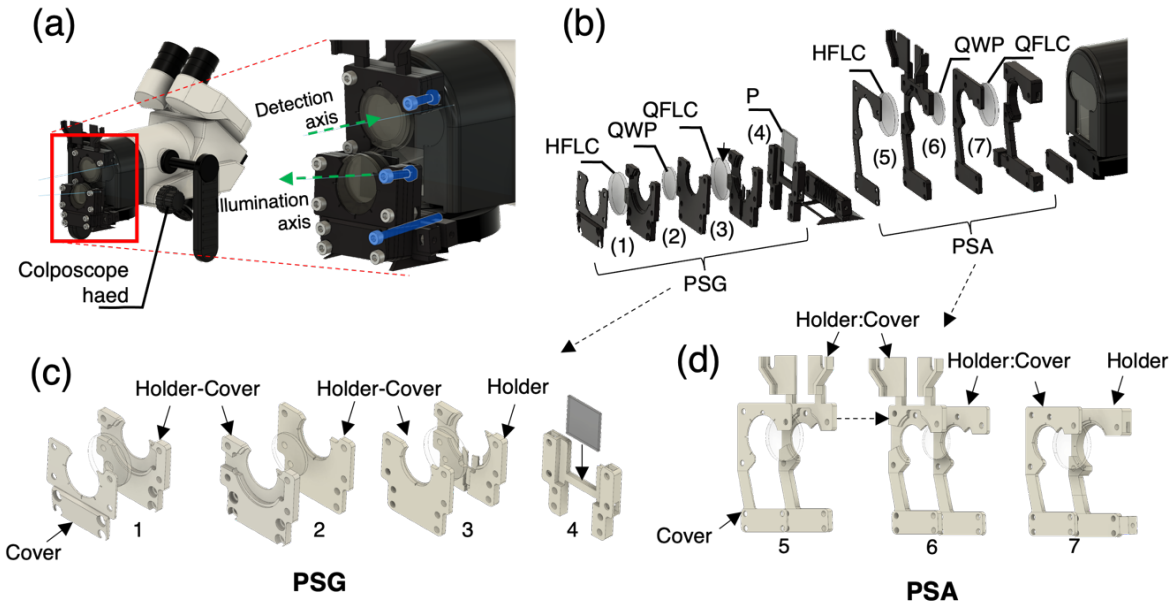

Figure 3.1 The mechanical design of the polarimetric system of the new MPC. (a) The appearance of the polarimetric system attached on the colposcope head. The system is assembled by screws as highlighted as blue. (b) The representation of each element of the polarimetric system. The assembly of each optical element with numbering 1-7 is shown below. (c) The assembly of the PSG. Each optical element is sandwiched by 2 components called the cover and holder. (d) The assembly of the PSA. It has the same assembly to the PSG.

In particular, the PSG is composed, in order, with respect to the direction of light propagation, of a linear polarizer (P), a first FLC operating as a quarter waveplate at 510 nm (QFLC), a waveplate operating as a quarter waveplate at 633 nm (QWP), and a second FLC operating as a half waveplate at 510 nm (HFLC). The PSA is the specular image of the PSG. Indeed, it is composed of the same optical elements as the PSG but placed in the reverse order. The structure of the PSG and PSA is shown in detail in Figure 3.1b.

The PSG and PSA components are assembled in a compact way. However, it can be observed that only three of the four PSA components are located in front of the colposcope head. This is because the PSA polarizer has been put in front of the 3-CMOS camera, as explained in more detail later. The PSG and PSA optical components, placed in front of the colposcope head, are held by 3D printed plastic mechanical mounts, as shown in Figure 3.1c and d.

A first set of screws of medium length is used to fix the PSA components together. In addition, a second set of similar screws is used to secure the PSG components together.

Finally, a third set of longer screws is used to attach the PSG and the PSA simultaneously to the colposcope head. Each optical component of the PSA is placed in the upper part of the mount and covers the imaging field. The lower part of each mount, placed on the illumination axis, remains empty to allow light to pass through.

More specifically, the mount of each PSG optical component is characterized by a C-shape. It partially surrounds the optical components by having an upward opening. This mechanical design has resulted in a space-saving PSG that does not interfere with the field of view of the two colposcope eyepieces. In addition, this particular shape of the PSG optical component holders allows, also because of the modular structure of the PSG, to independently modify the orientation of the individual optical components by slightly loosening the screw system described above.

In this way, the optimum relative orientation of PSG optical components can be easily determined, which is necessary to optimize the condition number of the PSG that will improve the accuracy of the polarimetric measurement. In addition, the holder of each FLC for the PSG has a groove inside, close to the bottom of the optical component, in which the electrical cables are placed so as not to interfere with the light flow.

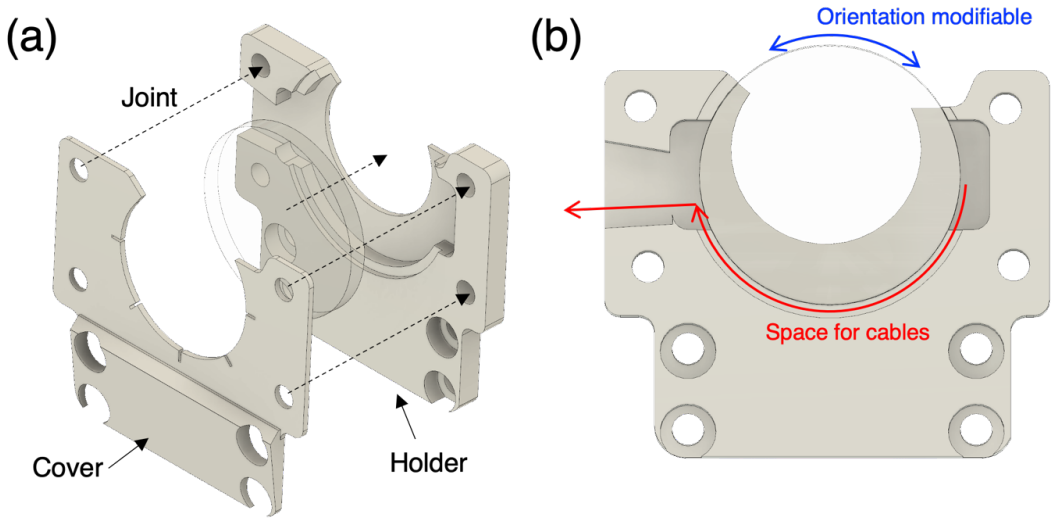

Figure 3.2 (a) The concept of the sandwich assembly for the FLCs and QWP of the PSG. The PSG's optomechanics is characterized by the upper C-shape mount. Each filter is sandwiched by the 2 3D-printed components, called the cover and holder. (b) The front view of the holder. The cables from the FLC can be laid out in a stepped space around the edge of the filter so that it does not interfere with assembly. The opening at the top allows easy orientation of each filter.

The upper part of the mounts of each PSA optical component is also characterized by a C-shape. It partially encloses the optical component with an opening to the left (with respect to the operator). Indeed, the optical components of the PSA, in particular the QWP, have a slightly larger diameter than the aperture of the right eyepiece in front of which they are positioned. Therefore, the edge of these components strongly interferes with the field of view of the left eyepiece.

As these optical components are placed far from the image plane (which is at a distance of about 30 centimeters from the colposcope head), being almost transparent thanks to the

absence of a plastic housing, they are not perceived by the operator during the use of the binocular system for the same principle for which we do not notice the scratches on our glasses if we look at an object placed far from us.

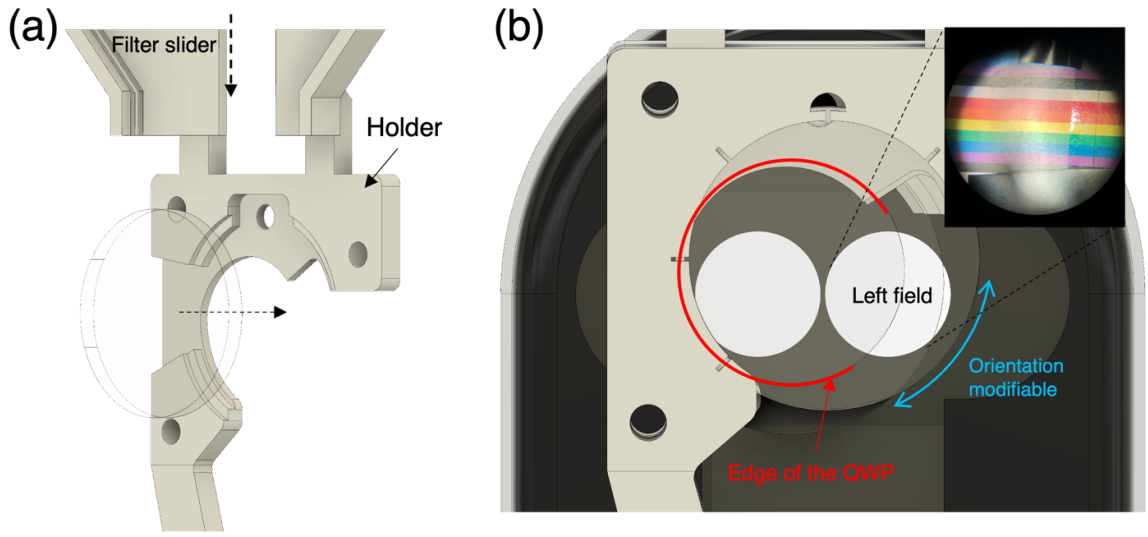

Figure 3.3 (a) The concept of the sandwich assembly for the FLCs and QWP of the PSA. The cover is not shown. The filter slider is mounted on the PSA, which will be explained later in this chapter. (b) The optimecanics of the PSA is characterized the C-shape that minimizes the interference to the binocular. Inset: the view seen in the left eyepiece with the C-shape mount. The orientation of each filter can be changed from the opening (the blue arrow).

On the other hand, the presence of the PSA polarizer would have created a difference in brightness between the right and left eyepiece. For this reason, we decided to place the PSA polarizer in front of the camera. In this case, the transmittance of the other components of the PSA being very high, we obtain approximately the same brightness image for both eyepieces.

Therefore, even if the total diameter of the PSA does not perfectly fit the binocular system, the described configuration allows the user not to move the polarimetric head to use the MPC as a conventional colposcope and to have a stereoscopic vision with the simultaneous use of both eyepieces.

Finally, without moving the polarimetric box, the MPC can be used in both Mueller polarimetric imaging mode and conventional colposcopy mode, which has been a significant improvement with respect to the previous dual-wavelength prototype.

3.2.2 Optimization of the polarimetric system

Automatization of calibration

The MPC is calibrated using the eigenvalue calibration method (ECM), explained in detail in Chapter 1. As a reminder, the ECM consists of acquiring the 16-component intensity matrix $\boldsymbol{B}$ consecutively for three reference optical elements, namely a first polarizer whose transmission axis is oriented at 0° with respect to the laboratory reference (P0), a second polarizer whose transmission axis is oriented at 90° with respect to the first polarizer (P90), and a waveplate whose fast axis is oriented at 30° with respect to the first polarizer (L30).

In the case of the dual-wavelength MPC, the user had to manually place the 3 optical elements in front of the PSA, as explained in Chapter 2. We found that this procedure is very sensitive to the user's ability and makes the procedure very slow. Indeed, almost 15 minutes are needed to calibrate the MPC with this system. In addition, it can produce movements of the polarimetric box that affect the repeatability of calibrations.

To solve this problem, we automated the filter change by placing a motorized filter slider (Tholrabs ELL9) on the polarimetric box, as shown in Figure 3.4a. With this system, the 3 filters are automatically placed in front of the PSA during the different steps of the calibration. This makes the calibration procedure easier, more stable and faster. Indeed, only 2 minutes are needed to calibrate the MPC with this motorized system.

In the clinical environment, the optical components of the MPC can be easily exposed to contaminants such as blood, secretions, or disinfectants that can cause misfunction of the polarimeter. To avoid possible contamination, the polarimeter housing described above was completely covered with a black (anodized) aluminum housing, as shown in Figure 3.4b.

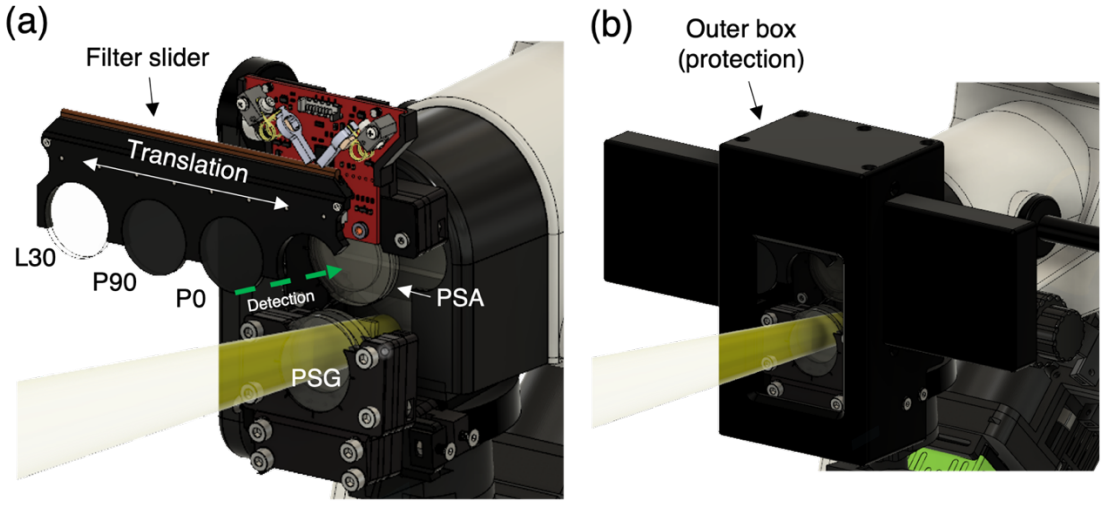

Figure 3.4 (a) The filter slider mounted on the PSA can automatically place the three reference filters consecutively during the calibration process. (b) The anodized aluminum box that protects the sensitive polarimetric system from any possible contamination.

Minimization of internal reflections

The attachment of an additional optical system, such as a polarimetric box, to the colposcope head introduces stray reflections that can reach the detector, thus creating artefacts in the polarimetric images of the target under analysis.

These stray reflections are mainly generated by the light incidence on the transparent surface of the PSG optical components. They are strongly dependent on the inclination of these components with respect to the light propagation direction, as well as on the divergence of the light beam. These stray reflections can be minimized if the direction of light propagation is perpendicular to the optical component surface of the PSG. Therefore, the PSG has been designed to meet this condition as shown in Figure 3.5.

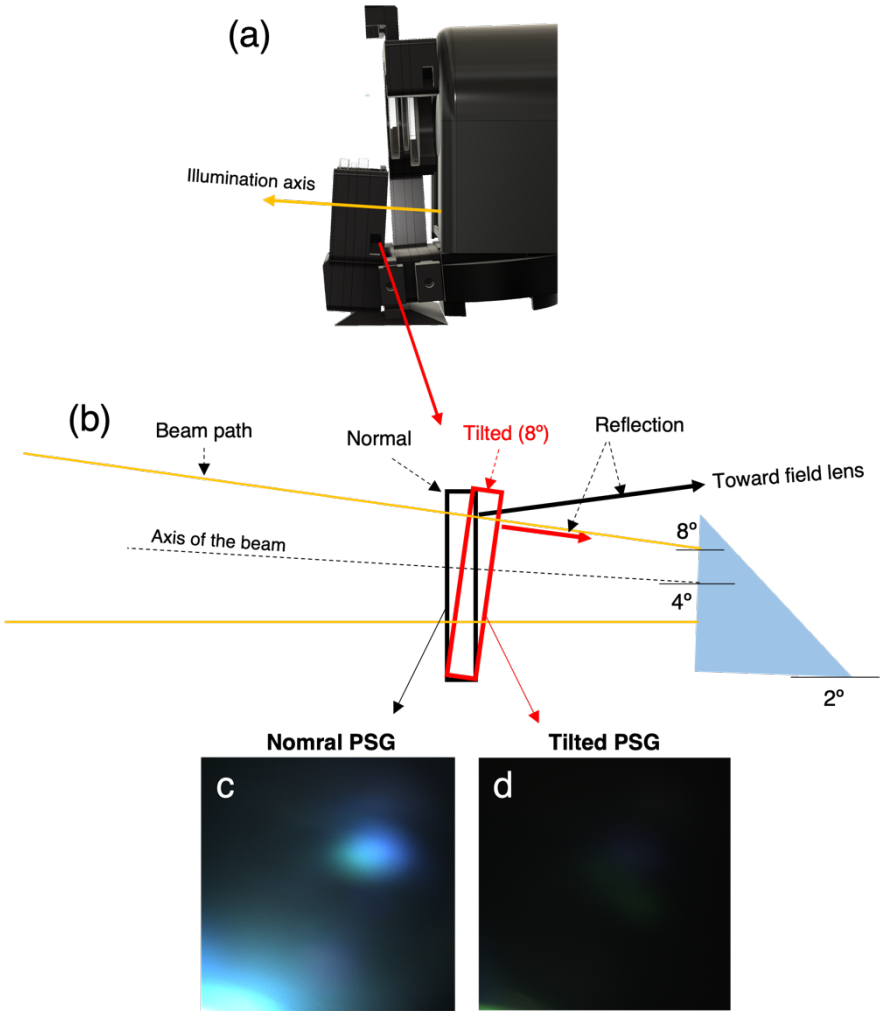

Figure 3.5 (a) the tilted configuration of the PSA. In this configuration, the illuminated light is normally incident to the PSG, which is oblique with respect to the laboratory frame. (b) The schematic illustration of the PSG and illumination. (c) the stray light image taken with the normal (vertical) configuration. Strong stray light beams are observed. (d) the stray light image with the tilted configuration. The stray light seen in the normal configuration significantly disappear.

Temperature regulation

Mueller polarimeters based on ferroelectric liquid crystals (FLCs) are very sensitive to temperature fluctuations. Indeed, temperature fluctuations can change the degree of disorder of liquid crystal molecules, which is generally related to the phase retardance. Thus, it is clear that temperature fluctuations can change the W matrix related to the polarization states produced by the PSG. The same can happen to the A matrix related to the polarization configurations of the PSA. For this reason, a Mueller polarimeter based on FLCs needs some warm-up time to reach a steady state, which is necessary before its use.

The main heating source in our case is the absorption of light by the polarizer of the PSG, which in turn generates the heating of the polarimetric box and consequently of the liquid crystals. Ultimately, the heating of the FLCs is primarily by thermal contact. Therefore, we placed a temperature sensor in the MTP to monitor the stability of the system. Typically, a warm-up time of 60 minutes is required to bring the MPC to a thermal steady state. However, in the context of a clinical study, this factor can create an uncomfortable wait time for patients.

For this reason, we designed an air-cooling system, as shown in Figure 1.6, consisting of a housing containing a fan that is directly connected to the polarimetric head. In particular, the whole system (polarimetric housing + cooling system) has been designed so that the cooling air directly reaches the polarizer, as shown in Figure 3.6.

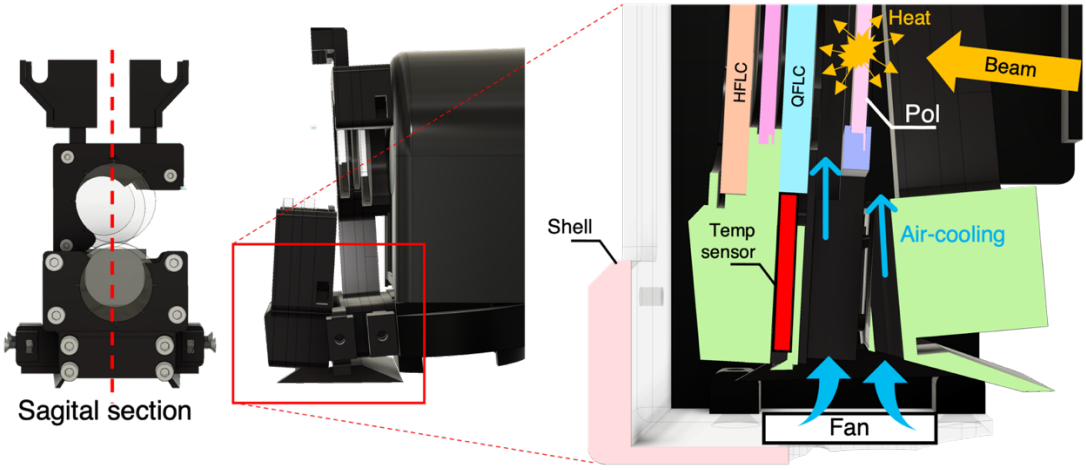

Figure 3.6 The sagittal section of the PSG. A cooling fan at the bottom of the PSG blows wind into the PSG. This accelerates the heat dissipation from the polarizer. The light absorption by the polarizer (PSG) is the main heat source in the polarimetric system. A temperature sensor attached on the QFLC monitors the temperature fluctuations of the system.

A temperature sensor (Minco S665) was pasted on the QWP of the PSG to monitor temperature fluctuations. Figure 3.7 shows the temperature stabilization curve with and without the cooling system. The light was turned on at t=0 and the temperature was measured every 10 seconds. The initial temperature of the PSG was 25.5°. Figure 3.7a shows that the temperature of the PSG reaches a maximum equilibrium value of 40° without the cooling system after 60 minutes. With the cooling system, the temperature reaches a maximum equilibrium value of 27° after 20 minutes. Figure 3.7b shows the curve related to the temperature differences occurring every 10 seconds. These differences become negligible when the system reaches thermal equilibrium. The cooling system not only shortened the warm-up time, but also significantly reduced the value of the maximum equilibrium temperature reached.

Moreover, since the total temperature increase in the presence of the cooling system is only 1.5°C, prior pre-heating of the system is probably not necessary in this condition. Nevertheless, to be sure of the experiments' reproducibility, we decided to heat the MPC for 30 minutes immediately after turning it on at the beginning of each measurement day. Finally, we also verified that the mechanical vibrations produced by the fan do not generate fluctuations in the measurements, which is the case.

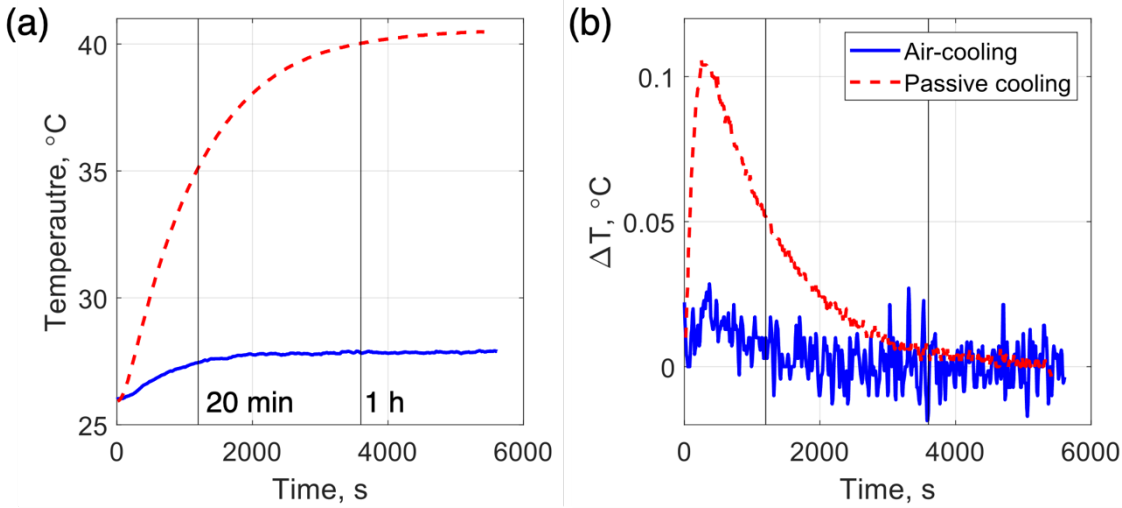

Figure 3.7 Temperature changes with/without the air-cooling system. With the air-cooling system, the system reached the thermal steady state 3 times faster (60 -> 20 minutes).

Condition number optimization

The PSG and the PSA of the MPC polarimetric box was constructed using bistable V-shaped C-phase smectic FLCs [55] described in detail in Chapter 1. More precisely, we used a Quarter Waveplate at 510 nm as FLC1 (indicated as QFLC), a Quarter Waveplate at 510 nm as WP (indicated as QWP), and a Half Waveplate at 510 nm as FLC2 (indicated as HFLC). The relative orientation between the optical elements composing the PSG and the PSA have been found to maximize $\kappa^{-1}(\mathbf{W})$ and $\kappa^{-1}(\mathbf{A})$ between 450 nm and 700 nm. The achieved values are resumed in table 3.2.

A very good agreement has been obtained for $\kappa^{-1}(\mathbf{W})$ and $\kappa^{-1}(\mathbf{A})$ between experimental and theoretical results, as shown in Figure 3.8. The values obtained for $\kappa^{-1}(\mathbf{W})$ and $\kappa^{-1}(\mathbf{A})$ are generally greater than 0.3 for all wavelengths considered with a peak of 0.57 for **W** and 0.5 for **A** around 550m. If the signal to noise ratio is maximized the values obtained for $\kappa^{-1}(\mathbf{W})$ and $\kappa^{-1}(\mathbf{A})$ at all wavelengths are large sufficiently to obtain accurate measurements[14]. Therefore, we have done a huge experimental work to maximize the signal-to-noise ratio under measurement conditions on biological tissues in vivo, as we will explain later in the text.

Table 3.2 The optimal orientations of the polarimetric components of the PSG and PSA. The switch angles of the FLCs measured by two crossed polarizers. The values were cross checked by the spectroscopic Mueller polarimeter MM16.

Component		Switch angle	Optimal $\hat{\theta}$
PSG	QFLC	38°	161°
	HFLC	43°	69°
	QWP	-	0°
PSA	QFLC	41°	160°
	HFLC	44.5°	68°
	QWP	-	0°

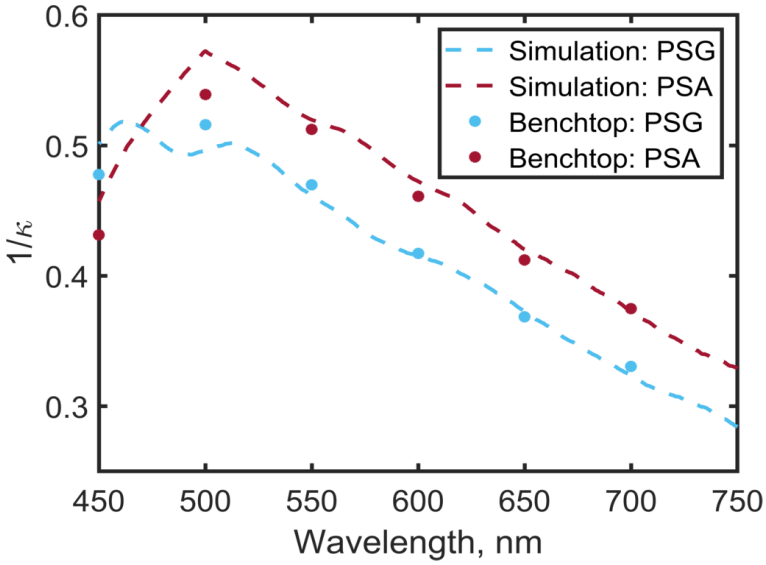

Figure 3.8 The optimized condition numbers in the estimation (dotted lines) and on the benchtop (circles). The condition numbers of the PSG and PSA were optimized based on the retardance values measured by MM16.

3.2.3 Imaging system

While the miniaturized Mueller polarimetric box primarily impacts on the polarimetric functionality, the imaging system is the most important component of the colposcope that actually determines the overall quality of the images such as resolution, color, sharpness, as well as the time required to acquire them, and the size of the field of views. The optical resolving power is, in fact, determined by the quality of optics and the numerical aperture of the colposcope. However, the choice of an appropriate sensor size and configuration is not straightforward as camera performance is often the result of trade-offs among resolution, acquisition speed and sensitivity (brightness). Furthermore, because the early discovery of the correlation between gestational ages and depolarizing ability of the cervix during pregnancy implies the importance of exploration into deeper tissues, the capability of the imaging system to acquire cervical images in longer wavelengths has emerged as a new requirement.

3-sensors camera

First, we replaced the bi-chromatic imaging system described in Chapter 2, consisting of two monochromatic CCD-cameras coupled to appropriate dichroic filters, with a color imaging system. The most common RGB color CCD or CMOS cameras are equipped with a Bayer filter that does not provide an efficient separation between red, green, and blue wavelengths ranges because of a strong color-crosstalk effect [110], as shown in Figure 3.9, resulting in undesirable correlations between the 3 colors.

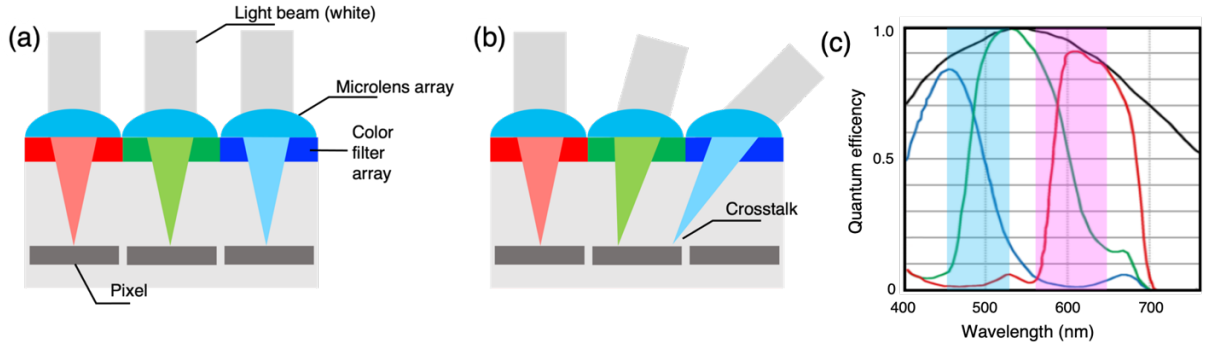

Figure 3.9 (a) The scheme of the Bayer filter array. The microlens array on the top of the detector functions to enhance the light collection. (b) The Bayer filer is vulnerable to the color crosstalk. The crosstalk can cause unwanted artifacts in multispectral polarimetric imaging. (c) Typical spectral response of a Bayer filter camera (JAI GOX-3201) which has the same CMOS sensor to the 3-CMOS camera AP-3200. The overlap (colored areas) between blue-green and green-red represents the strong color crosstalk.

On the other hand, RGB cameras based on the use of three different monochromatic CCD or CMOS sensors, one for each wavelength of interest, allow for a sharper separation of the different colors through the combination of three dichroic prisms, as shown in Figure 3.10. Blue and red light are effectively separated by total internal reflection at the various interfaces between two adjacent prisms encountered by the incident light. Green light, on the other hand, is fully transmitted. In particular, for the new MPC prototype, we used a 3-CMOS camera (JAI AP3200-PMCL-NF) whose performance meets our requirements, while remaining small enough to be mounted on the colposcope OCS-500. The specifications of this 3-CMOS camera are charted in Table 3.3.

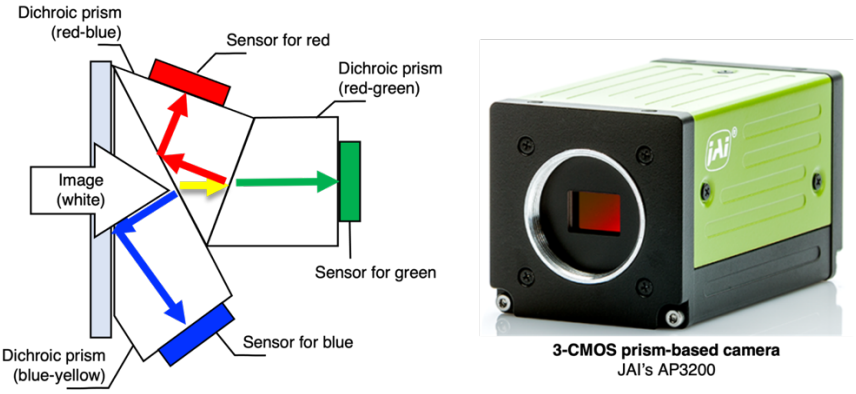

Figure 3.10 The concept of the 3-sensor camera with 3 dichroic prisms. 3 sensors capture images in 3 different colors (left). The appearance of the 3-CMOS camera, JAI AP-3200 (right).

Table 3.3 The specification of the 3-CMOS camera JAI AP-3200

	Specification
Sensor	1/1.8" 3-CMOS (SONY IMX265LLR)
Active pixels	2064 × 1544 × 3
Active area	7.12 mm × 5.33 mm
Pixel pitch	3.45 μm
Full-well capacitance	10.7k e-
Read out noise	2.3 e-
Dynamic range	73 dB
Signal output	12 bit (36-bit RGB)
Clock	84.85 MHz
FPS	26.0 FPS @2064 × 1544
Interface	Camera Link (Medium)

The spectral response of each sensor in the 3-CMOS camera used is illustrated in Figure 3.11. In particular, the solid lines drawn in red, green, and blue indicate the transmittance of the prism system for the respective colors. The solid black line denotes the external quantum efficiency (EQE) which is approximately the same for each sensor. The camera comes from a special order where the IR-cut filter has been removed to increase the amount of light collected above 650 nm.

In order to remove the remaining small overlaps between the red and green as well as the green and blue, a tri-band filter (Chroma 69002m) was inserted in front of the 3-CMOS camera, whose transmission curve is represented by the dotted black line in Figure 3.11a. The 3-band filter allows the selection of wavelengths at 460 nm (30 nm FWHM), 530 nm (35 nm FWHM), and 630 nm (60 nm FWHM). Furthermore, two additional filters were added as shown in Figure 3.11b, the first one to select light at 650 nm (40 nm FWHM) to validate the results obtained in the previous feasibility study described in Chapter 2 and the second one at 700 nm (50 nm FWHM) to explore longer depth of cervical tissue. Figure 3.11c shows the effective spectral response of our detection system for the 5 selected wavelength bands, calculated using the following expression:

$$\text{Response} = T_{filter} \times T_{prism} \times EQE_{sensor} \times 100\ (\%) \tag{3-1}$$

where T_{filter} is the transmission coefficient of filters, T_{prism} is the transmission coefficient of the camera prism, and EQE_{sensor} is the external quantum efficiency of the sensor. The curve in Figure 3.11c represents the conversion factor between the emitted photoelectrons and the incident photons.

The conversion factor is about 50~60% for blue/green (460 nm and 530nm) light and 30~35% for red light (530nm, 650nm, and 700nm). The photoelectrons produced are converted into a 12-bit digital signal by the capacitor diode and the analog-to-digital converter (ADC).

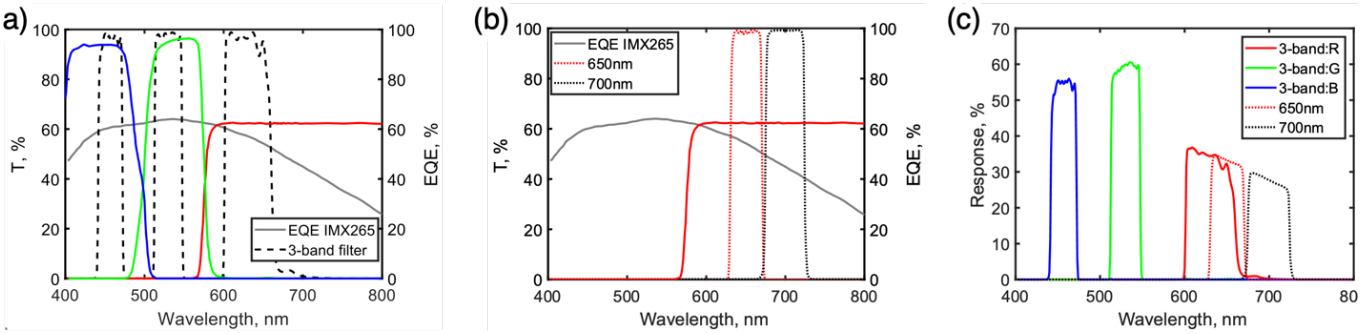

Figure 3.11 (a) The spectral transmittance of the three bands of the dichroic prisms of the AP-3200. The color of the lines respectively correspond to the red, green, and blue sensors. The solid black line represents the EQE of the image sensor in photoelectrons/photon, %. The dotted black line represents the spectral transmittance of the 3-band filter. (b) The spectral transmittance of the 2 additional color filters. The dotted red line and black line correspond to the 650 nm and 700 nm filter, respectively. (c) The serial conjugation of the components. It represents the efficiency of the spectral system in photoelectrons/incident photon, %.

Conversion factor of the 3-CMOS camera

The conversion between the number of photoelectrons and the number of analog-to-digital units (ADUs) is defined by a factor *G* which can be calculated as:

$$G = ADUs/photoelectrons \tag{3-2}$$

The estimation of G provides important information for determining the expected signal level under given experimental conditions, such as lighting level. The digital signal *S* results from the multiplication of *G* with the number of photoelectrons n_{pe}. It can be calculated as:

$$S = G \times n_{pe} = G \times EQE \times n_p \tag{3-3}$$

where EQE is the external quantum efficiency and n_p is the number of photons. The sensitivity K of the sensor is defined by the number of photons required to increase the digital signal S of 1 ADU and can be calculated as:

$$K = \frac{n_p}{S} = \frac{1}{G \times EQE} \tag{3-4}$$

To estimate this parameter, we assume that the number of photons n acquired over the integration time of the detector follows the Poisson statistical distribution given by:

$$f(n, n_p) = P(X = n) = \frac{{n_p}^n e^{-n_p}}{n!} \tag{3-5}$$

where n_p denotes the average number of photons acquired. In conventional imaging applications, where n is large, this distribution approximates the normal (Gaussian) distribution.

For the Poisson statistical distribution, the mean and the variance of n are given by:

$$\mathbb{E}(n) = n_p \tag{3-6}$$

$$\mathbb{V}\mathrm{ar}(n) = n_p \tag{3-7}$$

where $\mathbb{E}(X)$ and $\mathbb{V}\mathrm{ar}(X)$ denote the expectation (mean) value and the variance of n, respectively. Since the signal S and the photoelectrons n_{pe} are linearly proportional to the photons n by (3-3), the expectation and variance of S can be written as:

$$\mathbb{E}(S) = G \times EQE \times n_p = G \times n_{pe} \tag{3-8}$$

$$\mathbb{V}\mathrm{ar}(S) = G^2 \times EQE \times n_p = G^2 \times n_{pe} \tag{3-9}$$

Then, the conversion factor G is given by:

$$\frac{\mathbb{V}\mathrm{ar}(S)}{\mathbb{E}(S)} = G \tag{3-10}$$

where G is the slope of the linear curve correlating the mean value and the variance of S. In order to estimate G experimentally, we mounted the setup shown in Figure 3.12.

A white LED light source was placed at a distance of almost 20 centimeters from the 3-CMOS camera. A diaphragm was placed in front of the source, followed by a diffuser. An aspherical lens placed after the diffuser was used to collect the light on the detector.

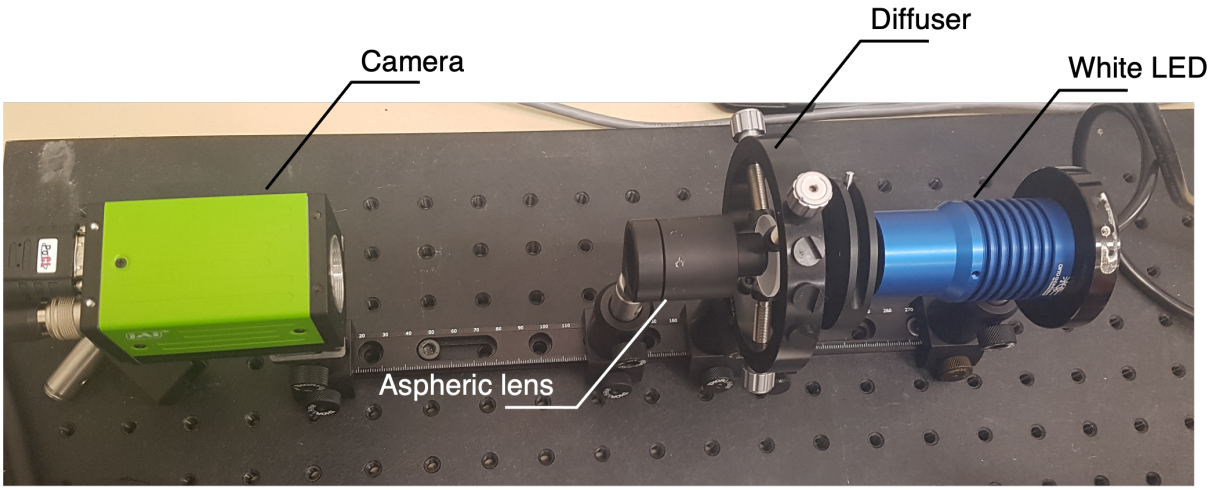

Figure 3.12 The experimental configuration for the measurement of the conversion factor. A wide gaussian beam created by the diffuser and lens is illuminated on the camera. The images were acquired without the objective lens.

With this experimental configuration, we obtained a fairly uniform illumination on the detector. In order to experimentally estimate G, we acquired a set of 48 consecutive images with a fixed value for the integration time of the 3-CMOS camera. This measurement was repeated for six different exposure times. We considered the total size of the sensor (2064 x 1544 pixels). For each integration time and for each pixel, we calculated the mean value μ_i and the variance σ_i^2 of the signal over the 48 repeated acquisitions ($i = 1 \ldots . n$ where n is the total number of pixels). For each pixel, we plotted the linear curve between the mean value and the variance of the signal for the different exposure times chosen. In this way, the G factor was calculated for each pixel.

Figure 3.13a shows the linear curve that correlates the average value of μ_i over all pixels with the average value of σ_i^2 over all pixels for different integration times, for each sensor. Figure 3.13b shows the distribution of G for all pixels of the three sensors of the 3-CMOS camera.

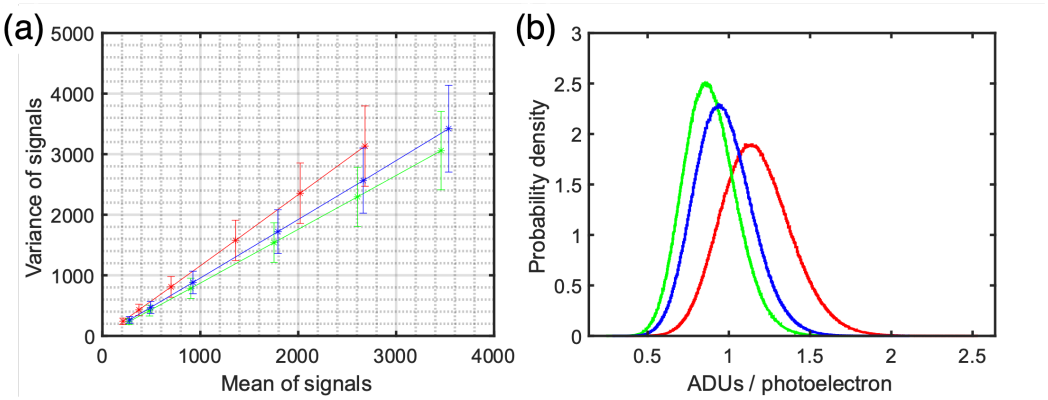

Figure 3.13 (a) The linear model (3-10) for 2064×1544 pixels. The error bars represent the standard deviation. (b) The histogram of the conversion factor for 2064×1544 pixels.

The spectral responses of the three sensors are shown in Table 3.4. The values of G for the three sensors are the mean values of the three distributions shown in Figure 3.13b. The sensitivity K of each sensor is calculated using the expression (3-4). The values of K

calculated for the three sensors of the 3-CMOS camera have been compared with that obtained for the monochromatic CCD-camera (GT1920 @550 nm) used for the old dual-wavelength prototype of MPC.

The 3-CMOS camera is clearly less sensitive than the old monochromatic camera. That's why we have worked a lot on improving the lighting system, as will be explained in more detail later in the text.

Table 3.4 The mean conversion factor and sensitivity of the 3-CMOS camera in 3 colors. The *G* and *K* of GT1920 are scaled to 14-bit digital output.

	EQE	G	K
R	0.35	1.13	2.53
G	0.61	0.85	1.93
B	0.55	0.93	1.95
GT1920 @550 nm	0.75	1.47	0.91

Although the new camera is less sensitive than the old one, it has the advantage of being able to acquire RGB images and to perform Mueller polarimetric imaging simultaneously at three different wavelengths. In this way, the new MPC prototype developed during this thesis can provide both a color image of the cervix (reference image for the practitioner) and a multispectral polarimetric analysis.

Signal-to-noise ratio of the 3-CMOS camera

To complete the characterization of the 3-CMOS camera, we estimated the SNR for different exposure times of the camera (0.01 ms ~ 9 ms in 0.5 ms step). To do so, we acquired 48 intensity images for each exposure time with the same experimental setup already used to measure the conversion factor. We selected a ROI (100 x 100 pixels) in the center of the images where the illumination is more uniform. For each pixel of the selected ROI, we calculated the SNR_i as:

$$SNR_i = 10\log_{10}\frac{\mu_i}{\sigma_i} \approx 10\log_{10}\sqrt{n_p} \tag{3-11}$$

where μ_i and σ_i are the mean value and standard deviation of the signal over 48 repeated acquisitions. Figure 3.14a shows the mean value and the standard deviation of SNR_i over all pixels in the selected ROI as a function of light intensity for all wavelengths of interest.

We observed that the SNR increases with light intensity. The same trend is approximately observed for all three sensors, although the blue curve does not reach a higher intensity due to the lower irradiance of the LED source for that wavelength. The SNR decreases significantly when the light intensity is below 500 AUD.

Then we measured the SNR as a function of camera gain. To perform the experiments, the exposure time was adjusted to obtain 500 AUD for each sensor. Different gain values

(1~6.4 in 0.5 steps) were tested. The SNR remains constant with increasing gain value, as shown in Figure 3.14b.

This means that the camera gain does not affect the SNR at a fixed intensity, although it linearly amplifies the measured signal, as shown in Figure 3.14c. Therefore, increasing the gain results in brighter images, but does not improve the actual accuracy of the photodetection.

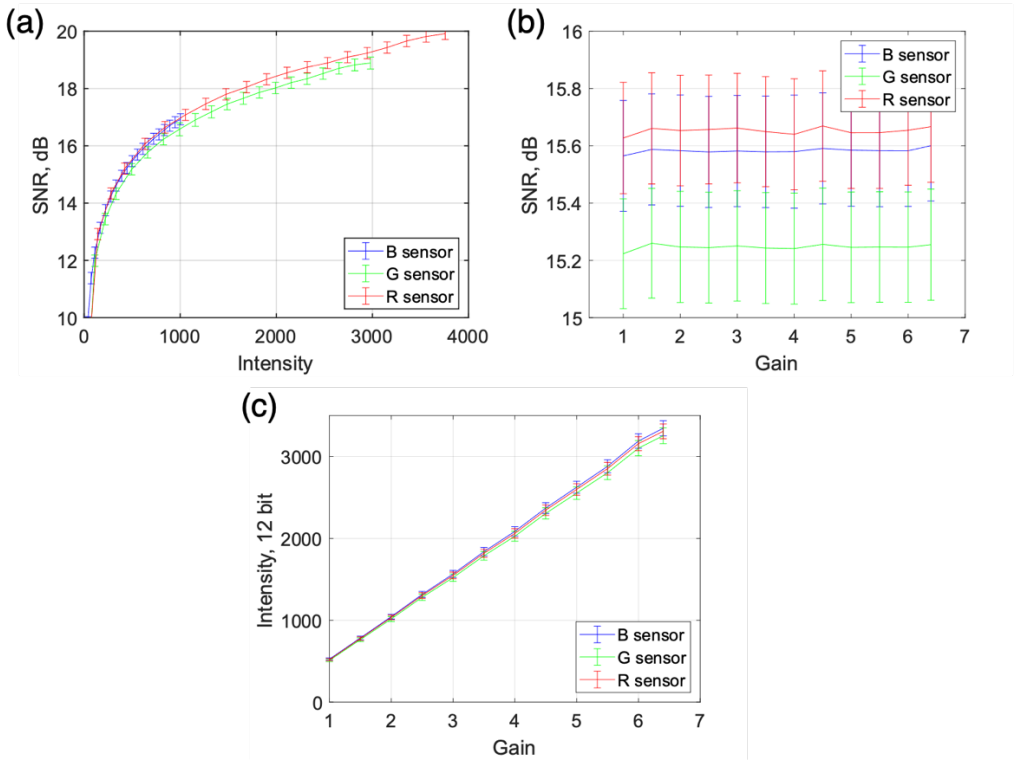

Figure 3.14 (a) The SNR of the AP-3200 as a function of light intensity. (b) The SNR as a function of the gain setting. (c) Intensity levels as a function of gain.

Optimization of imaging optics and settings

For in vivo applications, it is necessary to acquire images in less than 1.5 s to limit blurring effects generated by involuntary patient movements due to breathing or heartbeat. In our specific case, the Mueller matrix measurement requires the acquisition of at least 16 intensity images, as explained in Chapter 1.

However, 16 intensity images should be acquired and averaged multiple times to significantly improve the signal-to-noise ratio. Our previous experiments revealed that, by acquiring and averaging at least 4 times 16 intensity images, it is possible to obtain good quality Mueller polarimetric images, provided that the detected signal is high enough and the condition number of the $\boldsymbol{W}$ and $\boldsymbol{A}$ matrices is maximized.

At full resolution (2064 × 1544 pixels), the 3-CMOS camera operates at 26 FPS. Therefore, using full resolution is not very well suited for our purpose. The eyepiece of the colposcope produces an image of the target at infinity. Therefore, an objective lens is needed to reproduce the target image on the 3-CMOS camera sensor. As explained in Chapter 2, the 3-CMOS camera must be coupled to one of the two posterior eyepieces of the colposcope.

The focal length of the lens, coupled to the eyepiece of the colposcope, determines the size of the target on the sensor.

However, only 2 objective lenses were available for the chosen 3-CMOS camera: the first with a focal length of 8 mm and the second with a focal length of 25 mm. Finally, we selected the lens with a focal length of 25 mm because it can reproduce the image of 3.8 centimeters square target on a ROI of 1120×1120 pixels which enables the 3-CMOS camera to work with a frame rate of 64 FPS.

a) Resolving power of the 3-CMOS camera

To measure the spatial resolution of the camera using the objective lens with a focal length of 25 mm we used the slanted edge target (Thorlabs R2L2S2P). This method is explained in the Appendix (Chapter 6.5). The image of the target was taken at a distance of 24 centimeters, in order to have a field of view similar to that of the colposcope in use. The aperture of the lens was opened to the maximum (#*f*/1.8). A white screen (Thorlabs EDU-VS1/M) was placed 10 cm behind the target and a white light source obliquely illuminated the screen.

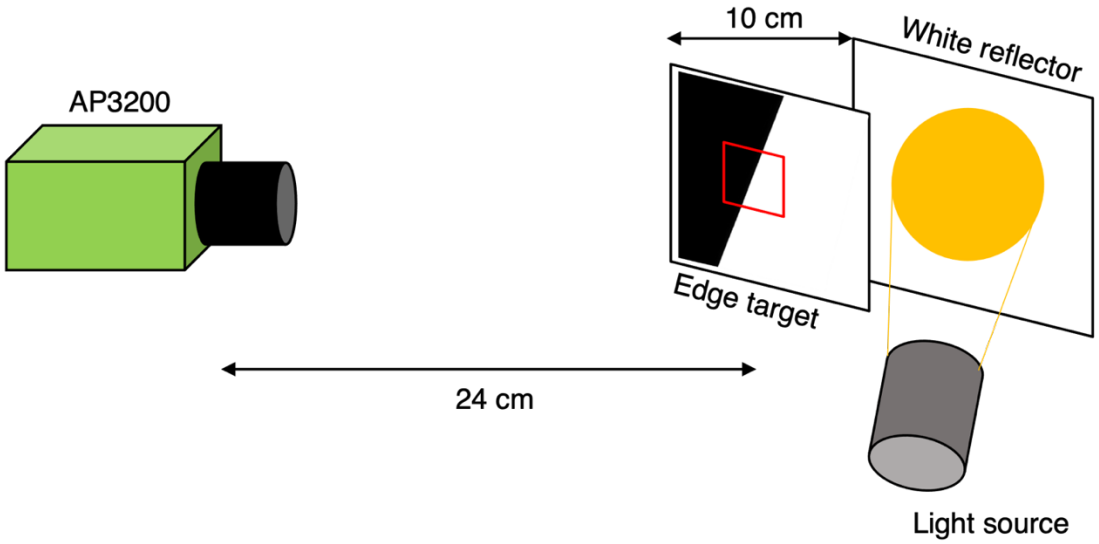

Figure 3.15 The configuration of the slanted edge method. A white diffuser is placed behind the edge target as a background.

The modulation transfer function (MTF) curve calculated by the red square ROI is shown Figure 3.16b. The spatial frequencies were converted to the image plane scale (pixel pitch). 2 dotted lines, MTF10 and MTF50 as spatial frequencies at 10% and 50% contrast, are chosen as 2 criteria for the comparison of our imaging systems. The vertical solid line indicates the Nyquist sampling limit by the discretized sensor array, 1/(2×3.45μm)=144.9 line pairs/mm.

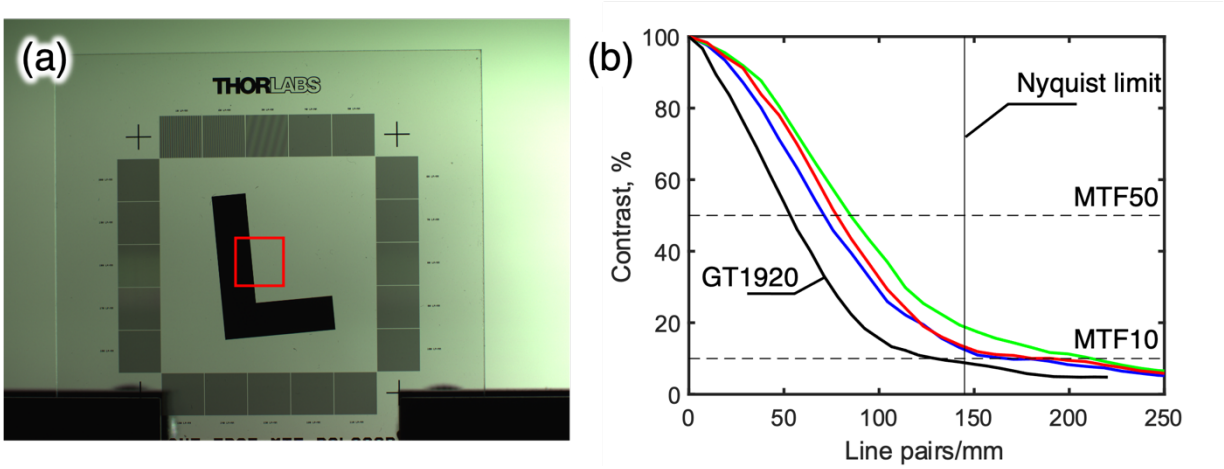

Figure 3.16 (a) the image of the slanted edge target acquired by AP3200 + *f*=25 mm objective lens (VS technology VS-2518H) at #*f*/1.8. The resolving power at the red box is estimated. (b) the corresponding MTF curve (#*f*/1.8). The pixel is scaled to the pixel pitch at the sensor side. The objective lens shows no chromatic aberration. It barely has 10% contrast at the Nyquist limit of the sensor.

The resolution is calculated with a contrast of 10% and 50%. The results obtained are resumed in Table 1.5. For comparison, the resolution of the previous camera, Prosilica GT1920, was measured with an objective of a 25mm focal length with white light. Although the 3-CMOS camera exhibits the best resolution at the green, no significant chromatic aberration is observed. Overall, the 3-CMOS camera showed higher resolution than the previous camera regardless of color. Finally, this imaging system is combined to the colposcope's optics. The final resolution of the MPC, the combination of the 3-CMOS camera and the colposcope, will be presented in the next chapter.

Table 3.5 The resolution of AP3200 + VS-2518H (*f*/1.8).

(μm)

	R	G	B	GT1920
MTF10	3.0	2.4	2.6	3.9
MTF50	7.1	5.9	6.4	9.4

b) *Design of the camera adapter and filter wheel*

The 3-CMOS camera is connected to one of the two eyepieces of the colposcope, as shown in Figure 3.17a. Each dichroic filter, when used, is placed in front of the tri-CMOS camera objective. The PSA polarizer is placed immediately after the dichroic filter. As explained earlier, we decided to work with three different dichroic filters. In particular, the tri-band filter allows the simultaneous acquisition of a color image as well as three polarimetric images at 460 nm, 530 nm and 630 nm. In addition, we added two other monochromatic dichroic filters to obtain polarimetric images at 650 nm and 700 nm.

We designed and fabricated an optomechanical system capable of securely attaching the imaging system to the eyepiece of the colposcope in order to eliminate blurring effects in the images due to machine vibrations and at the same time allow for the automatic change of the three dichroic filters through a motorized system.

In fact, the three dichroic filters, which have approximately the same size, are placed inside a 3D printed plastic gear wheel, as shown in Figure 3.17c. Precisely, they are arranged at the vertices of an equilateral triangle around the axis of symmetry of the gear wheel, which is connected to a second, smaller 3D printed plastic gear wheel connected to a stepper motor as shown in Figure 3.17d. The alignment of each filter on the optical axis of the 3-CMOS camera is controlled automatically by the stepper motor. The initial position of the filter wheel is set when the stopper placed on the filter wheel touches a pressure sensor. Then, the number of steps to align each filter on the 3-CMOS camera axis is determined.

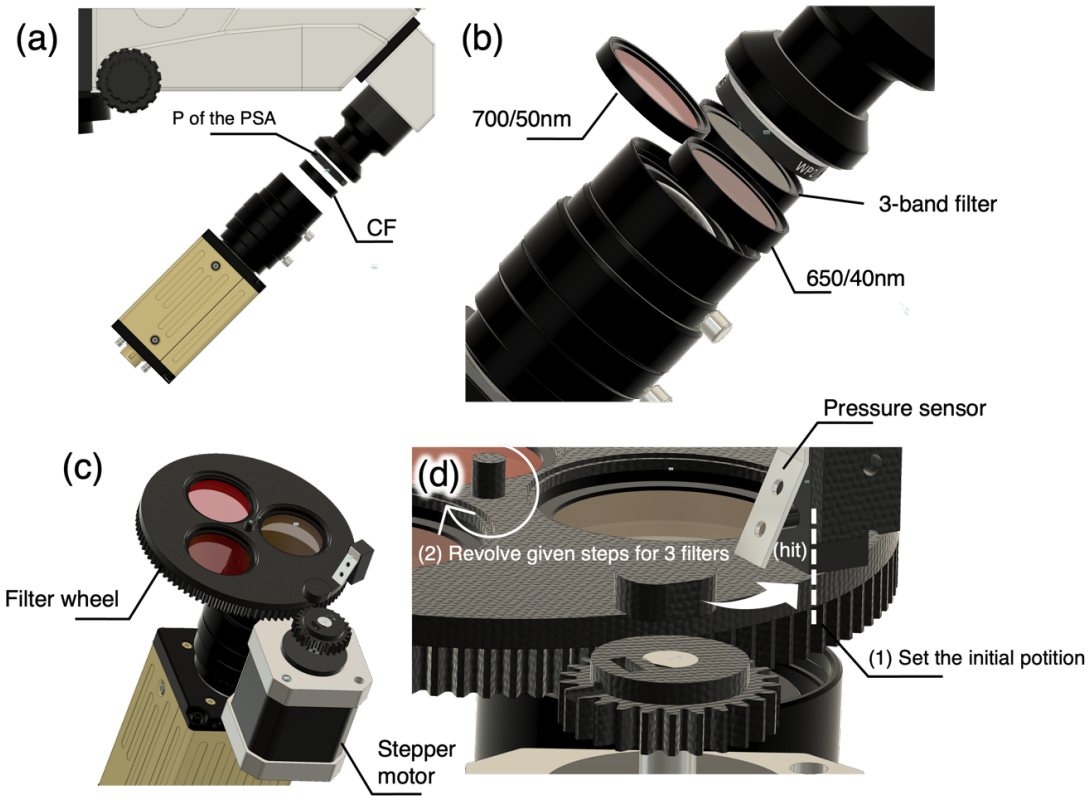

Figure 3.17 (a) The desired configuration for the imaging system. A polarizer (P) and color filter (CF) need to be placed between the camera and the colposcope. (b) The three color filters should be consecutively exchanged for multispectral imaging. (c) The concept for the motorized filter wheel system. (d) The detailed mechanism of the filter wheel system. If the wheel touches the pressure sensor by rotation, the initial position of the wheel with respect to the camera can be set. Then, the three filters can be precisely placed in front of the camera by a given step number for each filter.

The entire setup consisting of the 3-CMOS camera and motorized system is enclosed in a 3D printed plastic holder that is directly connected to the eyepiece of the colposcope, as shown in Figure 3.18. The position of the 3-CMOS camera can be manually optimized inside the camera holder with respect to the optical axis of the colposcope eyepiece.

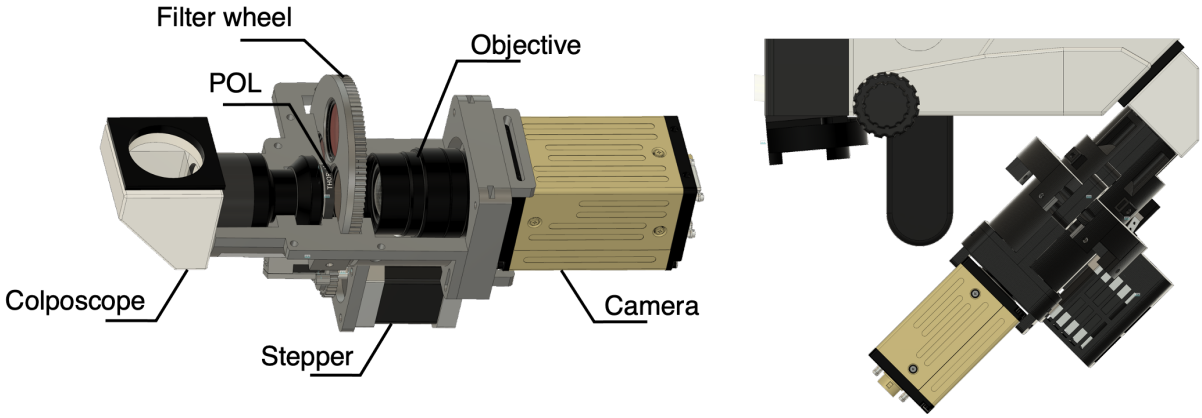

Figure 3.18 The components of the imaging system (left) and the appearance of the filter wheel + camera adapter (right).

3.2.4 Illumination system

Full-field Mueller polarimetric imaging for biological tissue analysis does not require coherent light that would produce unwanted effects such as speckle. In addition, a laser provides light at a specific wavelength with a very narrow bandwidth of about 5 nm, whereas we want to explore several wavelengths in the visible spectrum with a much wider bandwidth of about 40-50 nm. Therefore, we opted for an incoherent xenon white light source (Sopro COMEG230), shown in Figure 3.19a, coupled with several interference filters (as explained before) to select the wavelengths of interest with the desired bandwidth. This source makes use of a xenon lamp (Osram XBO R 300W/60C OFR) with a power of 300 W. It produces a much greater amount of light than the halogen source, originally used for the colposcope, at all wavelengths of the visible spectrum. In particular, it emits a larger amount of blue light.

Indeed, the luminous flux must be considerably increased for the new multispectral MPC prototype compared to the old one for two reasons. First, the pixel size of the 3-CMOS camera sensors in the new prototype (on the order of 3.65 µm x 3.65 µm) is smaller than that of the monochromatic CCD camera sensor (on the order of 4.54 µm x 4.54 µm) in the old prototype. Therefore, the sensors of the 3-CMOS camera can collect fewer photons than those of the monochromatic CCD camera with light flux parity. Second, the 3-CMOS camera in the new prototype operates at 64 FPS (~15 ms per frame) with the required field of view, whereas the monochromatic CCD camera in the old prototype operated at 16 FPS (~62 ms per frame). Therefore, the 3-CMOS camera must use a much shorter exposure time than the monochromatic CCD camera, which can result in a significant decrease in the acquired light signal.

We also tested white light LED sources. However, we found that existing commercial white light sources are not powerful enough for our needs. An interesting alternative could be to use a rack of individual LED sources to obtain the required light output. However, at this stage of our research, without precise knowledge of the optimal wavelengths for the intended application, we would have to use a large number of individual LED sources, which results in a much more cumbersome and expensive solution than using a xenon lamp with interference filters.

Optimization of the xenon light source

The xenon light source employed for the new MPC is commonly used in hospitals for endoscopic systems and has therefore been extensively tested on human tissue *in vivo*. The xenon lamp is installed in the left side of the source, as shown in Figure 3.19. The light emitted by the lamp passes through two band-pass filters that significantly cut off infrared and ultraviolet rays, allowing mainly the visible radiation to be transmitted.

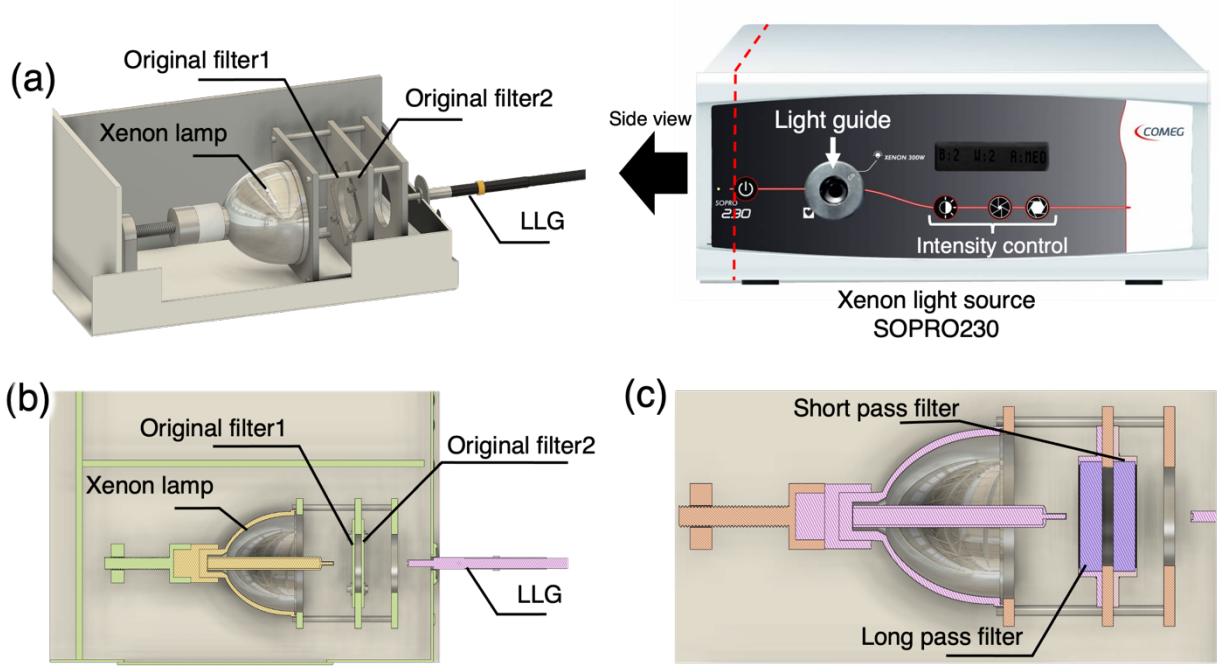

Figure 3.19 (a) Illustration of the interior of the light source module. (right) The 2 filters eliminate light with a wavelength longer than 700 nm before it is collected by a liquid light guide (LLG). (left) (b) The transverse plane of (a). (c) Two filters have been replaced to 1 long pass filter (cut-off=400 nm) and 1 short pass filter (cut-off=750 nm).

As described above, our objective is to explore the polarimetric response of the cervix at different depths using several wavelengths selected with appropriate spectral filters. As a reminder, we used a 3-band (RGB) filter to simultaneously select wavelengths around 460 nm, 530 nm, and 630 nm. Furthermore, we added two more spectral filters to select light at 650 nm and 700 nm.

The first problem we encountered when coupling the xenon source to the 3-CMOS camera described above is a lack of signal in the red/near infrared part of the visible spectrum, especially around 700 nm. This is due to a decrease in the sensitivity of the 3-CMOS camera, but also toa decrease of the light intensity in this wavelength range.

Indeed, a more detailed characterization of the emission spectrum of the source using a spectrometer (Ocean optics Frame UV-VIS) showed that it is characterized by the highest emission between 500 nm and 650 nm. A relative emitted intensity of about 60% was measured for this wavelength range. On the other hand, the emission of the source decreases rapidly from 680 nm to become almost zero around 750 nm. It also decreases below 500 nm to a relative emission intensity of about 20% around 400 nm and 10% around 350 nm. It

should be noted that, if the near infrared is completely eliminated, a contribution from the ultraviolet above 350 nm, albeit small, is still present.

A second spectrophotometer (Varian Cary 500) was used to determine the spectral transmittance of the two filters placed in front of the xenon lamp. Both filters are characterized by a transmittance that begins to decrease rapidly above 700 nm. On the other hand, the transmittance decreases more slowly below 400 nm and becomes completely zero at 350 nm. A residual transmittance is also observed between 300 nm and 350 nm. However, the xenon lamp used is ozone-free and does not emit any ultraviolet wavelengths below 350 nm. In addition, both filters have a transmittance of about 80% between 400 nm and 700 nm. Coupling the two filters produces a relatively low transmittance of about 64% in the same spectral range, as shown in Figure 3.20.

The two filters were therefore removed to characterize the spectrum of the xenon lamp alone. The spectral profile thus measured is very similar to that obtained in the presence of the two filters between 350 nm and 800 nm, as shown in Figure 3.20b. In the absence of the filters, the light produced by the source is about 20% higher than that produced in the presence of the filters for the entire spectral range considered. When both filters are removed, about 20% of the light is recovered over the entire spectral range of interest. However, in the absence of the filters, a relative emission intensity of 10-40% was also found in the ultraviolet between 350 nm and 400 nm, as well as 10-20% in the near infrared. For this reason, the two filters cannot simply be removed, as their presence significantly reduces potentially hazardous infrared and ultraviolet light for patients.

Therefore, we replaced these two filters with two new ones: a first bandpass filter (Edmund optics #84-728) which allows to transmit only the light between 400 and 750 nm with a transmittance of about 95% and a second high-pass filter (Edmund optics #84-754) which allows to transmit only the light at a wavelength above 400 nm with a transmittance of about 93%, as shown in Figure 3.20a. The superposition of the two new filters gives a total transmittance of about 86% between 400 nm and 750 nm, which allows to recover nearly 20% more light than the initial configuration. In addition, the transmittance between 350 nm and 400 nm is almost zero. It is the same for the transmittance in the near infrared. On the other hand, the transmittance in the ultraviolet below 350 nm remains considerable, but again this is not a problem since the xenon lamp used is ozone-free. Finally, the emission spectrum of the source with the two new filters is almost superposable to that of the lamp alone between 400 nm and 750 nm.

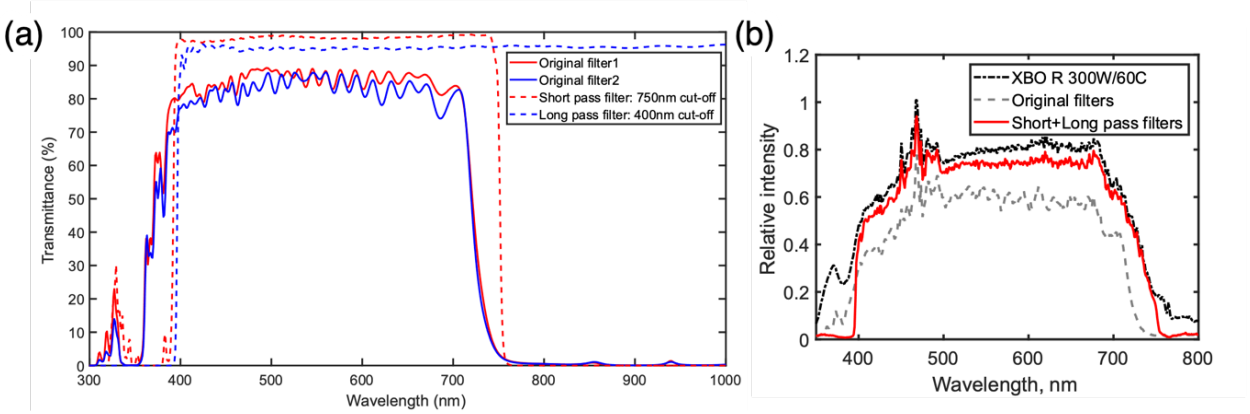

Figure 3.20 (a) The spectral transmittance of the four different pass filters (the two original filters and two new filters). They were measured by a spectrophotometer Varian Cary 500. (b) The measured relative spectral intensity (flux) of 3 combinations. 1. Lamp alone, 2. Original filters, 3. Short + long pass filter.

The effect of filter replacement was finally tested with the MPC imaging system using Spectralon® (Edmund optics #58-611), a translucent tetrafluoroethylene-based polymer, as a white reference target. Intensity images were acquired at 5 wavelengths with the two different light source configurations, i.e. before and after the filter replacement. The intensity distributions of the acquired images by the MPC at each wavelength of interest for the two conditions are charted in Figure 3.21 using a box plot. Overall, the use of the two new filters increases the light intensity measured on the 3-CMOS camera in ADC units by 20-40% for the wavelengths chosen between 460 nm and 650 nm. At 700 nm, the measured light intensity increases by about a factor of 10.

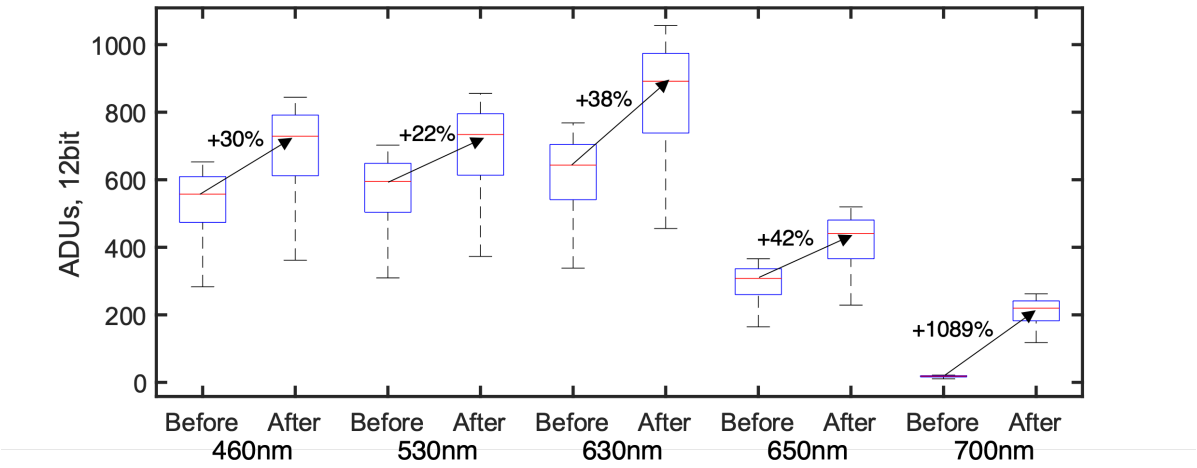

Figure 3.21 The increased intensities after replacing the original filters to the short + long pass filters. Drastic increment (~+1000%) at 700 nm is observed.

a) *Optimization in light delivery: liquid light guide*

The unpolarized light from the source is transported to the colposcope head by a light guide. A commercial Olympus OCS-500 colposcope uses a halogen source coupled to a silica fiber bundle (SFB) as illumination system. The SFB is connected to the front part of the colposcope head by a metal housing containing a collimator followed by a prism, as described in Chapter 2. The collimator refocuses the diffracting beam coming out of the

guide and the prism changes its propagation direction to straighten it towards the cervix to be explored.

For the new MPC, we have not only replaced the halogen source with a xenon source as explained in the previous paragraph, but also the SFB with a liquid light guide (LLG), shown in Figure 3.22. The LLG is much like a single silica fiber with a large diameter, in the order of about 3 to 5 mm. It has a cross-section of an open pipe. The propagation of light in such a tube can be described by using geometric optics. The light is transmitted through the LLG by means of total internal reflection using all the available space. This is why the LLG is able to deliver light to the target with much greater intensity and more spatial uniformity with respect to a conventional SFB as shown in Figure 3.22d and e. Indeed, many fibers of SFB can be easily damaged when handling it due to their sensitivity, as shown in Figure 3.22d, which doesn't happen for LLG, as shown in Figure 3.22e In addition, the LLG is characterized by a high acceptance that is comparable or better than SFB, whic enables to further maximize the amount of collected light from the source.

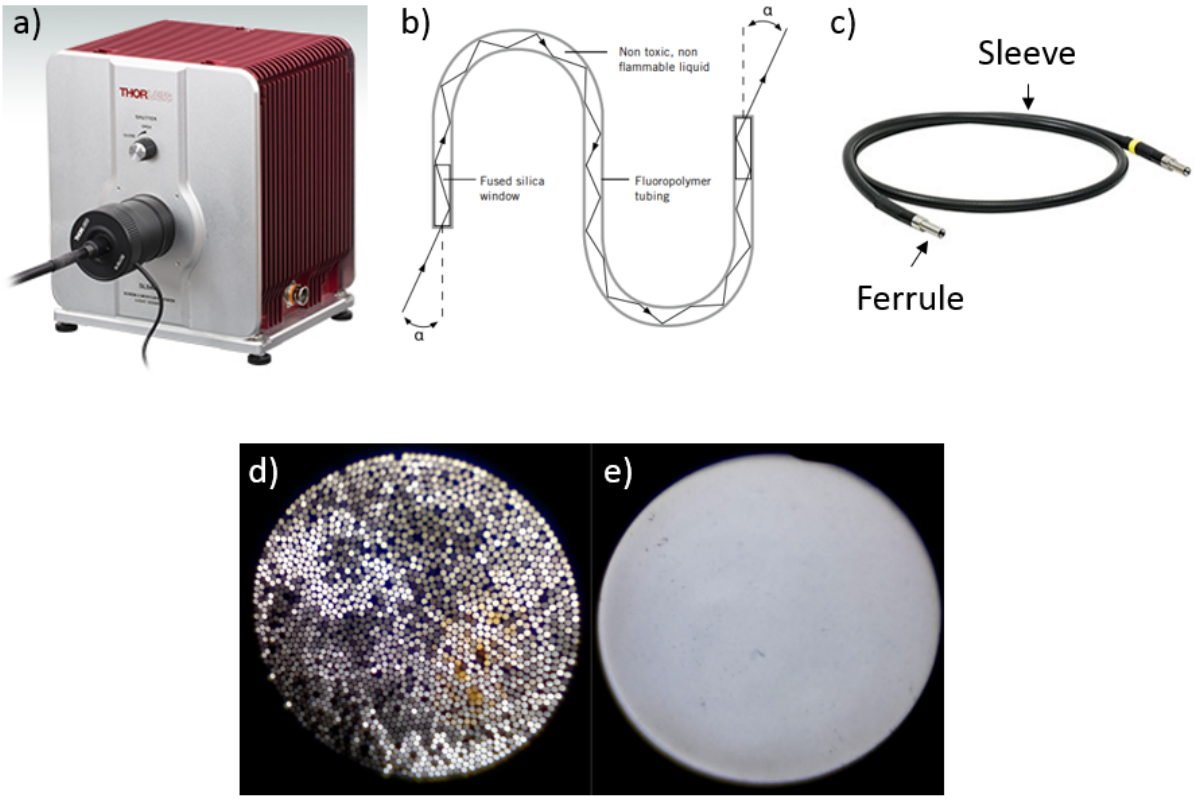

Figure 3.22 (a) Photo of an LLG connected to a light source. (b) The general principle of operation of a liquid light guide based on total internal reflection. The image is taken from Lumatec Brochure. (c) Photo of LLG from Thorlabs (LLG05-04H) used in this thesis work. (d) Cross-sectional image of the end tip of a conventional silica fiber bundle (S_700382, Sopro-Comeg). (e) Cross-sectional image of the end tip of the used liquid light guide. The liquid light guide has smoother and more uniform interface with respect to that of the silica fiber bundle due to the single liquid core. The bundle has uneven illumination due to the individual broken fibers accumulated during its lifetime.

We initially used a LLG with a diameter of 5 millimeters, a length of 1.2 meters and a numerical aperture of 0.59 (Thorlabs LLG05-4H). This guiding system allows efficiently transporting the light from the source to the colposcope head with a transmission coefficient

of about 80% in the spectral range between 400 nm and 800 nm, which is not possible with a conventional silica fiber bundle.

The light produced by the source is injected in the LLG. The bulb of the xenon lamp is placed in one of the two foci of an elliptical mirror indicated as F1 in Figure 3.23(a) In this way, the emitted light rays, after being reflected by the mirror, converge towards the second focus of the ellipse, indicated as F2 in Figure 3.23a. One end of the LLG, also indicated as the input end, is placed near F2 to maximize the amount of light injected. The output end of the LLG is connected to the metal housing of the colposcope head, containing the collimator and prism, by means of a homemade mechanical system described in more detail in the next section.

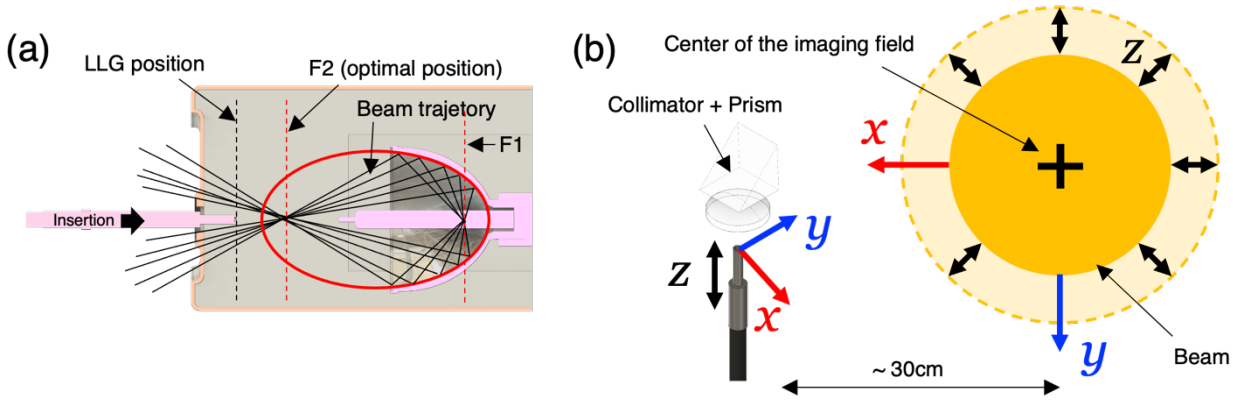

Figure 3.23 (a) The scheme of the light extraction from the xenon lamp. The elliptical reflector of the lamp concentrate the light illuminated from F1 into the point F2. Thus, lateral positioning of the LLG is important for light extraction. (b) the scheme of the mechanical adaption of the LLG on the colposcope side. The position and size of the beam with respect to the imaging field can be changed by the position of the LLG relative to the prism in the colposcope at a working distance around 30 centimeters.

The collimator of the colposcope images the tip of the LLG onto the object plane. The beam profile and the image size on this plane are strongly dependent on the diameter of the LLG as well as on the diameter and focal length of the collimator. Specifically for the initially selected LLG, characterized by a diameter of 5 millimeters, the image size is 6.5 centimerters at a working distance of 30 centimeters from the colposcope head (corresponding approximately to the position of the cervix being examined). The beam size is much larger than the diameter of the cervix, which is about 3 centimeters. For this reason, we decided to reduce the beam size to dramatically increase the amount of light illuminating the cervix.

We tested a new LLG with the same characteristics as the previous one in terms of length, numerical aperture, and transmittance, but with a smaller diameter of about 3 millimeters, which makes it possible to significantly reduce the beam size at the considered working distance. Figure 3.24 shows the optical paths for the two LLGs considered. It can be observed that the 3 mm diameter LLG produces a beam of about 3.9 centimeters in diameter, considerably smaller than that produced by the 5 mm diameter LLG initially chosen.

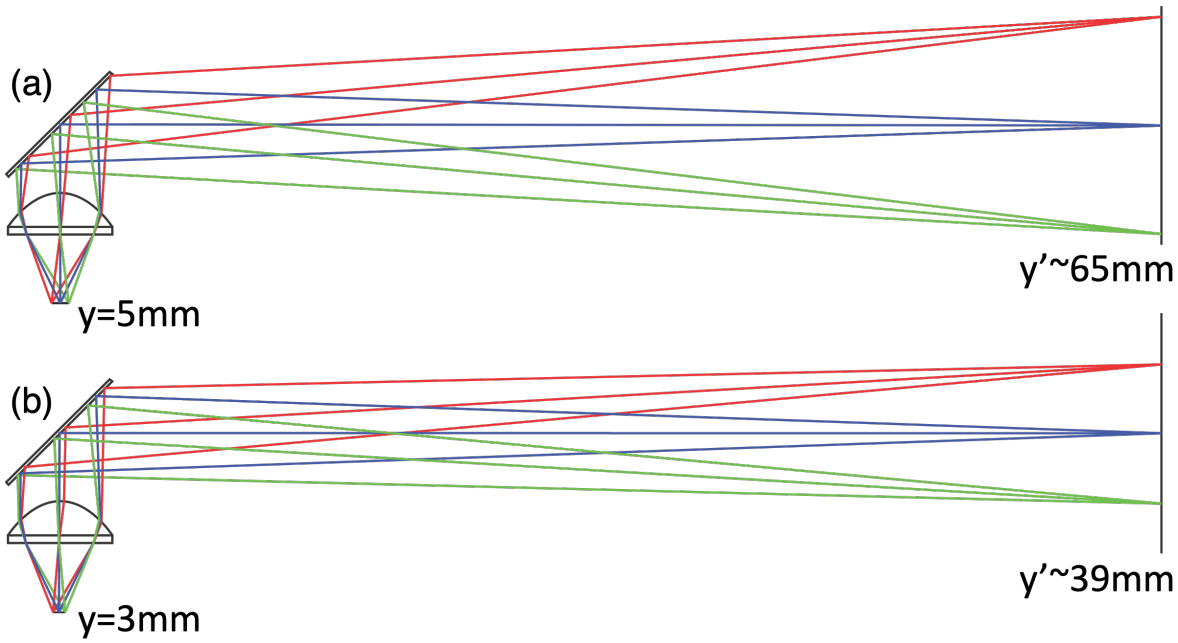

Figure 3.24 The virtual scheme of the illumination system. The actual system does not form a clear image of the source as illustrated in this figure. (a) The LLG with a tip of a diameter of 5 millimeters forms ~65 millimeters of beam size at a working distance of 30 centimeters. (b) The LLG with a tip of a diameter of 3 millimeters forms ~40 millimeters of beam size at a working distance of 30 centimeters.

The amount of light injected into the smaller diameter LLG decreases mainly on the tails of the Gaussian beam. However, this energy loss at injection is much smaller than the increase in light intensity due to the densification of the photon flux at the other end as a result of beam focusing by the collimator.

Figure 3.25a and b show the two-dimensional beam profiles obtained with the two different LLGs at the working distance of 30 centimeters. The x-y plane corresponds to the 2D image plane of the camera (1120×1120 pixels). The beam obtained with the 5 mm diameter guide has a flatter profile than the beam obtained with the 3 mm diameter guide that appears narrower and therefore more intense.

The 1D profile of the beam along the mid-horizontal line shown in Figure 3.25c confirms a considerable increase of light intensity up to 37% in the central part of the 3 cm diameter area of interest corresponding approximately to the effective size of the cervix. This increase is of the order of 20% near the edges of the region of interest.

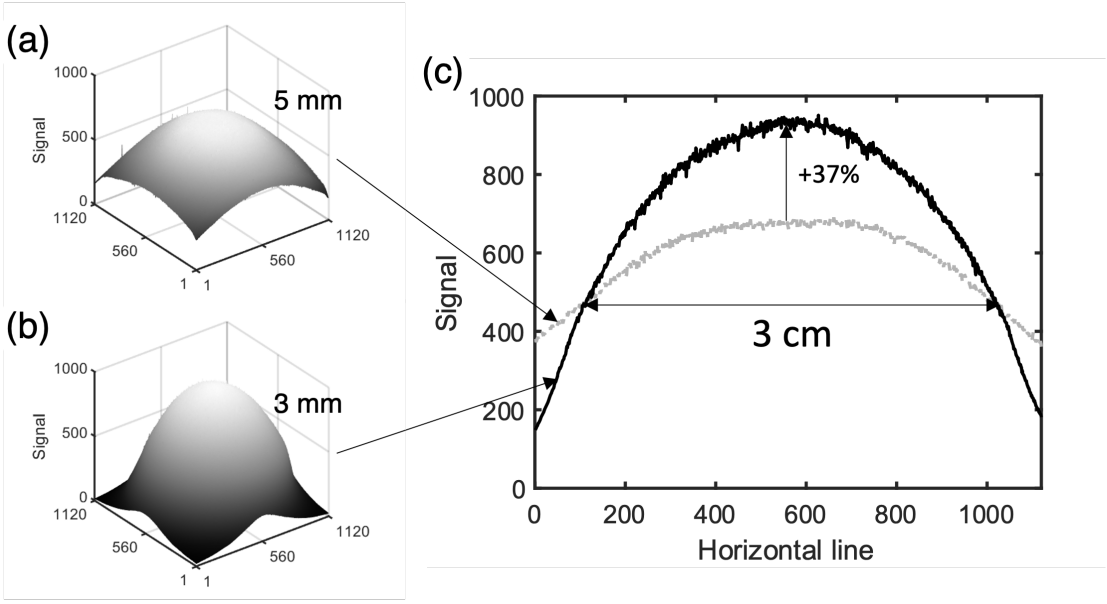

Figure 3.25 The 2D beam profile measured by the colposcope+AP3200. (a) with the LLG with the tip of a diameter of 5 millimeters. (b) the tip of a diameter of 3 millimeters exhibits a narrower and higher profile than its of a diameter of 5 millimeters. (c) The 1D beam profile (the middle horizontal line). It confirms that the a diameter of 3 millimeters tip illuminates brighter light at least in the field of a diameter of 3 cm, which corresponds to the cervix size.

Ultimately, reducing the divergence of the beam and its size on the object plane not only has the advantage of greatly improving the illumination, but also of directing the light primarily onto the cervix, as shown in Figure 3.26. In this way, it is possible to significantly reduce stray reflections of light from surrounding parts (vaginal walls, speculum, etc.) that can significantly decrease the quality of the acquired images.

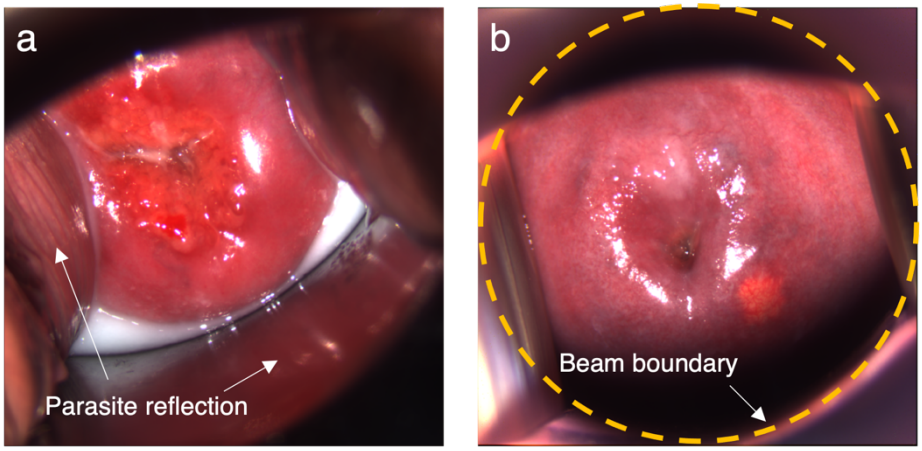

Figure 3.26 (a) A cervical image taken by the LLG with a diameter of 5 mm. The beam unnecessarily illuminates the speculum and vagina, which might cause stray light. (b) A cervical image taken by the LLG with a diameter of 3 mm. The cervix is placed within the circular beam boundary where the light intensity starts to significantly decrease.

b) *Adaptation of the liquid guide*

As explained above, the LLG connects the light source to the colposcope head. The adaptation of the LLG to the xenon source and the metal housing of the colposcope head containing the collimator is pivotal to the reproducibility of the experiments. Indeed, the illumination intensity measured on the 3-CMOS camera fluctuates drastically depending on

the optical alignment between the LLG input tip and the xenon bulb as well as between the LLG exit tip and the collimator.

For this reason, we have designed and implemented very stable mechanical adaptation systems that do not allow the two LLG tips to move during the use of the MPC. The tip of the LLG has to be placed where the photon flux is higher, as shown in Figure 3.23a. In particular, the input tip of the LLG has to be placed near F2 where the rays produced by the xenon bulb are maximally focused by the elliptical mirror. To this end, a source-side adapter, shown in Figure 3.27, was 3D printed to allow alignment of the LLG with the optical axis of the xenon lamp. This system was designed to smoothly move the LLG to determine its optimal position relative to F2, thus ensuring maximum light injection. The optimal position of the LLG is finally fixed by a screw on the side of the adapter.

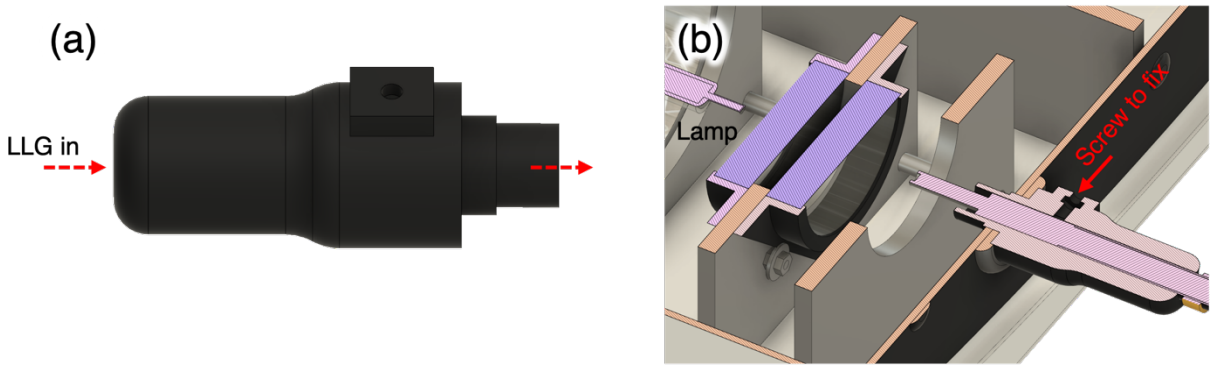

Figure 3.27 (a) The side view of the LLG adapter on the light source side. The LLG is inserted from left to right. (b) The sagittal sectional view of the light source. The LLG needs to be placed at a position where the light intensity is maximized. In that position, the position of the LLG can be fixed by a screw.

As shown in Figure 3.28, the mechanical adapter to the metal housing of the colposcope head (where the collimator and prism are placed) must provide more degrees of freedom at the output end of the LLG in the x-y plane orthogonal to the collimator optical axis. In addition, it must also allow a fairly accurate adjustment in the *z*-direction parallel to the optical axis of the collimator.

This adapter is composed of 3 pieces as shown in Figure 3.28a. In particular, the LLG is inserted in a piece, colored in red, which can move in the x direction. In addition, the red piece is attached to another piece, colored blue, which can move in the y direction. In this way, the position of the LLG exit tip can be adjusted in the x and y directions independently to properly align the beam with the collimator axis, which is crucial to produce an image of the LLG exit tip centered on the MPC imaging axis.

Once the optimal position in the x-y plane has been determined, the red and blue pieces are firmly attached to another piece, colored white, which is also firmly attached to the metal collimator housing. In addition, the LLG can slide inside the red piece parallel to the z direction. In this way, the optimal position can be determined to image the output end of the LLG about 30 centimeters from the colposcope head. Finally, the LLG can be firmly attached to the red piece with a screw. The rectangular box attached to the red piece is the cage for the sliding filter electronics.

.

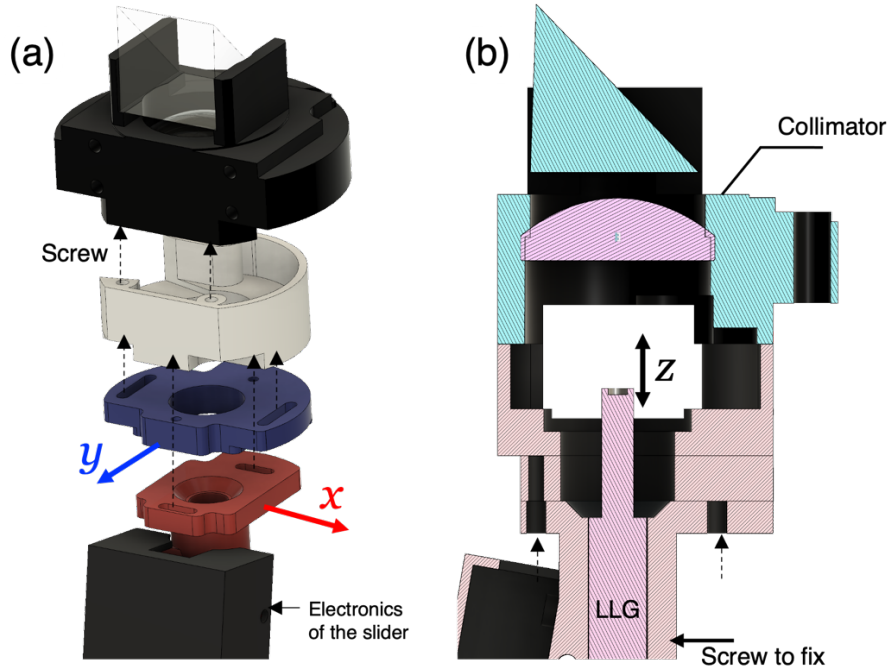

Figure 3.28 (a) The optomechanics for fitting the LLG to the colposcope head. It consists of 3 pieces mounted along the black dashed arrows. The bottom part (red) can be moved along the *x*-direction. The middle part (blue) can be moved along the *y*-direction. These 2 pieces allow the user to adjust the position of the LLG with respect to the collimator of the colposcope head. (b) The sagittal sectional view of the complete assembly. The LLG is inserted from the bottom and can be moved along the *z*-direction. The optimal position of the LLG can be fixed by a screw.

Figure 3.29 shows the final MPC assembly including the polarimetric box, the imaging system, and the illumination system that were adapted to the Olympus OCS-500 colposcope.

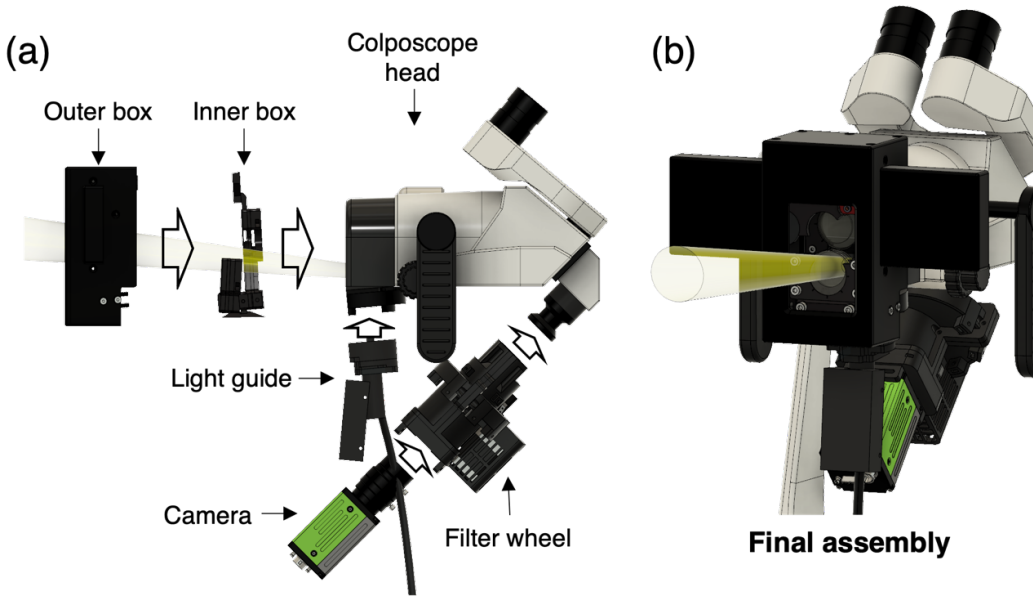

Figure 3.29 (a) Assembly of the main components of the MPC. (b) Conceptual appearance of the Mueller polarimetric imaging system of the MPC. Electronic cables are omitted for clearer illustration.

Optimization in the selection of the polarizer of the PSG

Another cause of a large decrease in the light intensity detected in a Mueller polarimeter is the use of two polarizers, one in the PSG and one in the PSA. A low transmittance polarizer is supposed to attenuate more than 50% of incident unpolarized light by absorption or reflection. In particular, in the case of a dichroic polarizer that polarizes the light by an anisotropic absorption process, the absorbed light is transformed into thermal energy that can heat up considerably and damage it. Figure 3.30a shows several examples of dichroic polarizers (Melles-Griot 03 FPG003) damaged when used in the PSG of the former MPC. Indeed, a bleaching is observed on these polarizers, which determines a decrease of its polarizing power.

Inorder to better characterize the observed phenomenon, we studied the effect of increasing temperature on this type of polarizers using a heating plate (IKA ECT basic). For this purpose, four initially intact polarizers were wrapped in an aluminum foil for better heat conduction, as shown in Figure 3.30b. Four different temperatures were tested to determine the heat tolerance of this type of polarizers, as shown in Figure 3.30c. A temperature sensor (Thorlabs TSP01 and TH) was placed on each polarizer to monitor its temperature during heating. Each polarizer started at an ambient temperature of about 25°C and reached the plateau temperature after about 5 minutes, as shown in Figure 3.30c. A full-field Mueller polarimetric imager from our laboratory was used to characterize the degree of polarization (DoP) of each polarizer at different temperatures for three different wavelengths, namely 450nm, 550nm and 650nm. The DoP starts to decrease slightly at 450nm for a temperature of 125°C, while it decreases drastically for all three wavelengths at 150°C and above, as shown in Figure 3.30d. As an example, the inset in Figure 3.30b shows the polarizer heated to 200°C which has completely bleached, thus losing its polarizing power.

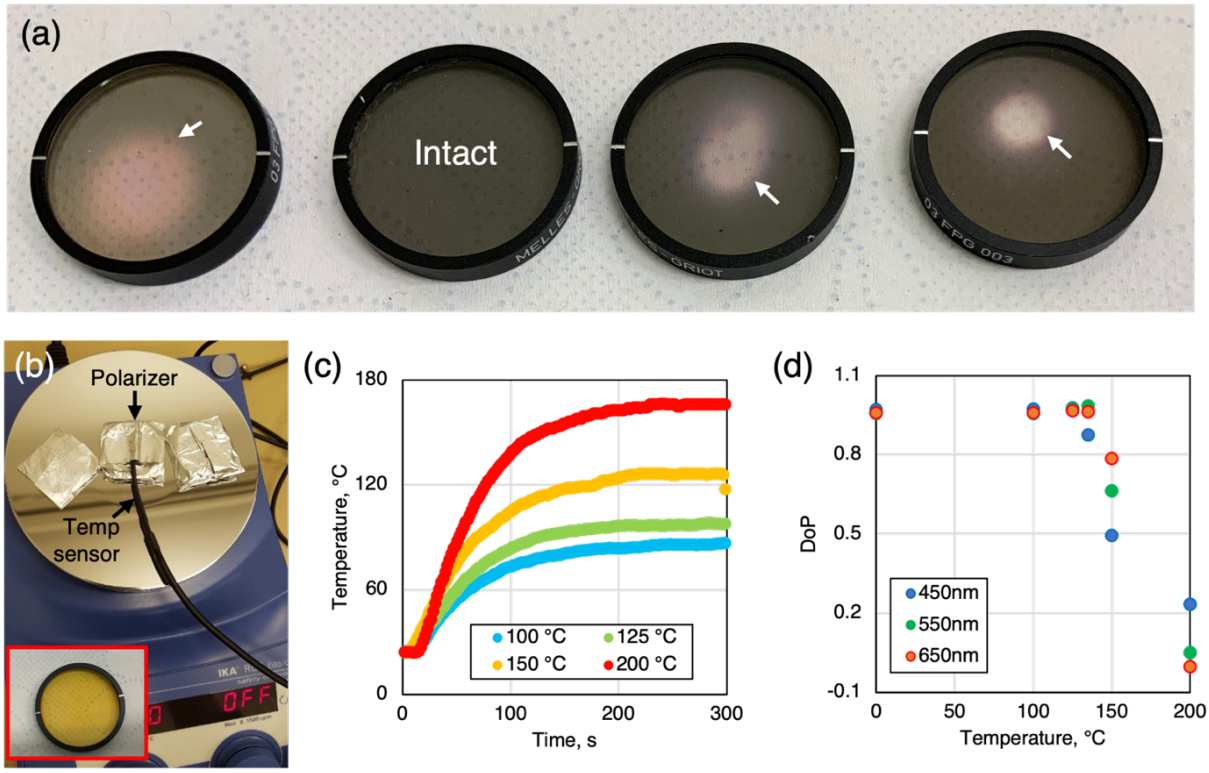

Figure 3.30 (a) Melles-Griot's polarizers bleached by the xenon light source (the white arrows). (b) The configuration of the thermal bleaching test. The polarizer was covered with an aluminum foil to increase heat transfer. (c) Temperature curves of four polarizers heated over time at different temperature of the heat place. (d) The DoP of the light beam that the bleached polarizers generated. The polarizers heated by higher temperature than 125 °C loses its dichroic property.

Hence, the dichroic polarizer of the PSG was replaced with a heat-resistant wire-grid polarizer (Thorlabs WP25L-VIS). The wire-grid polarizer causes strong diattenuation by an anisotropic reflection process. Therefore, it is much less heated than dichroic polarizers and can withstand temperatures up to 400°C. The great advantage of the wire-grid polarizer is that it has higher transmittance than the dichroic polarizers over the broad-spectral range of interest, i.e., between 400 nm and 800 nm. The transmittance curves of the 2 polarizers are compared in Figure 3.31(a). The extinction ratio of the wire-grid polarizer (100~1000) is lower than that of the dichroic polarizer (>10000), as shown in the Figure 3.31b. However, a critical decrease in the condition number of the PSG occurs when the extinction ratio becomes less than 10 [15]. Therefore, the extinction ratio of the wire-grid polarizer is widely sufficient to ensure high measurement accuracy.

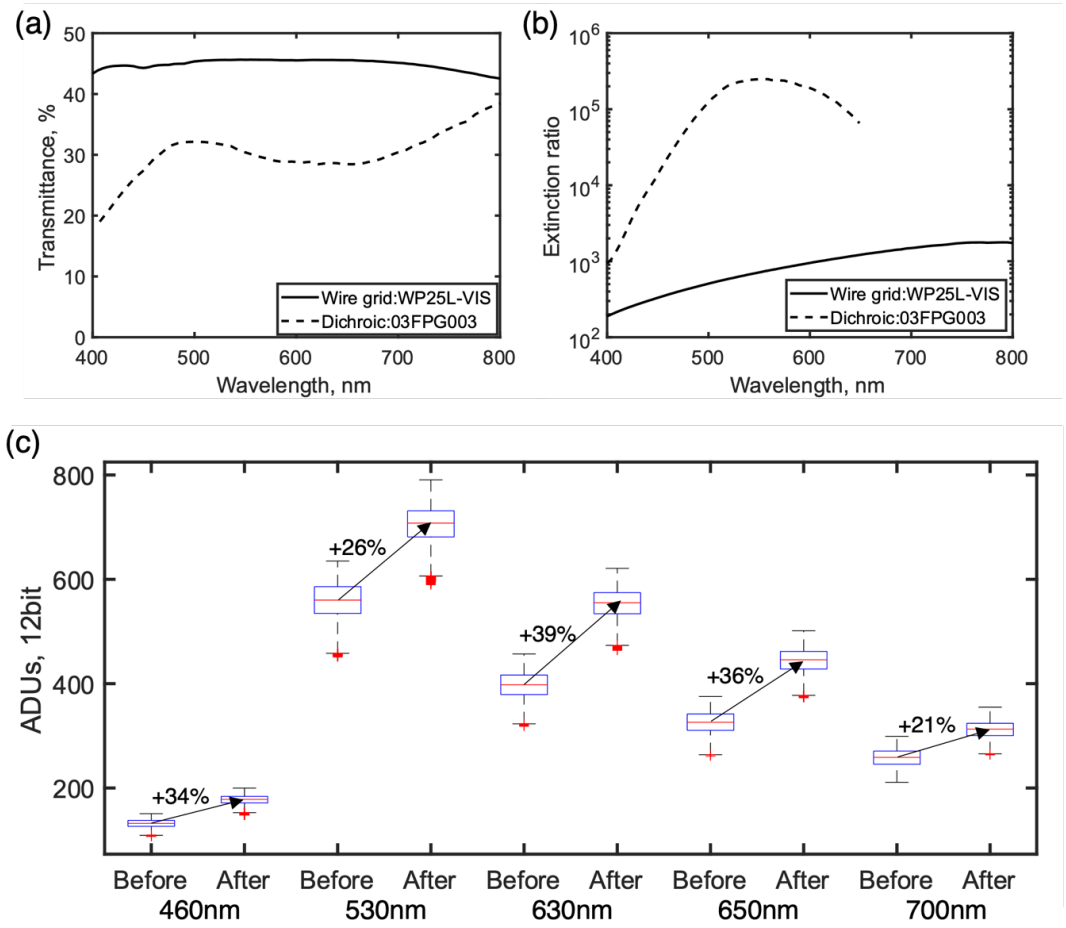

Figure 3.31 (a,b) The transmittance (unpolarized light) and extinction ratio of the 2 types of polarizers. The wire-grid polarizer has ~10% higher transmittance in the visible range. (c) Comparison of the signal before/after replacing the polarizer. The wire-grid polarizer leads to an intensity gain of about 30%.

After replacing the dichroic polarizer with the wire-grid polarizer, the signal acquired by the camera under the same imaging conditions is increased by an average value of 30% for all wavelengths, as shown in Figure 3.31c.

Table 3.6 The summary of the intensity increases by the illumination system optimization. The second column represents the increase of light intensity by exchanging the two IR-cut filters with a long and short pass filter in Figure 3.19. The third column represents the increase of light intensity by changing the LLG of 5 millimeters tip to 3 millimeters. The fourth column represent the increase by changing the dichroic polarizer to the wire-grid polarizer. The 'Total' column represents the overall increase after all changes.

	IR-cut filter	LLG	Polarizer	Total
460nm	+30%	+35%	+34%	+135%
530nm	+22%	+37%	+26%	+111%
630nm	+38%	+38%	+39%	+165%
650nm	+42%	+41%	+36%	+172%
700nm	+1089%	+43%	+21%	+1784%

3.3 Conclusions

The primary objective of this thesis work was to initiate a clinical trial focused on the use of Mueller polarimetric imaging to monitor cervical microstructure remodeling during pregnancy and provide more objective criteria to improve the diagnosis of prematurity.

During the first phase of this thesis work, we focused on the development of a new prototype of a multispectral Mueller polarimetric colposcope for *in vivo* use in a hospital setting. The development of a medical device is a real challenge as it must provide high quality and repeatable measurements in a short time while remaining very ergonomic and easy to use, thus limiting discomfort for the practitioner and the patient.

In this chapter, we have presented the key steps to develop such a device based on the use of polarized light. The main novelty of the new MPC prototype designed and realized during this thesis work is the use of a 3-CMOS color camera that allows both to acquire an RGB image of the cervix and to perform its polarimetric analysis at different wavelengths of the visible spectrum in order to explore the cervical tissue at several depths.

The new MPC consists of three main components: an illumination system, a detection system and the polarimetric housing. These three main components have been integrated into a conventional colposcope in a compact manner so as not to change established medical practice. Extensive experimental work was performed to characterize and optimize each component until we obtained a system capable of acquiring accurate *in vivo* images on a massive number of patients in a clinical trial. In addition, we also worked to obtain a user-friendly software and a relational database allowing to manage large amounts of data. Finally, a lot of work has been done on the ergonomics to obtain a system that can be used by a practitioner like a classical colposcope.

The new multispectral MPC prototype is currently installed at the Kremlin-Bicêtre University Hospital, and will be able to collect polarimetric images of the cervix on 650 patients *in vivo*. It is a world first. Indeed, for the first time, the Mueller polarimetric imaging system is being tested on a massive number of patients in a clinical study. The system is easy to use and does not change the established medical procedure.

Chapter 4

Ergonomics and performance assessment

The novel multispectral MPC was fabricated by integrating the various components described in previous chapter on a commercial Olympus OCS-500 colposcope. Although all these components have been characterized in detail one by one and the potential improvement that each of them brings to the image quality, the ergonomics, and the usability of the new MPC has been discussed, a detailed assessment of the assembled system's performance is necessary.

This chapter presents the results of the MPC performance evaluation, including its ergonomics, which allowed identifying the main sources of error in the system and quantifying their impact on the accuracy of the polarimetric measurements performed during the clinical trial. Furthermore, the procedure for using the MPC *in vivo* in a hospital setting is described in detail. Indeed, the prior definition of the different steps to be performed by the practitioner to examine the cervix of each patient was a crucial step to guarantee the repeatability of the measurements and the high quality of the acquired images.

4.1 Physical ergonomics

For an experimental device intended to be used for scientific research in the laboratory or for the analysis of a small number of *ex vivo* biological tissue samples or in vivo patients in a hospital setting, the ergonomics of the system is not a critical point. However, the multispectral MPC must be able to be used by a hospital practitioner (gynecologist, midwife, etc.), who is not accustomed to handling this type of technology, for an extended period of time (approximately 36 months on a weekly basis), in order to collect cervical images from a massive number of patients. That's why we designed and built the novel prototype to provide a system with good physical ergonomics and user-friendly software that allows hospital practitioners to perform rapid and accurate repeat measurements, which ultimately contribute significantly to the success of the clinical trial.

4.1.1 Arrangement of the physical components

The previous prototype of dual-wavelength MPC was very difficult to use in medical practice, especially in a clinical study with a massive number of patients to be examined. The primary reason for this low usability is that the system was designed to spatially separate the colposcope and the computerized machine management system.

In the former MPC, the polarimetric box was always integrated into the colposcope head. In addition, the FPGA and the light source were mounted on a metal support attached to the colposcope body. In contrast, the computer system (workstation, keyboard, etc.) was mounted on a separate vertical cart. In particular, the most important problem with the physical ergonomics of the former MPC was that the screen and keyboard were located far away from the user during practice. This drawback required an additional user to operate the computer system and acquire the images. In addition, this prototype was very bulky and difficult to move. The use of three cameras (one color and two monochromatic) connected to the colposcope head made its use *in vivo* very difficult.

On the contrary, the new MPC has been designed as a completely stand-alone system in which all the optical, electronic and computer components are integrated directly onto the metal body of the colposcope, providing a much more compact system that can be used by a single operator. The overview of the novel MPC, compared with the older dual-wavelength prototype, is shown in Figure 4.1. The actual appearance of the novel multispectral MPC is shown in Figure 4.2.

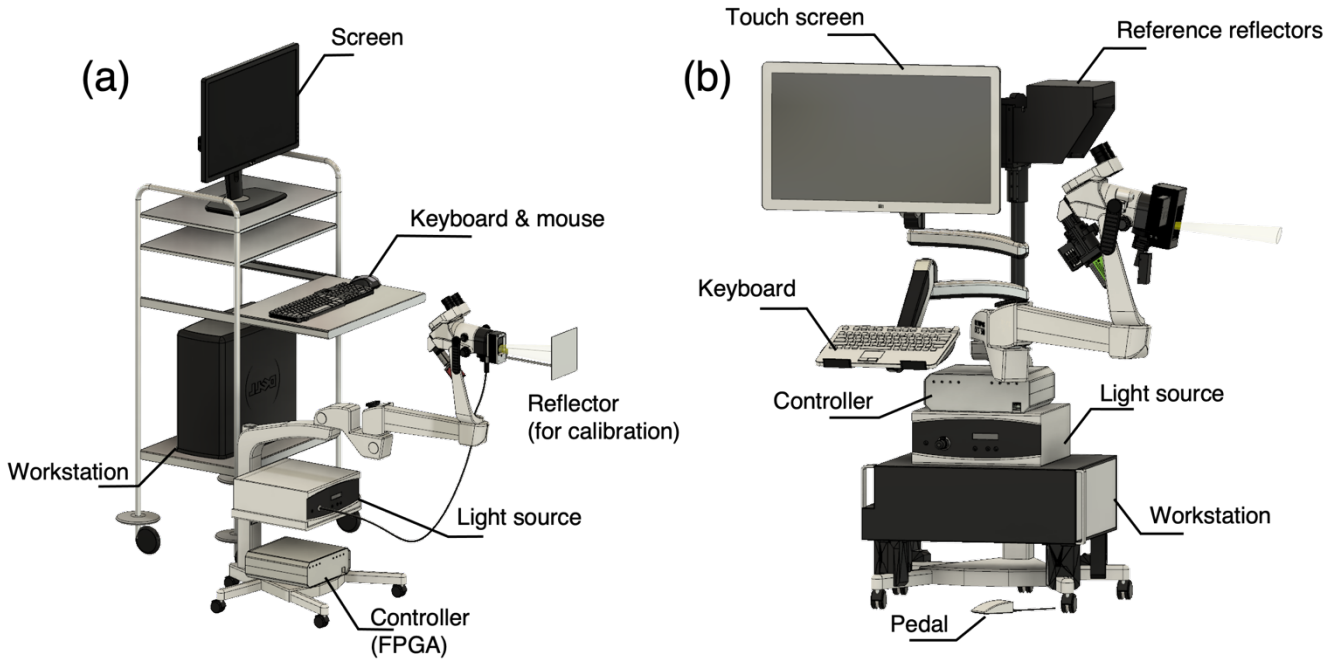

Figure 4.1 (a) 3D Model of the former dual-wavelength MPC. (b) 3D Model of the novel multispectral MPC.

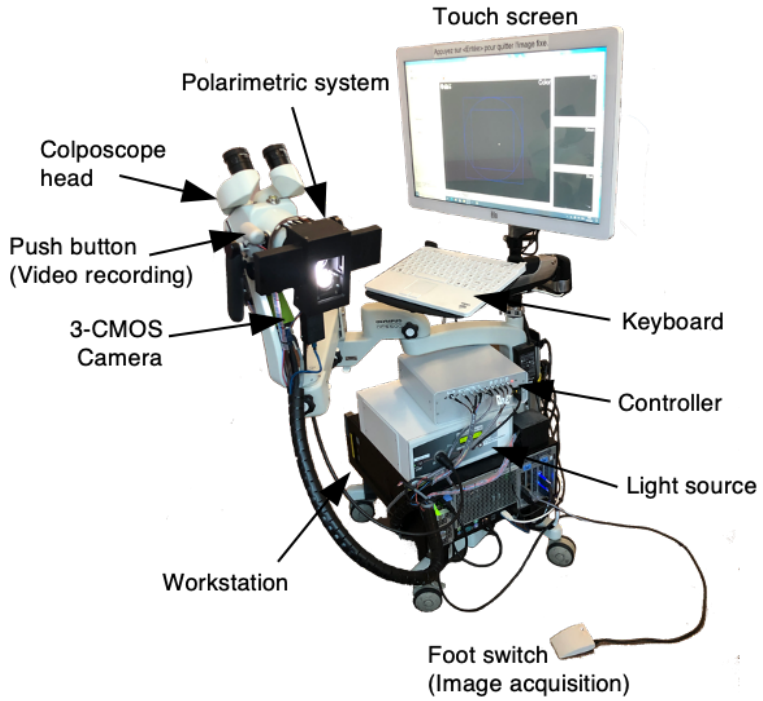

Figure 4.2 The picture of the novel multispectral MPC

Unlike the previous prototype, we used waterproof touch screen (Elo 2403LM) and keyboard (Man&Machine Slim Cool Plus), designed for medical devices in a clinical or operating room setting, directly attached to the metal body of the colposcope by flexible arms, as shown in Figure 4.3a. A simulation using 3D modeling presented in Figure 4.3b shows the geometric requirement for the monitor and keyboard to allow the user to use them during a typical colposcopic examination. It shows that the required length for the monitor and keyboard arms are 25 cm (Ø 50 cm) and 60 cm (Ø 120 cm), respectively. Based on this simulation, two flexible arms (Duronic DM65L1X1) attached to the vertical metal bar, which make it possible to place the touch screen and the keyboard at the right distance from the user, as shown in Figure 4.3b.

The touch screen associated with the graphical interface is one of the key solutions that have improved the ergonomics of the system. Indeed, the operator can easily adjust the colposcope head to find its optimal position for image acquisition and at the same time access the computer system and the screen on his left. The mechanical arms of the screen and keyboard are equipped with mechanical joints that allow the operator to easily regulate their position. In this way, the user can control the MPC software while manipulating the colposcope head at the same time.

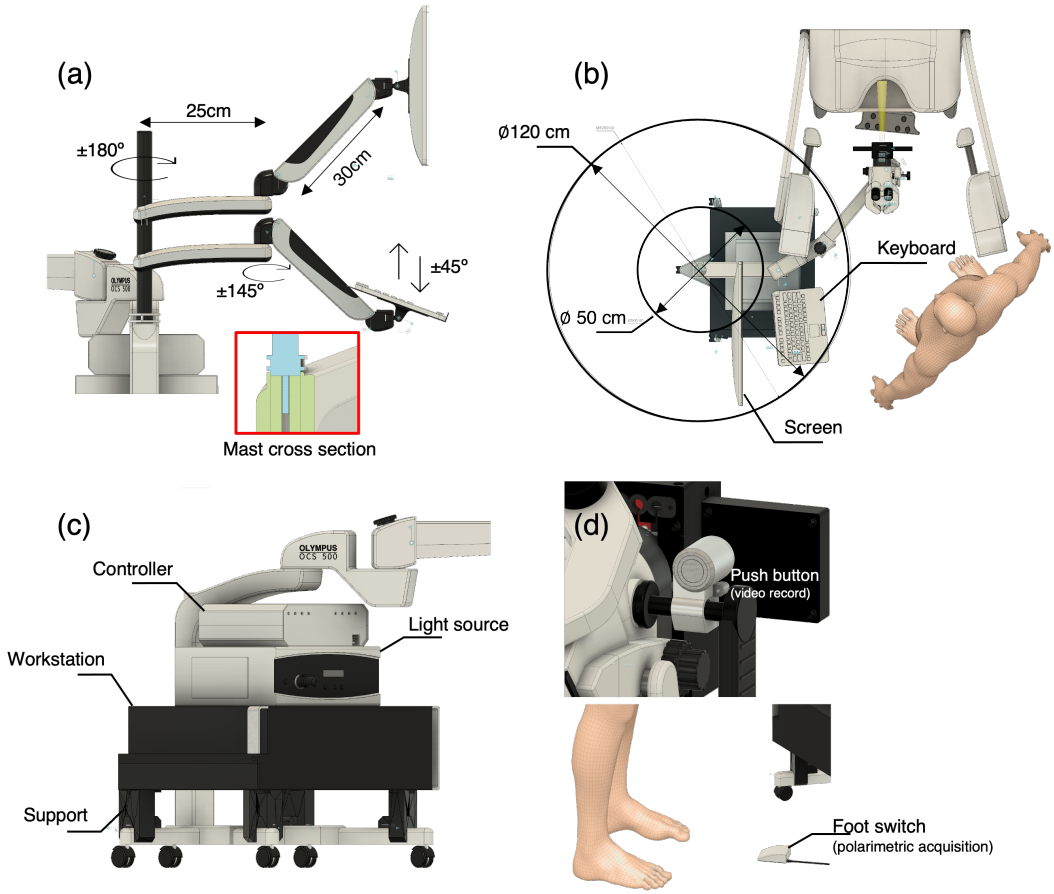

Figure 4.3 (a) The configuration of the monitor and keyboard arms. (b) The geometry of a typical colposcopic examination. (c) The arrangement of the 3 main components, the workstation, light source, and controller. This arrangement increases the mobility of the MPC. (d) The push button for triggering video record and stop (top). The foot switch for triggering a Mueller image acquisition(bottom). The user can prevent mechanical vibrations to the colposcope head when he/she pushes the buttons.

The light source and the FPGA are stacked on the computer workstation which is placed on the rolling floor stand of the colposcope by means of four 3D-printed supports, as shown in Figure 4.3c.

To further improve the usability of the system, a push button was attached to the right handle of the colposcope head as shown in Figure 4.3d. The switch is connected to the FPGA and the practitioner can use it to trigger the start and the end of a color video recording during an examination. A foot switch also connected to the FPGA is placed on the floor. It is used to trigger the acquisition of Mueller polarimetric images for all wavelengths of interest. These two new features allow the user to acquire the video and the images while observing the cervix through the binocular system of the colposcope. The video recording is automatically blocked during the entire polarimetric image acquisition process activated by the operator using the foot pedal. At the end of the polarimetric image acquisition process the video recording is automatically restarted. The operator can block the video recording definitively by touching the push button on the colposcope head for the second time.

4.1.2 Calibration stage

For the calibration of the novel MPC, we used the eigenvalue calibration method (ECM) described in detail in Chapter 1. As a reminder, the ECM consists of acquiring the 16-component intensity matrix B consecutively for three optical reference elements, namely a first polarizer whose transmission axis is oriented at 0° to the laboratory reference (P0), a second polarizer whose transmission axis is oriented at 90° to the first polarizer (P90), and a waveplate whose fast axis is oriented at 30° to the first polarizer (L30).

To calibrate the MPC in reflection configuration, we always used a sandblasted aluminum plate able to scatter the light after reflection without changing its polarization. In addition, a spectralon [111], [112], providing an ideal spectral reflectance, is used for the estimation of the effective light intensity illuminating the cervix to be analyzed as well as for the color balance.

Both reflectors have to be installed so that they can always be placed in the same position with respect to the incident beam. Indeed, a significant variation in the positioning of the sandblasted aluminum plate and the spectralon can significantly affect the reproducibility of the calibration and lead to an inaccurate estimation of the incident light intensity, respectively.

To ensure the correct positioning of the sandblasted aluminum plate and the spectralon, a mechanical system such as the one shown in Figure 4.4 has been designed. Both reflectors are placed opposite each other and locked inside a 3D printed plastic mechanical support that can rotate 360° inside a second support attached to the extremity of the same metal bar to which the arms used for the keyboard and touch screen are also attached, as shown in Figure 4.4. With this system, the operator can easily change the sandblasted metallic plate with the spectralon. In addition, he/she can place the colposcope head always in approximately the same position with respect the two-reflector system, at a distance of about 30 cm corresponding to the distance between the colposcope head and the cervix. Finally, the two reflectors can be easily interchanged without any movement of the colposcope head.

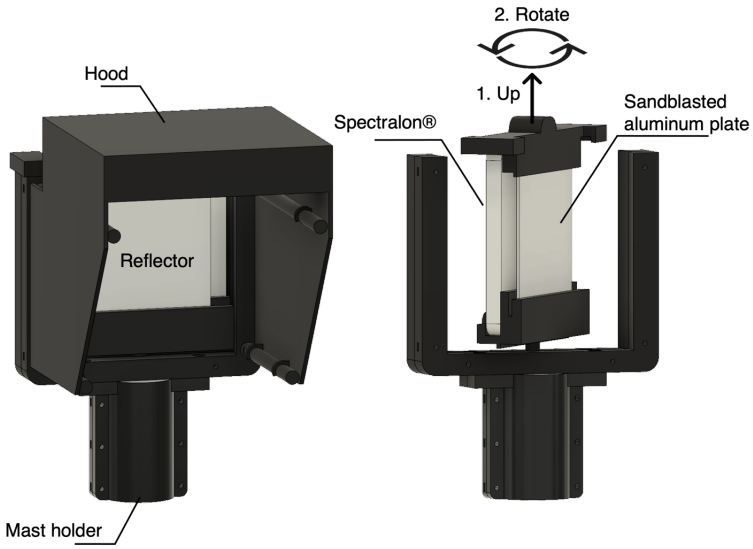

Figure 4.4 The concept of the calibration stage. The reference reflectors, a spectralon and sandblasted metal plate, are vertically placed on the mast holder. The mast holder is connected to the colposcope stand. The hood functions to block ambient light (left). The 2 reference reflectors can be exchanged by rotation (right).

This procedure greatly increases the repeatability of the calibration and measurement of the total reflected light intensity. Finally, a 3D printed black plastic cover surrounds the mechanical system containing the two reflectors to effectively block ambient light during the calibration stage.

The final appearance of the new MPC in a typical gynecologic and obstetric consultation room is shown in Figure 4.5. This image illustrates the actual scale and layout of the usual clinical environment for colposcopic examination, which is usually performed on a gynecology chair. Because the new MPC is a stand-alone mobile system, the user can perform a polarimetric examination on her/his own.

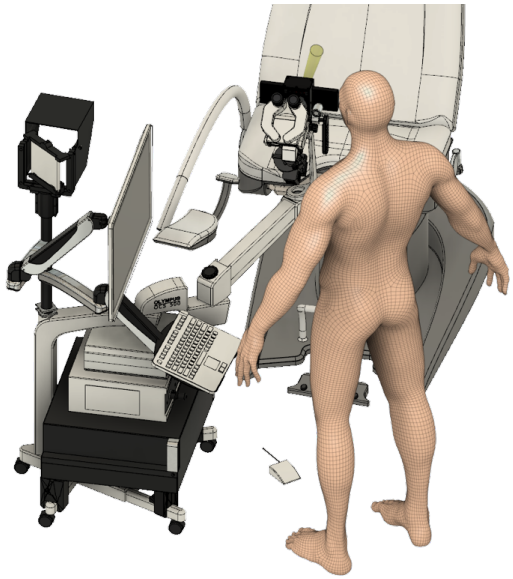

Figure 4.5 The simulated geometry of a gynecological examination with the MPC. (The source of the 3D model of the gynecological chair: https://grabcad.com/library/gynaecological-examination-chair-1, human: https://free3d.com/3d-model/male-base-mesh-6682.html.

4.2 Performance assessment

4.2.1 Estimation of the MPC irradiance

The modifications to the lighting system described in Chapter 3 made it possible to significantly increase the amount of light delivered to the cervix to be examined in vivo compared to the former prototype, thereby improving the signal-to-noise ratio and the quality of the measurements. However, we found that the lighting produced by the improved illumination system was very intense. For this reason, we first verified that this increase in lighting power did not represent any danger to patients or practitioners. The energy transfer from a light source to a sample is estimated in terms of irradiance, which is the light power (number of photons per second striking the surface of interest) per unit of illuminated area. The aim is to estimate the actual irradiance at the surface of the cervical surface. The size of the beam illuminating the target depends on the distance between the target and the colposcope head. Accordingly, the irradiance also varies with this distance. Therefore, it was measured in the same conditions as during the colposcopic examination where the cervix is approximately 30 centimeters away from the colposcope head, as shown in Figure 4.6.

More precisely, as the lighting is spatially non-uniform over the illuminated area, the maximum light power was measured at the center of the beam using a broadband power meter (Melles-Griot 13PEM001) with a photosensitive surface of approximately 0.8 mm^2.

In the first step, the total white light irradiance was measured by considering as illumination surface that of the detector. Then, the spectral irradiance was also measured using 5 different bandpass filters placed in front of the detector, able to select different spectral regions between 450 nm and 750 nm close to those chosen for the MPC. The bandwidth of each selected spectral region is 40 nm. The results are charted in Table 4.1. The irradiance was reasonably assumed to be uniform over the sensor surface. In addition, for each spectral region considered, the measured irradiance was normalized by the transmittance of the spectral filter used.

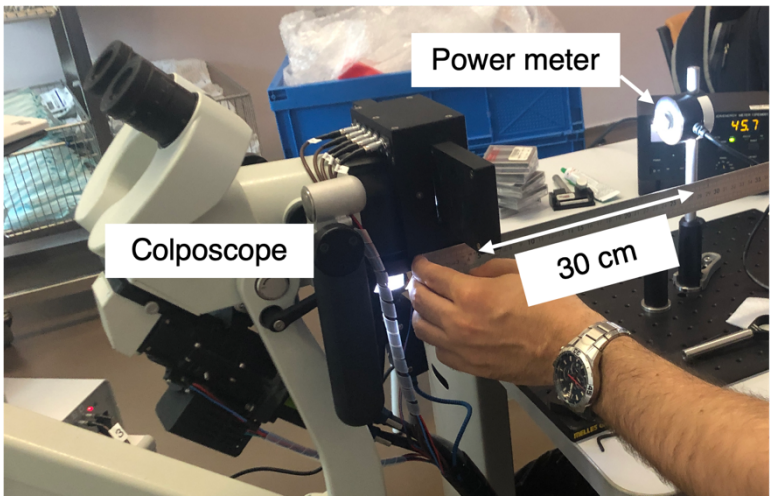

Figure 4.6 The experimental configuration for irradiance assessment.

Table 4.1 The irradiance of the illumination system measured at the center of the beam in a working distance of 30 centimeters.

	White	450nm	500nm	550nm	600nm	650nm	700nm
Irradiance (mW/cm^2)	71.68	5.88	11.28	10.55	7.82	10.00	7.09

Since the light source does not produce harmful frequencies (UV-A/B and IR-A/B/C) and the total measured white light irradiance is well below 1 W/cm^2[113], the MPC illumination is not hazardous to the skin or cervical mucosa although it may cause a slight heating sensation.

The eye, on the other hand, is much more vulnerable to light damage, even in the visible spectral range [113]. However, the light can never reach the baby's eyes because it is blocked by the cervix, which operates as a real barrier. In addition, every precaution has been taken to avoid sending light directly into the eyes of patients or practitioners during and after data acquisition.

4.2.2 Resolution & aberrations

Estimating the resolving power of the MPC is crucial in determining the limit of observable details in the image produced by this system. As mentioned in Chapter 3, the used 3-CMOS camera is characterized by a resolution of 2064 × 1544 pixels for each sensor and it is limited to 26 FPS at full-resolution. However, it is possible to increase the number of FPS by decreasing the size of the region of interest (ROI). The selected objective lens produces an image of the cervix well suited to a ROI of 1120 × 1120 pixels that provides 64 FPS as explained in Chapter 3.

Specifically, the actual image size for the selected square ROI is 3.8 centimeters, which corresponds to a nominal optical resolution of 34 microns/pixel, significantly higher than the imaging system used for the previous two-wavelength MPC prototype characterized by a nominal resolution of 75 microns/pixel.

However, the effective resolution of the MPC can be very different from the nominal resolution because it strongly depends on the conjugation of the 3-CMOS camera objective lens with the intrinsic colposcope optics. The effective resolution of the MPC was always measured by the slanted edge method. This method is explained in detail in Appendix (Cahpter 6.5). In particular, it is determined not only at the center of the field of view but also in peripheral regions in order to verify the spatial uniformity of the MPC's resolving power over the entire ROI selected.

More precisely, the MPC's resolution is measured in three different locations of the selected ROI, the center, the inner boundary, and the outer boundary (indicated by 1, 2, and 3, respectively, in Figure 4.7a of the effective circular area whose diameter corresponds approximately to the typical size of the cervix (about Ø3 centimeters). To do this, the slanted-edge target in Figure 4.7b has been moved in the image plane to assess the resolution in the three different locations. This approach enabled to evaluate the stigmatism of the optical

system (intrinsic optics of colposcope coupled to the 3-CMOS camera objective lens) used to reconstruct the image of the cervix inside the selected ROI for each wavelength range of interest. The resolution at the center (area 1) is reassessed using the USAF 1951 target in Figure 4.7c as a cross-validation.

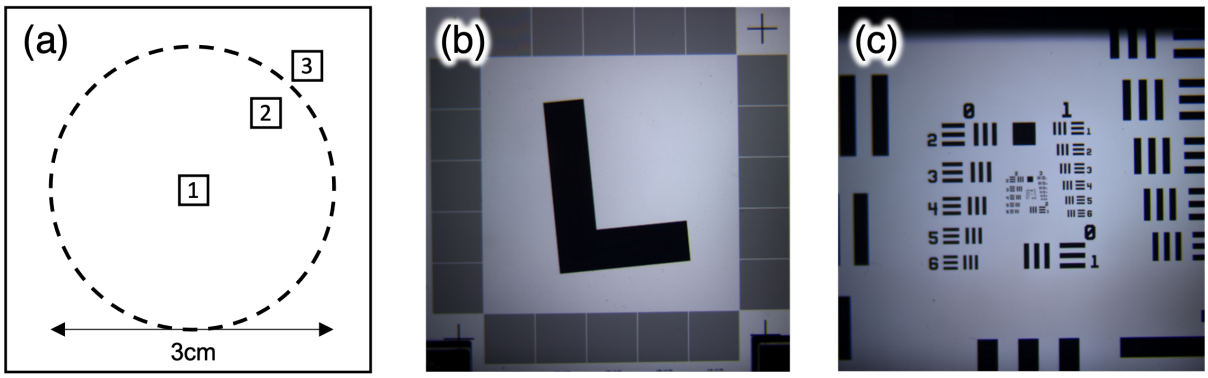

Figure 4.7(a) The selected areas for resolution measurements. (b) The image of the slanted edge target acquired by the MPC. (c) The image of the USAF1951 target acquired by the MPC.

The MTF curve at the center of the ROI, obtained using the slanted edge method, is shown in Figure 4.8. The black dashed line (i) represents the resolution of the 3-CMOS camera at 530 nm that we showed in Chapter 3. The colored solid lines (ii) represent the resolution of the 3-CMOS camera combined with the optics of the colposcope at 5 wavelengths of interest. The black dotted line (iii) represents the resolution of the monochromatic camera GT1920 (used for the former dual-wavelength MPC prototype) coupled to the colposcope at 550 nm.

The most noticeable difference from Figure 3.16b is that the coupling of the 3-CMOS camera objective lens to the colposcope optics is not optimal and degrades the system resolution for all wavelengths. In particular, this degradation is higher at 460 nm and 700 nm. However, the resolution of the new multispectral MPC (using the 3-CMOS camera) at 530 nm, 630 nm, and 650 nm is significantly higher than the resolution of the former dual-wavelength MPC. For 460 nm and 700 nm, the resolution of the multispectral MPC degrades and becomes comparable to that of the dual-wavelength MPC.

Being the 3-CMOS camera objective lens completely achromatic, as shown in Chapter 3, we attributed the chromatic aberration observed for the MPC to the intrinsic optics of OCS-500 colposcope. This optics is unmodifiable and irreplaceable unless the colposcope is entirely redesigned, which is not the objective of this study. For this reason, the chromatic aberrations of the MPC remain out of hand.

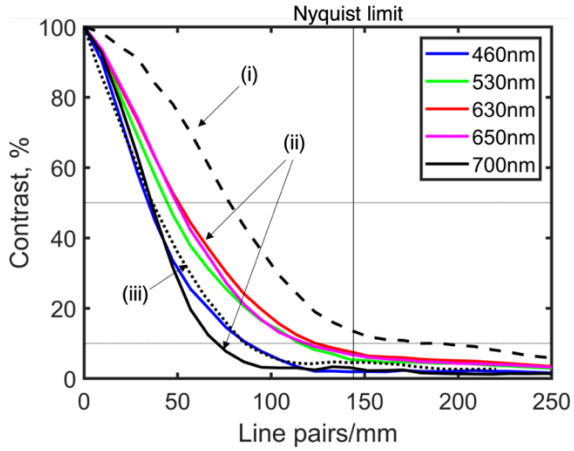

Figure 4.8 The MTF curve measured at the center (marked by 1). (i) the resolution of the 3-CMOS camera without the colposcope (black dashed line). (ii) the resolution of the 3-CMOS camera combined with the colposcope (colored solid lines) in 5 wavelengths of interest (see the legend). (iii) The resolution of GT1920 with the colposcope (black dotted line). The horizontal lines denote MTF50 and MTF10. The vertical line denotes the Nyquist limit of the sensor.

The resolution values measured by the slanted-edge method in the three regions of interest are resumed in Table 4.2. At points 1 and 2, the resolution at 530 nm, 630nm and 650 nm does not change too much compared to the nominal resolution considering a contrast of 10%. Indeed, we obtained a resolution on average 1.3 times lower than the nominal one. On the contrary, the measured resolution degrades much more at 460 nm and 700 nm, for which it is on average 2.4 times lower than the nominal resolution. At point 3, the resolution is essentially the same as at points 1 and 2 at 630 nm and 650 nm. On the other hand, the resolution degrades a little more at 460 nm where it reaches a value 1.8 times lower than the nominal value. Moreover, a degradation of the resolution is also observed at 460 nm and 700 nm where it becomes about 1.8 times lower than the nominal value. This degradation remains lower than that observed at points 1 and 2 for the same wavelengths. For a contrast of 50%, the resolution follows the same trend as that described for 10%. However, the resolution obtained for 50% contrast is degraded by a factor of about 2 compared to that obtained for 10% for all wavelength ranges considered and for the three locations analyzed.

Table 4.2 The object plane resolution at the 3 spots at 5 wavelengths. The pixel unit is converted by the object side length (pixel pitch=3.8 cm/1120 pixels=34μm).

(Unit: μm)

	Contrast	460nm	530nm	630nm	650nm	700nm
1	10%	71.291	40.734	39.94	44.019	76.793
	50%	129.72	74.574	73.203	80.799	143.04
2	10%	80.89	43.13	44.47	49.28	79.11
	50%	151.64	78.78	81.57	90.33	148.04
3	10%	62.511	60.794	47.92	49.436	65.297
	50%	116.56	113.24	88.173	90.916	121.43

Overall, the new multispectral MPC has a higher resolution than the previous prototype. The resolution measured by the USAF1951 target is charted in the Appendix (Chapter 6.6).

4.3 Precision in polarimetric measurements

Estimating the correctness of a polarimetric measurement is crucial to verify its reliability. Measurement correctness is defined by two terms, namely the accuracy and precision. Accuracy refers to the deviation from the true value and precision refers to the arbitrary fluctuations in the measured value. However, estimating the accuracy of a polarimetric measurement is not straightforward due to the lack of reference samples whose Mueller matrix is known precisely, especially in the case of depolarizing samples. Therefore, we focused exclusively on precision estimation of the MPC in measuring Mueller matrices.

4.3.1 Sampling on an ex-vivo cervix

In the end, we only evaluated the precision of the MPC measurements by experimentally estimating the standard deviation of a set of repeated polarimetric measurements performed under “identical” conditions. These measurements were performed on a formalin-fixed cervix specimen instead of using conventional optical components with well-known polarimetric properties (polarizers, waveplates, etc.) as is usually done for this type of characterization.

Indeed, the polarimetric response of the cervix is quite complex and different from that obtained with simpler optical components. All polarimetric effects are "entangled" in this type of sample, and the accuracy in determining one particular polarimetric parameter can be strongly affected by the value of the others, as will be explained in more detail later in the text. Therefore, using a piece o*f ex vivo* cervix, we were able to estimate the performance of the MPC under real measurement conditions.

Although this sample was analyzed *ex vivo* and in a fixed state (without blood perfusion), the characterization of the experimental errors in the measurement of its polarimetric properties allowed us to identify the main possible error sources that could be encountered in vivo on the same type of tissue. Such a sample is characterized by a strong spatial inhomogeneity for the absorption, as well as for its polarimetric properties. Thus, we were able to characterize the influence of the illumination level on the accuracy of the MPC in measuring Mueller matrices. Moreover, we evaluated the numerical errors derived from the Lu-Chipman decomposition on the determination of the main polarimetric properties of the explored tissue (in particular the depolarization and the linear birefringence) [114].

To do so, the specimen was held vertically on a lens holder and imaged at a working distance of 30 centimeters from the head of the MPC as shown in Figure 4.9. As explained earlier, by selecting a ROI of 1120×1120 pixels, the 3-CMOS camera works at 64 FPS. In this way, it is possible to acquire and average 4 times per second the 16-component intensity matrix $\boldsymbol{B} = \boldsymbol{AMW}$. The exposure time was optimized separately for each selected wavelength range using the cervical specimen as a target to maximize the signal-to-noise ratio by always operating the 3-CMOS camera at the acquisition rate of 64 FPS.

The measurement procedure was repeated 32 consecutive times. Specifically, the 16-component intensity matrix $\boldsymbol{B}$ was acquired 128 times (4 times/second × 32) for a total duration of 32 seconds. The $\boldsymbol{B}$ matrix was averaged in groups of 4 to obtain 32 times the Mueller matrix of the sample given by $\boldsymbol{M} = \boldsymbol{A}^{-1}\boldsymbol{B}\boldsymbol{W}^{-1}$ as given by equation (1-35) in Chapter 1.

All formalin residues were gently removed with a paper, and the specimen was heated for 30 minutes by light to reach a thermal equilibrium condition before starting the measurement procedure. For this reason, it is reasonable to assume that the sample did not undergo significant changes during the entire measurement duration and that the differences observed between the 32 obtained Mueller matrices are mainly due to statistical fluctuations in the measurement system.

For the statistical analysis, 10 000 pixels were randomly selected from the obtained cervical images. Figure 4.9a shows the experimental setup mounted for these measurements. Figure 4.9b-e show the unpolarized intensity image (the M_{11} coefficient of the measured Mueller matrix), the linear phase retardance, the depolarization, and the slow axis azimuth of the linear phase retardance, respectively, obtained for the Mueller matrix of cervical sample after application of the Lu-Chipman decomposition.

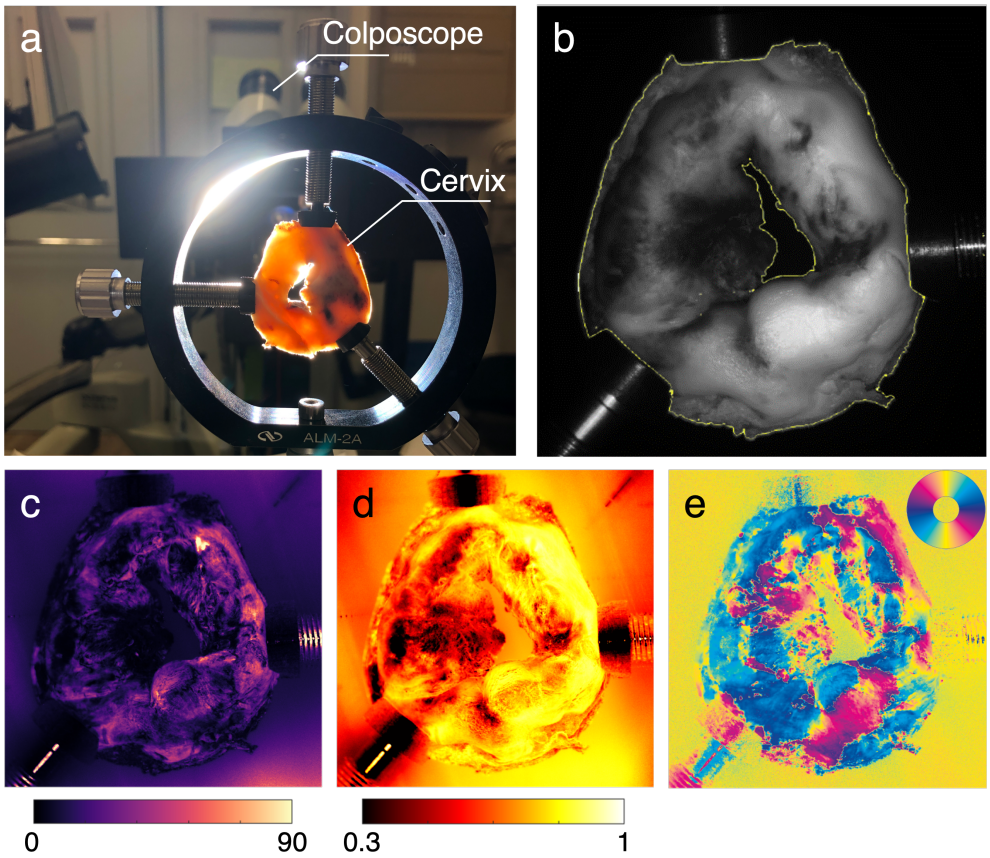

Figure 4.9 The experimental configuration of the precision estimation. (a) The MPC acquired the ex-vivo cervix sample at 30 cm of working distance with zoom ×1. (b) The acquired intensity image. The yellow contour represents the cervical area where 10,000 pixels were sampled. (c) the retardance *R* image, (d) the depolarization *Δ* image, (e) the azimuth *α* image of the sample at 530 nm.

4.3.2 Precision in the acquisition of the Mueller matrix

In this section, we will estimate the precision in Mueller matrix measurement, in terms of standard deviation of each element of the Mueller matrix. The Mueller matrix of a sample is given by $\boldsymbol{M} = \boldsymbol{A^{-1}BW^{-1}}$, which is a linear transformation of $\boldsymbol{B}$. It is possible to demonstrate (see Appendix 6.7) that the standard deviation $\sigma_{M_{ij}}$ of each component (i,j) of the Muller matrix $(i,j = 1,\ldots,4)$ over 32 repeated measurements is given by:

$$\sigma_{M_{ij}} = \frac{b_{ij}}{\sqrt{\mu_{M_{11}}}} + c_{ij} \tag{4-1}$$

where $\mu(M_{11})$ is the average value of the unpolarized intensity image (over the set of 32 repeated measurements), c_{ij} is the asymptotic value of $\sigma_{M_{ij}}$ obtained for high values of $\mu_{M_{11}}$ and b_{ij} is a parameter strictly related to the degree of uncertainty. Indeed, the higher the coefficient b_{ij}, the greater is the uncertainty. The expression (4-1) is valid for each pixel of the image.

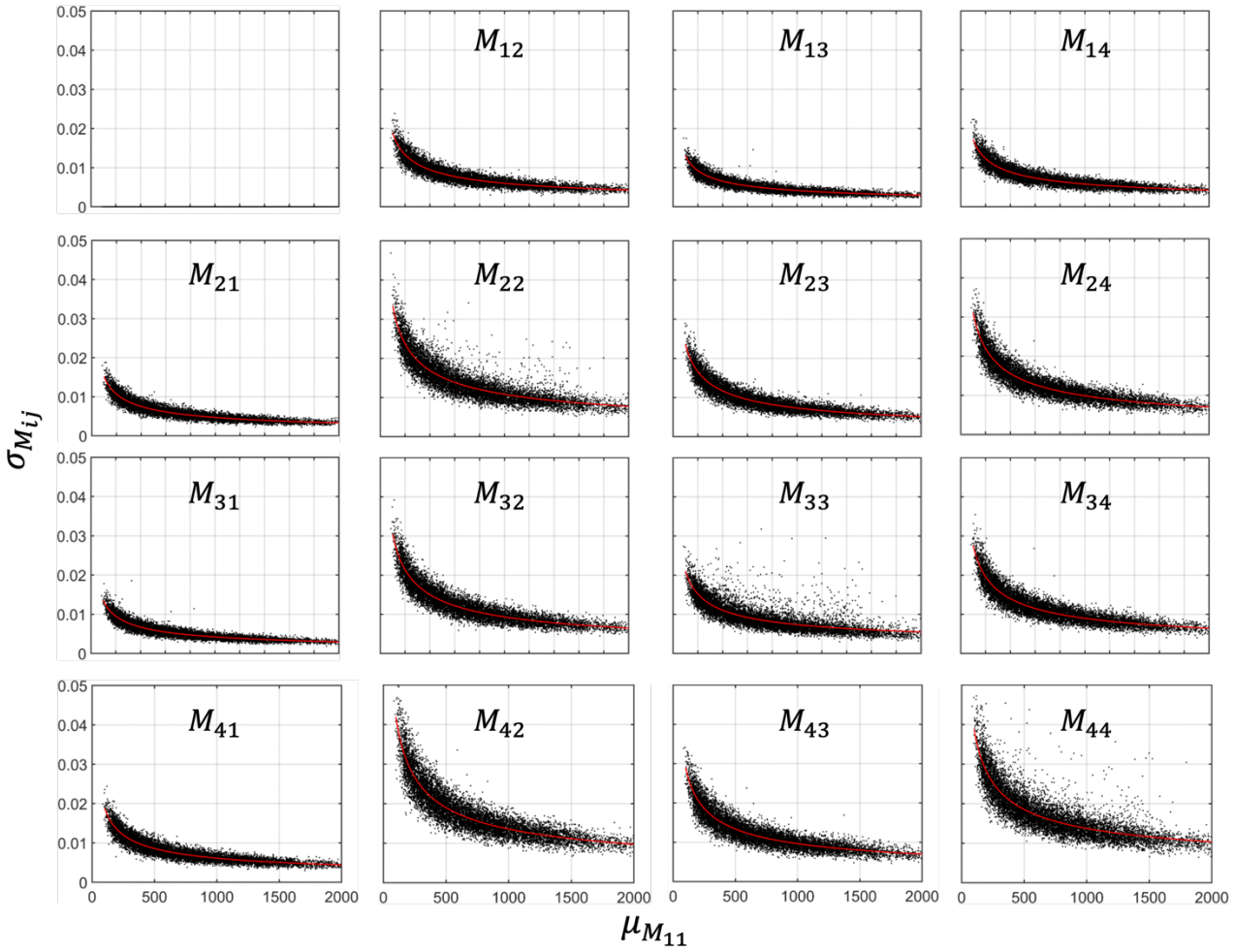

Figure 4.10 The unpolaried light intensity $\mu_{M_{11}}$ vs standard deviation of 16 elements of the Mueller matrices at 530 nm. The standard deviation increases when the intensity is low because of the shot noise. The red lines denote the non-linear model (4-1).

Figure 4.10 shows the curve of $\sigma_{M_{ij}}$ at 530 nm as a function of $\mu_{M_{11}}$ for 10,000 randomly selected pixels. The experimental curve for each component of the Mueller matrix

is well fitted by the equation (4-1). This result shows that $\sigma_{M_{ij}}$ decreases with increasing $\mu_{M_{11}}$. In other words, the uncertainty in the determination of each component of the Mueller matrix decreases with increasing detected light intensity.

The asymptotic value of $\sigma_{M_{ij}}$, given by c_{ij}, is near to zero, and the coefficient b_{ij} at 5 wavelengths is charted in Table 4.3. This table shows that the uncertainty in the determination of Mueller matrix components depends on the wavelength. In particular, we observed that this uncertainty is minimal at the 530 nm wavelength for which the values of $\kappa^{-1}(\mathbf{W})$ and $\kappa^{-1}(\mathbf{A})$ are maximized.

We found that, under the chosen condition of 4 acquisitions and averages of the $\boldsymbol{B}$ matrix from which we calculated the Mueller matrix $\boldsymbol{M}$, as explained before, the uncertainty in the determination of the different components of the measured Mueller matrix strongly increases in the zones of the cervix where the intensity of the light is less than 250 ADUs for all wavelengths. Above this threshold intensity the uncertainty is less than 0.01. This threshold has been determined in the condition where the intensity matrix $\boldsymbol{B}$ is acquired and averaged 4 times in 1 second, which is the condition used for in vivo measurements. For this reason, the intensity threshold that we determined (250 ADUs) has been used to eliminate the pixels with too little illumination in the post-treatment of the measured Mueller matrices.

Table 4.3 The coefficient *b* of the 16 elements of the Mueller matrix at 5 wavelengths.

Row \ Column		1	2	3	4
1	460nm		0.169	0.160	0.171
	530nm		0.187	0.130	0.167
	630nm		0.213	0.148	0.178
	650nm		0.228	0.164	0.184
	700nm		0.281	0.214	0.217
2	460nm	0.127	0.271	0.257	0.273
	530nm	0.153	0.331	0.238	0.310
	630nm	0.189	0.427	0.304	0.360
	650nm	0.203	0.456	0.346	0.378
	700nm	0.254	0.540	0.418	0.421
3	460nm	0.150	0.320	0.311	0.313
	530nm	0.136	0.309	0.201	0.273
	630nm	0.175	0.414	0.294	0.330
	650nm	0.190	0.445	0.336	0.355
	700nm	0.258	0.557	0.447	0.431
4	460nm	0.178	0.391	0.355	0.413
	530nm	0.186	0.415	0.284	0.366
	630nm	0.197	0.443	0.301	0.369
	650nm	0.200	0.455	0.327	0.374
	700nm	0.236	0.502	0.391	0.411

4.3.3 Precision in decomposition of the Mueller matrix

For the analysis of cervical tissue, we used the polarimetric parameters derived from measured Mueller matrix by using the Lu-Chipman decomposition. The most relevant polarimetric parameters for the cervix are the depolarization Δ, the linear phase retardance R, and the azimuth α of the slow axis of the linear phase retardance defined by the equations (1-22) and (1-23) respectively, in Chapter 1.

The precision in measuring the Mueller matrix of the fixed-state cervical specimen represents the first performance indicator of the MPC and it also impacts the precision in determining the main polarimetric parameters derived from the Lu-Chipman decomposition. However, the precision in determining these parameters can also be strongly affected by numerical errors.

Indeed, Lu-Chipman decomposition is a fairly complex algebraic procedure that uses the singular value decomposition to factorize the measured Mueller matrix into a canonical form. In particular, this procedure allows the measured Mueller matrix to be written as a product of three matrices, including the matrix of a depolarizer $\boldsymbol{M}_{\Delta}$, the matrix of a retarder $\boldsymbol{M}_{\mathrm{R}}$, and the matrix of a dichroic element $\boldsymbol{M}_{\mathrm{D}}$, as explained more in detail in Chapter 1. In addition, arithmetic calculations between the different components of the obtained matrices as well as the use of trigonometric formulas, are required to obtain the most relevant polarimetric parameters for the cervical tissue, including Δ, R and α. Therefore, extracting these parameters from the measured Mueller matrix is a multi-step computational process that can introduce significant numerical errors.

The magnitude of these numerical errors depends on the quality of the initial measurement but also on the polarimetric properties of the sample. To assess the accuracy in determining these parameters, each of the 32 Mueller matrices obtained for the fixed cervix sample, according to the procedure described in the previous section, was decomposed using Lu-Chipman decomposition. From the decomposed matrices, we calculated the Δ, R and α parameters. For each parameter, the standard deviation was calculated at the single pixel level over the 32 images obtained for the 10,000 selected pixels.

The standard deviations thus determined are indicated as σ_{Δ}, σ_{R}, and σ_{α}, for Δ, R and α, and the means are indicated as μ_{Δ}, μ_{R}, and μ_{α}, for Δ, R and α, respectively.

Linear phase retardance

First, we investigated the variation of σ_R as a function of μ_{Δ} and $\mu_{M_{11}}$ coefficient, as shown in Figure 4.11. The general trend observed is that σ_R increases with μ_{Δ} for all wavelengths of interest, as shown in Figure 4.11a-e. Therefore, the precision in determining R decreases with increasing μ_{Δ}. In addition, the depolarizing ability of the sample increases overall with increasing wavelength. For this reason, for wavelengths in the red part of the visible spectrum, especially at 650 nm and 700 nm, the measurement of R becomes relatively imprecise, whereas it is much more precise at 460 nm and 530 nm.

In particular, for the wavelengths at 630 nm, 650 nm, and 700 nm, it is possible to empirically set a threshold for μ_{Δ} around 0.85 below which σ_R mostly remains smaller than

3°. This threshold is around 0.8 at 530 nm. In this case σ_R is smaller than 3° for the majority of the pixels. On the contrary, σ_R is greater than 3° for almost all pixels and tends to reach very high values (of the order of 20 degrees) at 700 nm. The trend observed at 530nm was similarly found at 460 nm but with a slightly lower threshold around 0.7.

Moreover, σ_R varies very slightly with $\mu_{M_{11}}$ as shown in Figure 4.11f-j. It seems that σ_R increases when $\mu_{M_{11}}$ becomes very low while always remaining smaller than 5°. The cyan dots correspond to the pixels with depolarization above the threshold discussed before. For these points, one can find that σ_R is greater than 5° and reaches very high values especially at 700 nm. These points are rather randomly distributed and do not seem to correlate with $\mu_{M_{11}}$.

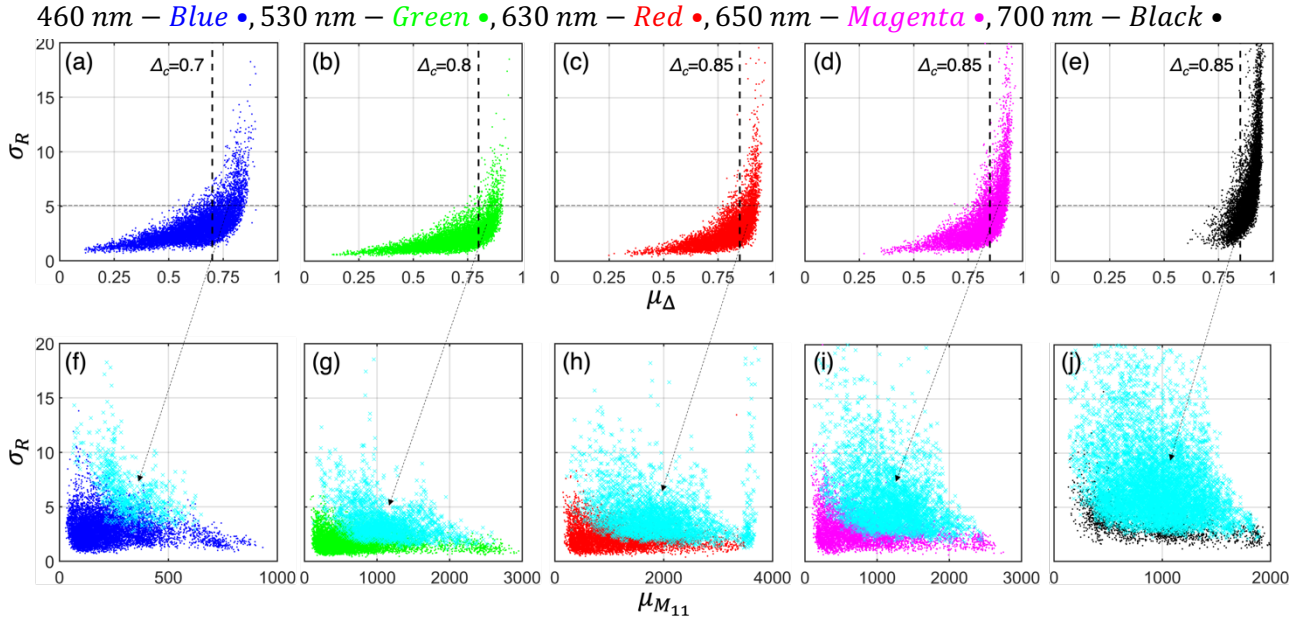

Figure 4.11 (a)-(e) The standard deviation of retardance σ_R in a function of depolarization Δ. The vertical dotted lines indicate the depolarization thresholds Δ_C (criteria.) μ denotes the mean among the 32 acquisitions. (f)-(j) σ_R in a function of light intensity M_{11}. The cyan dots correspond to the pixels over Δ_C.

These preliminary results show that σ_R strongly depends on the depolarization degree of the target. The illumination level also seems to affect σ_R but more weakly than the depolarization. Indeed, an increase in σ_R (whose value remains below 3°) as a function of the illumination variation can be observed for very low values of light intensity at all wavelengths of interest. However, our observation revealed that errors in the R measurement are predominantly affected by depolarization.

The Mueller matrix $\boldsymbol{M}_R$ of the linear phase retardance is obtained by the Lu-Chipman decomposition using the singular value decomposition of the 3×3 submatrix $\boldsymbol{m}'$ of $\boldsymbol{M}=\boldsymbol{M}_\Delta\boldsymbol{M}_R$, as explained in equation (1-66) in Chapter 1. For this reason, the precision in the measurement of R is expected to be related to the numerical stability of $\boldsymbol{m}'$ which can be described by the inverse of the condition number $\kappa^{-1}(\boldsymbol{m}')$. The numerical stability decreases with $\kappa^{-1}(\boldsymbol{m}')$ that varies between 0 and 1. We observed that $\kappa^{-1}(\boldsymbol{m}')$ decreases with the increase of the depolarization for all wavelengths of interest, as shown in Figure 4.12a-e.

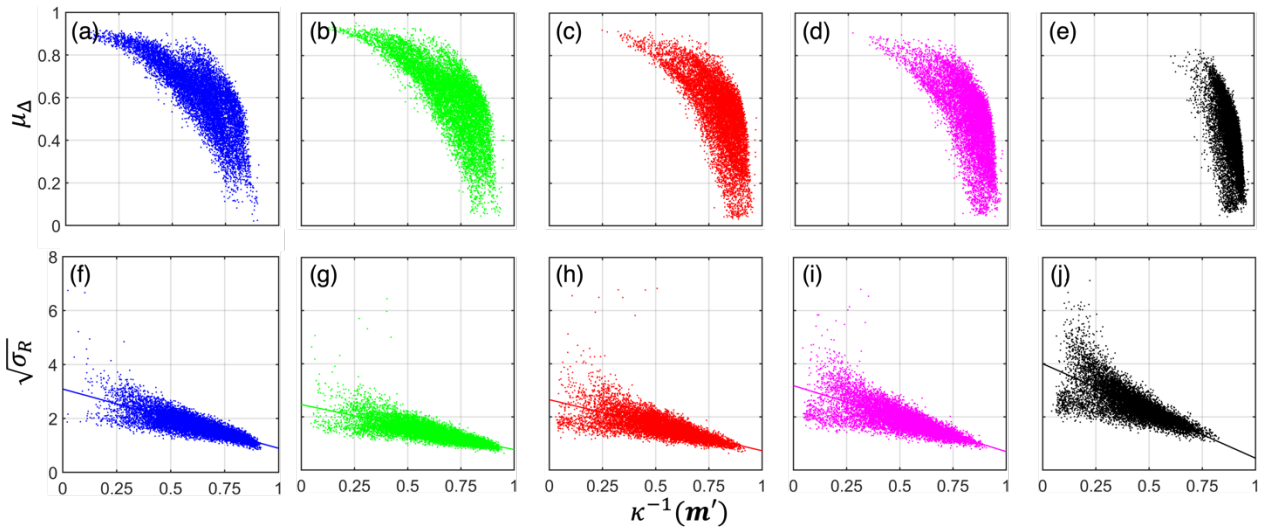

Figure 4.12(a)-(e) The mean depolarization μ_Δ in a function of the reciprocal condition number $\kappa^{-1}(m')$ of m'. Depolarization is inversely proportional to the condition number. (f)-(j) The square root of σ_R in a function of $\kappa^{-1}(m')$. $\sqrt{\sigma_R}$ has a linear correlation to $\kappa^{-1}(m')$.

An empirical analysis showed that $\sqrt{\sigma_R}$ is linearly correlated to $\kappa^{-1}(\boldsymbol{m}')$ by the following expression:

$$\sqrt{\sigma_R} = -b \times \kappa^{-1}(\boldsymbol{m}') + c \qquad (4\text{-}2)$$

Indeed, $\sqrt{\sigma_R}$ decreases linearly as a function of $\kappa^{-1}(\boldsymbol{m}')$ for all wavelengths of interest, as shown in Figure 4.12. This analytical curve is very useful for determining the precision of the MPC in measuring the linear phase retardance for all wavelengths of interest. The coefficient b and c are charted in Table 4.4 for all wavelengths. The absolute value of the slope increases with wavelength in 530 nm ~ 700 nm range, showing that the measurement of R becomes less precise because of a significant increase of depolarization.

Table 4.4 The coefficients b and c of the linear model (4-2). A higher slope denotes more vulnerable.

	460 nm	530 nm	630 nm	650 nm	700 nm
b	2.19	1.70	1.94	2.50	3.59
c	3.08	2.47	2.66	3.19	4.02

Azimuth of linear phase retardance

The parameter σ_α strongly depends on the value of α and R. Figure 4.13a shows σ_α as a function of μ_R and Figure 4.13b shows σ_α as a function of μ_α. We can distinguish three different zones.

The Zone 1 corresponds to the pixels for which $\mu_R > \tilde{R} = 6° \pm 2°$. In this case σ_α doesn't depend on μ_α and μ_R for all wavelengths considered, as shown in Figure 4.13a and b.

The Zone 2 corresponds to $\mu_R < \tilde{R} = 6° \pm 2°$. In this case σ_α can be very high and vary randomly, which denotes strong uncertainty in the measurement of α, as shown in Figure 4.13a and 4.12b. This is essentially due to the procedure for calculating α using equation (1-23), as discussed in Chapter 1.

The Zone 3 corresponds to $\mu_R > \tilde{R} = 6° \pm 2°$ and $\alpha \approx 0°$. In this case, σ_α can vary significantly assuming discrete values. For these angles, the calculation of α using the equation (1-23) becomes unstable, as discussed in Chapter 1.

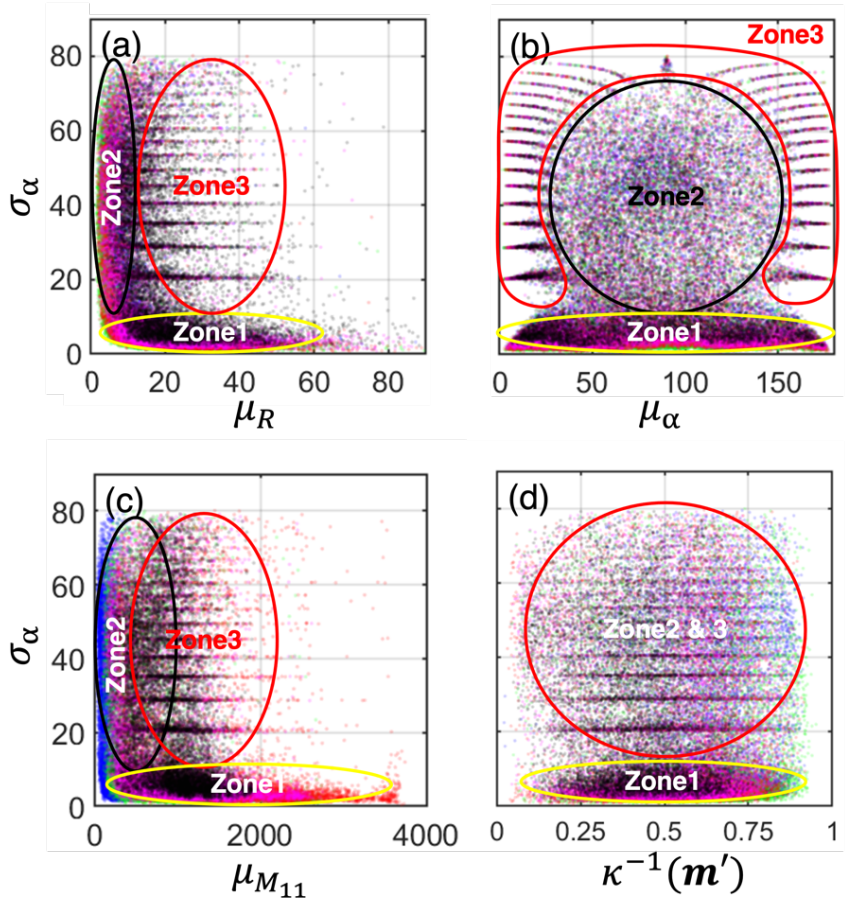

Figure 4.13 (a) The relation between R and σ_α. The uncertainty drastically increases when retardance is less than 10°. (b) The relation between α and σ_α. discrete σ_α observed in the peripheric zone (Zone3). It is attributed to arbitrary sign of $M_{R,24}$ and $M_{R,34}$. (c) The relation between M_{11} and σ_α. The uncertainty seems to drastically increase in low intensity below 500. (d) The relation between the condition number of m' and σ_α. No significant relation is found.

Figure 4.13c shows σ_α as a function of $\mu_{M_{11}}$ coefficient. For $\mu_R > \tilde{R} = 6° \pm 2°$, the measurement of α weakly depends on the light intensity value. This means that α can be accurately measured also for low light intensity. Finally, Figure 4.13d shows σ_α as a function of $\kappa^{-1}(\boldsymbol{m}')$. Also in this case, σ_α doesn't depends on $\kappa^{-1}(\boldsymbol{m}')$ if $\mu_R > \tilde{R} = 6° \pm 2°$. The calculation of α seems to be not unaffected by the depolarization.

Depolarization

The uncertainty in depolarization measurement σ_Δ is not affected by $\kappa^{-1}(\boldsymbol{m}')$, as shown in Figure 4.14a-e. However, σ_Δ decreases with decreasing $\mu_{M_{11}}$ for all wavelengths, as shown in Figure 4.14f-j.

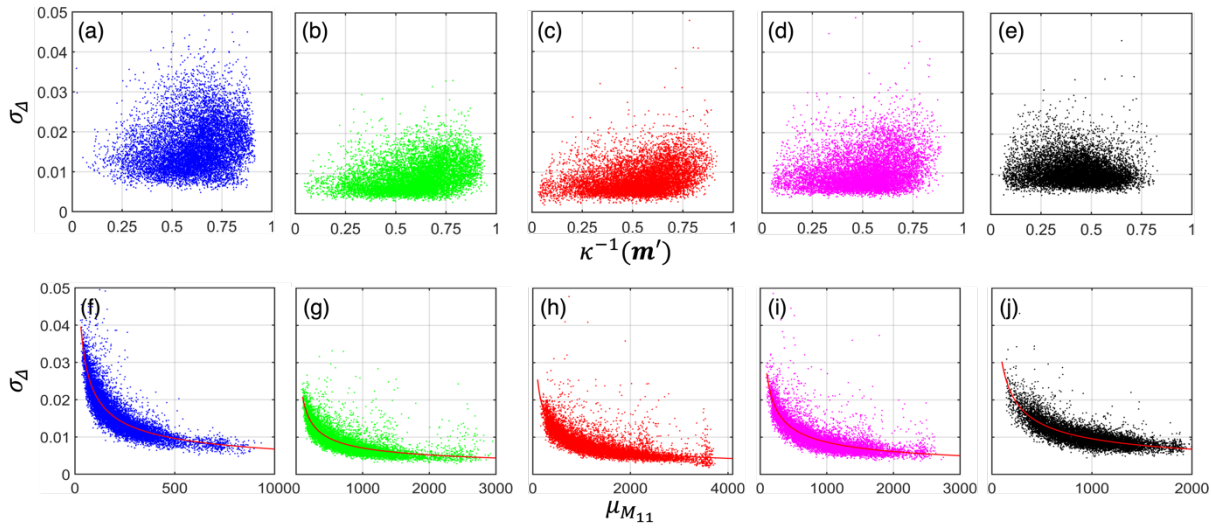

Figure 4.14 (a-e) the condition number of m' is not related to the standard deviation of depolarization σ_Δ. (f-j) σ_Δ is a function of intensity $\mu_{M_{11}}$. σ_Δ can be fitted by the nonlinear model (4-1).

The SNR determines the stability of the depolarization measurements. Then, σ_Δ can be empirically modeled using an equation similar to the equation (4-1) which can be rewritten as:

$$\sigma_\Delta = \frac{b}{\sqrt{\mu_{M_{11}}}} + c \tag{4-3}$$

The coefficients b and c from the non-linear model are charted in Table 4.5 for all wavelengths of interest.

Table 4.5 The vulnerability coefficient *b* for depolarization. The intercept *c* is nearly 0.

	460 nm	530 nm	630 nm	650 nm	700 nm
b	0.218	0.201	0.252	0.270	0.303
c	-1.2×10^{-4}	7.4×10^{-4}	3.3×10^{-4}	9.5×10^{-5}	-8.9×10^{-6}

Overall, the precision of the polarimetric measurement using the MPC is charted in Table 4.6. The table represents the mean value of standard deviations of each parameter grouped by several criteria.

Table 4.6 The mean standard deviations of three polarimetric parameters, R, α, and Δ.

		460 nm	530 nm	630 nm	650 nm	700 nm
	Δ_C	0.7	0.8	0.85	0.85	0.85
σ_R	$\mu_\Delta < \Delta_C$	2.2	1.8	2.1	2.7	3.4
	$\mu_\Delta > \Delta_C$	4.1	3.6	4.3	5.7	7.4
σ_α	$\mu_R > 10°$ $\alpha \neq 0°$	4.9	3.2	3.7	4.9	7.0
	$\mu_R > 10°$ $\alpha \approx 0°$	40.0	43.7	43.7	41.3	37.3
	$\mu_R < 10°$	35.1	27.6	28.7	32.9	37.3
	I_C	250	500	500	500	500
σ_Δ $\times 10^{-3}$	$\mu_{M_{11}} > I_C$	11.1	7.3	7.4	8.6	9.8
	$\mu_{M_{11}} < I_C$	19.4	12.6	13.4	15.9	16.0

4.4 Stability of the polarimetric system of the MPC

The stability of the polarimetric system is mainly related to the ***W*** and ***A*** matrices because they reflect the physical state of the PSG and the PSA which can change over time. Indeed, the ***W*** and ***A*** matrices can be modified by several factors, such as the mechanical stability of the PSG and PSA components, as well as the repeatability of their switching behavior. Temperature fluctuations also have a strong impact on the ***W*** and ***A*** matrices because they modify the microscopic order of the liquid crystal molecules thus changing the retardance of FLCs at different wavelengths of interest [115]. Therefore, investigating the temporal fluctuations of the ***W*** and ***A*** matrices obtained by the Eigenvalue Calibration Method (ECM), makes it possible to assess the stability of the polarimetric system and the repeatability of measurements.

4.4.1 Repeatability of polarimetric measurements

The repeatability of measurements performed by an experimental system refers to its ability to consistently produce the same results, within a specified uncertainty range, when operated without changing either its settings or external experimental conditions over a certain established time interval.

We evaluated the repeatability of the MPC measurements by performing 30 consecutive calibrations in the colposcopy room of the Kremlin-Bicêtre University Hospital where it is currently installed for the study. Before starting the first calibration, the MPC was heated based on the thermal stability test charted in Figure 3.7 in Chapter 3. Although the system reaches the thermal steady state in 20 minutes, it was warmed-up for 60 minutes to make sure the thermal consistency. Furthermore, an additional 60 minutes were required to perform the 30 consecutive calibrations (approximately 2 minutes per calibration). At the end of the whole process, the ***W*** and ***A*** matrices were obtained from each calibration performed. If the PSG and PSA are changed significantly within the whole measurement period, this results in a modification of the ***W*** and ***A*** matrices.

The Stokes vectors of the ***W*** matrix are arranged in columns, while those of the ***A*** matrix are arranged in rows. All the columns of the ***W*** matrix are normalized with respect

to the first row, as well as the rows of the ***A*** matrix, are normalized with respect to the first column. Therefore, the first row of the ***W*** matrix is a vector [1, 1, 1, 1] and the first column of the ***A*** matrix is a vector $[1, 1, 1, 1]^T$.

In order to assess the fluctuations in the ***W*** matrix, it is necessary to analyze how each of its components evolves over time, excluding the first row. The same should be done for the ***A*** matrix, excluding the first column. As an example, Figure 4.15 and Figure 4.16 show the 12 components of interest for the ***W*** and ***A*** matrices at 530 nm obtained from the 30 calibrations. For each component of the ***W*** and ***A*** matrices, we calculated the mean value and standard deviation in a circular ROI with a diameter of 800 pixels. Measurements show that the different components of the ***W*** and ***A*** matrices fluctuate over time. The same trend has been observed for the other wavelengths. It is worthwhile to note that a maximum variation of about 0.01 for the average value of ***W*** and ***A*** matrices was observed at 530 nm.

This effect was attributed to a physical modification of FLCs composing the PSG and the PSA predominantly due to temperature fluctuations. Indeed, the consulting room is not thermally insulated and regulated, and its temperature can change noticeably during the whole measurement period. In addition, the beam may continue to slightly heat the liquid crystals even if thermal equilibrium was expected before starting the measurements. Meanwhile, also random fluctuations in the light intensity emitted by the source, as well as changes in the operation of the 3-CMOS camera, can generate fluctuations in the ***W*** and ***A*** matrices.

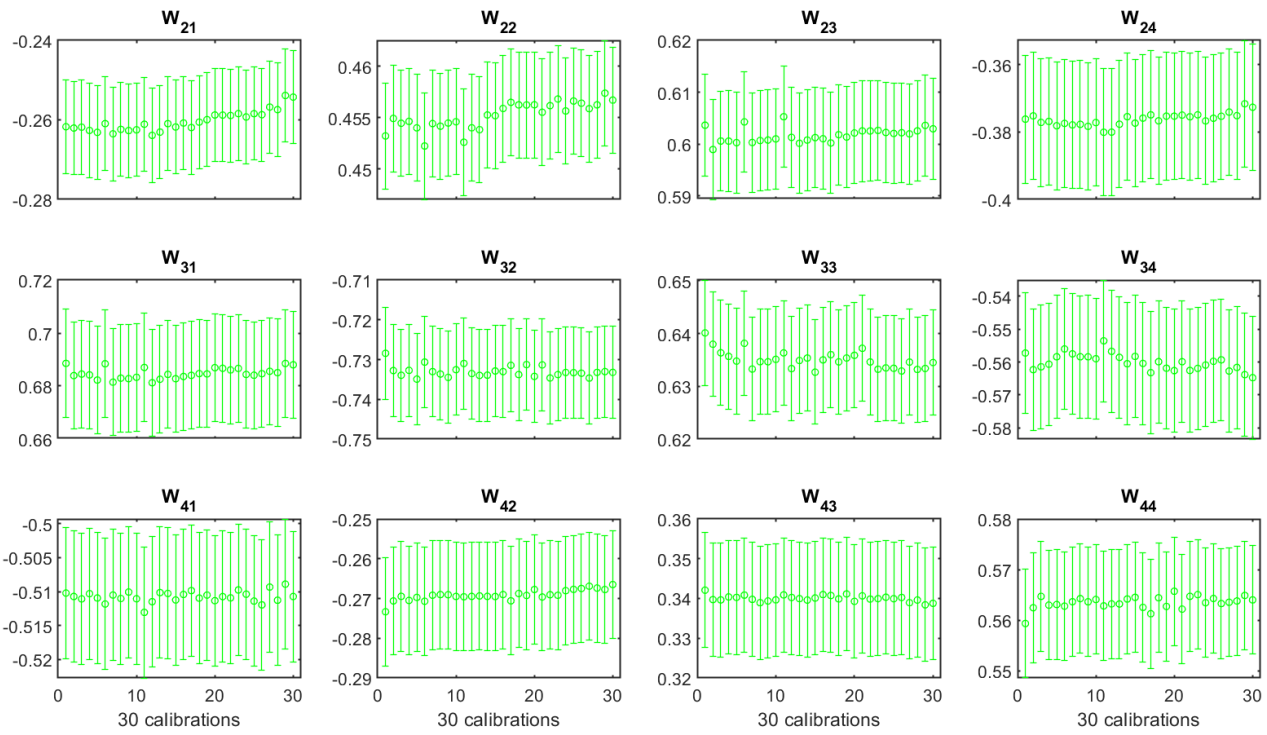

Figure 4.15 The *W* matrices at 530 nm from 30 calibrations performed in a row. The first row is not presented because it is always 1. Continuous changes are significantly observed at W_{21}, W_{22}, and W_{33}.

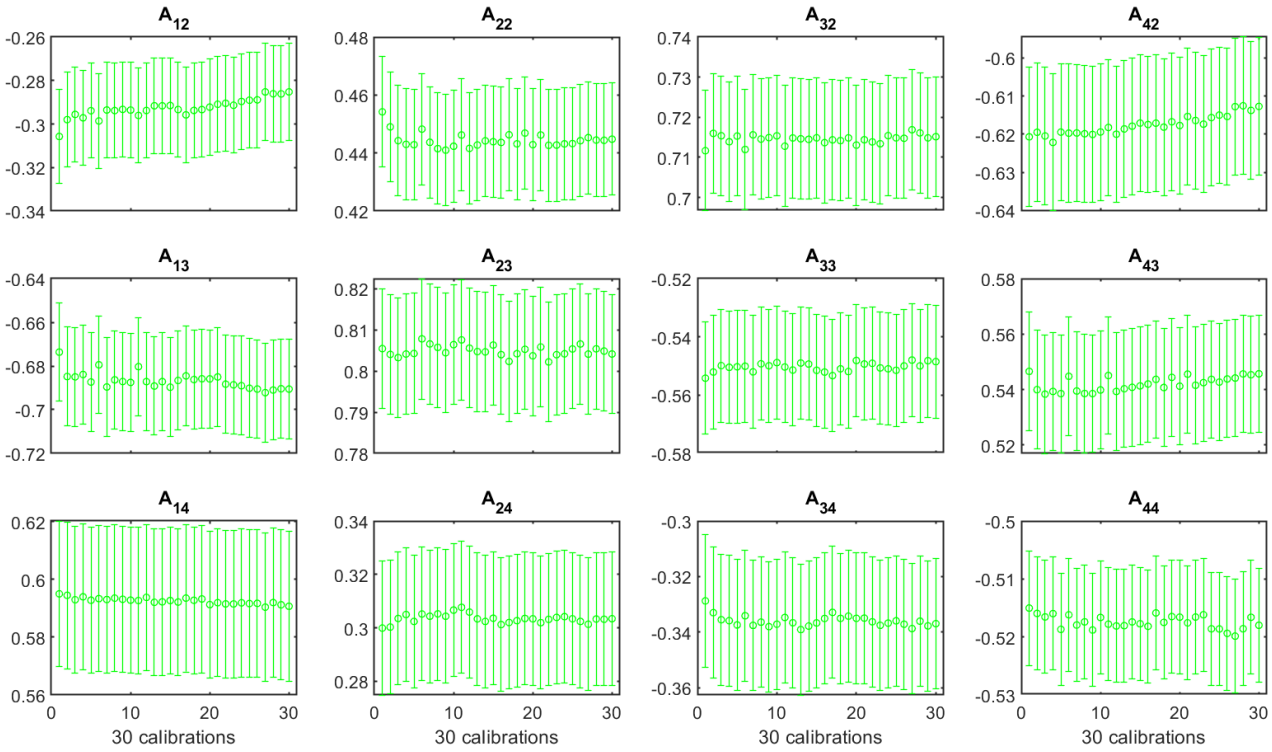

Figure 4.16 The transposed *A* matrices at 530 nm from 30 calibrations performed in a row. The first row is not presented because it is always 1. Continuous changes are significantly observed at A_{12}, A_{22}, and A_{42}.

The crucial point is to what extent the fluctuations observed for the $\boldsymbol{W}$ and $\boldsymbol{A}$ matrices can affect the polarimetric measurements. As a reminder, the ECM consists in acquiring the 16-component intensity matrix $\boldsymbol{B}$ consecutively for three optical reference elements, namely a first polarizer whose transmission axis is oriented at 0° with respect to the laboratory reference (P0), a second polarizer whose transmission axis is oriented at 90° with respect to the first polarizer (P90), and a waveplate whose fast axis is oriented at 30° with respect to the first polarizer (L30).

We indicate the 16-component intensity matrix $\boldsymbol{B}$ measured for $\boldsymbol{P}_0$, $\boldsymbol{P}_{90}$, and $\boldsymbol{L}_{30}$ as $\boldsymbol{B}_{P0}$, $\boldsymbol{B}_{P90}$, and $\boldsymbol{B}_{L30}$, respectively. The ECM allows obtaining $\boldsymbol{W}$ and $\boldsymbol{A}$ matrices from $\mathbf{B}_{P0}$, $\boldsymbol{B}_{P90}$, and $\boldsymbol{L}_{30}$, as explained in detail in Chapter 1. In particular, we consider here the matrix $\boldsymbol{B}_{L30}$ obtained for L30, which can be written as:

$$\boldsymbol{B_{L30}} = \boldsymbol{A M_{L30} W} \tag{4-4}$$

where $\boldsymbol{M}_{L30}$ is the Mueller matrix of L30. In order to verify the quality of calibration, $\boldsymbol{M}_{L30}$ can be obtained from the equation (1-35) as:

$$\boldsymbol{M}_{L30,n} = \boldsymbol{A}_1^{-1} \boldsymbol{B}_{L30,n} \boldsymbol{W}_1^{-1} \tag{4-5}$$

In addition, we also acquired the 16-component $\boldsymbol{B}_{sp}$ intensity matrix using the spectralon as a target only one time at the beginning of the whole procedure. This matrix can be written as:

$$\boldsymbol{B}_{\mathrm{sp}} = \boldsymbol{A}\boldsymbol{M}_{\boldsymbol{sp}}\boldsymbol{W} \tag{4-6}$$

where $\boldsymbol{M}_{\mathrm{sp}}$ is the Mueller matrix of the spectralon. This matrix can be also obtained using the expression:

$$\boldsymbol{M}_{sp} = \boldsymbol{A}^{-1}\boldsymbol{B}_{\boldsymbol{sp}}\boldsymbol{W}^{-1} \tag{4-7}$$

For simplicity, let $\mathbb{W}=\{\boldsymbol{W}_1, \ldots, \boldsymbol{W}_{30}\}$ and $\mathbb{A}=\{\boldsymbol{A}_1, \ldots, \boldsymbol{A}_{30}\}$ be the set of matrices $\boldsymbol{W}$ and $\boldsymbol{A}$ obtained during the whole measurement process. In addition, let be $\mathbb{B}_{\mathrm{L30}}=\{\boldsymbol{B}_{\mathrm{L30,1}}, \ldots, \boldsymbol{B}_{\mathrm{L30,30}}\}$ the set of $\boldsymbol{B}_{\mathrm{L30,n}}$ intensity matrices obtained for n-th L30 (where n=1,…,30) and $\boldsymbol{B}_{\mathrm{sp,1}}$ be the only intensity matrix measured at the beginning of the whole procedure.

In order to evaluate the repeatability of polarimetric measurement, we first calculated $\boldsymbol{M}_{L30,n}$ from the matrix $\boldsymbol{B}_{L30,\mathrm{n}}$ using $\boldsymbol{A}_1$ and $\boldsymbol{W}_1$ from the first calibration as:

$$\boldsymbol{M}_{L30,n} = \boldsymbol{A}_1^{-1}\boldsymbol{B}_{\boldsymbol{L30,n}}\boldsymbol{W}_1^{-1} \tag{4-8}$$

From $\boldsymbol{M}_{\mathrm{L30,n}}$ we obtained the linear phase retardance, R_{n}, using the formula (1-22) and the azimuth of linear phase retardance, α_n, using the formula (1-23).

In a second step we calculated $\boldsymbol{M}_{sp,n}$, from $\boldsymbol{B}_{\boldsymbol{sp,1}}$ using $\boldsymbol{A}_{\mathrm{n}}$ et $\boldsymbol{W}_{\mathrm{n}}$ as :

$$\boldsymbol{M}_{Sp,n} = \boldsymbol{A}_n^{-1}\boldsymbol{B}_{\boldsymbol{sp,1}}\,\boldsymbol{W}_n^{-1} \tag{4-9}$$

From $\boldsymbol{M}_{\mathrm{sp,n}}$ we obtained the total depolarization Δ_{n} using the formula (1-31).

Figure 4.17 shows R_{n}, α_{n} and Δ_{n} (n=1, …, 30) for all wavelengths of interest. For each of these parameters, we calculated the mean value and the standard deviation in the same ROI used for the $\boldsymbol{W}$ and $\boldsymbol{A}$ matrices (the circular ROI.) The changes of $\boldsymbol{W}$ and $\boldsymbol{A}$ matrices over 30 calibrations resulted in a maximum variation of 0.5° for the average value of linear phase retardance and a maximum variation of 0.2° for the average value of the azimuth of linear phase retardance for all wavelengths of interest. Moreover, the maximum fluctuation observed for the mean value of depolarization is about 0.001 for all wavelengths.

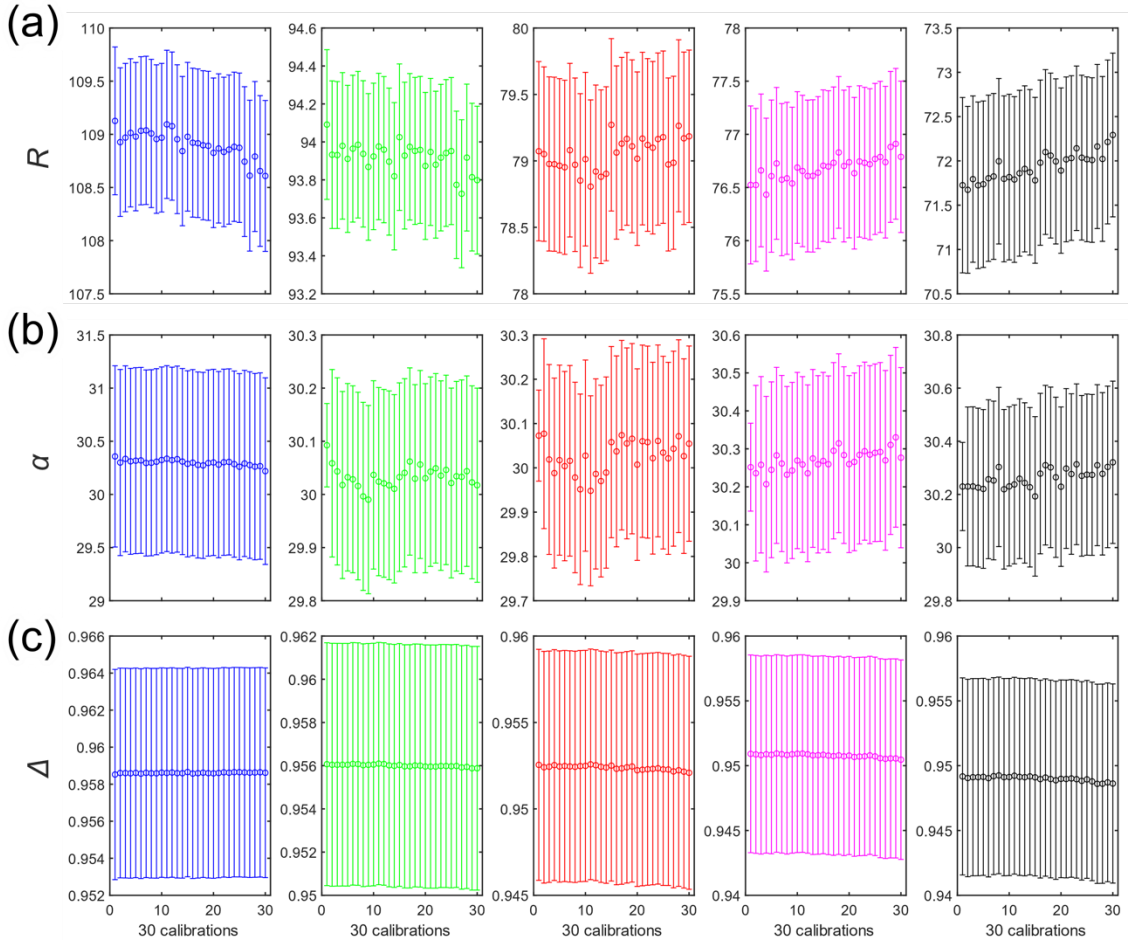

Figure 4.17 Despite of fluctuations in the *W* and *A* matrices, no significant impact (less then 0.5° in retardance and less than 0.1 ° in orientation) on the measured polarimetric properties of the L30 and spectralon.

As a result, the performance of the MPC remains extremely stable during 1 hour of operation without the need for additional calibration, which is more than sufficient for our purpose, given that the acquisition time of cervical images from a patient is about 20 minutes.

4.4.2 Reproducibility of polarimetric measurements

The "reproducibility" of a measuring system refers to its ability to obtain the same results, within a specified uncertainty range, under different conditions and over a long period of time relative to the characteristic fluctuation time of the machine. This period of time may be of the order of a day, a month or a year. During this period, the measurement conditions can change considerably due to, among other things, changing environmental conditions. In addition, the MPC can be used by different operators during the clinical study. Like repeatability, reproducibility can also be studied by considering the ***W*** and ***A*** matrices. For this purpose, we considered the ***W*** and ***A*** matrices obtained from 253 calibrations performed between January 2021 and October 2021.

Figure 4.18 and Figure 4.19 show the evolution of the 12 components of interest for the ***W*** and ***A*** matrices at 530 nm, respectively, obtained over the period of time considered. We calculated the average value for the components of the ***W*** and ***A*** matrices, always using the circular ROI of 800 pixels in diameter. In this case, much larger fluctuations are observed

for the ***W*** and ***A*** matrices than those observed in the repeatability assessment described in the previous section.

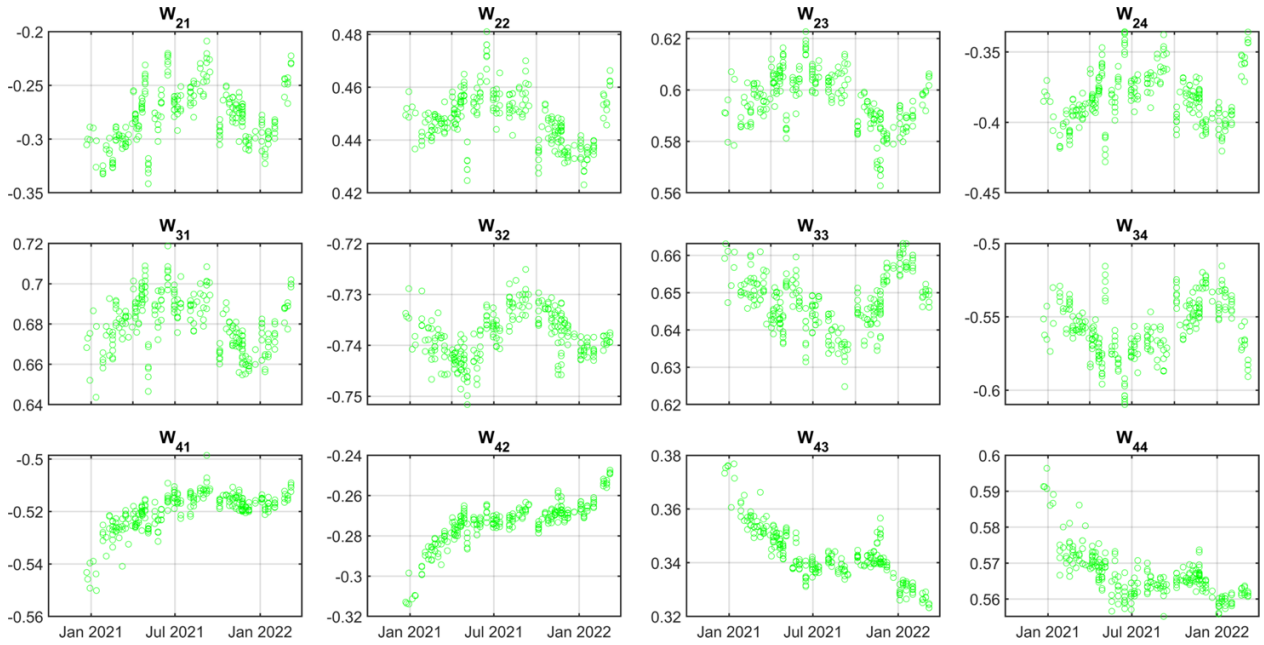

Figure 4.18 The W matrices performed over 10 months period. Each dot represents the spatial mean in the Ø800 pixels ROI. W_{21}, W_{42}, W_{43}, and W_{44} are significantly changing over the period.

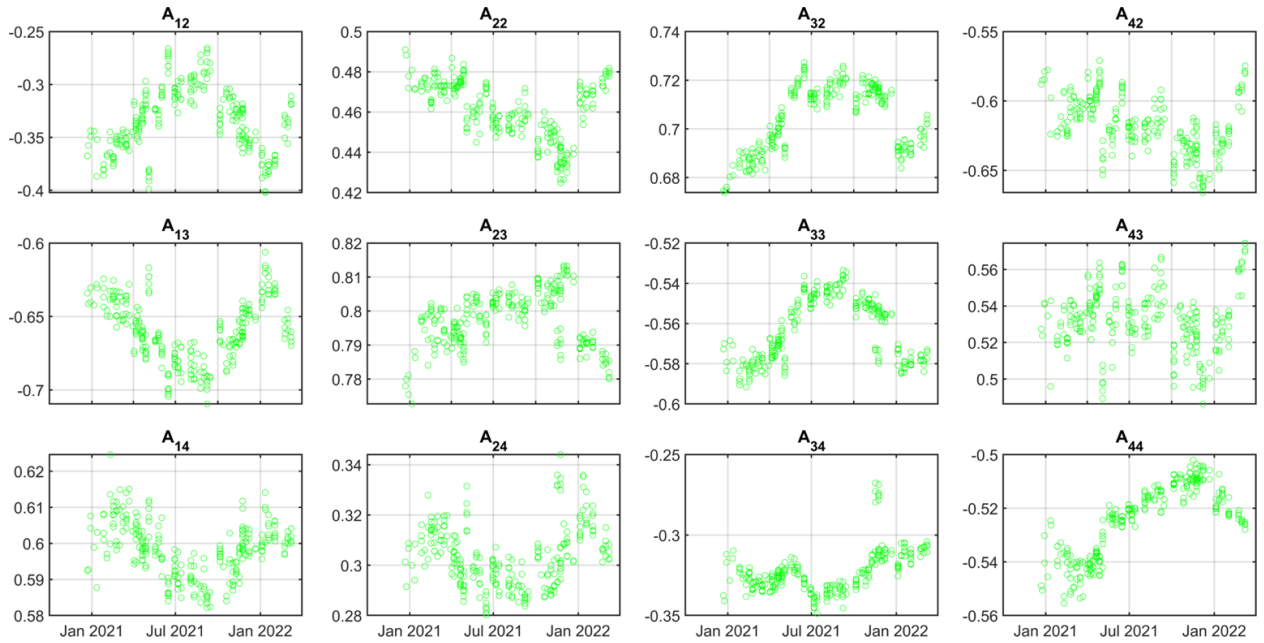

Figure 4.19 The A matrices performed over 10 months period. Each dot represents the spatial mean in the Ø800 pixels ROI. A_{12}, A_{13}, A_{33}, and A_{44} are significantly changing over the period.

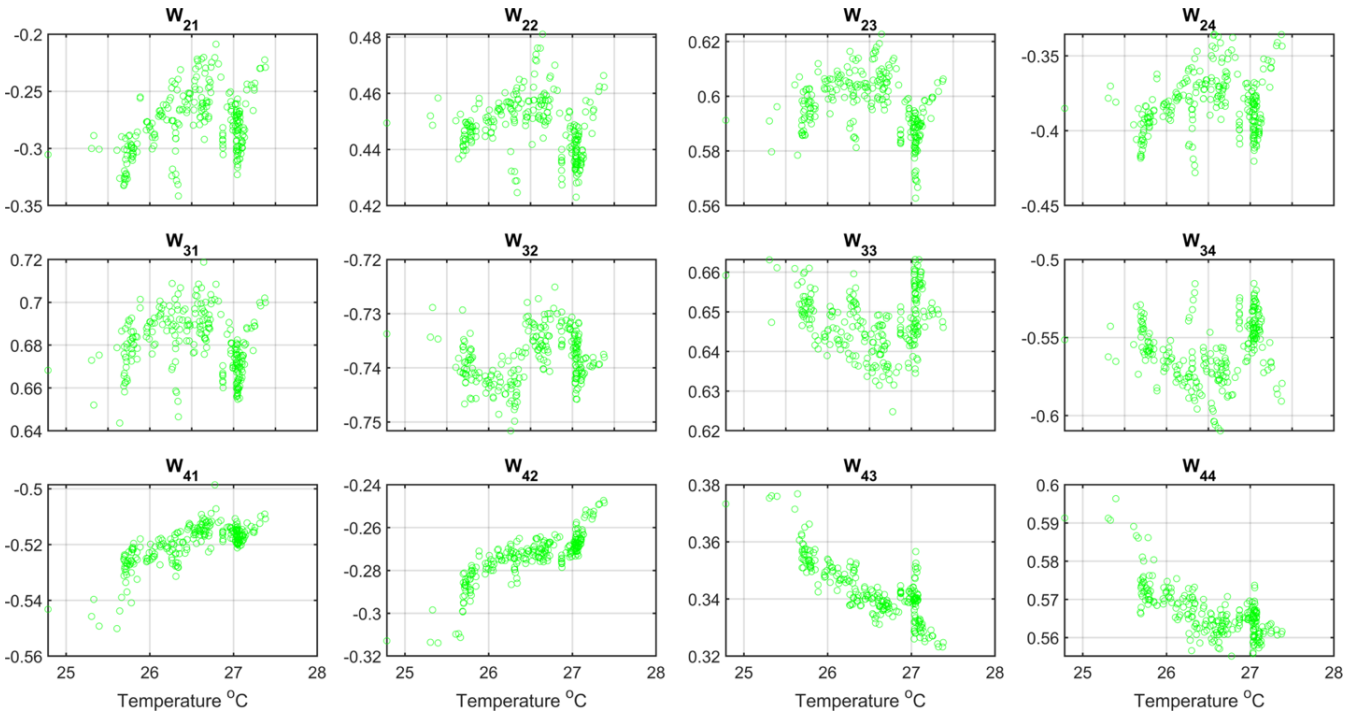

Figure 4.20 The *W* matrices as a function of temperature. Each dot represents the spatial mean in Ø800 pixels ROI. The correlation between the elements of *W* and temperature implies fluctuations of the polarimeter occurred over time have been attributed to the seasonal change.

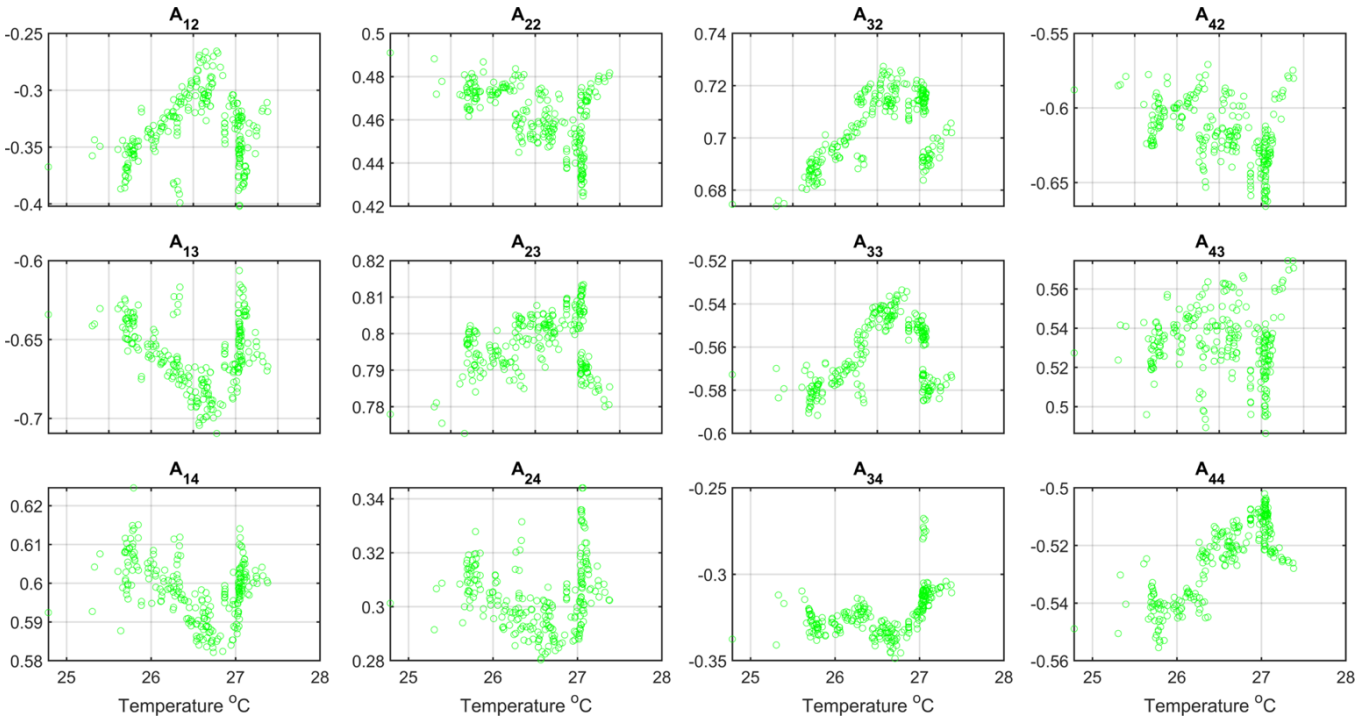

Figure 4.21 The *A* matrices as a function of temperature. Each dot represents the spatial mean in Ø800 pixels ROI. The correlation between the elements of *A* and temperature implies fluctuations of the polarimeter occurred over time have been attributed to the seasonal change.

These fluctuations appear to be continuous over time, clearly showing that the operating mode of the MPC can change significantly. Meanwhile, Figure 4.20 and Figure 4.21 show the evolution of the ***W*** and ***A*** matrices, respectively, as a function of the temperature measured at the polarimeter head, as explained in Figure 3.6 in Chapter 3.

Linear correlations were found between several elements of the ***W*** and ***A*** matrices and temperature. This effect is particularly evident for W_{43} and A_{44} coefficients, as shown in Figure 4.22a and b, respectively.

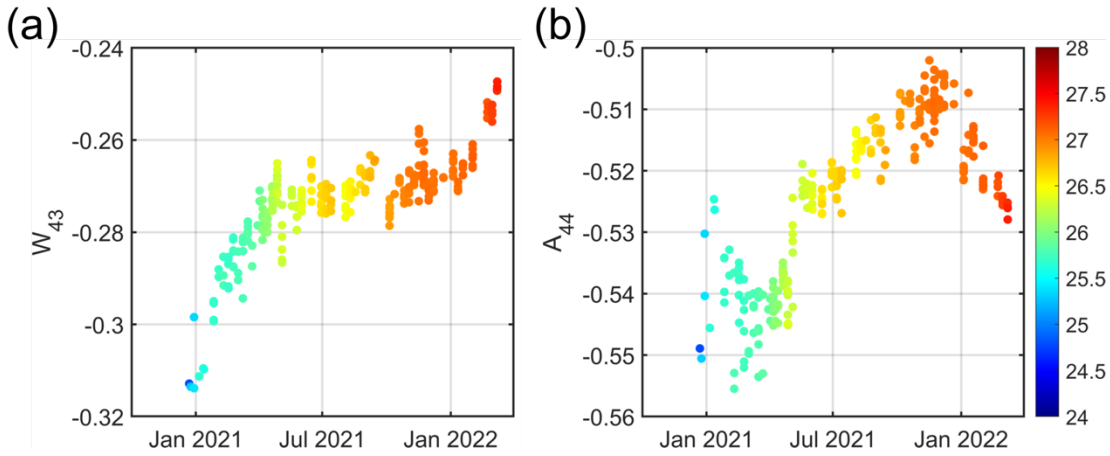

Figure 4.22 (a) Changes in the element W_{43} of the matrix *W* and (b) the changes in the element A_{44} of the matrix *A* for 10 months. Color of each dot corresponds to temperature on the color bar. Fluctuations of the matrices *W* and *A* are strongly related to temperature change.

We, therefore, studied the impact of the variation of the ***W*** and ***A*** matrices on the polarimetric measurements. To do this, we used the same procedure as for the repeatability study described in the previous section. In particular, we studied the variation of the Mueller matrix $\boldsymbol{M}_{L30}$ of the linear phase retardance of the waveplate L30 used in the calibration procedure and the $\boldsymbol{M}_{sp}$ Mueller matrix of the spectralon. In particular, we studied the variation of the parameters R, α, and Δ always obtained using the formulas (1-22), (1-23) and (1-31), respectively.

In the first step, the $\boldsymbol{M}_{\mathrm{L30}}$ matrix and the $\boldsymbol{M}_{\mathrm{sp}}$ matrix for each experiment were calculated by using the ***W*** and ***A*** matrices obtained at the beginning of the trial (22nd Dec 2020). In this case, we observe strong fluctuations of R, α over time for all wavelengths of interest. Specially, the fluctuations appeared in R is similar to the fluctuations in the element A_{13} of the matrix ***A***. On the other hand, no significant difference was found in Δ measurement in comparison to Δ in Figure 4.25, which is correctly calculated by their corresponding ***W*** and ***A*** matrices. This denotes that Δ can be measured robustly regardless of the influence of surroundings.

Consequently, a variation corresponding to a standard deviation σ=0.736° was observed in retardance R at 530 nm for the whole period considered as shown in Figure 4.23a. Furthermore, a variation corresponding to σ=0.299° was observed in α at 530 nm as shown in Figure 4.23b. Finally, a variation corresponding to a σ=0.0021 was observed at 530 nm for Δ as shown in Figure 4.23c. The standard deviations were calculated on the set of average values obtained for each parameter.

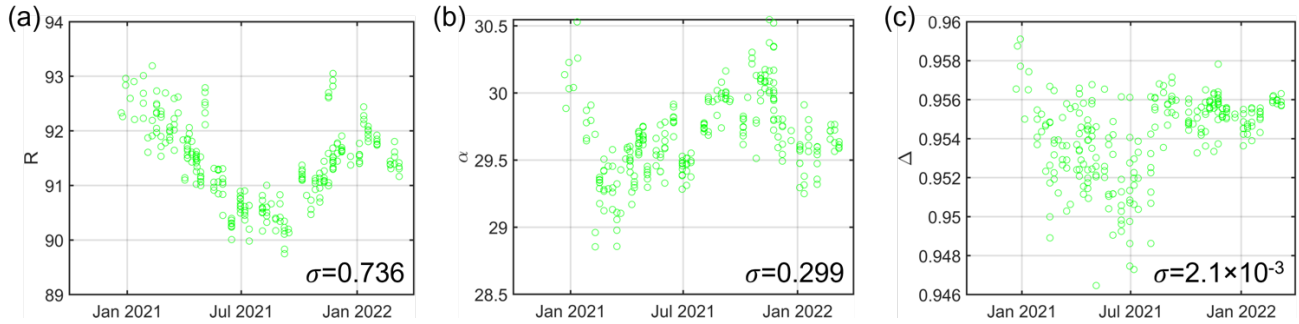

Figure 4.23 Temporal fluctuations of *R*, *α* of L30 and *Δ* of the spectralon calculated by a single calibration. The changes of the *W* and *A* matrices shown Figure 4.18 and Figure 4.19 caused biased *R* and *α* over 10 months. No significant changes are found in *Δ* in comparison to *Δ* in Figure 4.25.

Then, we calculated $\boldsymbol{M}_{L30}$ and $\boldsymbol{M}_{sp}$ for each experiment using the $\boldsymbol{W}$ and $\boldsymbol{A}$ matrices obtained for the same session. In this case, despite the strong changes in the experimental conditions throughout the period considered and also the different operators who used the MPC, we observed that the average values of R, α and Δ are very stable for all wavelengths of interest. Indeed, a maximum variation corresponding to a standard deviation σ=0.319° was observed at 700 nm for the whole period considered as shown in Figure 4.24a. Furthermore, a maximum variation corresponding to a sigma=0.108° was observed at 700 nm for α as shown in Figure 4.24b. Finally, a maximum variation corresponding to a σ= 2.6×10^{-3} was observed at 700 nm for Δ as shown in Figure 4.25.

The standard deviations were always calculated on the set of average values obtained for each parameter. In particular, the small variations observed for the depolarization can also be attributed to systematic errors due to the alignment between the MPC and the target. Scratches on the surface of the spectralon could also contribute to these variations.

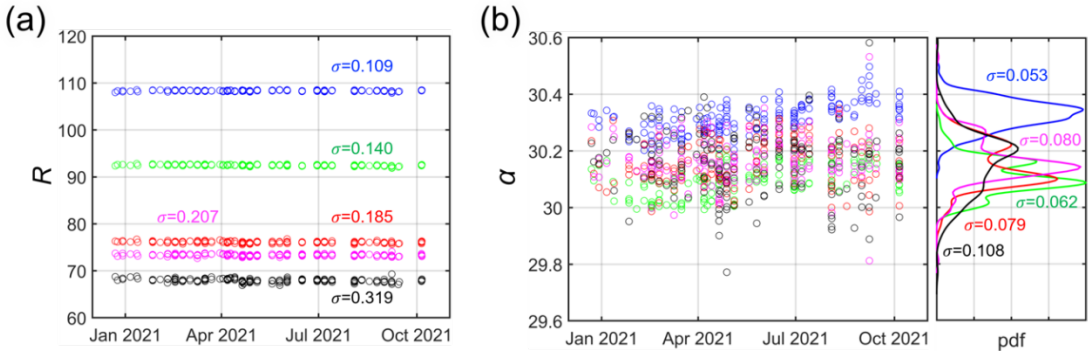

Figure 4.24 retardance *R* and azimuthal orientation *α* of L30 acquired during the ECM over the period. These represent that the ECM consistently corrects the thermal fluctuations of the polarimeter in order to acquire the correct value for the L30. *σ* denotes the standard error of the mean.

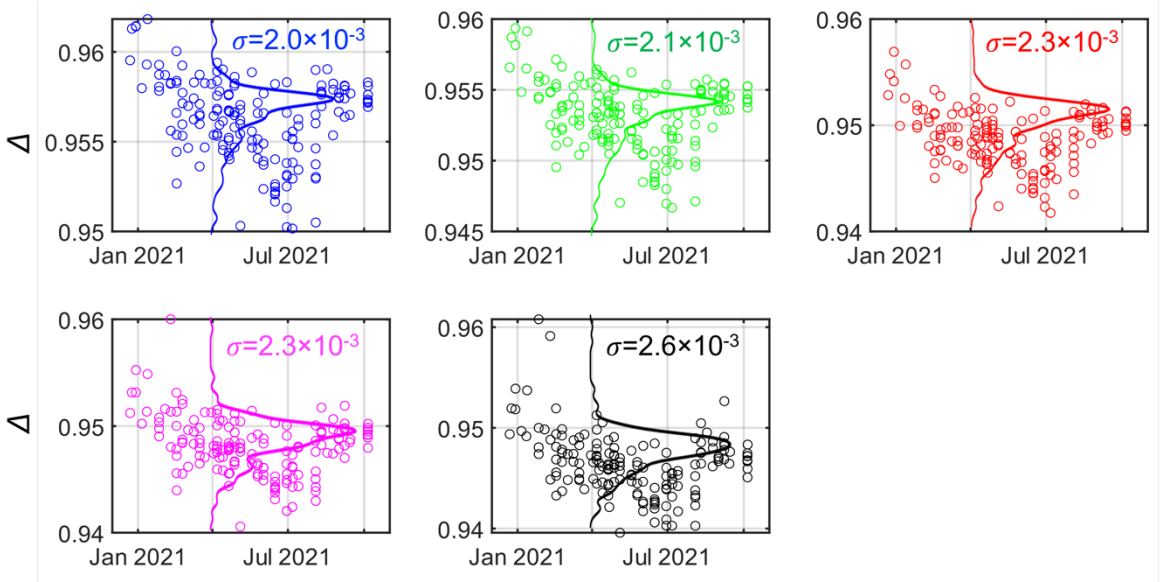

Figure 4.25 The changes of depolarization of the spectralon. Because the spectralon is not included in the ECM, it can represent the actual stability of the MPC including human factors. 0.01 difference can occur by various errors in the clinical setting.

The use of the ECM for MPC calibration allows the determination of the effective $\boldsymbol{W}$ and $\boldsymbol{A}$ matrices at a given time without the need for detailed knowledge of the PSG and PSA operating mode, as well as of the other system components. The ability to access the effective $\boldsymbol{W}$ and $\boldsymbol{A}$ matrices allows the polarimetric properties of a target to be measured correctly, even if the operating mode of the system is significantly changed. In order to obtain reliable measurements, we decided to calibrate the MPC at the beginning of a measurement day and also at the end of the imaging session for each patient.

4.5 Conclusions

This chapter first summarizes all the developments that have been made to improve the ergonomics of the new Mueller polarimetric colposcope. Compared to the old prototype, the new one is very compact, fast, and easy to use by a single practitioner, without the intervention of a second operator. Moreover, it can be used as a conventional colposcope without changing the medical practice. Then, the performance of the machine in terms of precision in the measurement of a Mueller matrix was evaluated for all wavelengths.

In addition, we also characterized the numerical errors created by the Lu-Chipman decomposition, widely used for the analysis of measured Mueller matrices. These characterizations were performed on a piece of cervix in order to estimate the precision of the machine under real conditions. Finally, we determined the reproducibility and repeatability of the experiments in hospital setting.

Chapter 5

Preliminary results of the trial

In this chapter, polarimetric cervical images collected during the trial are presented. The images revealed that cervical tissue exhibit different polarimetric responses dependent on its overlying epithelial types that we explained in Chapter 2, namely the SSE, MSE, and CE. Several representative cases for each epithelial type are described in this chapter. Based on these observations, 97 individual cervices were analyzed to conduct a statistical significance of our discovery. Consequently, this study has found that the metaplastic transformation leads to remodeling and restructuring of underlying connective tissue not only the epithelial transition.

5.1 Polarimetric appearances of in-vivo cervical epithelia

Preliminary results of this study have shown that multispectral Mueller polarimetric colpophotography can provide quantitative criteria to discriminate among the different types of epithelia covering the ectocervical surface much more effectively than conventional colposcopy, even after the application of the acetic acid and iodine. The greater discriminatory power of this technique is due to the fact that it also allows characterizing, among other things, the polarimetric properties of the connective tissue close to the basement membrane, whose microscopic structure is highly dependent on that of the overlying epithelium.

In particular, Mueller polarimetric imaging is effective in distinguishing the stratified squamous epithelium (SSE) from the columnar epithelium (CE), thus providing a fairly accurate visualization of the metaplastic transition zone (TZ). In addition, it can provide information on the progression of metaplastic transformation. In this section, the most significant polarimetric features of each cervical epithelium type are described and discussed in relation to its physiological and histological properties.

5.1.1 Polarimetric properties of the stratified squamous epithelium (SSE)

Previous studies in the literature on the microscopic morphological organization of cervical connective tissue revealed that dense collagen fibers are oriented circumferentially around the endocervical canal [60], [62], [63], [116], as explained in Chapter 2.

In this study, the examination of cervical tissue by multispectral Mueller polarimetric colpotopography showed that the microstructure of the connective tissue near the basement membrane is very complex and highly dependent on the type of overlying epithelium. In particular, the circular arrangement of the collagen fibers around the endocervical canal, already described in the literature, is mainly observed in the connective tissue underlying the stratified squamous epithelium (SSE).

For instance, in multiparous pregnant women who are likely to have an uneverted endocervix throughout the whole gestation period [117], the SSE can be predominantly observed in the ectocervix. Figure 5.1 shows an example of such a cervix for a 33-year-old multiparous pregnant woman at 38 weeks of amenorrhea and 5 days. The SSE can be usually recognized on conventional colposcopy by an expert practitioner because it has a very smooth appearance to the naked eye. Based on this qualitative assessment, the practitioner involved in the study has established that the ectocervix shown in Figure 5.1a is almost completely covered by the SSE. In this case, the SCJ, close to the cervical os, is only partially visible due to the presence of mucus, which is usually very abundant for pregnant women.

Mueller polarimetric images of the ectocervix provide valuable information about the cervical microstructure that is not directly visible in the color image, as shown in Figure 5.1b and c, displaying the linear phase retardance image (R) and the slow axis azimuth (of the linear phase retardance) image (α), respectively, at 530 nm.

For most of the pixels contained in the selected ROI, corresponding to the whole ectocervix (area inside the white dotted line in Figure 5.1a), the value of R at 530 nm is very high, varying between 60° and 120°. The ectocervix covered by the SSE is characterized by a strong optical anisotropy. Since the SSE is composed of flat cells arranged in a compact manner and lacks well-organized cytoskeletons such as actin, the origin of the observed strong optical anisotropy should be attributed to the underlying connective tissue, which is mainly composed of very dense fibrous structures, especially collagen. The R image at 530 nm shows the presence of densely clustered elongated structures that may be associated with connective tissue collagen fiber bundles [61]. These fiber bundles appear to be parallel to the directions given by the pixel-by-pixel mapping of the slow axis azimuthal orientations α shown in Figure 5.1c. In particular, the α image reveals that the collagen fiber bundles are arranged circularly around the endocervical canal.

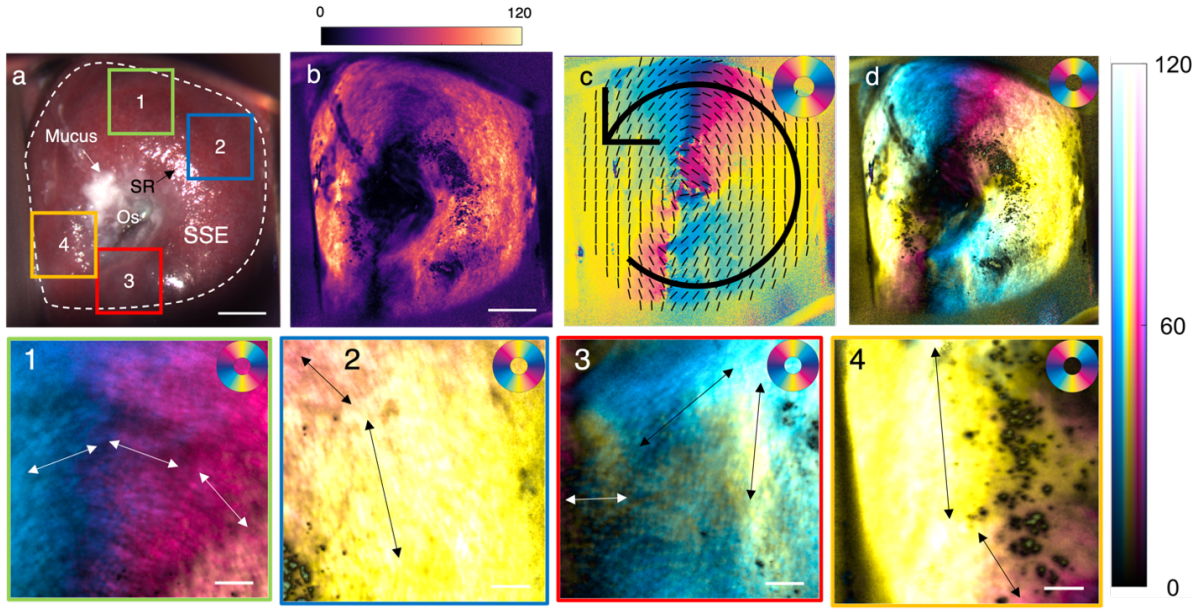

Figure 5.1(a) A color image of the cervix of a 33-year-old multiparous pregnant woman. The SSE is predominantly observed in the ectocervical area (the white dotted line.) The areas marked with the four rectangles in different colors are cropped and magnified as shown in the second row. The solid arrows represent the overall direction of the azimuth. (b) The linear retardance (*R*) image at 530 nm. The SSE is represented by high linear retardance between 30° and 90°. (c) The image of the slow axis azimuth (*α*) of linear retardance at 530 nm. The color represents the in-plane azimuth as [0° 180°], and corresponds to the azimth of the same color in the circular phase bar at the upper right corner. The black lines represent the spatially averaged azimuth at each location (40×40 pixels). (d) The image of the combination (*R*+*α*) of linear phase retardance and its azimuth. The color represents the azimuth of linear retardance corresponding to the phase bar, while brightness represents the degrees of linear retardance corresponding to the rectangle color bar on the right. The scale bar in (a) and (b) represents 5 millimeters, the scale bar in (1)~(4) represents 1 millimeter.

Figure 5.1d merges the *R* image with the *α* image (*R*+*α*). The merged image of the two polarimetric parameters is further analyzed for areas 1, 2, 3 and 4 selected in Figure 5.1a. The parameter *α* is characterized by well-defined orientations for all selected areas where *R* is very high. The *R*+*α* images clearly illustrate that the fiber structures visible on *R* images are well parallel to the orientations provided by *α* images.

The presence, on the surface of the cervix, of mucus as well as specular reflections (SR) that saturate the detectors of the 3-CMOS camera can affect the *R* measurement with a significant decrease of its value for the concerned pixels, while they have less impact on the *α* measurement.

A decrease of *R* at 530 nm is also observed in two small areas placed at the north (12 o'clock) and south (18 o'clock) poles of the cervix. Collagen fiber bundles are still visible in these areas. They are always parallel to the orientations provided by *α* but appear to be much less dense than in the other zones of the cervix. The *R* image clearly shows the presence of collagen fiber bundles and can also provide information about their organization and density. At the same time, the *α* image allows the detailed visualization of the orientation of collagen fiber bundles in the image plane. The *R*+*α* image can provide unique information on the collagen structure of subepithelial connective tissue, as shown in Figure 5.1d.

The results described in this section are quite general and have been consistently observed in the areas of the ectocervix covered by the SSE also in other patients, as will be described later in the text.

5.1.2 Polarimetric properties of the columnar epithelium (CE)

The CE usually covers the surface of the endocervical canal, as explained in Chapter 2. For a non-everted cervix, as in the case of multipara, an example of which was presented in the previous section, the SCJ remains close to the cervical os and the CE is only visible in the immediate vicinity of the entrance to the endocervical canal. However, due to an increase in estrogen and mechanical pressure from the fetus and amniotic fluid, which occurs during pregnancy, the endocervix may be everted and the CE becomes clearly visible on the surface of the ectocervix. This particular structure of the ectocervix is called ectopy or ectropion and is usually found in primigravid pregnant women [117], [118].

As already mentioned in Chapter 2, the CE has a grape-like aspect and appears as composed by clearly separated villi to conventional colpophotography. The spaces between the villi are also called crypts. Reddish microcapillaries are visible in the connective tissue that constitutes the villi, beneath the CE that covers their surface. Indeed, these capillaries are visible in transparency through the CE, which is characterized by a very low thickness. In general, collagen fiber bundles run parallel to the endocervical canal in the central region of the cervix [50], as explained in Chapter 2. However, the connective tissue underlying the CE is relatively isotropic [62], [63], [116].

Figure 5.2 shows, as an example, the cervix of a 31-year-old primigravid woman at 30 weeks of amenorrhea and 6 days. The practitioner identified on the color image of the cervix in Figure 5.2a, obtained using the MPC as a conventional colposcope, a broad, fairly rough, and very reddish central area that seems to be covered by the CE. It is an area of possible ectopy that extends over almost the entire surface of the ectocervix. In addition, the practitioner also identified a second, more peripheral area surrounding the first one with a much smoother visual aspect that seems to be covered by the SSE.

Most of the pixels in the central area are characterized by very low R values (3° on average) and a rather spatially disordered α, as shown in Figure 5.2b and c, respectively. On the contrary, the peripheral area is characterized by much higher R (between 30° and 70°) than the central one. In particular, the R image shows the presence of fiber bundles parallel to the directions given by α distributed circularly around the endocervical canal. The polarimetric signature of the peripheral area is very similar to that of the cervix described for the multiparous pregnant woman presented in the previous section, confirming that this zone is mainly covered by the SSE.

Merging the R image and the α image enhances the contrast between the two identified main areas by highlighting their structural difference in the connective tissue, as shown in Figure 5.2d. The region inside the green box in Figure 1.2a is analyzed in more detail in Figure 5.2e-g.

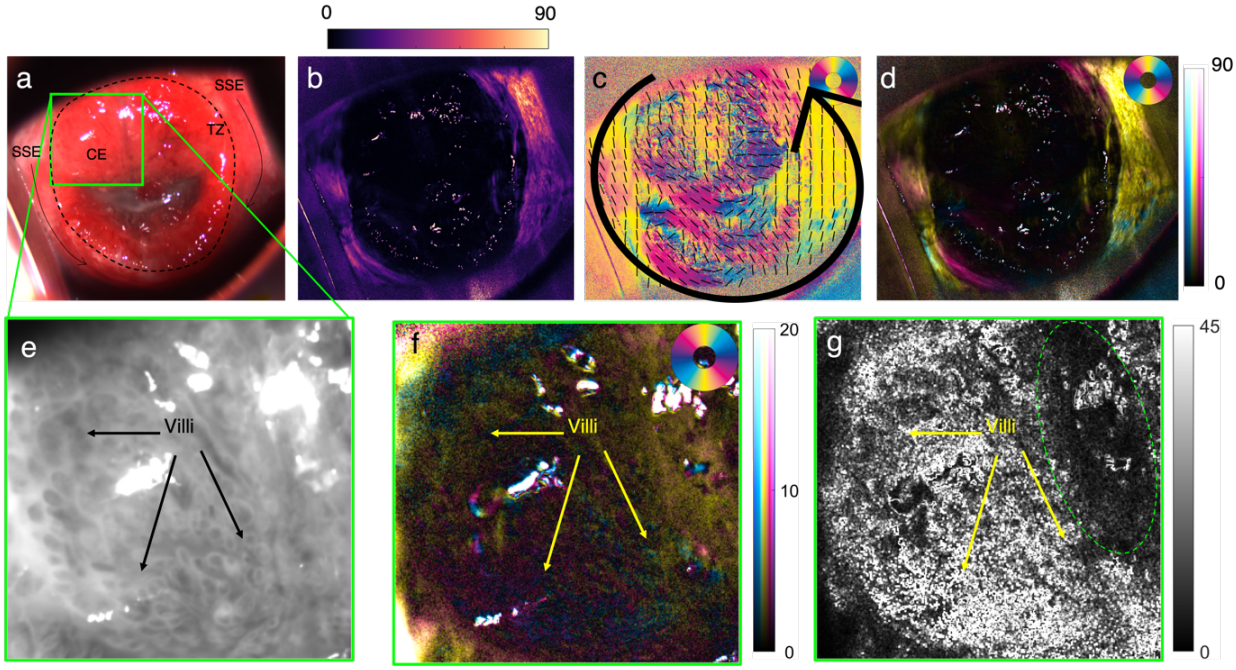

Figure 5.2 The cervix of a 31-year-old primigravid woman. (a) The color image of the cervix. An eversion of the endocervix is observed (ectropion,) and the CE is predominantly observed in the everted area (the black dotted line.) The SSE is found in the peripheral region. (b) The image of linear retardance (*R*) at 530 nm. The CE exhibit extremely low *R* around 3° while the SSE exhibits much higher retardance around 60°. (c) The image of the azimuth (*α*) of linear retardance at 530 nm. The linear retardance in the SSE is circumferentially oriented, while *α* in the CE is arbitrary. (d) The image of the combination of retardance and azimuth, namely *R*+*α*. (e) The M_{11} (unpolarized intensity) image at 530 nm of the area marked with the green rectangle in the color image (a). Clearly separate villi are predominantly observed (the arrows). (f) The *R*+*α* image of the green rectangle. The dark area corresponds to *R* around 3°. (g) The image of the randomness of azimuth, $Rand_\alpha$ in equation (5-1). The CE with villi exhibits high $Rand_\alpha$ nearly 40. Low randomness is observed in a metaplastic region (the green dotted circle).

The unpolarized intensity image (corresponding to the M_{11} coefficient of the measured Mueller matrix) at 530 nm in Figure 5.2e shows very clearly the presence of villi and crypts typical of the CE, confirming the occurrence of ectopy over most of the considered region. This region is globally characterized by very low linear phase retardance (between 2° and 5°), as shown in Figure 5.2b, probably due to the isotropic organization of the collagen underlying the CE.

Due to the lack of optical anisotropy, the selected region is mainly characterized by a randomly distributed pixel-by-pixel mapping of the slow axis azimuth. Therefore, we calculated the degree of randomness of α as a function of the (x, y) coordinates on the image plane using the following expression:

$$Rand_\alpha(x,y) = \sigma\left(\left\{\alpha_{x,y}, \alpha_{x+1,y}, \alpha_{x,y+1}, \alpha_{x+1,y+1}\right\}\right) \quad (5\text{-}1)$$

where $\alpha_{x,y}$ denotes the specific value of the slow axis azimuth at (x, y) position in the image plane. Thus, the parameter $Rand_\alpha$ represents the standard deviation (σ) of α in a 2×2 window around each pixel of the selected window.

The image of $Rand_\alpha$ is shown in Figure 5.2g. The value of $Rand_\alpha$ is very high in almost the entire cropped image, except for a small zone in the upper right (indicated by a dotted green circle) where it becomes very low. This is because R is about 10° on average and the slow axis azimuth is very well oriented in this zone. By comparing the$Rand_\alpha$ image with the M_{11} image in Figure 5.2e, it can be observed that the villi and crypts typical of the CE are slightly fused (then less visible) in the zone indicated by the dotted green circle that has been identified to be a metaplasia, as will be explained in more detail later in the manuscript.

The analysis presented in this section is crucial to identify the polarimetric signature of the CE which is characterized by very low value of R (typically 4° on average) and high value of $Rand_\alpha$.

5.1.3 Polarimetric properties of metaplasia

When the CE of an everted cervix is exposed for a long period of time to the high acidity of the vagina, it begins to transform into SSE, which is better adapted to this type of environment, as explained in Chapter 2. Metaplastic transformations are usually found in the transition zone (TZ) around the SCJ between the CE and the SSE. In conventional colpophotography, metaplastic transformations appear as morphological changes of the CE [54], [117]. However, the accurate determination of the TZ as well as the classification of the different stages of metaplasia by simple visual inspection, without histological analysis of tissue samples taken from the areas of interest (biopsies), remains a real challenge.

On the other hand, Mueller polarimetric imaging shows great promise for accurately detecting TZ as well as distinguishing between different grades of metaplasia. To characterize the polarimetric behavior of the metaplasia, we considered the same cervix presented in the previous section to describe the polarimetric signature of the CE. Indeed, the cervix of this patient has been examined at different weeks of amenorrhea (longitudinal study), which allowed us to study how the progression of pregnancy can modify the polarimetric properties of the cervix.

Figure 5.3 compares the images acquired for the considered cervix using the MPC at 30 weeks of amenorrhea and 6 days on the left and at 34 weeks of amenorrhea and 6 days on the right. Specifically, we analyzed the time course of cervical polarimetric properties in the green zone. Color images acquired at two different gestational ages during pregnancy, shown in Figure 5.3a and h, do not reveal substantial differences in cervical structure.

On the contrary, the unpolarized intensity images (corresponding to the M_{11} coefficient of the measured Mueller matrix at 530 nm clearly show that the structure of the cervical epithelium has changed considerably with pregnancy progression. In the green area, we observed that the villi and crypts, typical landmarks of the CE, are clearly observable on the surface of the cervix at the earlier gestational age, as shown in Figure 5.3b, while they are no longer observable after 4 weeks of pregnancy progression, as shown in Figure 5.3g. Noticeably, at 37 weeks of amenorrhea, the villi have fused to form a relatively smooth surface and branching vessels appear on the cervical surface.

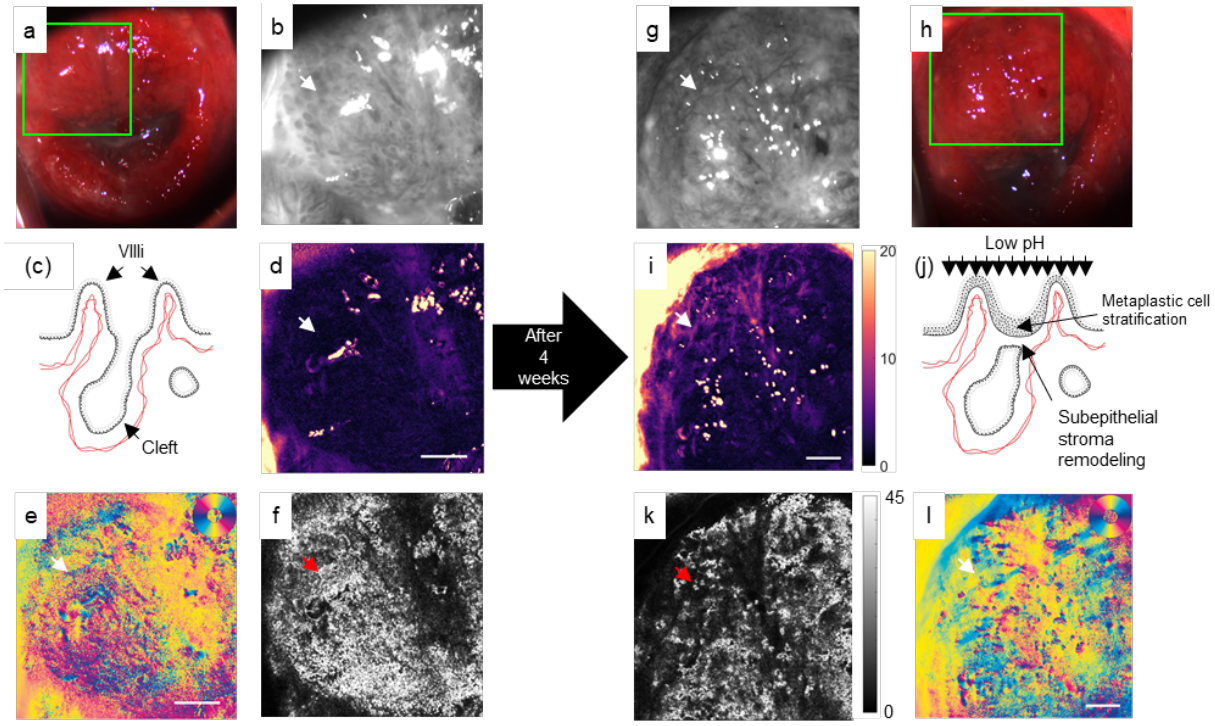

Figure 5.3(a) The color image of the cervix of a primigravida at 30 weeks and 6 days of amenorrhea. (b) The M_{11} image at 530 nm. (c) A schematic illustration of the CE. (d) The R image at 530 nm. (e) The α image at 530 nm. (f) The $Rand_\alpha$ image. (g) The M_{11} image of the cervix of the same patient at 34 weeks and 6 days of amenorrhea. The villi at the white arrow appear to be smoother than (b). (h) The color image. (i) The R image at 530 nm. An increase of R is observed along with disappearance of the villi (j) An schematic illustration of the MSE. (f) The $Rand_\alpha$ image. The randomness decreases with the progression of metaplasia. (l) The α image at 530 nm. The metaplastic transformation is thought to lead to remodeling of connective tissue as it results in an increase of R with decreased $Rand_\alpha$.

The described morphological change of the cervical epithelium with the pregnancy progression is a typical feature of metaplastic transformation where the proliferation of reserve cells flattens the structure of the villi [54], [117], [119], as illustrated in the schematics of Figure 5.3c and j.

From the polarimetric point of view, increased R appears in the same area with advancing pregnancy, as shown in Figure 5.3d and i. At the same time, a reorganization of connective tissue is also observed, as shown by the α images in Figure 5.3e and l. This effect is much more evident when looking at the $Rand_\alpha$ images shown in Figure 5.3f and k. Indeed, the value of $Rand_\alpha$ decreases significantly with advancing pregnancy, confirming that the connective tissue within the selected area becomes increasingly organized on a microscopic scale. This area of metaplastic transformation is indicated by white and red arrows in Figure 5.3. The increase in optical anisotropy clearly suggests that a metaplastic transformation not only involves a modification of the epithelium but also leads to a remodeling and restructuring of the underlying connective tissue, whose collagen becomes progressively more organized.

Figure 5.4 shows a cervix with different types of epithelia on the ectocervical surface, which is the most common case encountered in practice. It is a cervix of 33-year-old multiparous pregnant woman at 26 weeks of amenorrhea and 3 days. Only two significantly different areas to a visual impression were detected by the practitioner on conventional

colpophotography, namely a large central area with a rather rough appearance that was identified as possible ectopy, surrounded by a smoother-looking area that was assumed to be covered by SSE. In contrast, Mueller polarimetric imaging provides much higher contrast images that give detailed information about the microstructure of the subepithelial connective tissue. Indeed, the $R{+}\alpha$ images combined with the $Rand_{\alpha}$ images allow to highlight different areas of interest that conventional colpophotography has not been able to detect.

In addition, the central area of the ectocervix (indicated by the red arrows in Figure 5.4c) is characterized by very small value of R (around 3°) and a completely random α, leading to the conclusion that this part is covered by the CE. Meanwhile, R increases progressively and almost radially, with a decrease in $Rand_{\alpha}$, towards the more peripheral zones. Particularly, $Rand_{\alpha}$ becomes very low in the more peripheral zones where R is relatively high (about 10°). Moreover, α is circumferentially oriented with respect to the endocervical canal in these peripheral zones, which could lead to the conclusion that they are covered by the SSE. The intermediate area of the ectocervix between the CE zone and the SSE zone is the transition zone (TZ) where metaplastic transformations are present. Consequently, the $R{+}\alpha$ image allows the direct visualization of the connective tissue microscopic structure underlying the epithelium, near to the basement membrane. In fact, it is not yet clear at what depth light penetrates the tissue. However, the multispectral analysis of cervical tissue, discussed later in the text, confirms that the observed optical anisotropy effects are rather related to the most superficial layers.

Various spatial patterns have been observed in the subepithelial connective tissue of the TZ, indicating different modalities of subepithelial collagen reorganization near the basement membrane. This cervix exhibits a wide area of TZ despite its multiparity.

The cropped regions 1, 2, and 3 in Figure 5.4b are analyzed in more detail.

The $R{+}\alpha$ image in region 1 shows a spatially inhomogeneous structure of the connective tissue underlying the epithelium in the TZ (indicated by yellow arrows) that is very different from that of the region covered by the SSE (indicated by white arrows). Noticeably, circularly distributed collagen fiber bundles clearly appear in the TZ. These circular structures are arranged as rings of different diameters characterized by high R (about 15°) and a circular distribution for α. The optical anisotropy decreases considerably in the central region of these rings. At the same time, linearized and spatially separated collagen fiber bundles are also visible. In addition, areas where the fiber bundles begin to coalesce to produce rather smooth surfaces can be observed. Overall, macroscopically visible areas with higher and lower value of R alternate in the TZ of region 1. In particular, $Rand_{\alpha}$ becomes very low in the areas with higher R. On the contrary, it increases in the areas of decreasing R.

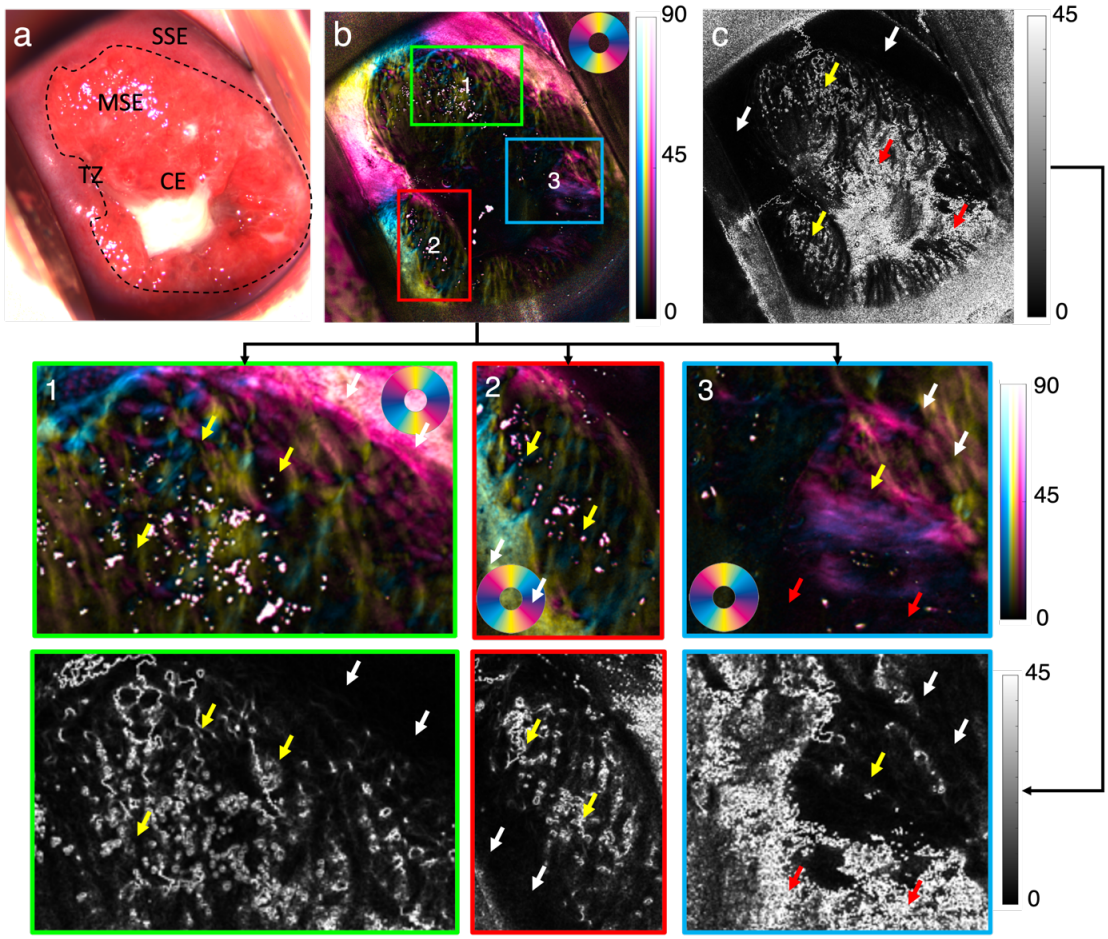

Figure 5.4 (a) The color image of the cervix of a 33-year-old multiparous pregnant woman at 26 weeks and 3 days of amenorrhea. The TZ can be found within the black dotted line. The coarse surface near the SSE exhibits metaplastic features. (b) The $R+\alpha$ image at 530 nm. The areas marked with the three rectangles are cropped and magnified as shown in the images in the 2nd and 3rd rows for more detailed description. (c) The $Rand_\alpha$ image at 530 nm. Various degrees of randomness are observed in this cervix. (Cropped images) The white arrows indicate the SSE, and the red arrows indicate the CE. Finally, the yellow arrows indicate the MSE.

This results in a spatial pattern for $Rand_\alpha$ in the TZ that can be clearly distinguished from that of the CE and SSE. In addition, the mean value of $Rand_\alpha$ for the TZ in region 1 has an intermediate value between that of the CE and SSE.

Region 2 shows predominantly the presence of well-separated linearized collagen fibers in the TZ (indicated by yellow arrows) whose $Rand_\alpha$ is very similar to that observed for region 1.

Lastly, region 3 shows a TZ (indicated by yellow arrows) between the CE (indicated by red arrows) and the SSE (indicated by white arrows) where the collagen fiber bundles merge into a smoother surface. In this region the TZ begins to have a structure very similar to that of the SSE with a significant decreasing of $Rand_\alpha$.

We now focus on the rings observed in the TZ of region 1. During the metaplastic transformation process, the basement membrane in the areas of the ectocervix covered by the CE begins to generate reserve cells that produce a thickening of the epithelium to gradually create a smoother surface, as shown in Figure 5.5a and b. Connective tissue is also

produced beneath the basement membrane that seals the crypts. Several crypts may coalesce to form larger, empty, or mucus-filled follicles.

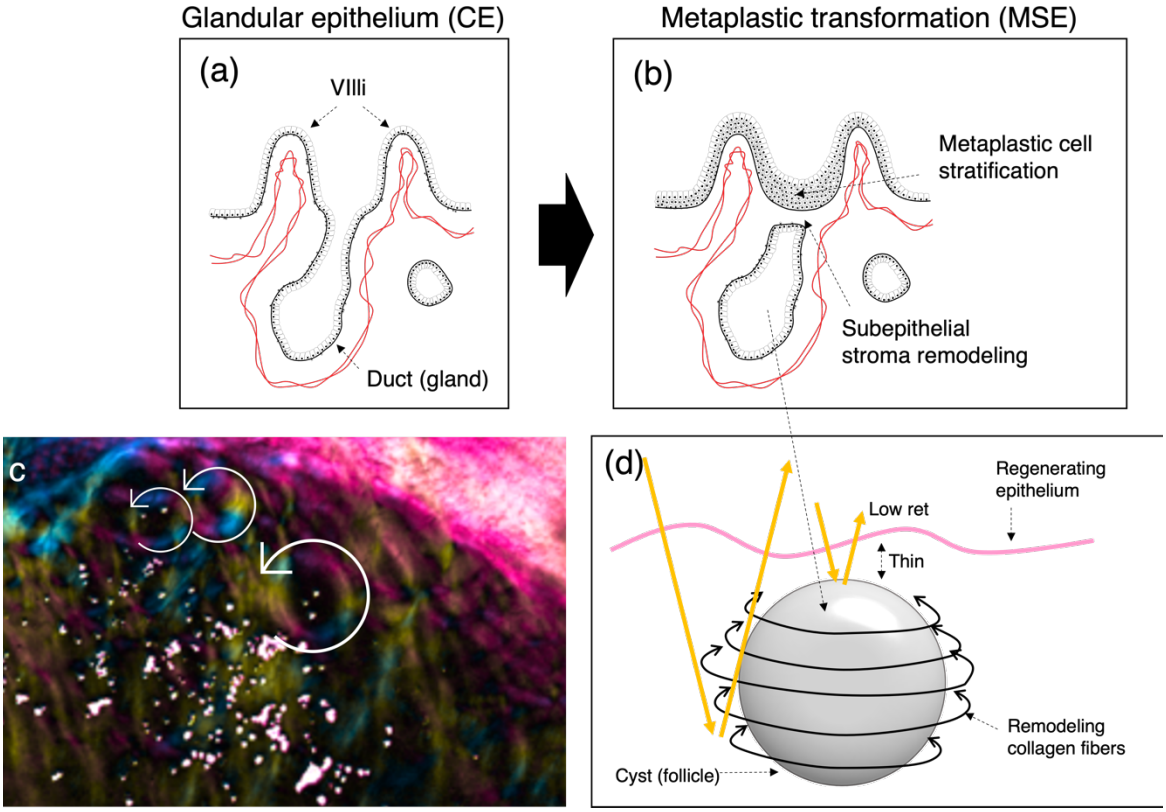

Figure 5.5 (a) The schematic illustration of the CE. (b) The schematic illustration of the MSE. (c) Circular patterns appear in the cropped R+α image of region 1 in Figure 5.4. (d) The schematic illustration of the possible origin of the circular patterns. Tissue remodeling around a cyst can create a circular *R* pattern. The low *R* at the center of the circle is thought to be attributed to effaced connective tissue between the cyst and basement membrane.

Bundles of collagen fibers begin to form and distribute themselves circularly around these structures. This is why the optical anisotropy increases around the follicles. On the contrary, it remains low in their central area. This effect is due to the fact that the collagen layer between the follicles and the basement membrane is still very thin, especially at the beginning of their formation.

The description of this process helps to explain the appearance of ring structures, shown in Figure 5.5c, which are often observed in the TZ. In some cases, the collagen layer beneath the basement membrane becomes thick and the rings are no longer visible. In other cases, the follicles become quite large and they remain visible on the surface of the cervix as open crypts or as mucus-filled Nabothian cysts. The presence of these structures in the areas of the ectocervix covered by the SSE can be an evidence of previous or ongoing metaplastic transformation.

The results presented in this section show that a process of restructuring and reorganizing connective tissue is present in the TZ. This process has been visualized for the first time to our knowledge in vivo using high-resolution Mueller polarimetric imaging. A more quantitative analysis of the metaplastic transformation process of the cervical epithelium, based on polarimetric images, will be presented later in this chapter.

5.1.4 Polarimetric properties of cysts

For completeness we describe also the polarimetric response of cysts that are often visible on the surface of the cervix. Cervical cysts are also called Nabothian cysts or Nabothian follicles [50]. Visually, they appear as mucus-containing pockets positioned beneath the epithelium. They are thought to form as a result of the process of covering the crypts of the glandular epithelium typical of metaplastic transformations [118], as explained in the previous section. Therefore, cysts are often seen near the SCJs and can be considered as evidence of metaplasia if found in the ectocervix. Gland openings can be also found if ducts are not completely covered by newly formed epithelium [118]. In general, they are located close to the basement membrane or a little more deeply as shown in Figure 5.6.

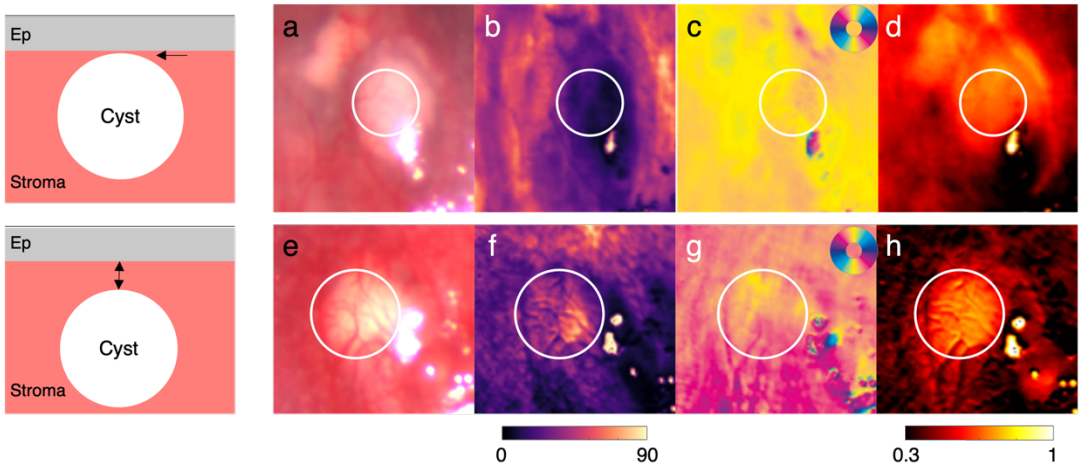

Figure 5.6 Polarimetric images of two cysts from two different cervix. (a, e) The color images of the cysts. White mucus is clearly seen in the white circle. (b, f) The *R* images at 530 nm. Lower *R* is measured at the center of the cyst in (b) because of effaced connective tissue, while *R* remains high at the center of the cyst in (f). (c, g) The *α* images at 530 nm. No noticeable difference is found at the center despite of low *R* in (b). (d, h) The *Δ* images at 530 nm. High *Δ* is observed in the cysts due to a high scattering property of mucus. The schematic illustrations of the 2 cases are depicted on the left.

In addition, the study of the typical polarimetric response of a cyst can provide, in an empirical way, useful information concerning the depth of exploration in the cervical tissue of different polarimetric parameters.

Figure 5.6a shows a cropped image of a cyst in a region of metaplasia for a 31-year-old multiparous pregnant woman at 33 weeks of amenorrhea and 2 days. The white follicle under the translucent cervical epithelium, shown in Figure 5.6a, suggests that the cyst is filled with mucus and is located very superficially, near the basement membrane. Low value of *R* was measured on the zone where the cyst is present. This is because the cyst is probably very close to the basement membrane. Then, the connective tissue between the cyst surface and the basement membrane can be effaced. In this case, the connective tissue between the cyst and the basement membrane is very thin and weakly anisotropic.

In addition, the mucus in the cyst is an isotropic colloidal, which explains the low value of *R* observed in this area. Despite the weak retardance of the collagen layer overlying the cyst, the measured α remains very well oriented and spatially uniform in the area under consideration, as shown in Figure 5.6c. Meantime, the mucus is highly scattering as it

appears white, which explains the higher depolarization Δ of the cist area compared to the surrounding tissue, as shown in Figure 5.6d.

On the other hand, Figure 5.6e shows the cropped image of another cyst in a 37-year-old multiparous pregnant woman at 34 weeks of amenorrhea. The R image in Figure 5.6f is spatially uniform and shows no decrease in anisotropy in the region where the cyst is present, compared to the surrounding areas. In addition, the α image in Figure 5.6g is also spatially uniform and shows no discontinuity in the region of the cyst, which is probably positioned further away from the basement membrane. Therefore, the strong optical anisotropy is determined by the connective tissue layer between the cyst and the basement membrane, which is thicker in this case. The observed anisotropy depends strongly on the position of the cyst in relation to the basement membrane. This result suggests that the optical anisotropy is mainly determined by the most superficial layers of the connective tissue.

Finally, depolarization Δ of the cyst, always due to the mucus, is higher than that of the surrounding tissue, as shown in Figure 5.6h. The increase in depolarization even in this second case where the cyst is placed farther from the basement membrane shows that the depolarization of the cervical tissue comes mainly from the deeper layers of the connective tissue.

5.2 Multispectral Mueller polarimetric analysis of the cervix

The light penetration depth into the cervical tissue varies considerably with the wavelength. This is because the absorption of light by hemoglobin is higher in the blue/green region than in the red/near infrared region of the visible spectrum. Therefore, red/near-infrared light penetrates deeper into the cervical tissue than blue/green light. In this section, we investigate the spectral polarimetric response of the cervix for the different types of cervical epithelia.

As an example, the color image, the R+α image, and the $Rand_{\alpha}$ image at 530 nm are shown in Figure 5.7a-c, respectively. Based on the criteria established above, we selected three squares corresponding to the areas of the ectocervix covered by the SSE (green square - area 1), the MSE (orange square - area 2), and the CE (blue square - area 3), respectively.

The histograms of the three main polarimetric parameters are plotted for all pixels within these three squares for all wavelengths of interest (blue-460 nm, green-530 nm, red-630 nm, magenta-650 nm and black-700 nm). Specifically, the green box, the orange box, and the red box on the right side of Figure 5.7 represent the histograms of the linear phase retardance R, the slow axis azimuth α, and the depolarization Δ for the areas 1, 2, and 3, respectively.

This analysis clearly reveals that linear phase retardance and slow axis azimuth change very slightly for the three selected zones as a function of wavelength. On the contrary, the mean value of the depolarization increases significantly with wavelength while the spread of the histograms progressively decreases. This result shows that the depolarization globally increases with wavelength while becoming more and more spatially homogeneous.

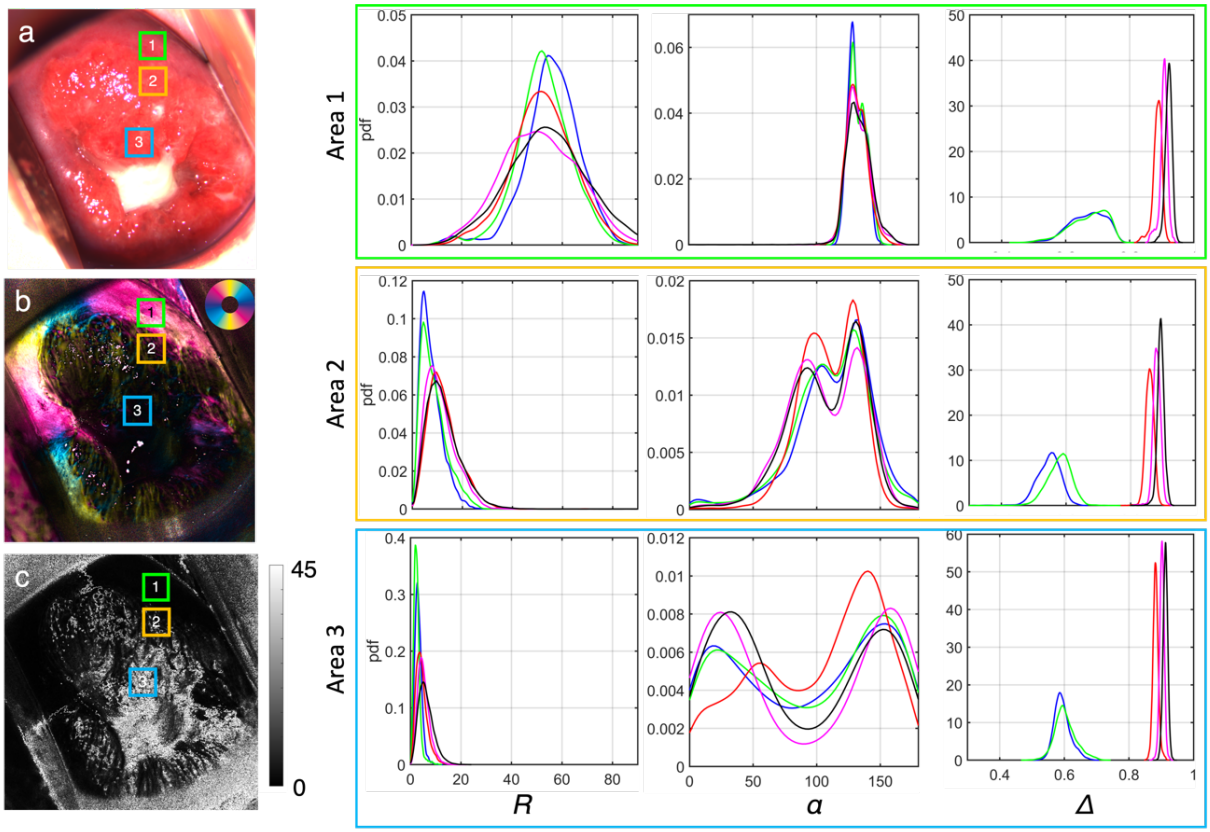

Figure 5.7 The histograms of 3 polarimetric properties at 5 wavelengths (blue-460 nm, green-530 nm, red-630 nm, magenta-650 nm and black-700 nm). The 3 regions are chosen for the SSE (1, marked by the green square), MSE (2, marked by the orange square) and CE (3, marked by the blue square) according to our observations. (a) The color image. (b) The R+α image at 530 nm. (c) The $Rand_{\alpha}$ image at 530 nm. The histograms for each region can be found in the corresponding colored rectangle on the right.

The weak spectral dependency of linear phase retardance and the azimuth indicates that the light signal measuring the optical anisotropy of cervical tissue originates from the same microscopic structures for all wavelengths, even though red light penetrates the tissue much more than blue/green light. Therefore, given the shallow penetration depth of blue/green light, the optical anisotropy observed at all wavelengths, even in the red part of the visible spectrum, is supposed to originate from photons weakly scattered by the most superficial layers of the cervical connective tissue. The penetration length of blue/green light into the cervix being of the order of 500 microns, this could be a confirmation of the fact that the observed anisotropy is the signature of the connective tissue near the basement membrane.

On the contrary, the depolarization at different wavelengths is generated by strongly scattered photons inside the cervical tissue. In particular, the light penetration depth increases with wavelength due to a progressive decrease in hemoglobin absorption. Consequently, the light scattering and thus the depolarization increase with wavelength. The strong spatial inhomogeneity of depolarization observed at 460 nm and 530 nm is predominantly due to the greater absorption of hemoglobin for these wavelengths, whose density can change significantly from one area to another in the most superficial layers of the cervix. In contrast, the higher spatial homogeneity observed at 650 nm and 700 nm is due to the lower absorption of hemoglobin for these wavelengths. In addition, because of

their longer penetration length, these wavelengths provide information about the volume scattering of the cervix, which appears to be very homogeneous.

Finally, for the three selected areas, we investigated the correlation between R and Δ at 530 nm. To do so, we calculated this correlation around each pixel of the image using a 5×5 pixel sliding window.

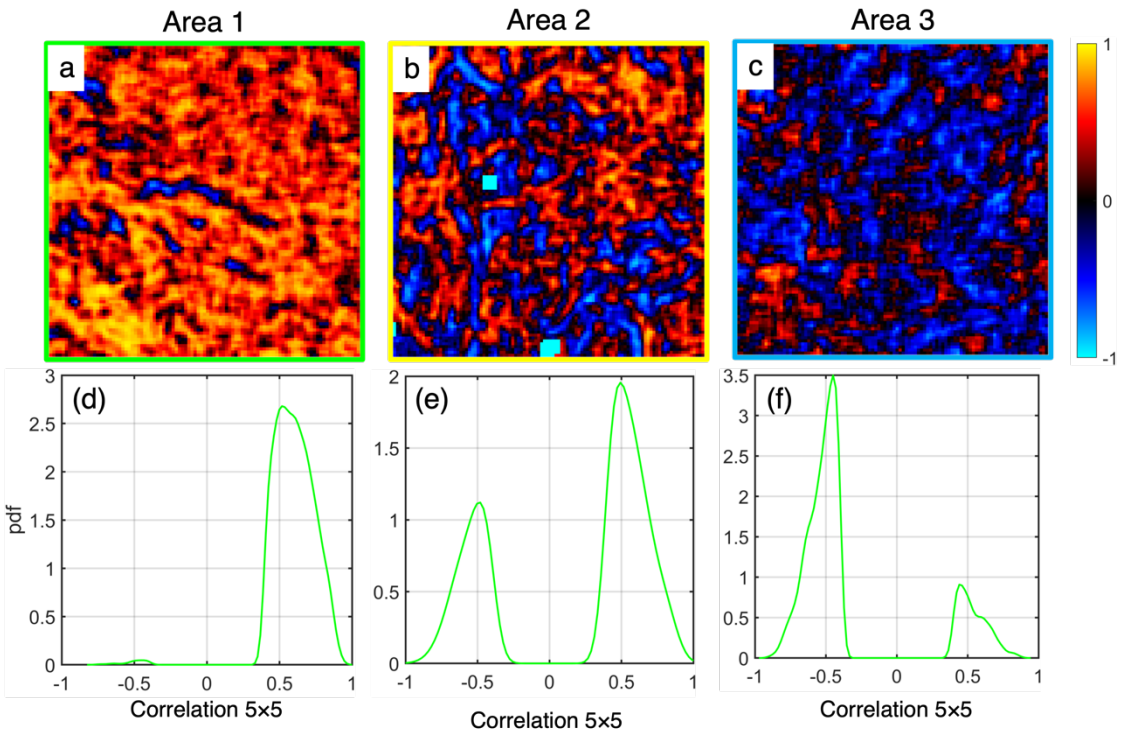

Figure 5.8 The images of linear correlation between α and Δ at 530 nm created by a 5×5 sliding window. For each pixel, correlation was calculated with the surrounding 25 pixels. (a) area 1 (the SSE), (b) area 2 (the MSE), (c) area 3 (the CE) in Figure 5.7. The presence of dense collagen fibers seems related to positive linear correlation between α and Δ. The progression of metaplastic transformation leads to positive correlations. (d-f) The histograms of correlation values in the 3 areas. Only the correlations with $p<0.05$ are considered for the histograms.

Positive linear correlations ($p<0.05$) was predominantly observed in the area corresponding to the SSE (the green square - area 1), as shown in Figure 5.8a. In this case, the linear phase retardance and depolarization seem to have the same microscopic origin. This signature could be attributed to the presence of highly structured and organized collagen fibers in the subepithelial connective tissue.

For the area corresponding to metaplasia (the orange square - area 2), we observed an equivalent distribution of pixels with a positive ($p<0.05$) and negative correlation ($p<0.05$), as shown in Figure 5.8b. This effect could be attributed to a lower density of organized collagen.

Finally, a high negative correlation ($p<0.05$) was observed for the most of pixels contained in the area corresponding to the CE (blue square - area 3), as shown in Figure 5.8c. This effect could be attributed to the almost complete disappearance of organized collagen. The histograms relative to the images shown in Figure 5.8a-c, are depicted in Figure 5.8e-f,

respectively. In the histograms, only the pixels with significant correlations ($p<0.05$) are charted. On the other hand, all the correlations images in Figure 5.8a-c are visualized with regardless of the p-value. For the wavelengths in the red part of the spectrum, these correlations are less obvious due to the considerable contribution of the light scattered by the cervical volume.

5.3 Quantitative analysis of cervical tissue stromal remodeling

5.3.1 Segmentation of the cervix by colposcopic impressions

In the previous sections, we provided detailed characterizations of the polarimetric properties for each type of epithelia that line the ectocervix. In order to quantify the ability of Mueller polarimetric imaging in distinguishing the different types of epithelia, a gold standard is required. The most reliable gold standard would be the histological analysis of biopsies taken from the area of interest on the cervical surface.

This well-defined gold standard allows the determination of established polarimetric criteria to classify the epithelial types according to the underlying relationship between the polarimetric properties and epithelial types. Finally, this segmentation can be used for guiding the biopsies for medical purposes.

However, such a procedure is not applicable in this study because cervical biopsies on pregnant women are not consented. We therefore decided to use a different procedure to evaluate the discriminatory power of the determined polarimetric criteria. To this end, we created a segmentation of the cervical images using criteria based on conventional colpophotography.

As explained above, the SSE has a very smooth appearance on conventional colpophotography. Otherwise, the CE has a grape-like aspect and looks to be composed of villi and crypts. In addition, reddish microcapillaries are visible in the connective tissue that constitutes the villi. The use of intensity images at 530 nm in combination with color images allows for better visualization of the areas covered by the CE.

The identification of metaplastic areas is much more difficult. The early study by Reid and Coppleson defined six possible stages of metaplasia [54]. Since such a detailed classification is not feasible by conventional colposcopic visual inspection, we have defined here only two main stages indicated as middle and late metaplasia.

In the middle metaplasia, the individual villi of the CE begin to fuse to form ridges. To do this, the clefts between the villi are filled with reserve cells that differentiate into squamous cells to form the middle-stage metaplastic epithelium (MME). The goal of this process is to eventually reproduce the SSE. Therefore, the fused villi form a continuous surface that gives the MME a smoother appearance than CE [50], [117]. On the other hand, the thickness of the MME remains quite thin compared to the SSE, which allows the visualization of the underlying connective tissue characterized, at this stage of metaplasia, by the presence of branched or long and parallel vessels [14]. Angiogenesis is indeed one of the main characteristics of the MME.

Late-stage metaplastic epithelium (LME) is characterized by much thicker layer of metaplastic cells than LME and has a visual appearance similar to the SSE. However, the observation of different vessel networks and extensive vascularization, as well as the presence of residual glandular clefts or Nabothian cysts, can help to distinguish the LME from the SSE [50] in conventional colposcopy.

The inspection of 530 nm intensity images in combination with color images allows for better visualization of the areas covered by the MME and LME as well. Mature metaplasia (also called regenerated squamous epithelium) is considered indistinguishable from the SSE by colposcopic observation. Similarly, early metaplasia is very difficult to differentiate from the CE.

The conventional colposcopy criteria used are summarized in Table 5.1.

Table 5.1 The typical features of 4 epithelial types in the colposcopic visual inspection. These features are used as the criteria in the hand-crafted segmentation of the 97 cervix images.

Type of epithelium	Appearance
Squamous epithelium (matured metaplasia)	Smooth surface, pinkish-red color [13], [14]
Late stage of metaplasia	Thick smooth surface, higher vascularity than the marginal squamous epithelia, branched vessels, presence of gland openings and cysts [14]
Mid stage of metaplasia	Loss of outline of component villi, elongated formations of villi coalesced into ridges, coarse surface without villi, branched vessels on the fused villi, thin epithelia with branched vessels[12]–[14]
Columnar epithelium	Individual villi, red color [12], [14]

While the identification of SSE and CE seems “possible” in conventional colposcopy (which is not always true), albeit in a very qualitative way, the accurate detection of TZ and different degrees of metaplasia using the criteria described above remains very difficult and cannot be done *in vivo*.

With the help of the practitioner involved in the project, based on the criteria summarized in Table 5.1, 97 cervical images were segmented with hand-drawn polygons without considering the polarimetric images. This task was time-consuming (approximately 4 weeks), which made us realize that the *in vivo* use of these criteria to accurately determine the TZ and distinguish different degrees of metaplasia is practically impossible.

Areas on the images that could generate artifacts, such as specular reflections, the external os, and mucus, were carefully excluded from the segmentations during the post-processing stage. Because individual areas were selected on the basis of qualitative criteria, without application of acetic acid or iodine and without biopsy, misclassification with respect to actual epithelial types may exist.

Figure 5.8 shows four segmented example images of the cervix compared to relative color images. Finally, we considered four different types of epithelia: the stratified squamous epithelium (SSE), the columnar epithelium (CE), the middle metaplastic epithelium (MME), and the late metaplastic epithelium (LME).

Then, in total three polarimetric parameters were chosen based on the observations in previous sections: the linear phase retardance R, the randomness of the slow axis azimuth $Rand_\alpha$, and the correlation between the depolarization and the linear phase retardance, at 530 nm.

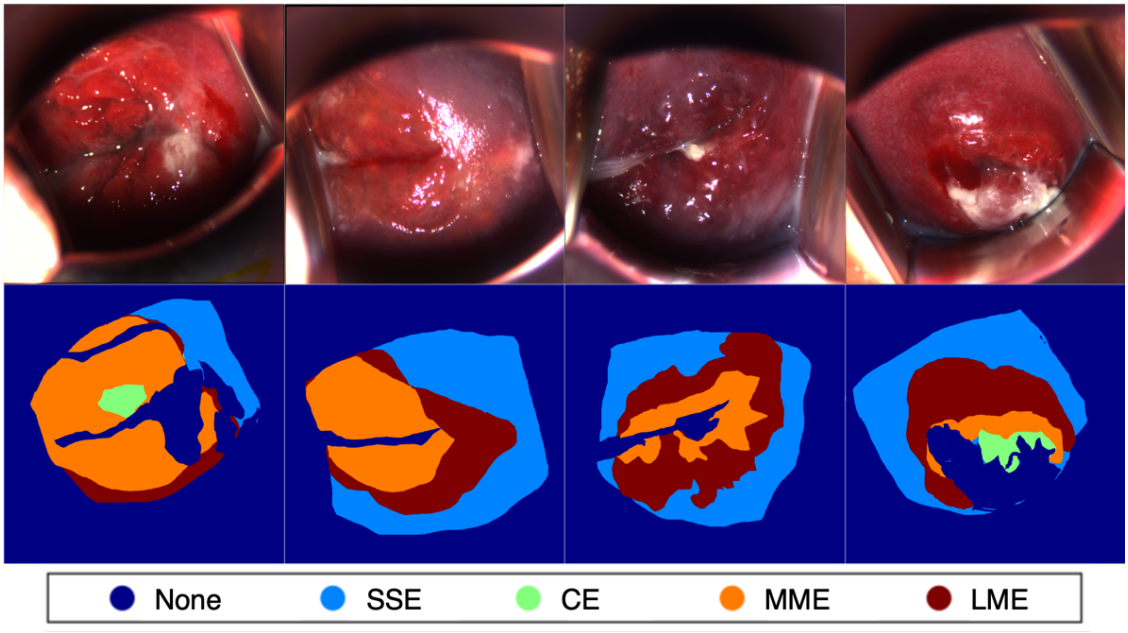

Figure 5.9 The color images of four different cervices (top) and their mask images segmented by conventional colposcopic impression (bottom). The color images along with the M_{11} images at 530 nm were thoroughly inspected according to the criteria in Table 5.1 to determine their epithelial types more reasonably. Despite these efforts, this segmentation method is not 100% reliable. The class 'None' denotes 'not classified' (not a cervical area).

Among the 97 cervices, 91, 88, 77, and 39 contained areas covered by SSE, LME, MME, and CE, respectively. Areas of CE were relatively rare because of the very active metaplastic transformations during pregnancy. In addition, the extensive presence of mucus on the cervix of pregnant women often prevented the visualization of the CE.

Figure 5.10 shows the statistical analysis performed to evaluate the ability of the selected polarimetric parameters to discriminate the four epithelial types. The SSE has the highest R (range between 23° and 37° at 25th and 75th percentile), and the lowest $Rand_\alpha$ (range between 1.7° and 4.3° at 25th and 75th percentile), whereas the CE has the lowest R (range between 3.0° and 4.5° at 25th and 75th percentile) and the highest $Rand_\alpha$ (range between 17° and 26° at 25th and 75th percentile). The metaplastic zones are characterized by R and $Rand_\alpha$ intermediate between those of the SSE and the CE.

In particular, the MME has higher R and lower $Rand_\alpha$ than the LME. The parameters R and $Rand_\alpha$ showed very strong discriminatory power between SSE and LME, between LME and MME, and between MME and CE with $p<10^{-5}$ (denoted by ***) in the t-test. This

statistical analysis quantitatively confirms the visual observations described in the previous sections, namely that the metaplastic transformations of the cervix involve both epithelium and underlying connective tissue. In particular, the progression of a metaplastic transformation produces an increase in optical anisotropy (consisting in an increase in R and a decrease in $Rand_\alpha$) due to a process of remodeling and reorganization of the connective tissue near the basement membrane.

Finally, also the correlation between R and Δ showed a discriminatory power between SSE and LME ($p<0.001$), between LME-MME ($<10^{-5}$), and between MME-CE ($p<0.001$) in the t-test. The correlation between R and Δ at 550 nm is lower for the CE while it is maximal for the SSE. For metaplastic areas, this correlation has an intermediate value between CE and SSE. In particular, it is higher for the LME than for the MME.

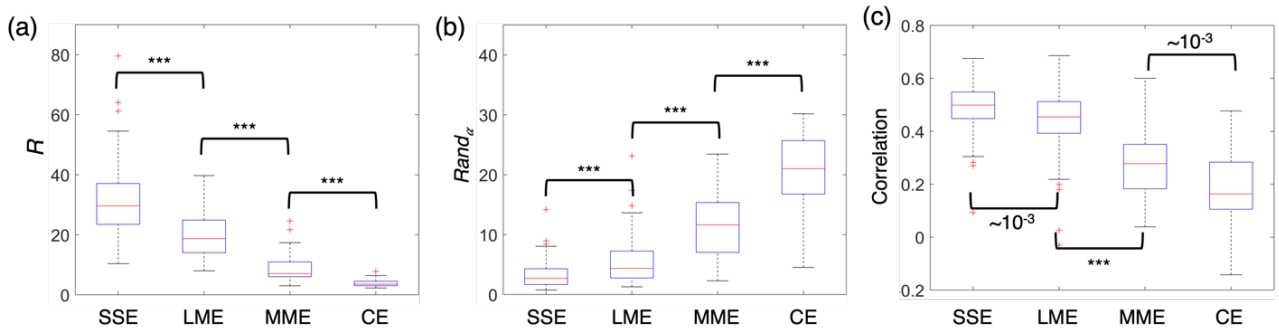

Figure 5.10 The box plots of three polarimetric parameters for the four different epithelial types. The spatial mean values of the parameters were calculated for each type and each cervix. (a) The box plot for linear retardance R. (b) The box plot for randomness of the slow axis azimuth of retardance $Rand_\alpha$. (c) The box plot for correlation between R and depolarization Δ. ***: $p<10^{-5}$. The 3 parameters are significantly discriminative for the four epithelial types.

5.3.2 Stromal dynamics during metaplastic transitions

Metaplastic transformations were observed in most of the cervixes analyzed. Indeed, metaplastic transformations are usually very frequent on the cervix of pregnant women because of the strong hormonal alterations during gestation. However, most of the analyzed cervixes were imaged at some time point. Therefore, the stage of the metaplastic modifications was different for each cervix analyzed. In addition, areas of metaplastic transformation at different stages were also observed on the same cervix.

To illustrate the overall dynamics of the metaplastic transformation process, Figure 5.11 shows 7 metaplastic regions at different advancement stages, selected from the images of 7 different cervixes. This approach allows a fairly intuitive description and direct visualization of the remodeling process of connective tissue underlying cervical epithelia during the metaplastic transformation.

Moreover, even if the images are taken by different cervixes, this description is very reliable because the different polarimetric parameters considered, in particular the linear phase retardance and the slow axis azimuth randomness, are characterized by well-defined

and very well-separated intervals of variability between the different types of epithelium considered, as shown in Figure 5.10a and b.

In Figure 5.11, the first row shows the reference color images. The second row shows the images of the M_{11} (unpolarized light intensity) at 530 nm. The third row shows the images that merge the linear phase retardance with the slow axis azimuth. The fourth row shows the images of the slow axis azimuth randomness. The fifth line shows the images of the correlation between the linear phase retardance and the depolarization at 530 nm.

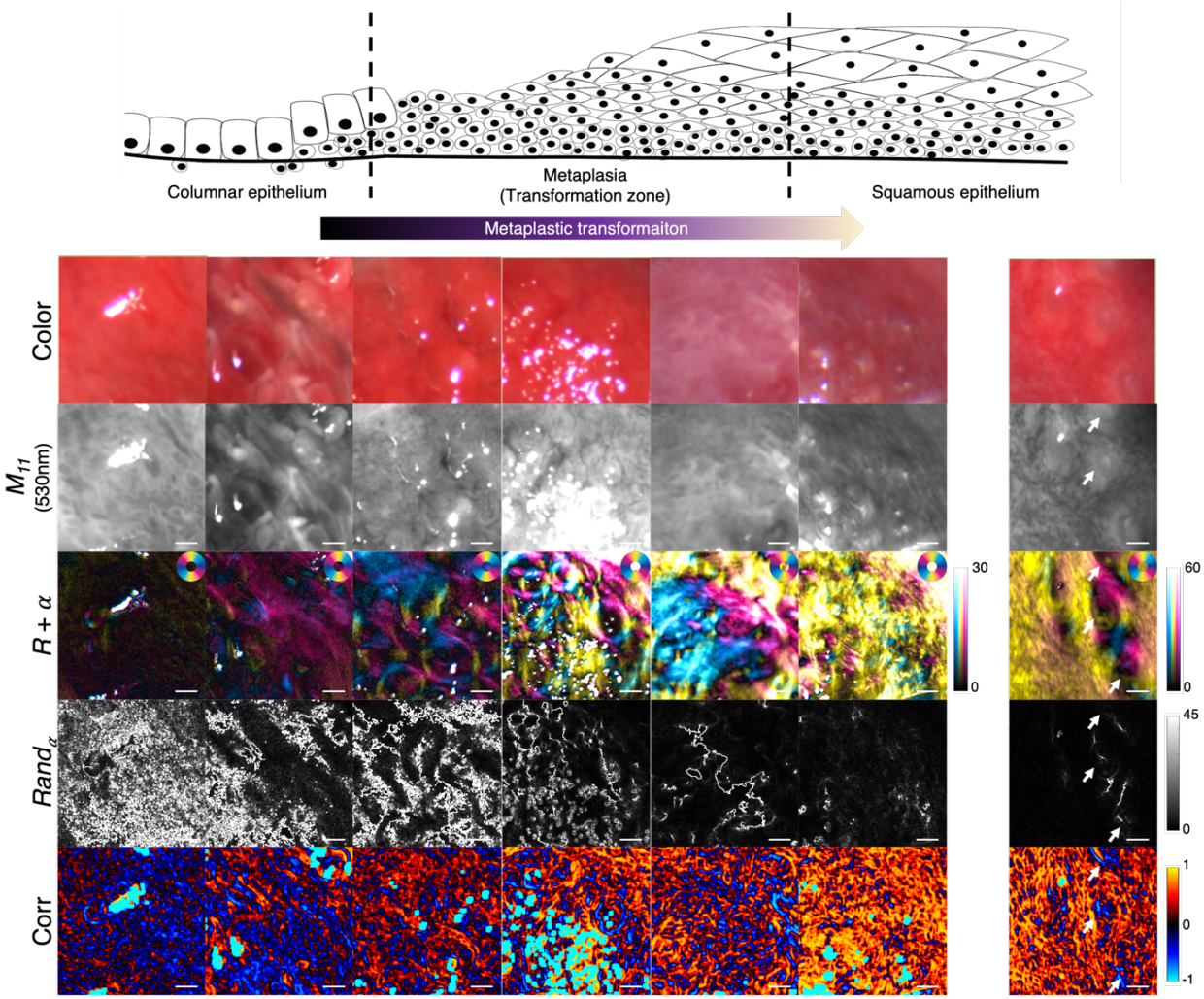

Figure 5.11 Seven cropped cervical areas from seven cervices. They are thought to be in different stages of metaplastic transformation. They are arranged based on the result of Figure 5.10. The first column corresponds to the CE. The second~fourth columns are thought to correspond to the MME. The fifth and sixth columns correspond to the LME. The last column is classified as the matured MSE because of the presence of gland openings (the white arrows).

One might notice that the different degrees of a metaplastic transformation are very difficult to detect with color images. The M_{11} images at 530 nm clearly show the presence of villi and crypts for the CE. These structures fuse together to form an increasingly smooth cervical surface as metaplastic transformation progresses. Vessels also appear during this process. In the final stage of transformation, the cervical surface appears more compact and composed of organized structures. Even the assessment of metaplastic progression using the M_{11} remains difficult. The combined use of color and M_{11} images to distinguish the different

stages of metaplasia development is a very qualitative procedure, which is also time consuming (thus difficult to use in clinic) and may require an experienced practitioner.

On the other hand, polarimetric images are much more contrasted and allow a clearer visualization of the different stages of a metaplastic transformation. Metaplastic transformation denotes an epithelial conversion from the CE into the SSE. This process involves not only the epithelium overlying the ectocervix but also the underlying connective tissue close to the basement membrane. As shown in Figure 5.11, polarimetric images allow a clear visualization of the connective tissue remodeling process. In particular, the $R{+}\alpha$ image combined with the $Rand_{\alpha}$ image allows clearly visualizing the different steps of this process.

Putting the results together, the CE is characterized by a low anisotropy which results in a low value of the linear phase retardance R and a very high randomness. The collagen in the connective tissue underlying the CE, which is highly disorganized and isotropic, gradually begins to form well-separated linearized fiber bundles that may have elongated shapes or be organized into rings. In this case, the optical anisotropy of tissue is spatially very inhomogeneous.

In a second phase, these bundles merge to create a smoother surface that mimics the structure of the SSE. In this case, the anisotropy is spatially more homogeneous in comparison to the CE. However, the subepithelial connective tissue remains predominantly disorganized.

The final stage of this process is the complete restructuring of the collagen, which is organized into well-compacted, highly dense bundles of linearized fibers distributed in a circularly relative to the endocervical canal.

During the progression of this connective tissue restructuring process, an overall increase in R is observed with a decrease in$Rand_{\alpha}$. The reconstructed SSE (the last column in Figure 5.11) is characterized by strong R and nearly zero $Rand_{\alpha}$.

Finally, the correlation image between R and the depolarization Δ also makes it possible to monitor the evolution of a metaplastic transformation. Indeed, this correlation is mainly negative for the CE. Areas of positive correlation begin to appear and become more frequent as metaplastic transformation progresses. At the end of the transformation process, a higher positive correlation is observed for the reconstructed SSE.

5.4 Conclusions

In this chapter, we analyzed the cervical polarimetric response of 97 pregnant women examined during the COLPOTERME study in the Department of Gynecology and Obstetrics at the University Hospital of Kremlin-Bicêtre.

In particular, we characterized the polarimetric response of each type of epithelium covering the surface of the cervix including glandular epithelium, squamous epithelium and different grades of metaplasia. Optical anisotropy parameters allow the direct visualization and quantitative characterization of the connective tissue underlying each type of epithelium by providing a direct information on the density and organization of collagen fiber bundles.

We found that the structure of the subepithelial collagen is highly dependent on the type of epithelium considered. In particular, the glandular epithelium is characterized by a very low optical anisotropy, the subepithelial collagen being strongly isotropic in this case. In contrast, the squamous epithelium is characterized by a very strong anisotropy, whose the subepithelial connective tissue is characterized by linearized and well-organized fiber bundles.

The metaplastic epithelium has an intermediate anisotropy between the glandular epithelium and the squamous epithelium. Specifically, during a metaplastic transformation, the totally isotropic connective tissue underlying the glandular epithelium begins to reorganize into discontinuous rings or linearized structures that gradually coalesce until they form a smooth surface with increased anisotropy. The final stage of the process is the formation of the squamous epithelium with an underlying connective tissue composed of highly structured, linearized and dense fiber bundles. Then, during a metaplastic transformation, a process of restructuring and reorganization of collagen is observed in the subepithelial connective tissue. More precisely, the optical anisotropy progressively increases with the progression of the metaplastic transformation.

For the first time to our knowledge, thanks to the unequalled performance of the polarimetric system built during this thesis, we are able to visualize and quantify the remodeling process of the connective tissue close to the basement membrane, information that is inaccessible to conventional colposcopy or to other techniques. This study has shown that metaplastic transformation is a very complex process involving not only the epithelium but also the connective tissue close to the basement membrane.

GENERAL CONCLUSIONS

This thesis was carried out within the framework of the COLPOTERME clinical project developed in collaboration with the Department of Gynecology and Obstetrics of the Bicêtre University Hospital (France). The objective of this thesis was to carry out the key steps to launch a clinical study dedicated to test the Mueller polarimetric imaging on a massive number of pregnant women in vivo in order to verify the capacity of this technique to follow the remodeling of the cervical microstructure during pregnancy.

To do so, we designed and built a novel multispectral Mueller polarimetric colposcope with unparalleled performance (in terms of acquisition speed, spatial resolution, etc.) that can acquire images at 5 different wavelengths to explore the cervical tissue at different depths. Important work has also been done to create an intuitive software with a simple user interface and to set up a relational database allowing the management of massive amounts of data.

In addition, we worked on the ergonomics of the system so that the novel MPC could meet the requirements of a clinical study. The new system is currently installed at the University Hospital of Kremlin-Bicêtre to be tested *in vivo*. After successfully completing this step, we worked on the analysis of the images acquired for 97 patients, focusing exclusively on the polarimetric characterization of the epithelium. To do so, we mainly considered the anisotropy parameters.

Thanks to the unparalleled performance of this new device, we were able to obtain information on the cervical microstructure that was totally inaccessible to conventional colposcopy. For the first time to our knowledge, we were able to visualize with a macroscopic field of view, the structure of the sub-epithelial connective tissue which undergoes a process of reorganization and restructuring during a metaplastic transformation. We were able to demonstrate quantitatively that metaplastic transformation is a very complex process involving both the epithelium and the underlying connective tissue.

The next step is to use the determined polarimetric parameters for discriminating the different phases of a metaplastic transformation to create an automated segmentation of the cervical tissue using machine learning or deep learning algorithms. Subsequently, the anisotropy parameters will be correlated with depolarization parameters at different wavelengths and their evolution as a function of pregnancy progression will be studied. The clinical study foresees the analysis of a total of 650 patients, 400 of them with full term delivery and 250 with high risk of preterm delivery. Each patient will be analyzed 1 to 5 times during the pregnancy (on average 3 times) depending on gestational age at the time of recruitment for a total of approximately 2000 colposcopies. This clinical study is a world first. Indeed, for the first time, Mueller polarimetry is tested *in vivo* on a cohort of patients.

The use of specific algorithms will be necessary for the management and statistical processing of such a large amount of data. For this purpose, a collaboration is underway with the CMAP laboratory of the École Polytechnique, specialized in data processing. It should also be noted that the study on metaplasias carried out so far will also have a considerable impact on the early detection of cervical cancer. Indeed, the greatest difficulty in the

detection of precancerous lesions lies in the fact that traditional colposcopy after the application of acetic acid is not able to distinguish them from metaplasias. The ability of Mueller polarimetry to effectively distinguish between different degrees of metaplasia could allow better visualization of precancerous areas of the cervix. A clinical study of 200 patients is currently in preparation.

REFERENCES

[1] D. H. Goldstein, *Polarized Light*. CRC Press, 2017. [Online]. Available: https://books.google.fr/books?id=w6PMBQAAQBAJ

[2] J. J. Gil Pérez and R. Ossikovski, *Polarized Light and the Mueller Matrix Approach*. Boca Raton, FL : CRC Press, Taylor & Francis Group, [2016] | "2016 | Series: Series in optics and optoelectronics ; 21: CRC Press, 2017. doi: 10.1201/b19711.

[3] S. Cloude, *Polarisation: Applications in Remote Sensing*. Oxford University Press, 2010. [Online]. Available: https://books.google.fr/books?id=K1SokgEACAAJ

[4] J. Vizet *et al.*, "In vivo imaging of uterine cervix with a Mueller polarimetric colposcope," *Sci Rep*, vol. 7, no. 1, pp. 1–12, 2017, doi: 10.1038/s41598-017-02645-9.

[5] J. J. Gil, "Polarimetric characterization of light and media," *The European Physical Journal Applied Physics*, vol. 40, no. 1, pp. 1–47, Oct. 2007, doi: 10.1051/epjap:2007153.

[6] R. Ossikovski, "Canonical forms of depolarizing Mueller matrices," *Journal of the Optical Society of America A*, vol. 27, no. 1, p. 123, Jan. 2010, doi: 10.1364/JOSAA.27.000123.

[7] J. Qi and D. S. Elson, "Mueller polarimetric imaging for surgical and diagnostic applications: a review," *J Biophotonics*, vol. 10, no. 8, pp. 950–982, Aug. 2017, doi: 10.1002/jbio.201600152.

[8] M. R. Foreman and F. Goudail, "On the equivalence of optimization metrics in Stokes polarimetry," *Optical Engineering*, vol. 58, no. 08, p. 1, Mar. 2019, doi: 10.1117/1.OE.58.8.082410.

[9] G. Anna and F. Goudail, "Optimal Mueller matrix estimation in the presence of Poisson shot noise," *Opt Express*, vol. 20, no. 19, p. 21331, Sep. 2012, doi: 10.1364/OE.20.021331.

[10] E. Compain, S. Poirier, and B. Drevillon, "General and self-consistent method for the calibration of polarization modulators, polarimeters, and Mueller-matrix ellipsometers," *Appl Opt*, vol. 38, no. 16, p. 3490, 1999, doi: 10.1364/AO.38.003490.

[11] G. H. Golub and C. F. van Loan, *Matrix Computations*. Johns Hopkins University Press, 1983. [Online]. Available: https://books.google.fr/books?id=g4gQAQAAIAAJ

[12] J. Brewer, "Kronecker products and matrix calculus in system theory," *IEEE Trans Circuits Syst*, vol. 25, no. 9, pp. 772–781, Sep. 1978, doi: 10.1109/TCS.1978.1084534.

[13] W. H. Steeb and Y. Hardy, *Matrix Calculus and Kronecker Product: A Practical Approach to Linear and Multilinear Algebra*. World Scientific, 2011. [Online]. Available: https://books.google.fr/books?id=-dia2irg1WQC

[14] A. Lindberg, J. Vizet, J. Rehbinder, C. Gennet, J.-C. Vanel, and A. Pierangelo, "Innovative integrated numerical-experimental method for high-performance multispectral Mueller polarimeters based on ferroelectric liquid crystals," *Appl Opt*, vol. 58, no. 19, p. 5187, Jul. 2019, doi: 10.1364/AO.58.005187.

[15] J. S. Tyo, "Design of optimal polarimeters: maximization of signal-to-noise ratio and minimization of systematic error," *Appl Opt*, vol. 41, no. 4, p. 619, Feb. 2002, doi: 10.1364/AO.41.000619.

[16] E. Garcia-Caurel, A. de Martino, and B. Drévillon, "Spectroscopic Mueller polarimeter based on liquid crystal devices," *Thin Solid Films*, vol. 455–456, pp. 120–123, May 2004, doi: 10.1016/j.tsf.2003.12.056.

[17] A. Peinado, A. Lizana, and J. Campos, "Optimization and tolerance analysis of a polarimeter with ferroelectric liquid crystals," *Appl Opt*, vol. 52, no. 23, p. 5748, Aug. 2013, doi: 10.1364/AO.52.005748.

[18] L. M. S. Aas, P. G. Ellingsen, M. Kildemo, and M. Lindgren, "Dynamic response of a fast near infra-red Mueller matrix ellipsometer," *J Mod Opt*, vol. 57, no. 17, pp. 1603–1610, Oct. 2010, doi: 10.1080/09500340.2010.515750.

[19] C. Macías-Romero and P. Török, "Eigenvalue calibration methods for polarimetry," *J Eur Opt Soc Rapid Publ*, vol. 7, p. 12004, Mar. 2012, doi: 10.2971/jeos.2012.12004.

[20] H. Hu, E. Garcia-Caurel, G. Anna, and F. Goudail, "Maximum likelihood method for calibration of Mueller polarimeters in reflection configuration," *Appl Opt*, vol. 52, no. 25, p. 6350, Sep. 2013, doi: 10.1364/AO.52.006350.

[21] A. N. Langville and W. J. Stewart, "The Kronecker product and stochastic automata networks," *J Comput Appl Math*, vol. 167, no. 2, pp. 429–447, Jun. 2004, doi: 10.1016/j.cam.2003.10.010.

[22] A. de Martino, E. Garcia-Caurel, B. Laude, and B. Drévillon, "General methods for optimized design and calibration of Mueller polarimeters," *Thin Solid Films*, vol. 455–456, pp. 112–119, May 2004, doi: 10.1016/j.tsf.2003.12.052.

[23] R. Ossikovski, M. Anastasiadou, S. ben Hatit, E. Garcia-Caurel, and A. de Martino, "Depolarizing mueller matrices: How to decompose them?," *Physica Status Solidi (A) Applications and Materials Science*, vol. 205, no. 4, pp. 720–727, Apr. 2008, doi: 10.1002/pssa.200777793.

[24] S.-Y. Lu and R. A. Chipman, "Interpretation of Mueller matrices based on polar decomposition," *Journal of the Optical Society of America A*, vol. 13, no. 5, p. 1106, May 1996, doi: 10.1364/JOSAA.13.001106.

[25] R. Ossikovski, "Interpretation of nondepolarizing Mueller matrices based on singular-value decomposition," *Journal of the Optical Society of America A*, vol. 25, no. 2, p. 473, Feb. 2008, doi: 10.1364/JOSAA.25.000473.

[26] D. H. Goldstein, “Mueller matrix dual-rotating retarder polarimeter,” *Appl Opt*, vol. 31, no. 31, p. 6676, Nov. 1992, doi: 10.1364/AO.31.006676.

[27] A. de Martino, Y.-K. Kim, E. Garcia-Caurel, B. Laude, and B. Drévillon, “Optimized Mueller polarimeter with liquid crystals,” *Opt Lett*, vol. 28, no. 8, p. 616, Apr. 2003, doi: 10.1364/OL.28.000616.

[28] A. Peinado, A. Lizana, J. Vidal, C. Iemmi, and J. Campos, “Optimization and performance criteria of a Stokes polarimeter based on two variable retarders,” *Opt Express*, vol. 18, no. 10, p. 9815, May 2010, doi: 10.1364/OE.18.009815.

[29] O. Arteaga, J. Freudenthal, B. Wang, and B. Kahr, “Mueller matrix polarimetry with four photoelastic modulators: theory and calibration,” *Appl Opt*, vol. 51, no. 28, p. 6805, Oct. 2012, doi: 10.1364/AO.51.006805.

[30] S. Alali, A. Gribble, and I. Alex Vitkin, “Rapid wide-field Mueller matrix polarimetry imaging based on four photoelastic modulators with no moving parts,” *Opt Lett*, vol. 41, no. 5, p. 1038, Mar. 2016, doi: 10.1364/OL.41.001038.

[31] A. Pierangelo *et al.*, “Multispectral Mueller polarimetric imaging detecting residual cancer and cancer regression after neoadjuvant treatment for colorectal carcinomas,” *J Biomed Opt*, vol. 18, no. 4, p. 046014, Apr. 2013, doi: 10.1117/1.JBO.18.4.046014.

[32] J. M. Bueno and P. Artal, “Double-pass imaging polarimetry in the human eye,” *Opt Lett*, vol. 24, no. 1, p. 64, Jan. 1999, doi: 10.1364/OL.24.000064.

[33] J. M. Bueno, “Measurement of parameters of polarization in the living human eye using imaging polarimetry,” *Vision Res*, vol. 40, no. 28, pp. 3791–3799, Dec. 2000, doi: 10.1016/S0042-6989(00)00220-0.

[34] S. L. Jacques, J. R. Roman, and K. Lee, “Imaging superficial tissues with polarized light,” *Lasers Surg Med*, vol. 26, no. 2, pp. 119–129, 2000, doi: 10.1002/(SICI)1096-9101(2000)26:2<119::AID-LSM3>3.0.CO;2-Y.

[35] Z. Huang, Y. Fu, Z. Li, and J. Wu, “A Portable 3×3 Mueller Matrix Polarimeter Prototype for Cancer Detection Ex Vivo,” in *Proceedings of the 3rd International Conference on Biomedical Signal and Image Processing - ICBIP ’18*, 2018, pp. 92–97. doi: 10.1145/3278229.3278244.

[36] J. Chung, W. Jung, M. J. Hammer-Wilson, P. Wilder-Smith, and Z. Chen, “Use of polar decomposition for the diagnosis of oral precancer,” *Appl Opt*, vol. 46, no. 15, p. 3038, May 2007, doi: 10.1364/AO.46.003038.

[37] M. Kupinski *et al.*, “Polarimetric measurement utility for pre-cancer detection from uterine cervix specimens,” *Biomed Opt Express*, vol. 9, no. 11, p. 5691, Nov. 2018, doi: 10.1364/BOE.9.005691.

[38] E. Du *et al.*, “Mueller matrix polarimetry for differentiating characteristic features of cancerous tissues,” *J Biomed Opt*, vol. 19, no. 7, p. 076013, Jul. 2014, doi: 10.1117/1.JBO.19.7.076013.

[39] J. Rehbinder *et al.*, “Diagnosis of uterine cervix cancer using Müller polarimetry: a comparison with histopathology,” in *Novel Biophotonics Techniques and Applications III*, 2015, vol. 9540, p. 95400W. doi: 10.1117/12.2192423.

[40] J. Rehbinder *et al.*, “Ex vivo Mueller polarimetric imaging of the uterine cervix: a first statistical evaluation,” *J Biomed Opt*, vol. 21, no. 7, p. 071113, 2016, doi: 10.1117/1.JBO.21.7.071113.

[41] M.-R. Antonelli *et al.*, “Mueller matrix imaging of human colon tissue for cancer diagnostics: how Monte Carlo modeling can help in the interpretation of experimental data.,” *Opt Express*, vol. 18, no. 10, pp. 10200–8, 2010, doi: 10.1364/OE.18.010200.

[42] A. Pierangelo *et al.*, “Polarimetric imaging of uterine cervix : a case study,” *Opt Express*, vol. 21, no. 12, pp. 281–289, 2013, doi: 10.1364/OE.21.014120.

[43] C. Bonnans, J. Chou, and Z. Werb, “Remodelling the extracellular matrix in development and disease,” *Nat Rev Mol Cell Biol*, vol. 15, no. 12, pp. 786–801, Dec. 2014, doi: 10.1038/nrm3904.

[44] J. Vizet *et al.*, “Optical fiber-based full Mueller polarimeter for endoscopic imaging using a two-wavelength simultaneous measurement method,” *J Biomed Opt*, vol. 21, no. 7, p. 071106, 2016, doi: 10.1117/1.JBO.21.7.071106.

[45] M. Dubreuil *et al.*, “Mueller matrix polarimetry for improved liver fibrosis diagnosis,” *Opt Lett*, vol. 37, no. 6, p. 1061, Mar. 2012, doi: 10.1364/OL.37.001061.

[46] Y. Wang *et al.*, “Mueller matrix microscope: a quantitative tool to facilitate detections and fibrosis scorings of liver cirrhosis and cancer tissues,” *J Biomed Opt*, vol. 21, no. 7, p. 071112, Apr. 2016, doi: 10.1117/1.JBO.21.7.071112.

[47] P. Schucht *et al.*, “Visualization of White Matter Fiber Tracts of Brain Tissue Sections With Wide-Field Imaging Mueller Polarimetry,” *IEEE Trans Med Imaging*, vol. 39, no. 12, pp. 4376–4382, Dec. 2020, doi: 10.1109/TMI.2020.3018439.

[48] J. B. de Tomasi, M. M. Opata, and C. N. Mowa, “Immunity in the cervix: Interphase between immune and cervical epithelial cells,” *Journal of Immunology Research*, vol. 2019. Hindawi Limited, 2019. doi: 10.1155/2019/7693183.

[49] A. S. C. C. Pathology, E. J. Mayeaux, and J. T. Cox, *Modern Colposcopy Textbook and Atlas*. Wolters Kluwer Health, 2011. [Online]. Available: https://books.google.fr/books?id=3lEtAxpNLewC

[50] E. J. Mayeaux and J. T. Cox, *Modern Colposcopy Textbook and Atlas*. Wolters Kluwer Health, 2011. [Online]. Available: https://books.google.fr/books?id=3lEtAxpNLewC

[51] F. Remoue, N. Jacobs, V. Miot, J. Boniver, and P. Delvenne, “High intraepithelial expression of estrogen and progesterone receptors in the transformation zone of the uterine cervix,” *Am J Obstet Gynecol*, vol. 189, no. 6, pp. 1660–1665, Dec. 2003, doi: 10.1016/S0002-9378(03)00852-4.

[52] T. Kurita, P. S. Cooke, and G. R. Cunha, “Epithelial-stromal tissue interaction in paramesonephric (Müllerian) epithelial differentiation,” *Dev Biol*, vol. 240, no. 1, pp. 194–211, Dec. 2001, doi: 10.1006/dbio.2001.0458.

[53] P. Gariglio, J. Gutiérrez, E. Cortés, and J. Vázquez, “The Role of Retinoid Deficiency and Estrogens as Cofactors in Cervical Cancer,” *Archives of Medical Research*, vol. 40, no. 6. pp. 449–465, Aug. 2009. doi: 10.1016/j.arcmed.2009.08.002.

[54] B. L. Reid and M. Coppleson, “Physiological Metaplasia on the Human Cervix Uteri.,” *Aust N Z J Obstet Gynaecol*, vol. 4, no. 2, pp. 49–61, Jun. 1964, doi: 10.1111/j.1479-828X.1964.tb00254.x.

[55] B. L. Reid, W. J. Garrett, and J. V. M. Coppleson, “Two Types of Squamous Epithelium of the Human Ectocervix A Histological and Colposcopic Study,” *Aust N Z J Obstet Gynaecol*, vol. 3, no. 1, pp. 1–8, Mar. 1963, doi: 10.1111/j.1479-828X.1963.tb00207.x.

[56] H. K. Zinser and K. A. Rosenbauer, “Studies on the angioarchitectonics of the cervix uteri in normal and pathological conditions,” *Arch Gynecol Obstet*, vol. 194, no. 1, pp. 73–112, 1960, doi: 10.1007/BF00668894.

[57] A. Singer, “THE UTERINE CERVIX FROM ADOLESCENCE TO THE MENOPAUSE,” *BJOG*, vol. 82, no. 2, pp. 81–99, Feb. 1975, doi: 10.1111/j.1471-0528.1975.tb02204.x.

[58] J. P. Nott, E. A. Bonney, J. D. Pickering, and N. A. B. Simpson, “The structure and function of the cervix during pregnancy,” *Translational Research in Anatomy*, vol. 2, pp. 1–7, Mar. 2016, doi: 10.1016/j.tria.2016.02.001.

[59] P. Fratzl, *Collagen: Structure and mechanics*. Boston, MA: Springer US, 2008. doi: 10.1007/978-0-387-73906-9.

[60] R. M. Aspden, “Collagen Organisation in the Cervix and its Relation to Mechanical Function,” 1988.

[61] G. Yao and L. v. Wang, “Two-dimensional depth-resolved Mueller matrix characterization of biological tissue by optical coherence tomography,” *Opt Lett*, vol. 24, no. 8, p. 537, 2008, doi: 10.1364/ol.24.000537.

[62] T. Y. Lau, H. K. Sangha, E. K. Chien, B. L. Mcfarlin, A. J. Wagoner Johnson, and K. C. Toussaint, “Application of Fourier transform-second-harmonic generation imaging to the rat cervix,” *J Microsc*, vol. 251, no. 1, pp. 77–83, Jul. 2013, doi: 10.1111/jmi.12046.

[63] Y. Gan, W. Yao, Kristin. M. Myers, J. Y. Vink, Ronald. J. Wapner, and C. P. Hendon, “Analyzing three-dimensional ultrastructure of human cervical tissue using optical

coherence tomography," *Biomed Opt Express*, vol. 6, no. 4, p. 1090, Apr. 2015, doi: 10.1364/boe.6.001090.

[64] B. L. Reid, W. J. Garrett, and J. V. M. Coppleson, "Two Types of Squamous Epithelium of the Human Ectocervix A Histological and Colposcopic Study," *Aust N Z J Obstet Gynaecol*, vol. 3, no. 1, pp. 1–8, Mar. 1963, doi: 10.1111/j.1479-828X.1963.tb00207.x.

[65] B. L. Reid and M. Coppleson, "Physiological Metaplasia on the Human Cervix Uteri A Colposeopie and Histological Correlative Study of the Earliest Stages," 1964.

[66] C. Bonnans, J. Chou, and Z. Werb, "Remodelling the extracellular matrix in development and disease," *Nature Reviews Molecular Cell Biology*, vol. 15, no. 12. Nature Publishing Group, pp. 786–801, Dec. 11, 2014. doi: 10.1038/nrm3904.

[67] M. Herfs, P. Hubert, and P. Delvenne, "Epithelial metaplasia: adult stem cell reprogramming and (pre)neoplastic transformation mediated by inflammation?," *Trends Mol Med*, vol. 15, no. 6, pp. 245–253, Jun. 2009, doi: 10.1016/j.molmed.2009.04.002.

[68] D. R. Lowy, D. Solomon, A. Hildesheim, J. T. Schiller, and M. Schiffman, "Human papillomavirus infection and the primary and secondary prevention of cervical cancer," *Cancer*, vol. 113, no. S7, pp. 1980–1993, Sep. 2008, doi: 10.1002/cncr.23704.

[69] T. Novikova, "Optical techniques for cervical neoplasia detection," *Beilstein Journal of Nanotechnology*, vol. 8, pp. 1844–1862, Sep. 2017, doi: 10.3762/bjnano.8.186.

[70] J. M. Crow, "HPV: The global burden," *Nature*, vol. 488, no. 7413, pp. S2–S3, Aug. 2012, doi: 10.1038/488S2a.

[71] H. Lefèvre, C. Schrimpf, M. R. Moro, and J. Lachal, "HPV vaccination rate in French adolescent girls: an example of vaccine distrust," *Arch Dis Child*, vol. 103, no. 8, pp. 740–746, Aug. 2018, doi: 10.1136/archdischild-2017-313887.

[72] M. Drolet *et al.*, "Population-level impact and herd effects following human papillomavirus vaccination programmes: a systematic review and meta-analysis," *Lancet Infect Dis*, vol. 15, no. 5, pp. 565–580, May 2015, doi: 10.1016/S1473-3099(14)71073-4.

[73] M. Quinn, P. Babb, J. Jones, and E. Allen, "Effect of screening on incidence of and mortality from cancer of cervix in England: evaluation based on routinely collected statistics," *BMJ*, vol. 318, no. 7188, pp. 904–904, Apr. 1999, doi: 10.1136/bmj.318.7188.904.

[74] M. Arbyn, P. Autier, and J. Ferlay, "Burden of cervical cancer in the 27 member states of the European Union: estimates for 2004," *Annals of Oncology*, vol. 18, no. 8, pp. 1423–1425, Aug. 2007, doi: 10.1093/annonc/mdm377.

[75] M. Mitchell, “Colposcopy for the diagnosis of squamous intraepithelial lesions: A meta-analysis,” *Obstetrics & Gynecology*, vol. 91, no. 4, pp. 626–631, Apr. 1998, doi: 10.1016/S0029-7844(98)00006-4.

[76] O. B. Olaniyan, “Validity of Colposcopy in the Diagnosis of Early Cervical Neoplasia: A Review,” *Afr J Reprod Health*, vol. 6, no. 3, p. 59, Dec. 2002, doi: 10.2307/3583258.

[77] F. F. B. TUON, M. S. BITTENCOURT, M. A. PANICHI, and Á. P. PINTO, “Avaliação da sensibilidade e especificidade dos exames citopatológico e colposcópico em relação ao exame histológico na identificação de lesões intra-epiteliais cervicais,” *Rev Assoc Med Bras*, vol. 48, no. 2, pp. 140–144, Jun. 2002, doi: 10.1590/S0104-42302002000200033.

[78] L. S. Massad and Y. C. Collins, “Strength of correlations between colposcopic impression and biopsy histology,” *Gynecol Oncol*, vol. 89, no. 3, pp. 424–428, Jun. 2003, doi: 10.1016/S0090-8258(03)00082-9.

[79] M. Sideri *et al.*, “Interobserver Variability of Colposcopic Interpretations and Consistency with Final Histologic Results,” *J Low Genit Tract Dis*, vol. 8, no. 3, pp. 212–216, Jul. 2004, doi: 10.1097/00128360-200407000-00009.

[80] ASCUS-LSIL Traige Study (ALTS) Group, “A randomized trial on the management of low-grade squamous intraepithelial lesion cytology interpretations.,” *Am J Obstet Gynecol*, vol. 188, no. 6, pp. 1393–400, Jun. 2003, doi: 10.1067/mob.2003.462.

[81] M. Underwood *et al.*, “Accuracy of colposcopy-directed punch biopsies: a systematic review and meta-analysis,” *BJOG*, vol. 119, no. 11, pp. 1293–1301, Oct. 2012, doi: 10.1111/j.1471-0528.2012.03444.x.

[82] D. G. Ferris and M. S. Litaker, “Colposcopy quality control by remote review of digitized colposcopic images,” *Am J Obstet Gynecol*, vol. 191, no. 6, pp. 1934–1941, Dec. 2004, doi: 10.1016/j.ajog.2004.06.107.

[83] S. B. Cantor *et al.*, “Accuracy of Colposcopy in the Diagnostic Setting Compared With the Screening Setting,” *Obstetrics & Gynecology*, vol. 111, no. 1, pp. 7–14, Jan. 2008, doi: 10.1097/01.AOG.0000295870.67752.b4.

[84] J. Ferlay, H.-R. Shin, F. Bray, D. Forman, C. Mathers, and D. M. Parkin, “Estimates of worldwide burden of cancer in 2008: GLOBOCAN 2008,” *Int J Cancer*, vol. 127, no. 12, pp. 2893–2917, Dec. 2010, doi: 10.1002/ijc.25516.

[85] M. Kyrgiou, G. Koliopoulos, P. Martin-Hirsch, M. Arbyn, W. Prendiville, and E. Paraskevaidis, “Obstetric outcomes after conservative treatment for intraepithelial or early invasive cervical lesions: systematic review and meta-analysis,” *The Lancet*, vol. 367, no. 9509, pp. 489–498, Feb. 2006, doi: 10.1016/S0140-6736(06)68181-6.

[86] M. Arbyn *et al.*, “Perinatal mortality and other severe adverse pregnancy outcomes associated with treatment of cervical intraepithelial neoplasia: meta-analysis,” *BMJ*, vol. 337, no. sep18 1, pp. a1284–a1284, Sep. 2008, doi: 10.1136/bmj.a1284.

[87] N. Thekkek and R. Richards-Kortum, “Optical imaging for cervical cancer detection: solutions for a continuing global problem,” *Nat Rev Cancer*, vol. 8, no. 9, pp. 725–731, Sep. 2008, doi: 10.1038/nrc2462.

[88] S. Bancelin *et al.*, “Determination of collagen fiber orientation in histological slides using Mueller microscopy and validation by second harmonic generation imaging,” *Opt Express*, vol. 22, no. 19, p. 22561, Sep. 2014, doi: 10.1364/oe.22.022561.

[89] T. Novikova *et al.*, “The origins of polarimetric image contrast between healthy and cancerous human colon tissue,” *Appl Phys Lett*, vol. 102, no. 24, 2013, doi: 10.1063/1.4811414.

[90] M. J. O’Callaghan, “Switching dynamics and surface forces in thresholdless ‘V-shaped’ switching ferroelectric liquid crystals,” *Phys Rev E*, vol. 67, no. 1, p. 011710, Jan. 2003, doi: 10.1103/PhysRevE.67.011710.

[91] “Practice Bulletin No. 171: Management of Preterm Labor,” *Obstetrics & Gynecology*, vol. 128, no. 4, 2016, [Online]. Available: https://journals.lww.com/greenjournal/Fulltext/2016/10000/Practice_Bulletin_No__171__Management_of_Preterm.61.aspx

[92] H. Feltovich, T. J. Hall, and V. Berghella, “Beyond cervical length: emerging technologies for assessing the pregnant cervix,” *Am J Obstet Gynecol*, vol. 207, no. 5, pp. 345–354, Nov. 2012, doi: 10.1016/j.ajog.2012.05.015.

[93] R. L. Goldenberg *et al.*, “The Preterm Prediction Study: Sequential cervical length and fetal fibronectin testing for the prediction of spontaneous preterm birth,” *Am J Obstet Gynecol*, vol. 182, no. 3, pp. 636–643, Mar. 2000, doi: 10.1067/mob.2000.104212.

[94] N. Suff, L. Story, and A. Shennan, “The prediction of preterm delivery: What is new?,” *Semin Fetal Neonatal Med*, vol. 24, no. 1, pp. 27–32, Feb. 2019, doi: 10.1016/j.siny.2018.09.006.

[95] K. Lim *et al.*, “Ultrasonographic Cervical Length Assessment in Predicting Preterm Birth in Singleton Pregnancies,” *Journal of Obstetrics and Gynaecology Canada*, vol. 33, no. 5, pp. 486–499, 2011, doi: 10.1016/S1701-2163(16)34884-8.

[96] W. Nicholson, “Economic burden of hospitalizations for preterm labor in the United States,” *Obstetrics & Gynecology*, vol. 96, no. 1, pp. 95–101, Jul. 2000, doi: 10.1016/S0029-7844(00)00863-2.

[97] S. Caritis, “Adverse effects of tocolytic therapy,” *BJOG*, vol. 112, pp. 74–78, Mar. 2005, doi: 10.1111/j.1471-0528.2005.00590.x.

[98] G. J. Kovacevich *et al.*, “The prevalence of thromboembolic events among women with extended bed rest prescribed as part of the treatment for premature labor or preterm premature rupture of membranes,” *Am J Obstet Gynecol*, vol. 182, no. 5, pp. 1089–1092, May 2000, doi: 10.1067/mob.2000.105405.

[99] K. M. Myers *et al.*, "The mechanical role of the cervix in pregnancy," *J Biomech*, vol. 48, no. 9, pp. 1511–1523, Jun. 2015, doi: 10.1016/j.jbiomech.2015.02.065.

[100] M. House, D. L. Kaplan, and S. Socrate, "Relationships Between Mechanical Properties and Extracellular Matrix Constituents of the Cervical Stroma During Pregnancy," *Semin Perinatol*, vol. 33, no. 5, pp. 300–307, Oct. 2009, doi: 10.1053/j.semperi.2009.06.002.

[101] G. Westergren-Thorsson *et al.*, "Differential expressions of mRNA for proteoglycans, collagens and transforming growth factor-β in the human cervix during pregnancy and involution," *Biochimica et Biophysica Acta (BBA) - Molecular Basis of Disease*, vol. 1406, no. 2, pp. 203–213, Mar. 1998, doi: 10.1016/S0925-4439(98)00005-2.

[102] M. Winkler and W. Rath, "Changes in the cervical extracellular matrix during pregnancy and parturition," *J Perinat Med*, vol. 27, no. 1, Jan. 1999, doi: 10.1515/JPM.1999.006.

[103] H. Maul, G. Saade, and R. E. Garfield, "Prediction of term and preterm parturition and treatment monitoring by measurement of cervical cross-linked collagen using light-induced fluorescence," *Acta Obstet Gynecol Scand*, vol. 84, no. 6, pp. 534–536, Jun. 2005, doi: 10.1111/j.0001-6349.2005.00806.x.

[104] N. Uldbjerg, G. Ekman, A. Malmström, K. Olsson, and U. Ulmsten, "Ripening of the human uterine cervix related to changes in collagen, glycosaminoglycans, and collagenolytic activity," *Am J Obstet Gynecol*, vol. 147, no. 6, pp. 662–666, Nov. 1983, doi: 10.1016/0002-9378(83)90446-5.

[105] T. Rechberger, N. Uldbjerg, and H. Oxlund, "Connective tissue changes in the cervix during normal pregnancy and pregnancy complicated by cervical incompetence.," *Obstetrics and gynecology*, vol. 71, no. 4, pp. 563–7, Apr. 1988.

[106] M. House, R. McCabe, and S. Socrate, "Using imaging-based, three-dimensional models of the cervix and uterus for studies of cervical changes during pregnancy," *Clinical Anatomy*, vol. 26, no. 1, pp. 97–104, Jan. 2013, doi: 10.1002/ca.22183.

[107] M. L. Akins, K. Luby-Phelps, and M. Mahendroo, "Second harmonic generation imaging as a potential tool for staging pregnancy and predicting preterm birth," *J Biomed Opt*, vol. 15, no. 2, p. 026020, 2010, doi: 10.1117/1.3381184.

[108] J. Rehbinder *et al.*, "Depolarization imaging for fast and non-invasive monitoring of cervical microstructure remodeling in vivo during pregnancy," *Sci Rep*, vol. 12, no. 1, p. 12321, Dec. 2022, doi: 10.1038/s41598-022-15852-w.

[109] D. B. Fogel, "Factors associated with clinical trials that fail and opportunities for improving the likelihood of success: A review," *Contemporary Clinical Trials Communications*, vol. 11. Elsevier Inc, pp. 156–164, Sep. 01, 2018. doi: 10.1016/j.conctc.2018.08.001.

[110] K. Hirakawa, “Cross-talk explained,” in *2008 15th IEEE International Conference on Image Processing*, 2008, pp. 677–680. doi: 10.1109/ICIP.2008.4711845.

[111] G. Bazalgette Courre`ges-Lacoste, “Modeling of Spectralon diffusers for radiometric calibration in remote sensing,” *Optical Engineering*, vol. 42, no. 12, p. 3600, Dec. 2003, doi: 10.1117/1.1622961.

[112] C. J. Bruegge, “Use of Spectralon as a diffuse reflectance standard for in-flight calibration of earth-orbiting sensors,” *Optical Engineering*, vol. 32, no. 4, p. 805, 1993, doi: 10.1117/12.132373.

[113] D. H. Sliney, M. Wolbarsht, and J. Mellerio, *Safety with Lasers and Other Optical Sources: A Comprehensive Handbook*. Springer US, 1980. [Online]. Available: https://books.google.fr/books?id=PjWsAAAAIAAJ

[114] D. M. Hayes, “Error propagation in decomposition of Mueller matrices,” Oct. 1997, p. 112. doi: 10.1117/12.278963.

[115] J. Li, S. Gauza, and S.-T. Wu, “Temperature effect on liquid crystal refractive indices,” *J Appl Phys*, vol. 96, no. 1, pp. 19–24, Jul. 2004, doi: 10.1063/1.1757034.

[116] J. Hao, W. Yao, W. B. R. Harris, J. Y. Vink, K. M. Myers, and E. Donnelly, “Characterization of the collagen microstructural organization of human cervical tissue,” *Reproduction*, vol. 156, no. 1, pp. 71–79, 2018, doi: 10.1530/REP-17-0763.

[117] A. Singer, “THE UTERINE CERVIX FROM ADOLESCENCE TO THE MENOPAUSE,” *BJOG*, vol. 82, no. 2, pp. 81–99, Feb. 1975, doi: 10.1111/j.1471-0528.1975.tb02204.x.

[118] J. Jordan, A. Singer, H. Jones, and M. Shafi, *The Cervix*. Wiley, 2009. [Online]. Available: https://books.google.fr/books?id=32Dgg1uvcTQC

[119] M. Coppleson, B. L. Reid, H. Queen Elizabeth, and B. And, “A COLPOSCOPIC STUDY OF THE CERVIX DURING PREGNANCY AND THE PUERPERIUM,” 1966.

[120] S. Perrin and P. Montgomery, “Fourier optics: basic concepts,” Feb. 2018, doi: https://doi.org/10.48550/arXiv.1802.07161.

[121] B. Theron, M. El-Desouki, F. M. R. Aljekhedab, M. S. I. Alayed, and M. S. D. Alsawadi, “Choice of spatial resolution measurement methods to implement,” in *2013 Saudi International Electronics, Communications and Photonics Conference*, Apr. 2013, pp. 1–5. doi: 10.1109/SIECPC.2013.6551003.

[122] F. Viallefont-Robinet *et al.*, “Comparison of MTF measurements using edge method: towards reference data set,” *Opt Express*, vol. 26, no. 26, p. 33625, Dec. 2018, doi: 10.1364/OE.26.033625.

[123] E. F. Codd, “A relational model of data for large shared data banks,” *Commun ACM*, vol. 13, no. 6, pp. 377–387, Jun. 1970, doi: 10.1145/362384.362685.

[124] S. Pertuz, D. Puig, and M. A. Garcia, “Analysis of focus measure operators for shape-from-focus,” *Pattern Recognit*, vol. 46, no. 5, pp. 1415–1432, May 2013, doi: 10.1016/j.patcog.2012.11.011.

[125] Q. Xu, K. Xie, K. Yuan, L. Yu, W. Wang, and D. Ye, “A statistical study of the factors influencing the extent of respiratory motion blur in PET imaging,” *Comput Biol Med*, vol. 42, no. 1, pp. 8–18, Jan. 2012, doi: 10.1016/j.compbiomed.2011.10.002.

[126] M. H. Phillips+, E. Pedroni, H. Blattmann, T. Boehringer, A. &ray, and S. Scheib, “Effects of respiratory motion on dose uniformity with a charged particle scanning method,” 1992. [Online]. Available: http://iopscience.iop.org/0031-9155/37/1/016

[127] V. N. Mahajan, “Degradation of an image due to Gaussian motion,” *Appl Opt*, vol. 17, no. 20, p. 3329, Oct. 1978, doi: 10.1364/AO.17.003329.

[128] M. Ben-Ezra and S. K. Nayar, “Motion Deblurring Using Hybrid Imaging,” 2003.

[129] M. Irani and S. Peleg, “Improving Resolution by Image Registration,” 1991.

[130] M. B. A. Haghighat, A. Aghagolzadeh, and H. Seyedarabi, “A non-reference image fusion metric based on mutual information of image features,” *Computers & Electrical Engineering*, vol. 37, no. 5, pp. 744–756, Sep. 2011, doi: 10.1016/j.compeleceng.2011.07.012.

[131] F. Viénot and J. le Rohellec, “Colorimetry and Physiology - The LMS Specification,” in *Digital Color*, Hoboken, NJ USA: John Wiley & Sons, Inc., 2013, pp. 1–28. doi: 10.1002/9781118562680.ch1.

[132] R. S. Hunter, “Photoelectric Tristimulus Colorimetry with Three Filters*,” *J Opt Soc Am*, vol. 32, no. 9, p. 509, Sep. 1942, doi: 10.1364/JOSA.32.000509.

[133] A. Abraham, P. Ariga, R. T. Maddula, and A. R. Jain, “Comparison of shade matching photos taken with gray card and without gray card,” 2018. [Online]. Available: https://www.researchgate.net/publication/328573000

[134] J. Miyajiwala, M. Kheur, A. Patankar, and T. Lakha, “Comparison of photographic and conventional methods for tooth shade selection: A clinical evaluation,” *Journal of Indian Prosthodontist Society*, vol. 17, no. 3, pp. 273–281, Jul. 2017, doi: 10.4103/jips.jips_342_16.

[135] N. Gat, “Imaging spectroscopy using tunable filters: a review,” Apr. 2000, pp. 50–64. doi: 10.1117/12.381686.

[136] M. J. Flynn, “Some Computer Organizations and Their Effectiveness,” *IEEE Transactions on Computers*, vol. C–21, no. 9, pp. 948–960, Sep. 1972, doi: 10.1109/TC.1972.5009071.

[137] J. Holewinski *et al.*, “Dynamic trace-based analysis of vectorization potential of applications,” *ACM SIGPLAN Notices*, vol. 47, no. 6, pp. 371–382, Aug. 2012, doi: 10.1145/2345156.2254108.

[138] Loren Shure, “Run Code Faster With the New MATLAB Execution Engine,” Feb. 12, 2016. https://blogs.mathworks.com/loren/2016/02/12/run-code-faster-with-the-new-matlab-execution-engine/ (accessed Jul. 16, 2022).

Chapter 6

Appendix

6.1 Requirements for the success of the trial

The minimum requirement for the duration of a single session

This trial targets 650 patients with longitudinal examinations. Given that the trial runs for 36 months, five patients per week have to newly enroll in the trial. Assuming that all patients complete an average of 3 longitudinal examinations, 15 will be performed per week. Due to OB/Bicêtre's schedule, it is only possible one day per week (9:00-18:00), so it must be a device that can process more than 15 tests within 8 hours. Accordingly, one examination, including obtaining informed consent, can take up to 30 minutes. Thus, an optimal protocol and machine should be designed to complete one data acquisition session within 30 minutes, which physically allows the collection of the target number of samples on the given schedule.

Image quality

In in vivo settings, image quality is not solely determined by the specifications of the imaging system, such as resolution. The clinical environment is more dynamic than the laboratory. The patient is constantly moving during image acquisition due to life activities such as breathing. This movement often reduces the sharpness of the image, known as motion blur. The amount of motion in the photo and the integration (exposure) time determines the degree of blur. The exact requirements of image resolution for actual examination of cervical tissue are not clear, but high-quality image clarity must be ensured. This includes imaging sensors and optics with high resolution, short exposure times, and imaging processes that can reduce motion blur. Exposure time is related to light intensity. Therefore, it may be necessary to increase the illuminance to shorten the exposure time. However, it is important to note that the increase in illuminance may be limited due to stringent regulations that apply to medical devices. Illuminance and exposure time are also related to the precision of the measurement. Precision refers to the deviation of a measurement and appears as noise in imaging. Therefore, it is necessary to determine the

appropriate illuminance-exposure time, taking into account optimal precision and minimal motion blur.

Repeatability and reproducibility

Repeatability and reproducibility indicate the reliability of repeated functions in the short and long term. During the trial period, 2,000 tests are repeated over a 36-month period. Environmental sensitivities of the machine, such as temperature changes, must be taken into account. For example, seasonal changes change the temperature in a room where the temperature is not normally stabilized. Temperature can significantly affect machine operation and performance. It is not possible to have a temperature-controlled consulting room in a hospital, so it is necessary to define a systematic calibration for the machine.

Reducing user-dependent variability of features is also important for high reproducibility. All such inspections should be performed with the same functionality and workmanship as far as possible. A variety of doctors and operators can perform the tests throughout the clinical trial. If the inspection is performed by different craftsmen of different experts, measurement variations may occur depending on the skills acquired during training in the use of the machine. Therefore, it is important to design a device that is very easy to use so that the operator can take measurements in a simple and repeatable way after a quick training.

Database

According to a survey on the problems of clinical research, about 22% of clinical researchers have difficulties in data analysis, and 17% have difficulties in data management [31]. To significantly reduce these difficulties, it is necessary to predict in advance the amount of data to be collected in clinical studies and design an appropriate database for management. A well-designed database optimized for the problem at hand greatly increases the efficiency and robustness of data processing. The COLPOTERME project will accumulate experimental data from 2,000 colposcopies and patient medical information over a 36-month period. Experimental data includes polarized images acquired at multiple wavelengths and an experimental logbook with descriptions of the instrument settings, temperature conditions, and each patient, which can lead to exceptional situations that can be very useful in data processing. Therefore, it is important to design a database structure that links each patient's inclusion number and its longitudinal data in a usable and readable form.

Patient satisfaction

As COLPOTERME is a longitudinal study, it is very important to retain participants for multiple consecutive visits. There are no payments for included patients who are expected to voluntarily sacrifice time for the study. Waiting time is one of the most important factors in evaluating the quality of care. In fact, long waiting times can cause anxiety and distrust among patients [36]. Therefore, clinical trial investigators must design optimized trial protocols and efficient schedules to minimize latency.

6.2 Limitations of the dual-wavelength MPC

Mechanics

The position, height, and tilt of the colposcopy head can vary significantly from patient to patient, depending on the patient's posture, weight, height, and other external factors. The practitioner must optimize the position of the colposcopy head for each patient. When imaging the patient's cervix, the colposcope's head may tilt significantly. In fact, since the two CCD cameras are connected to multiple electronic cables, displacement of the colposcopy head can cause the plastic holder to move and consequently affect the optical alignment of the imaging system. Given a pixel size on the order of 10 microns, mechanical and even lateral fluctuations can affect pixel alignment between two CCD cameras and cause the image to focus incorrectly on the sensor plane of each CCD camera. This system requires frequent checking and adjustment of optical settings. Moreover, in in vivo feasibility studies, doctors sometimes misused the dual CCD camera system as the handle of a colposcopy head. Therefore, a more simplified imaging system is needed.

Color imaging and image registration

The dichroic system allowed us to obtain the polarization response of cervical tissue at two different wavelengths, 550 nm and 650 nm. However, this did not provide the color image needed to give a visual impression of the cervical tissue, which is an important reference for the operator and polarized image processing. To address this issue, an additional color CCD camera (Pike-100C, Allied Vision) was coupled to the left eyepiece of the magnifier to acquire a reference RGB image after setting the polarization box to the “off” position. However, this leads to an inherent parallax problem that makes it difficult to match the color image and the polarization image. Also, since the sensor of a color CCD camera is different from that of a monochromatic CCD camera, RGB images do not have the same size and resolution as polarized images, making it more difficult to compare pixel-by-pixel. Eventually, adding a third CCD camera made the system much more complex and heavier and difficult to use in clinical settings.

Acquisition speed

Apart from its mechanics and system design, the overall performance of the imaging system was not sufficient for in vivo studies. Considering that the effective integration time for 1 Mueller image is 16 times longer than that of conventional intensity imaging, Mueller imaging is susceptible to motion blur and cannot resolve cervical details in vivo. Because the exposure time is limited by 1/FPS seconds, you need to make sure your lighting system is providing enough light to your imaging system for higer FPS. For example, although GT1920 has a high maximum FPS, it achieved 54 FPS with 2×2 binning at 800×600 resolution, but an exposure time of 30 to 90 ms was required to obtain an effective cervical image in the dual-camera MPC. This exposure time corresponds to 10-30 FPS. Therefore, in the case of 4-frame averaging, the effective integration time was 2 to 6 seconds due to the lack of light. This means that despite the binning mode that lowers the resolution and increases the effective pixel area, the illumination was not enough to fully utilize the maximum FPS.

Consequently, four factors must be compromised to improve image quality.

1. Compact and robust system
2. High resolution of the imaging sensor (no binning mode)
3. High FPS > 60 (1 s of integration time with 4-frame averaging)
4. Powerful illumination

Unoptimized optics

The optical conjugation of the imaging system was not appropriate. The colposcopy's eyepiece and camera are joined by a simple convex lens (Thorlabs AC254-035-A-ML) to form a parabolic image field (named Petzval field curvature) while the surface of the CCD is flat. This results in non-uniform resolution across the field, i.e. different sharpness in the central and peripheral regions of the colposcopy, as shown in Figure 6.1b. Because the endocervix (mainly glandular) is usually found in the middle of the cervix, whereas the ectocervix (mainly stratified squamous) is usually found at the periphery of the cervix, two different epithelial types can be brought with different qualities and the results may be inconsistent due to field curvature.

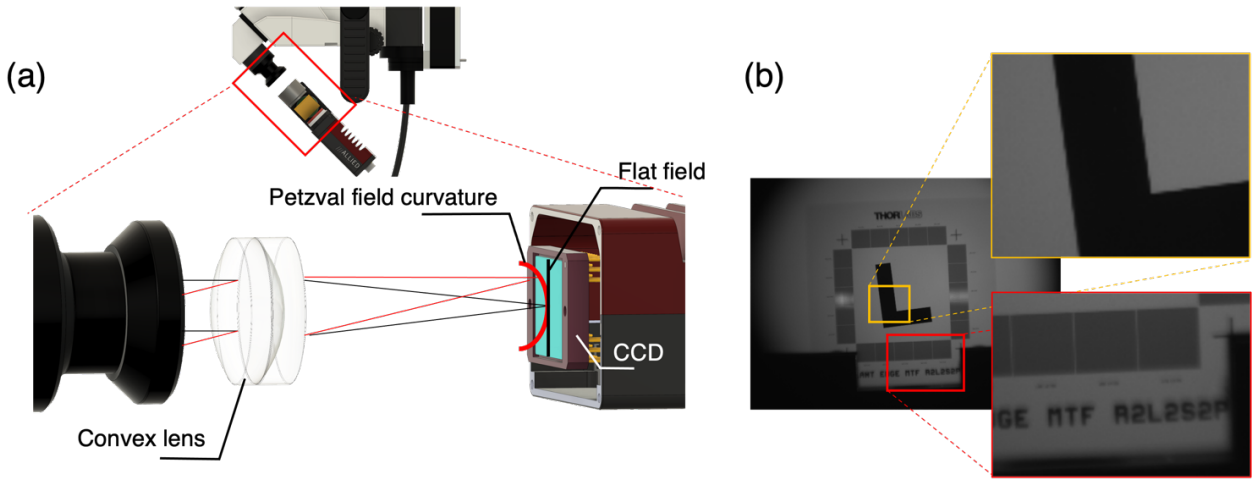

Figure 6.1 (a) The simple objective lens causes the field curvature. (b) The field curvature causes out-of-focus around peripheric regions (red box) compared to the center region (yellow box).

The limitations of the polarimetric system

The polarimetric box placed in front of the Colposcope OCS-500 head prevents the use of the left eyepiece and imposes a mechanical on/off system as shown in Figure 2.15b-c. In fact, due to the size of the ferroelectric liquid crystals that make up the PSA, the edge of the conventional filter holder surrounding these components will obstruct the field of view through the left eyepiece, as shown in Figure 6.2. When the polarimetric box is in the "on" position to perform Muller-polarized imaging, the practitioner can only use one of the two eyepieces of the MPC, thus losing the stereopsis needed to perceive distance and relief, important information in the visual examination of the cervix. If the doctor needs this

information, the polarimetric box can be moved to the "off" position and the MPC can be used as a conventional colposcopy.

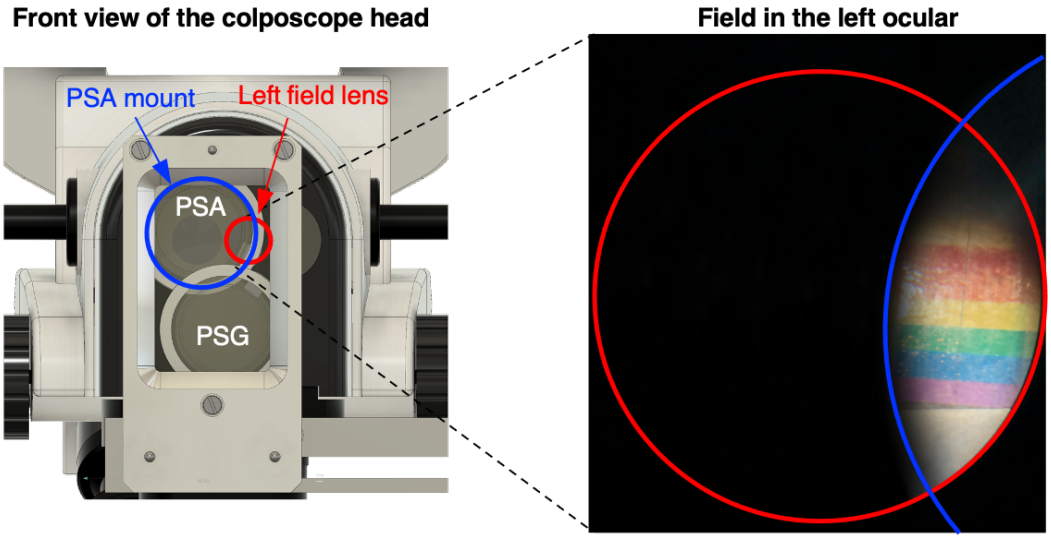

Figure 6.2 The optical mount of the PSA (blue circle) screens the binocular system's left field lens (red circle). It disables the left ocular, as shown in the image on the right.

Although this procedure may seem very simple, in practice, it became an obstacle for doctors to treat patients for a number of reasons. First, manual on/off systems had the potential to contaminate surgical sterility if the practitioner has to move the box to touch it. Second, if the polarimetric box is moved, the colposcopy head also moves, preventing the acquisition of a color image that can be superimposed on a polarized image on a pixel-by-pixel basis, which is a significant limitation in data processing. Third, the on/off movement causes a mismatch in the position of the polarimeter between measurement and calibration. Even if the system moves along the rail, repeatability of the move cannot be guaranteed as long as it is done manually. Calibration with the polarization system at the location of the discrepancy where the measurement was made will cause errors in the polarization measurement.

The box was indeed robust and protected the optical components effectively. However, once the parts were assembled, it was not possible to correct their orientation. In other words, it was impossible to optimize the condition number once the PSG and PSA were assembled. Optimization of condition number is a very important procedure in optimizing the quality of polarization measurements, which requires fine tuning of orientation. The development of the polarization system was a lot of hassle because every part had to be disassembled for every modification.

Manual calibration

The calibration requires acquisitions of 4 conditions (air, two polarizers, 1 QWP), and the user needs to manually place them in front of the box with the system in Figure 6.3. These manual processes might give the user more flexibility but can be too complicated for medical practitioners. Each filter must be placed on the polarimetric system in the correct order, and the plate must be carefully assembled to the system in which the filters are normally aligned with respect to the optical axis of the colposcope. These complexities of the manual processes increased the training cost and the likelihood of misfunctions of the machine.

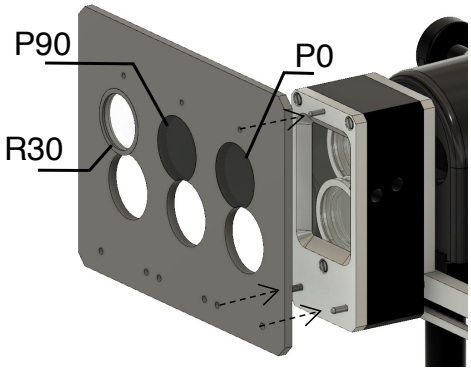

Figure 6.3 The manual calibration system of the former prototypes. The reference samples for the ECM were mounted on a plate, and the plate was mounted in front of the box. The exchange of the three filters is manually done.

Badly designed user-interface

The operation program in LabVIEW was not very usable. The program was a simple translation of the laboratory user interface with many options and parameters. The LabVIEW user-interface (UI) is described in Figure 6.4. It had three separate tabs for live video (camfast), measurement, and calibration with many parameters and options. The real-time video is streamed in the 'camfast' tab to place the target in the right position. The user can also adjust the gain and exposure time to have appropriate brightness in the video.

On the other hand, in the 'measurement' tab, the user can set the parameters for actual polarimetric measurement, such as gain, exposure time, and sample information. However, the user cannot see the video in this tab; therefore, the user cannot check if the sample is still in the right position. This may be trivial in the laboratory where the sample is inanimate. However, the target can be displaced while the user sets the parameters and triggers an acquisition.

In the 'calibration' tab, the user can perform a calibration. The user sets the parameters for calibration. As a result of calibration, the graphs of $\lambda_{16}/\lambda_{15}$ (the equation X) are shown. The user can infer the quality of calibration through these graphs. This laboratory UI provides extensive flexibility if the user is in the know of the system, but this 'guru' mode severely reduces usability for the end-user and increases training costs and potential for misfunctions.

Moreover, image processing and calibration are performed in MATLAB. However, MATLAB does not have a memory space shared with LabVIEW, and data in LabVIEW are copied into MATLAB's memory space instead of being referenced by pointers. This process may take several minutes for image data. Thus, MATLAB reads the image files from storage, which is relatively slow. After processing, the processed image data are transferred to LabVIEW's memory space. Because of the intrinsic independence of their memory space as well as unoptimized MATLAB codes, this image process takes 1 minute for decomposition and 5 minutes for calibration. This time consumption is incompatible with clinics with real patients present in the trial.

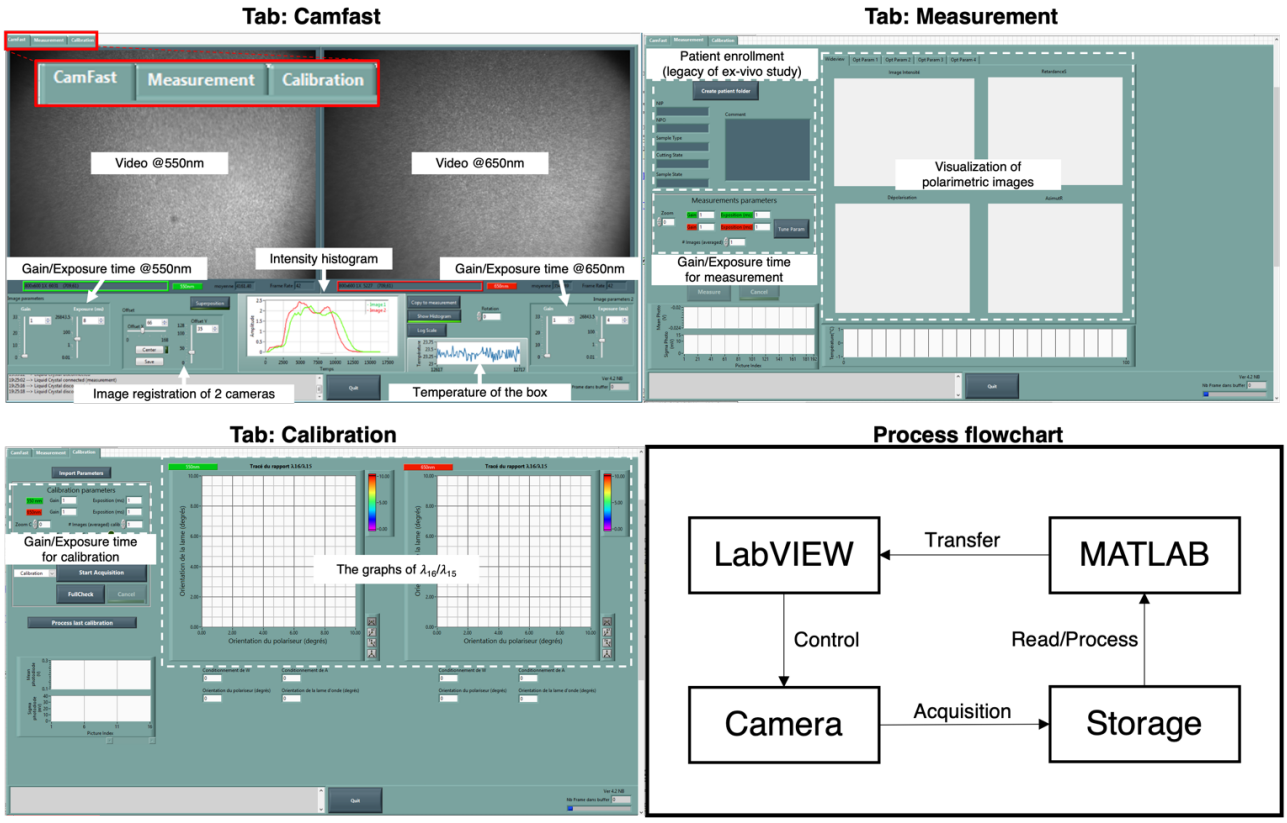

Figure 6.4 The UI of the data acquisition software of the double-camera MPC. The UI is divided into three tabs, camfast, measurement, and calibration. The user cannot watch the image while he/she is setting measurement or calibration. It processed acquired images through an interface to MATLAB scripts, and the processed results were visualized in LabVIEW's panels.

Poor database system

The data recording structure of the dual-wavelength MPC is not suitable for a study that will include 650 patients, corresponding to about 2000 colposcopies (each patient is analyzed on average three times during the study). In the new project, the following data are supposed to be acquired.

- *for each patient and each visit date
- Measurements (polarimetric image data)
- Calibrations
- Color videos/pictures
- Experimental logs include exposure time, gain, data hash, and commentaries.

- Basic patient information such as age and gestational age.

Users were required to write experimental logbooks and comments in unformatted colloquial language in separate text files for each experiment. This approach may be suitable for laboratory experiments where only a few dozen samples are collected so that colloquial records can be easily rearranged into spreadsheets or tables. However, it is not suitable for managing large numbers of samples. Improperly structured data sets significantly increase the cost of data processing. It also lacks robustness, resulting in low reliability and validity, as each user logs their experiments in different styles and levels of detail. Unless you are using natural language processing (NLP) techniques, colloquial style data must be converted to manually formatted data. A number of validation processes must be followed to achieve high reliability in manual conversion.

6.3 Camera setting

The camera connects to the workstation through a Camera Link frame grabber (NI PCIe-1437). The frame grabber is highly compatible with NI systems, namely LabVIEW. NI's frame grabber does not support the 3-CMOS camera AP-3200, but we could use the 'NI Camera File Generator' to create a driver to adapt the camera to our NI system. Communication between the NI system and the camera is then via the command line and serial interface provided by the manufacturer JAI. A minor issue was found in the RGB signal jumper between the camera and grabber. Bits 8-11 of the camera's blue signal are connected to bits 12-15 of the grabber's red signal. So signals in blue above 255 (bits 0-7) were read from the red buffer as if they were signals in bits 12-15 of red, resulting in saturation of the red image. The binary operation solved this problem by sampling the 12th-15th bits of red (AND), shifting 4 bits to the left (<<), and swapping the 8th-12th bits of blue (OR). This should be done for every frame of a 12-bit acquisition, combined with OpenCV + LabVIEW for faster computation speed.

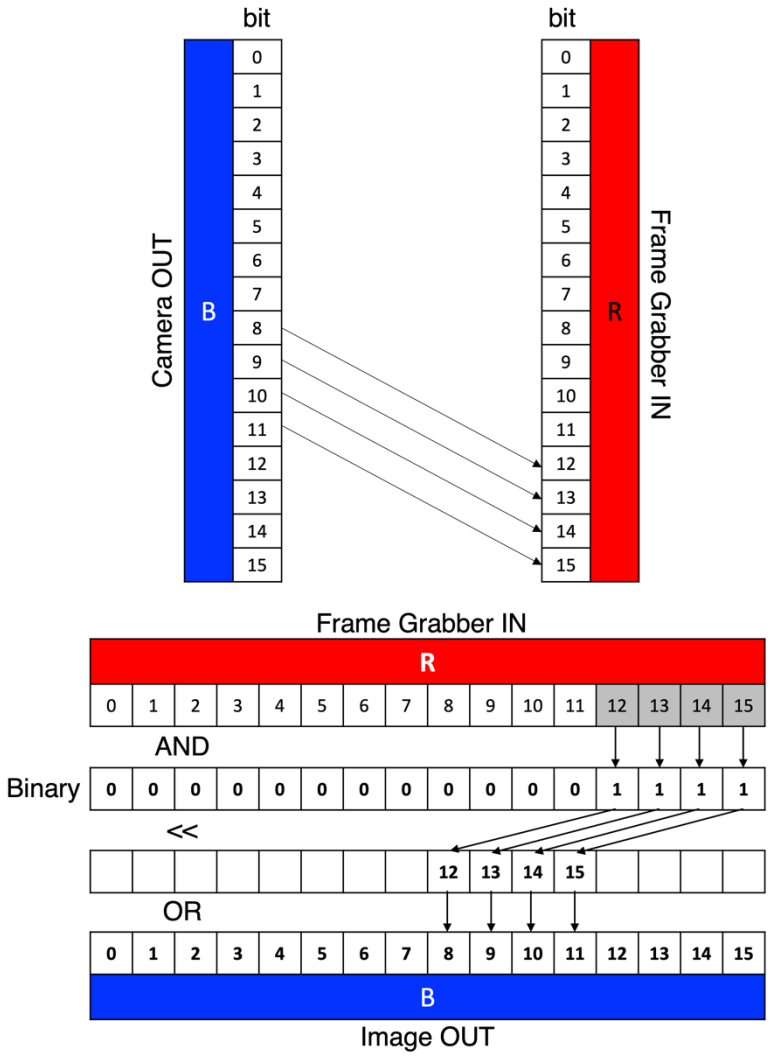

Figure 6.5 The scheme of the misconnection in the image data interface. 8th~11th bits of the blue detector is connected to the 12th~15th input of the frame grabber, which leads to saturation of the red channel. It can be corrected by simple binary operations shown at the bottom.

6.4 Resolution of imaging systems

Let B be the image of point A produced by an optical system. When all rays from A converge at B, the optical system is stigmatic. This means that a planar or spherical wave at point A is converted to a planar or spherical wave at point B, as illustrated in Figure 6.6. However, if there are aberrations such as spherical aberration, coma, astigmatism, and field curvature, the stigma condition may no longer be valid.

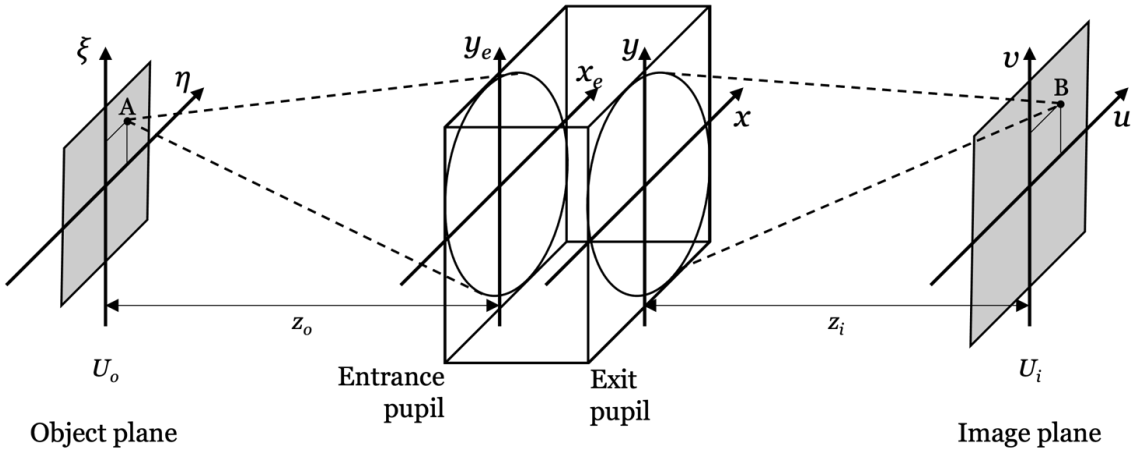

Figure 6.6 The image formation scheme from point A in the object plane to point B in the image plane through a pupil in the middle.

This image formation is often described by the Fourier transform of the object plane onto the image plane.[120]

$$U_i(u,v) = \iint_{-\infty}^{\infty} h(u-\xi, v-\eta) U_g(\xi,\eta) d\xi d\eta = h(u,v) * U_o(\xi,\eta) \tag{6-1}$$

Where U_i and U_o are the image and objective plane, respectively. (u, v) and (ξ, η) denote the image and object plane coordinates. h denotes the Fourier transform of the pupil function $P(x,y)$ such as a pinhole.

$$h(u,v) = \frac{A}{\lambda z_i} \iint_{-\infty}^{\infty} P(x,y) \exp\left\{-\frac{j2\pi}{\lambda z_i}[(u - M\xi)x + (v - M\eta)y]\right\} dxdy \tag{6-2}$$

M denotes the magnification. This convolution is simplified in incoherent wave case because only the intensity of light is taken into account and intensities are simply summed up, i.e., time-averaged

$$I_i(u,v) = \langle |U_i(u,v)|^2 \rangle = \langle |h(u,v) * U_o(u,v)|^2 \rangle \tag{6-3}$$

$$I_i(u,v) = \iint_{-\infty}^{\infty} |h(u-\xi, v-\eta)|^2 I_o(\xi,\eta) d\xi d\eta = |h|^2 * I_o \tag{6-4}$$

Herein, $|h|^2$ denotes the convolution (spread) function of the imaging optics, denoted by the point spread function (PSF). In other words, the image formation is a convolution of the PSF with the objective plane, as illustrated in Figure 6.7. The PSF is also known as the Airy pattern.

Now we consider 2 points in the object plane, as illustrated in Figure 6.7. The x-axis represents the 1-dimensional spatial coordinate, while the y-axis represents the normalized intensity. If an imaging system captures these 2 points (object), the PSF of the system will transfer the object to the image plane. In the image, the 2 points are spread by the PSF, and they may be no more distinguishable.

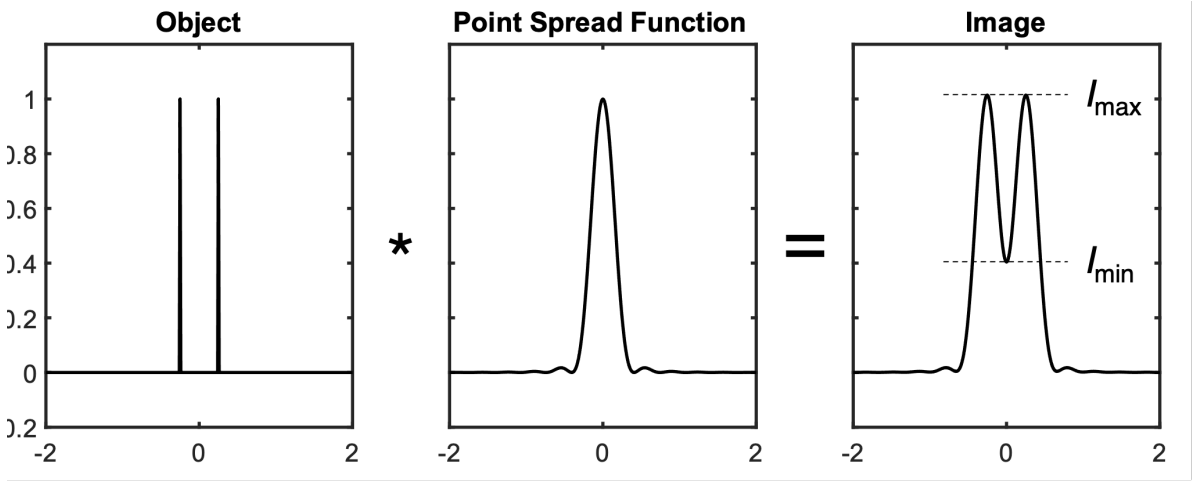

Figure 6.7 The scheme of the image formation. The image is the convolution of the point spread function. Then, the contrast at the given spatial frequency of the object is defined by the two intensities.

Herein, one can define the contrast between the 2 points in the image:

$$\text{Contrast} = \frac{I_{max} - I_{min}}{I_{max} + I_{min}} \times 100\ \% \tag{6-5}$$

When contrast=1, the two points are clearly distinguishable; on the other hand, when contrast=0, the two points are no more distinguishable. Thus, the resolving power of an imaging system is defined by the minimum distance at which two objects can be 'at least' distinguishable. Because it is the PSF that determines the spread of the point in the object plane, the resolution evaluation of an imaging system is performed by measuring the PSF of the system. The theoretical diffraction limit can be defined based on the PSF for an aberration-free system. There are several criteria for indicating distinguishable contrast, but the first zeros in the PSF are usually used as a standard called the Rayleigh criterion.[120]

$$\begin{aligned} d_{Rayleigh} &= \frac{1.22}{f_c} \\ f_c &= \frac{2D}{z_i \lambda} = \frac{2NA}{\lambda} \end{aligned} \tag{6-6}$$

Where f_c denotes the cut-off frequency in an incoherent imaging system, and λ denotes the wavelength of light. NA refers to the numerical aperture where D is the pupil's diameter.

Contrast maps, which are functions of spatial frequency, are often used to represent the resolution of imaging systems, which can be obtained by the Fourier transform of the PSF, called the optical transfer function (OTF). The OTF is a function resulting in complex values, where the absolute values are referred to as the modulation transfer function (MTF), while the complex values are referred to as the phase transfer function (PTF).[120] Although the PTF represents the transversal shift of the image, it is out of interest in this section. In contrast, the MTF represents the contrast as a function of spatial frequencies in the unit of the number of line pairs per mm.

$$MTF = |OTF| = |FT(|h|^2)| \tag{6-7}$$

6.5 Slanted edge method

Although the MTF can be obtained through several approaches[42], [43], in this study, the spatial resolution is measured by analyzing an image of a sharp edge, named the slanted edge method [44], [45]. The slanted edge target allows the discretized digital imaging sensor to over-sample the horizontal profile of a sharp edge, as described in Figure 6.8. The PSF (in this case, it is the line spread function LSF) can then be estimated by differentiating the profile because the falling speed of the sharp edge in the image represents the spatial frequency information because the edge image results from the convolution of the PSF with the sharp edge. Finally, the MTF is obtained by Fourier transforming the PSF.

$$PSF = \frac{d(profile)}{dx} \tag{6-8}$$

$$MFT = |FT(\mathrm{PSF})| \tag{6-9}$$

The slanted edge method enables us to easily obtain the MTF in a digital imaging system[3], as shown in Figure 6.8. It requires only a small area of a single edge image; thus, it also has the advantage of evaluating the local resolving power in different regions within the field of view.

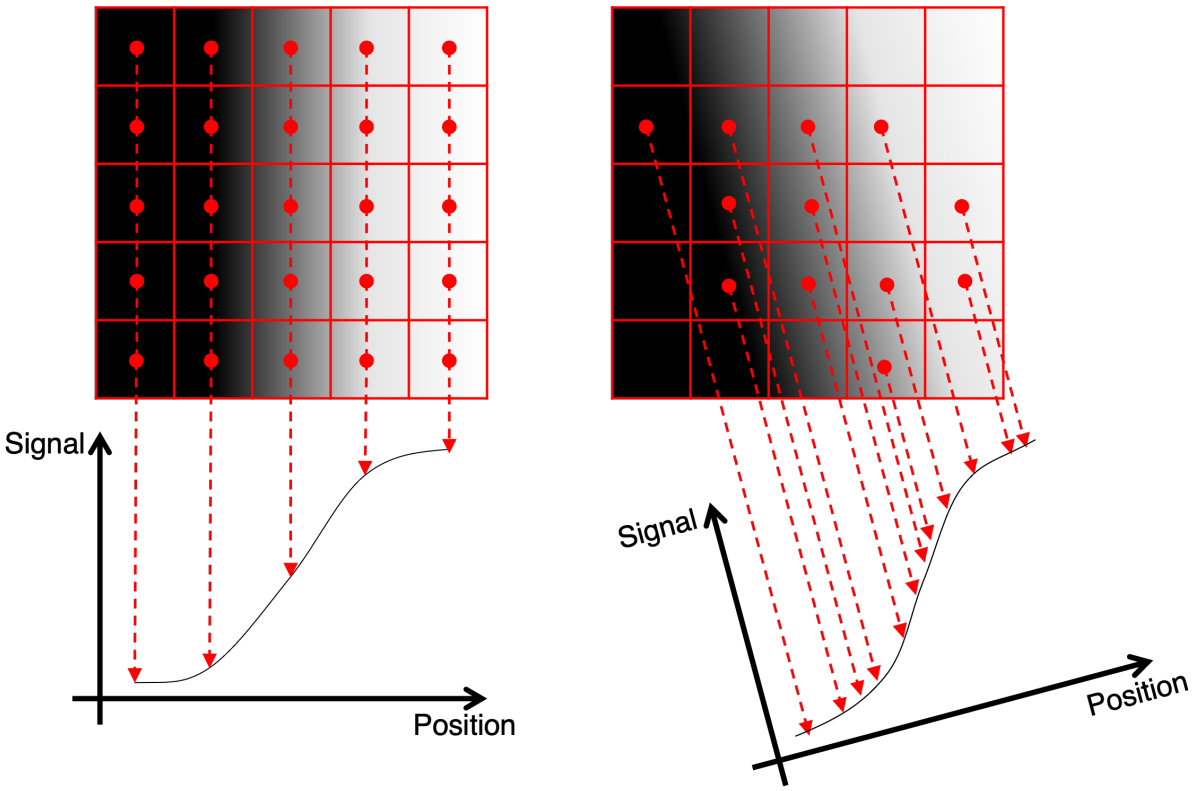

Figure 6.8 The description of the oversampling by the slanted edge pattern. The vertical pattern creates overlayed, therefore, sparse sampling along the horizontal line, while the slanted edge creates more dense sampling by avoiding the overlay between pixels along the sensor's matrix array. Relative tilting angles of 6~8º are optimal[122]**.**

In the case of a digital imaging system, since the MTF obtained by the slanted edge method is calculated for discrete pixels, the x-axis spatial frequency of the MTF has a pixel unit, not an actual length unit. Therefore, the spatial frequency must be converted to the equivalent of a single pixel in real space. The length per pixel of the object plane (field of view divided by number of pixels) can differ from magnification and working distance, so the length per pixel of the sensor plane (sensor size divided by number of pixels) is usually used. It represents the resolution of the optical system.

$$Spatial\ frequency_{@object} = \frac{line\ pairs}{pixel} \times \frac{\#\ of\ pixels}{FOV}$$
$$Spatial\ frequency_{@sensor} = \frac{line\ pairs}{pixel} \times \frac{1}{pixel\ pitch} \quad (6\text{-}10)$$

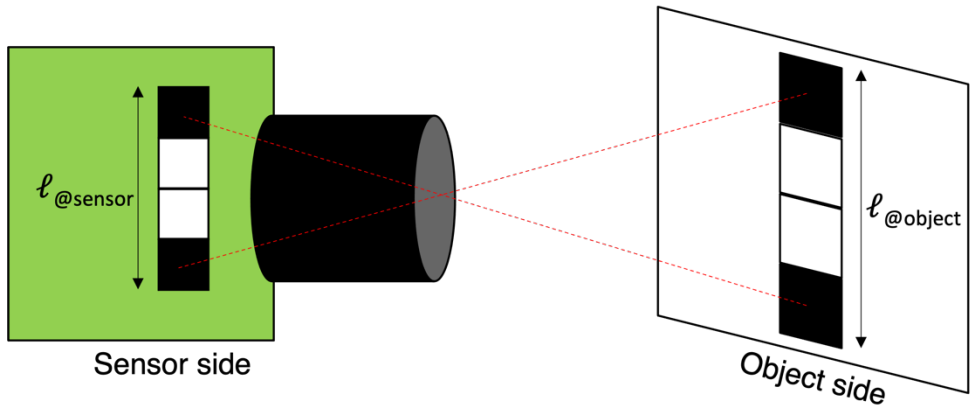

Figure 6.9 The spatial frequency in pixels can be scaled to 2 different planes. While the sensor size and pixel pitch are fixed, the object side length scale can vary by working distance and the focal length.

Then, as a thickness of a single line of a line pair (the distance between black-black lines or white-white lines), the resolution is given by:

$$Resolution = \frac{1}{2 \times Spatial\ frequency} \quad (6\text{-}11)$$

6.6 Resolution measured by USAF1951

The lines patterns with different gaps on the USAF 1951 target allows an imaging system to measure contrast in different spatial frequencies. The numbers on the top of the patterns denote the group number, and the numbers on the right/left of the patterns denote the segment number. The combination of the group-segment number is mapped to their spatial frequency. Using the intensity values measured on the patterned lines and empty lines, contrast for each frequency can be calculated.

Contrast in various spatial frequencies directly measured through the USAF 1951 target are charted in Table 6.1. The USAF 1951 target can validate the results measured by the slanted edge method, although this direct measurement can be vulnerable to the shot noise and luminous uniformity because contrast in the USAF 1951 target is determined by a line profile with only 3 line pairs, and each line pair group can have different background light intensity depending on the luminous uniformity. Around 10% contrast at 530 nm, 630 nm, and 650 nm were measured at the group 3-5 pattern corresponding to the 39.37 μm resolution. It validates the MTF10 measured by the edge method. Slightly higher resolutions at 460 nm and 700 nm and lower resolutions at 530 nm were measured in the USAF 1951. The results from the USAF 1951 also exhibit the strong axial chromatic aberration of the MPC. These results solely represent resolution in intensity imaging not polarimetric imaging. Thus, the actual resolution in polarimetric imaging can differ from these results dependent on the polarimetric contrast of the target because its optical anisotropy can enhance contrast in polarimetric imaging.

Table 6.1 The contrast measured in different spatial frequencies on the USAF1951 target.

#	Group	Contrast				
		460nm	530nm	630nm	650nm	700nm
1	3-5 39.37 μm	0.033	0.114	0.128	0.133	0.012
	3-4 44.19 μm	0.086	0.164	0.230	0.258	0.026
	3-2 55.68 μm	0.166	0.233	0.378	0.367	0.095
	3-1 62.50 μm	0.216	0.278	0.408	0.408	0.144
	2-6 70.15 μm	0.282	0.307	0.442	0.419	0.230
	2-5 78.75 μm	0.367	0.358	0.471	0.480	0.287
	2-4 88.39 μm	0.459	0.390	0.498	0.521	0.359
	2-3 99.21 μm	0.539	0.428	0.551	0.555	0.446
	1-6 140.31 μm	0.680	0.635	0.719	0.755	0.692
	0-2 445.45 μm	0.979	0.955	0.951	0.953	0.953

The really interesting result of this characterization is that, although the coupling between the 3-CMOS camera lens and the colposcope optics is not perfect, the resolution degradation, at 10% contrast, remains quite small compared to the nominal resolution (34 microns/pixel) in the three locations analyzed for the 530 nm, 630 nm and 650 nm wavelengths. However, this degradation becomes more significant at 460 nm and 700 nm.

6.7 The variance of the elements of the Mueller matrix

A measured Mueller matrix $\boldsymbol{M}$ results from a linear modification of the matrix $\boldsymbol{B}$ by the inverse of the matrix $\boldsymbol{W}$ of the PSG and the matrix $\boldsymbol{A}$ of the PSA. Thus, at each pixel, the standard deviation of the 16 elements of $\boldsymbol{M}$ can be defined by this linear relation. Note that the following 3 relations are satisfying for 2 independent random variable X and Y and a constant k.

$$\mathbb{V}ar(kX) = k^2\mathbb{V}ar(X) \tag{6-12}$$

$$\mathbb{V}ar(X+Y) = \mathbb{V}ar(X) + \mathbb{V}ar(Y) \tag{6-13}$$

$$\mathbb{V}ar(X/Y) = \mathbb{V}ar(X)\mathbb{V}ar(1/Y) + \mathbb{V}ar(X)\mathbb{E}(1/Y)^2 + \mathbb{E}(X)^2\mathbb{V}ar(1/Y) \tag{6-14}$$

As mentioned, an element of the intensity matrix $\boldsymbol{B}$, B_{ij}, results from the matrix multiplication of i-th row vector $\boldsymbol{A_i}$ of the matrix $\boldsymbol{A}$, j-th column vector $\boldsymbol{W}_j$ of the matrix $\boldsymbol{W}$, and the Mueller matrix $\boldsymbol{M}$ of a sample. Note that the Mueller matrix is normalized by the unpolarized light intensity M_{11}.

$$\begin{aligned} B_{ij} &= \boldsymbol{A_i M W_j} \\ &= M_{11} \times \begin{bmatrix} A_{i1} & A_{i2} & A_{i3} & A_{i4} \end{bmatrix} \begin{bmatrix} 1 & M_{12} & M_{13} & M_{14} \\ M_{21} & M_{22} & M_{23} & M_{24} \\ M_{31} & M_{32} & M_{33} & M_{34} \\ M_{41} & M_{42} & M_{43} & M_{44} \end{bmatrix} \begin{bmatrix} W_{1j} \\ W_{2j} \\ W_{3j} \\ W_{4j} \end{bmatrix} \end{aligned} \tag{6-15}$$

M_{11} denotes the unpolarized light intensity measured from the sample, and A_{in} denotes the element in i-th row and n-th column of the matrix $\boldsymbol{A}$, and W_{mj} denotes the element in m-th row and j-th column of the matrix $\boldsymbol{W}$. If we assume that the sample is in the steady-state and only one calibration is used for following measurements (the $\boldsymbol{W}$ and $\boldsymbol{A}$ are constant over the 32 acquisitions,) the $\boldsymbol{A}$, $\boldsymbol{W}$, and the normalized Mueller matrix are constant. Then, the multiplication of the three matrices results in a constant value, k_{ij}:

$$B_{ij} = M_{11} \sum_{n=1}^{4} \sum_{m=1}^{4} A_{in} M_{nm} W_{mj} = k_{ij} M_{11} \tag{6-16}$$

By the equation (6-12), the variance of B_{ij} is:

$$\mathbb{V}ar\left(B_{ij}\right) = k_{ij}^2 \mathbb{V}ar(M_{11}) \tag{6-17}$$

According to the equation (1-35) in Chapter 1, a measured Mueller matrix is obtained by matrix multiplication of the two inverse matrices $\boldsymbol{A}^{-1}$ and $\boldsymbol{W}^{-1}$ and the intensity matrix $\boldsymbol{B}$. Likewise, the element at i-th row an j-th column of the measured Mueller matrix $\boldsymbol{M}$ can be obtained as:

$$M_{ij} = \boldsymbol{A_i^{-1} B W_j^{-1}} = \sum_{n,m} A_{in}^{-1} B_{nm} W_{mj}^{-1} \tag{6-18}$$

A_{in}^{-1} and W_{mj}^{-1} denotes an in-th and mj-th element of the inverse matrices $\boldsymbol{A}^{-1}$ and $\boldsymbol{W}^{-1}$, respectively. Because the matrices $\boldsymbol{A}$ and $\boldsymbol{W}$ are constant and the Poisson noise in each intensity measurement is statistically independent, the variance of M_{ij} can be obtained by the equation (6-13) as:

$$\begin{aligned} \mathbb{V}ar\big(M_{ij}\big) = \sum_{n,m} \mathbb{V}ar\big(A_{in}^{-1} B_{nm} W_{mj}^{-1}\big) &= \sum_{n,m} \big(A_{in}^{-1} W_{mj}^{-1}\big)^2 (k_{nm}^2) \mathbb{V}ar(M_{11}) \\ &= h_{ij} \mathbb{V}ar(M_{11}) \\ h_{ij} &= \sum_{n,m} \big(A_{in}^{-1} W_{mj}^{-1}\big)^2 (k_{nm}^2) \end{aligned} \tag{6-19}$$

Another derivation of equation (6-19) using the Kronnecker product is found in [9]. Therefore, the variance of M_{ij} is proportional to the variance of M_{11}. However, the Mueller matrix is used in the form of the normalized matrix $\boldsymbol{M}/M_{11}$. The variance of the normalized Mueller matrix elements, then, can be obtained as by the equation (6-14):

$$\begin{aligned} &\mathbb{V}ar\left(\frac{M_{ij}}{M_{11}}\right) = \\ &\mathbb{V}ar\big(M_{ij}\big)\mathbb{V}ar(1/M_{11}) + \mathbb{V}ar\big(M_{ij}\big)\mathbb{E}(1/M_{11})^2 + \mathbb{E}\big(M_{ij}\big)^2 \mathbb{V}ar(1/M_{11}) \end{aligned} \tag{6-20}$$

Using the Tylor expansion, the variance of $1/X$ can be approximated for a random variable:

$$\begin{aligned} g(X) &= g\big(\mathbb{E}(X)\big) + \big(X - \mathbb{E}(X)\big) g'\big(\mathbb{E}(X)\big) + \frac{\big(X - \mathbb{E}(X)\big)^2}{2} \mathbb{E}(X)''\big(\mathbb{E}(X)\big) \\ &\quad + \cdots \\ \mathbb{V}ar\big(g(X)\big) &= \mathbb{V}ar\left(\big(X - \mathbb{E}(X)\big) g'\big(\mathbb{E}(X)\big) + \frac{\big(X - \mathbb{E}(X)\big)^2}{2} g''\big(\mathbb{E}(X)\big) \ldots \right) \end{aligned} \tag{6-21}$$

$$
\begin{aligned}
&= g'\big(\mathbb{E}(X)\big)^2\,\mathbb{V}ar\big(X-\mathbb{E}(X)\big) \\
&\quad + 2g'\big(\mathbb{E}(X)\big)Cov\Bigg(\big(X \\
&\quad - \mathbb{E}(X)\big), \frac{\big(X-\mathbb{E}(X)\big)^2}{2}g''\big(\mathbb{E}(X)\big)\ldots\Bigg) \\
&\quad + \mathbb{V}ar\left(\frac{\big(X-\mathbb{E}(X)\big)^2}{2}g''\big(\mathbb{E}(X)\big)\right) \\
\mathbb{V}ar\big(g(X)\big) &\approx g'\big(\mathbb{E}(X)\big)^2\,\mathbb{V}ar(X)
\end{aligned}
$$

where $g(X)=1/X$,

$$\mathbb{V}ar(1/X) \approx \frac{1}{\mathbb{E}(X)^4}\mathbb{V}ar(X) \tag{6-22}$$

M_{11} has a Poisson distribution (the shot noise):

$$\mathbb{V}ar(M_{11}) \propto M_{11} \tag{6-23}$$

Because M_{11} is measured in a 12-bit digital unit (0~4095), the variance of $1/M_{11}$ is extremely small. The variance of the normalized Mueller matrix can be obtained as follows:

$$
\begin{aligned}
\mathbb{V}ar\left(\frac{M_{ij}}{M_{11}}\right) &= \mathbb{V}ar\big(M_{ij}\big)\mathbb{E}(1/M_{11})^2 + c_{ij} \\
Where\ \mathbb{V}ar(1/M_{11}) &\approx \frac{1}{\mathbb{E}(M_{11})^3}\ and\ M_{11} \geq M_{ij} \\
c_{ij} &= \mathbb{E}\big(M_{ij}\big)^2\mathbb{V}ar(1/M_{11}) + \mathbb{V}ar\big(M_{ij}\big)\mathbb{V}ar(1/M_{11}) \\
&\leq \frac{1}{\mathbb{E}(M_{11})} + \frac{1}{\mathbb{E}(M_{11})^2} \approx 0
\end{aligned}
\tag{6-24}
$$

In addition, because M_{11} is a positive integer value, the following inequality is satisfied.

$$
\begin{aligned}
\mathbb{E}(1/M_{11}) &\geq \mathbb{E}(M_{11})^{-1} \\
\mathbb{V}ar\big(M_{ij}\big) &\geq \frac{h_{ij}\mathbb{V}ar(M_{11})}{M_{11}^2}
\end{aligned}
\tag{6-25}
$$

By the variance of a Poisson distribution (6-23), we finally obtain:

$$\sigma_{M_{ij}} \geq \sqrt{\frac{h_{ij}\mathbb{V}ar(M_{11})}{M_{11}^2}} = \frac{b_{ij}}{\sqrt{M_{11}}} + c_{ij} \tag{6-26}$$

Thus, the standard deviation of the Mueller matrix elements can be modeled by a nonlinear equation:

$$\sigma_{M_{ij}} = \frac{b_{ij}}{\sqrt{M_{11}}} + c_{ij} \tag{6-27}$$

c_{ij} corresponds to the asymptote of standard deviation and the higher the coefficient b_{ij}, the greater the uncertainty.

6.8 Relational database management system (RDBMS)

In general, a relational database consists of different "entities." The term "entity" refers to a real-world object and is described by its characteristics, for example 'weight'. In addition, an entity may consist of a set of sub-entities necessary for its detailed and complete characterization. In practice, an entity consists of a set of data tables that represent sub-entities. In the case where the entity is not composed of sub-entities, it consists of a single table. The columns of a table represent the properties of the entity. Each column component is called an "attribute" or "field." A row is a collection of attributes called a "record" or "tuple."

An entity is described by its properties, such as 'name' and 'age.' Each entity is a set of data tables composed of columns and rows, and the properties denote the features of entities that usually correspond to the columns of data tables. The columns of tables are termed by 'attribute' or 'field,' and each row (a collection of the values of the fields in a table) is termed by 'record' or 'tuple.' Especially in RDBMS, the tables are termed by 'relations.' Additionally, an entity can contain sub-entities that describe more complex properties of the main entity, for example, 'hospital'-'department'-'doctor.'

Figure 6.10 An example of a relation. Each row is called the Tuple and each column is called the attribute. Two attributes, hobby1 and hobby2, cause a redunduncy for emp_id=2 and 3.

In real-world applications, the number of entities and tables is huge, and their complexity can cause redundancy and vulnerability. For example, Figure 6.10 shows the 'Employees' relation with three tuples of 3 employees, representing personal information about employees. One can find multiple attributes that represent 'hobby' because the employees can have only one name, age, height, and weight while having many hobbies simultaneously. This table form causes redundancy with the empty value and a large expansion in the column because we need many attributes dependent on the maximum possible number of hobbies the employees can have.

Herein, the relational model forms robust connections between relations by defining keys between attributes of entities. E.F. Codd first suggested the relational database model in 1970 [123]. The keys in the relational model form 'key constraints,' and they function to prevent modifications of data invalid by the key constraints and make the 'entity'~'sub-entity' relationship clearer.

Key and key constraints

In RDBMS, a key can be defined as a set of attributes within a table. Four kinds of keys are defined: super key, candidate key, primary key, and foreign key.

The super key is a set of attributes within a table that can uniquely identify each tuple (row) of the table. Figure 6.11 represents the employee entity by a key constraint as an example. The squares represent relations, and the circles represent attributes. In the relation, the 'emp_id' denotes the numeric identification of each employee. Only the 'emp_id' attribute uniquely determines each tuple because a unique emp_id is supposed to be given for each employee, while employees can have the same name, age, height, or weight (none of the employees has the same profile in this given example, but potentially they can have the same profile.)

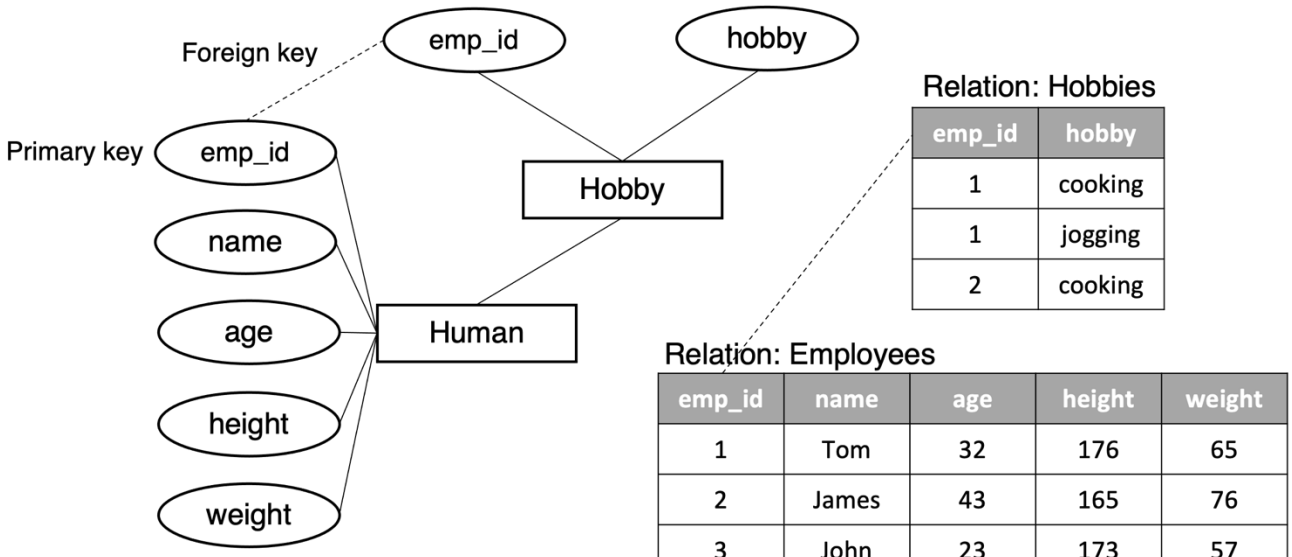

Figure 6.11 An example of a relational database. The rectangles represent a table, and the ellipses represent an attribution (column). Each table can be connected through the foreign key relation like the 'psg_id' attribute in the table Polarimeter and PSA.

Therefore, in this example, any combination of attributes that contain the 'emp_id' can uniquely determine each row. All these possible combinations form the sets called the super keys. The candidate keys are then the minimal subset of the super keys. Therefore, the candidate keys are the super keys with the minimum number of attributes. Therefore, the {emp_id} is the candidate key in this case. One of the candidate keys can be chosen as the primary key, and the primary key can uniquely identify the tuples of the table.

- Super key: {emp_id}, {emp_id, name}, {emp_id, age}, {emp_id, height}, {emp_id, weight}, {emp_id, name, age}, {emp_id, name, height}, {emp_id, name, weight},...,{emp_id, name, age, height, weight}

- Candidate key: {emp_id}
- Primary key ∈ Candidate key: {emp_id}

On the other hand, the foreign key is a set of attributes used to 'refer' to the primary key of another table. The 'emp_id' attribute in the relation Hobbies is a foreign key referring to the 'emp_id' attribute, the primary key of the relation Employees. Then it sets the foreign key constraint:

$$\text{emp\_id}_{Hobbies} \subseteq \text{emp\_id}_{Employees} \tag{6-28}$$

Therefore, all the values in the 'emp_id' attribute of the Hobbies have to exist in the 'emp_id' attribute of the Employees. For example, emp_id values out of {1,2,3} are invalid in the Hobbies relation by the foreign key constraint. The foreign key constraint forms dependency along referred keys and reduces the redundancy, as shown in Figure 6.11. The wide relation 'Employees' in Figure 6.10 is divided into two different relations, Employees and Hobbies. The Employees-Hobbies relations provide the same information about the hobbies of each employee with less redundancy (no repeated attributes, no empty cells, and no repeated tuples).

As shown in Figure 6.10 and Figure 6.11, an unstructured raw table with much redundancy can be transformed into multiple tables with minimized redundancy by the foreign key relationship. This process is termed by database normalization, and normalized databases are said to be in normal form (NF). Several NFs were defined in 1971 by Codd [123]. In the relational model, the foreign key constraint (6-28) enhances data integrity because any modifications such as deletion, update, and insertion are prohibited if they do not satisfy the constraint. For example, any hobbies cannot be added in the Hobbies relation for a non-exist employee such as emp_id=4. If one employee (emp_id=2) is deleted from the Employees relation, the corresponding tuple (emp_id=2, hobby=cooking) in the Hobbies relation must also be deleted. Otherwise, the employee (emp_id=2) cannot be deleted.

6.9 Relational database for the COLPOTERME

While the hardware of the system is crucial for acquiring reliable polarimetric images of a target, it is the software of the system that has an impact on practical research activities such as conducting experiments and analysis. Especially in the case of a project involving a large number of samples, data maintenance and data handling can be a real challenge. The more samples there are, the higher the cost of research activities. For example, researchers have to spend more time on data acquisition and analysis when a larger sample size is involved. Therefore, systematic monitoring and processing of data might be necessary to improve the productivity and robustness of research outcomes. However, the development of a sophisticated system capable of rapid and efficient data acquisition and systematic maintenance of large datasets requires resources that are incomparable to the development of a relatively naïve system in the proof-of-concept stage. Moreover, a system that is too sophisticated and therefore complicated can increase the training cost for users. Thus, an

estimation of the appropriate complexity of the system is necessary to determine the optimal cost in relation to the available resources (in terms of time and budget) in research activities.

Database management system for the COLPOTERME

In the COLPOTERME project, the acquisition of polarimetric images for approximately 2,000 colposcopies has been programmed. It is therefore crucial to check the consistency of the acquisition and processing of data. This means that the acquisition and processing are expected to follow a certain pipeline. The visualization of a large number of images can also be a challenge. In addition, for state-of-the-art data analysis, a collaboration with the 2 laboratories (CMAP and iCUBE) has already been planned. Consequently, a centralized database system that can organize the whole research pipeline is necessary. If all the data generated during the research project can be stored in a centralized database that can be accessed from any stages in the pipeline as illustrated in Figure 6.12, the data produced at each stage are easily transferable to the other stages. This can lubricate the interconnection between the various research activities, leading to betterment in research productivity.

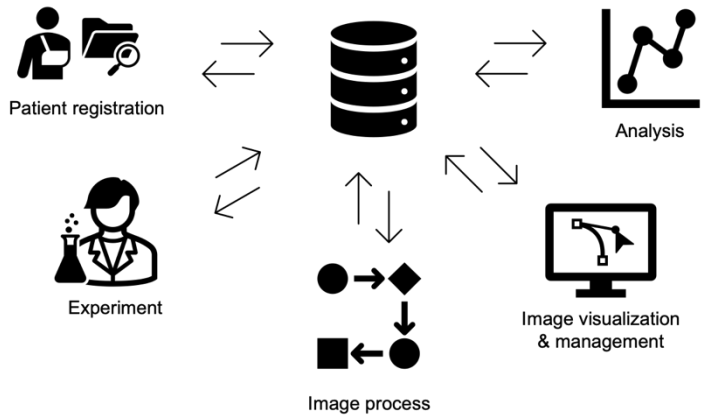

Figure 6.12 The concept of the centralized database for the research pipeline. For a research project involving large-scale data and collaborations, it is necessary to develop an accessible and consistent database system.

Thus, it is important to choose an appropriate database management system. Although spreadsheets and text files are the simplest and common data format in research fields because they are intuitive and do not require special training to use, they are not suitable for our main objective. In particular, the database management system has to meet the following main requirements:

- robustness and consistency in data acquisition and management;
- accessibility;
- compatibility with data acquisition, processing, visualization and analysis programs;
- forms familiar to data scientists.

To efficiently manage the data acquired during the COLPOTERME project, we worked on the implementation of a relational database often called Structured Query Language (SQL).

Database structures

The database for the COLPOTERME consists of 3 main entities, the device entity, hospital entity and operation entity as shown in Figure 6.13. The project can be described by 3 parts, the polarimetric device used for image acquisition, the patients, and the results of the experiments. The 3 entities can form the full description of the experiments performed in the project.

1. The polarimetric acquisition of the project is performed by the Mueller imaging device, the MPC.
2. Only a single patient can participate in the trial at a time, which corresponds to a patient visit (a session) for image acquisition.
3. Therefore, each experiment is carried out with 1 device and 1 patient, and the device will generate image data and log data about the patient.

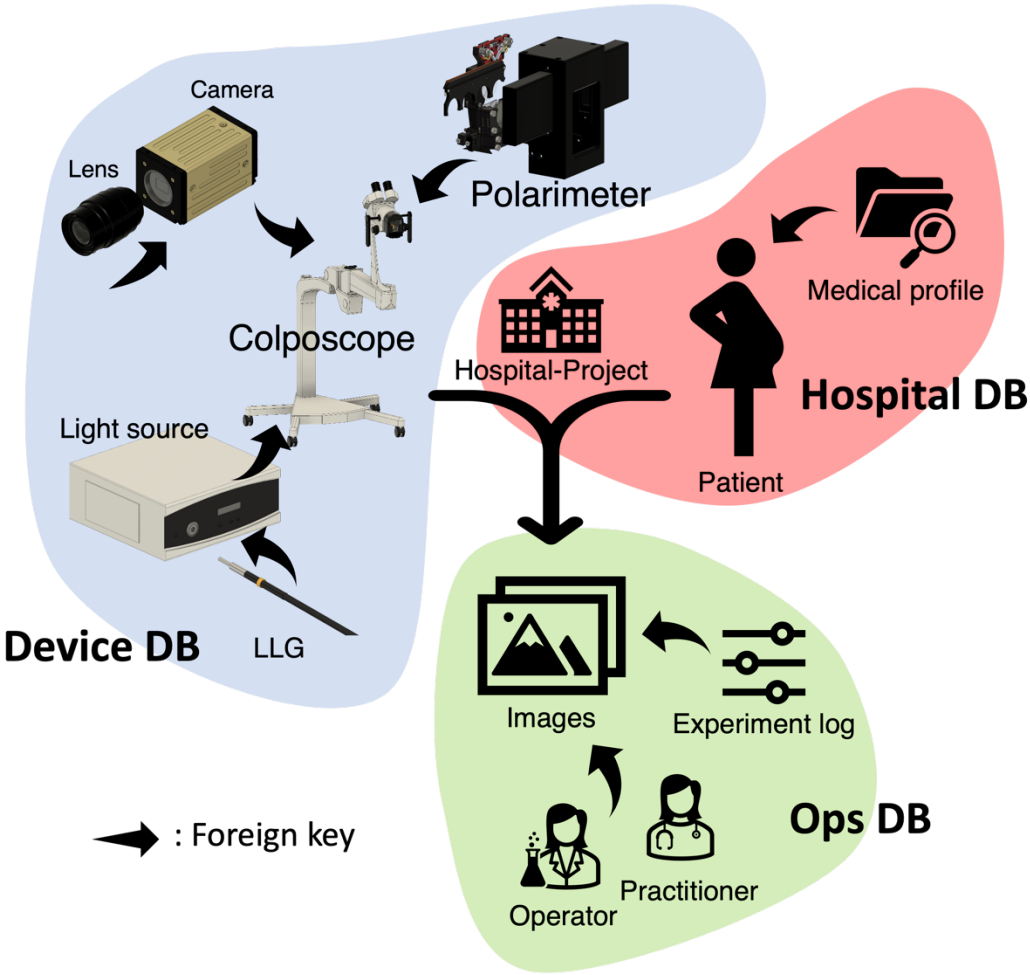

Figure 6.13 The conceptual design of the database for a clinical study using Mueller polarimetry. The arrows represent the foreign key relation between 2 relations.

For example, the device entity stores the information about the polarimetric device (hardware) used for the trial. Therefore, it describes the form of the device (the colposcope), its components (polarimeters, imaging systems, light sources,...) and its specifications (resolution, FPS, illumination power, ROI, wavelengths...). Its structure is inspired by the physical structure of the polarimetric system. The Mueller colposcope is fabricated by assembling 1 illumination system, 1 imaging system, and 1 polarimetric system on the

conventional colposcope. Therefore, a polarimetric device can be described by referring 1 component from each component relation.

An example of the foreign key relationship in the device entity is shown in Figure 6.14. The dotted lines represent the foreign key relationship. The attribute 'light source' in the relation 'Devices' refers to the tuple where lightsource_id=1 in the relation 'Light sources'. Similarly, the attribute 'light guide' refers to the tuple where lg_id=1 in the relation 'Light guides'. Therefore, one can find that the device referenced by device_id=1 usues the 300W xenon light source combined with the light guide LLG5 1.2m long.

This type of relationship is called 'one-to-many' relationship because 1 device can only reference 1 light source, whereas 1 light source can be referenced by several devices if many devices are using the same product. Note that this is an example to explain how the device entity is structured, so the actual details can be different from this example.

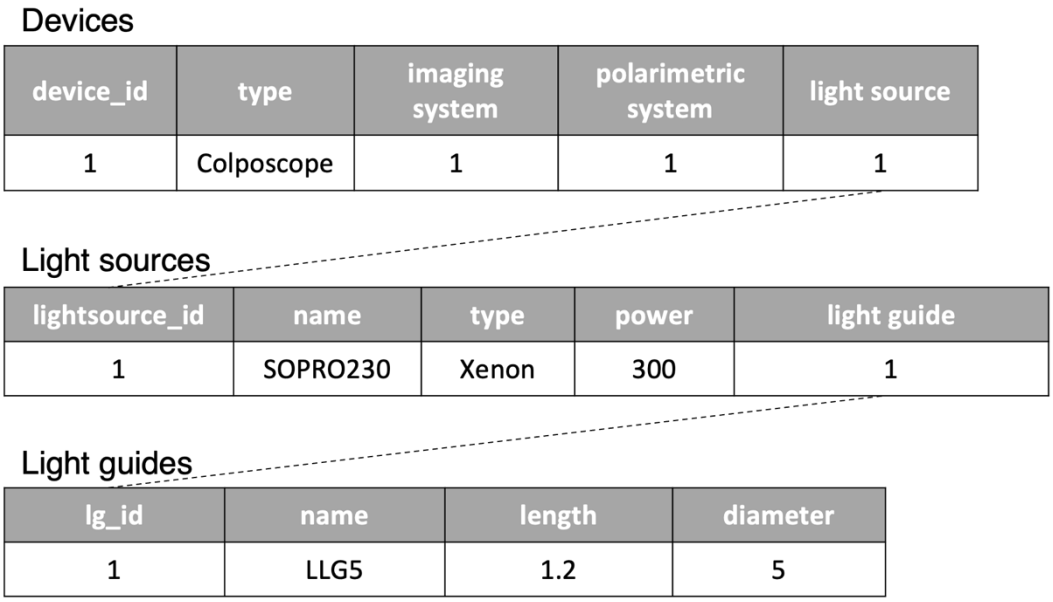

Figure 6.14 An example of foreign key relationship. The light source attribute in the Device relation refers to the lightsource_id in the Light sources relation.

6.10 The entity relationship (ER) diagrams of the 3 entities in the COLPOTERME

Device DB

The device entity stores information about the polarizer (hardware) used in the test. Therefore, describe the device's shape (colposcope), components (imaging systems, light sources, etc.), and specifications (resolution, FPS, lighting power, ROI, wavelength, etc.). A Mueller colposcope is manufactured by assembling one lighting system, one imaging system, and one polarization system onto the existing colposcope. Therefore, the polarimetric elements can be described by referring to one component in each component relationship.

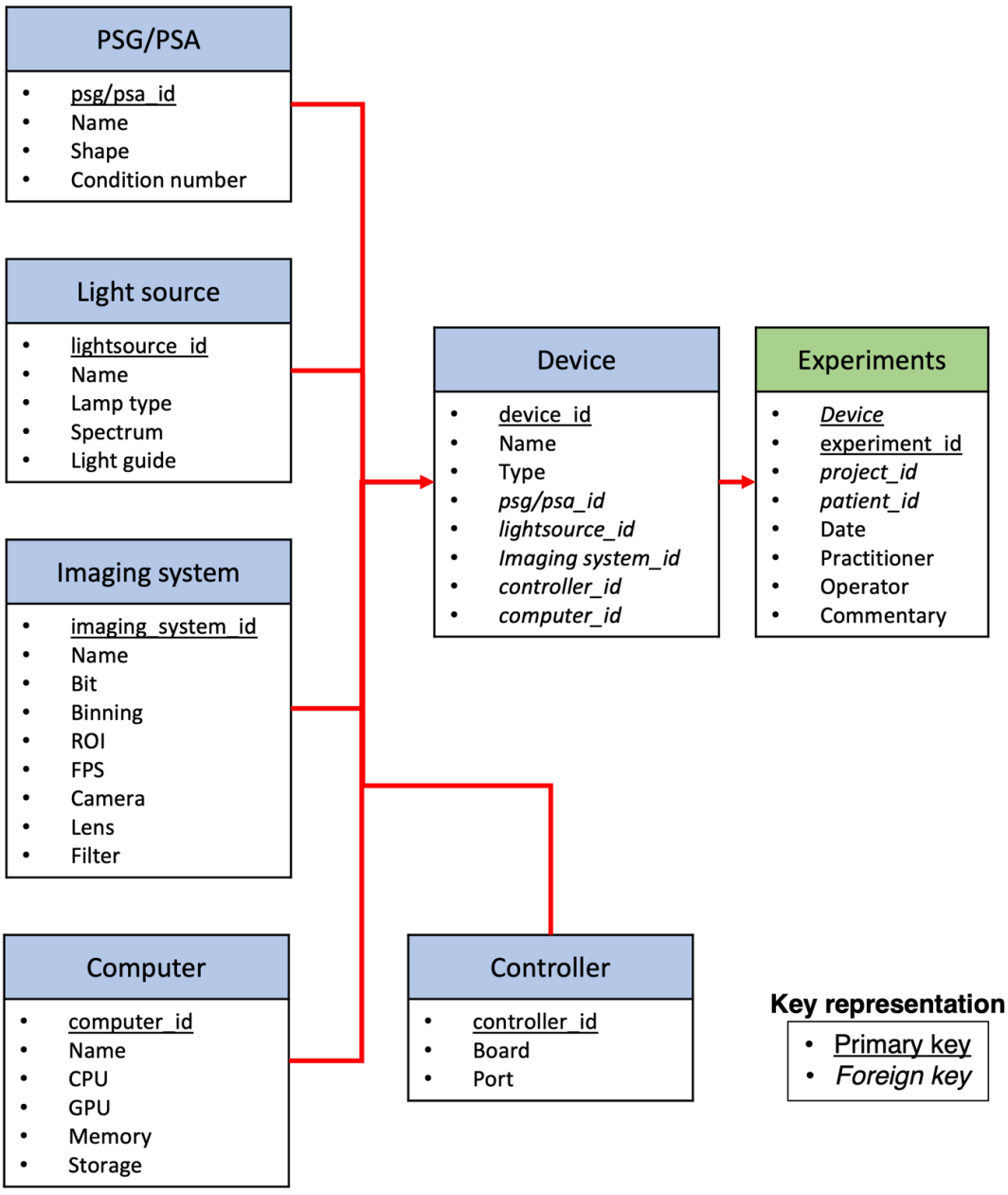

Figure 6.15 The simplified ER diagram of the device entity. The red arrows represent references by foreign keys.

The ER diagram of the hospital entity is shown in Figure 6.16. the hospital entity is designed for the 'patient' entity because the experiment results and medical information are determined by who the patient is and in which project the patient participates. Therefore, each patient is uniquely determined by their patient code and the project they are involved in.

The hospital and project relations are combined in the 'project_hospital' relation. A project can involve multiple hospitals in the case of a multicenter clinical study, and a single hospital can participate in multiple clinical studies. This relationship is mapped in the 'project_hospital' relation. While the 'patients' relation contains only the common patient information, such as birthdays, the patient medical data are stored in an additional relation, the 'Project1_meta' relation. The 'Project1_meta' relation provides additional information on the 'patients' relation, such as the pregnancy start date (DDG, debut de grossess). This type of relationship is called the 'ISA' (is-a) relationship.

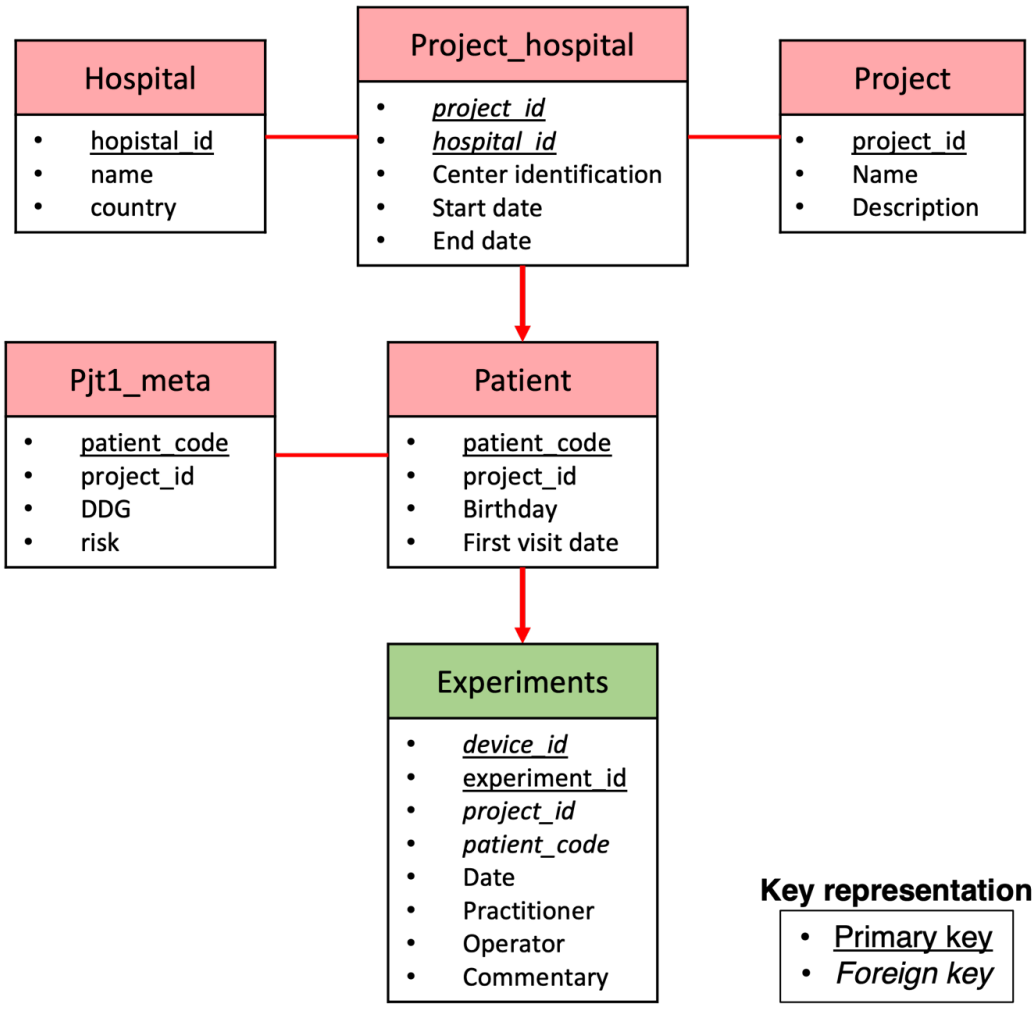

Figure 6.16 The simplified ER diagram of the hospital entity. The red arrows represent references by foreign keys.

The device and the patient entities are referred to in the operation entity shown in Figure 6.17. It is important to describe how each experiment was performed in the operation entity. Thus, the 'Experiments' relation refers to the 'device_id' attribute of the 'Devices' relation to describe the device used for each experiment. Then, it refers to the 'patient_code' and 'project_id' to describe the target and its involved project. More detailed information is

also described, such as who experimented, i.e., the (technical) operator and (medical) practitioner. A commentary can be written colloquially for exceptional descriptions in each experiment.

Each tuple of the 'Experiments' relation corresponds to a session of experiment. The three relations, the 'measurement,' 'calibration,' and 'spectralon,' describe the three different types of polarimetric acquisitions that can be performed in each session of the experiment. The measurement denotes the polarimetric image acquisition, i.e., the acquisition of Muller matrix images of the target – the cervix. On the other hand, the calibration denotes the eigenvalue calibration of the polarimetric system. The spectralon denotes the Mueller matrix image acquisition for the white reference reflector – the spectralon. The 'measurement_id,' 'calibration_id,' and 'spectralon_id' attributes identify multiple measurements, calibrations, and spectralons performed in a single session. The photographic conditions, such as exposure time and gain, are described in their 'condition' relation.

The 'Frame averaging' attribute denotes the number of averaged frames used for each acquisition. The 'Raw?' attribute denotes whether the multiple frames acquired for averaging are stored, or only the averaged image is stored. The 'File path' attribute indicates the file path where the corresponding acquisition results are stored. The 'File name' attribute is the file name of each acquired image in different wavelengths. This file path information is used to access the image data in image processes and visualizations.

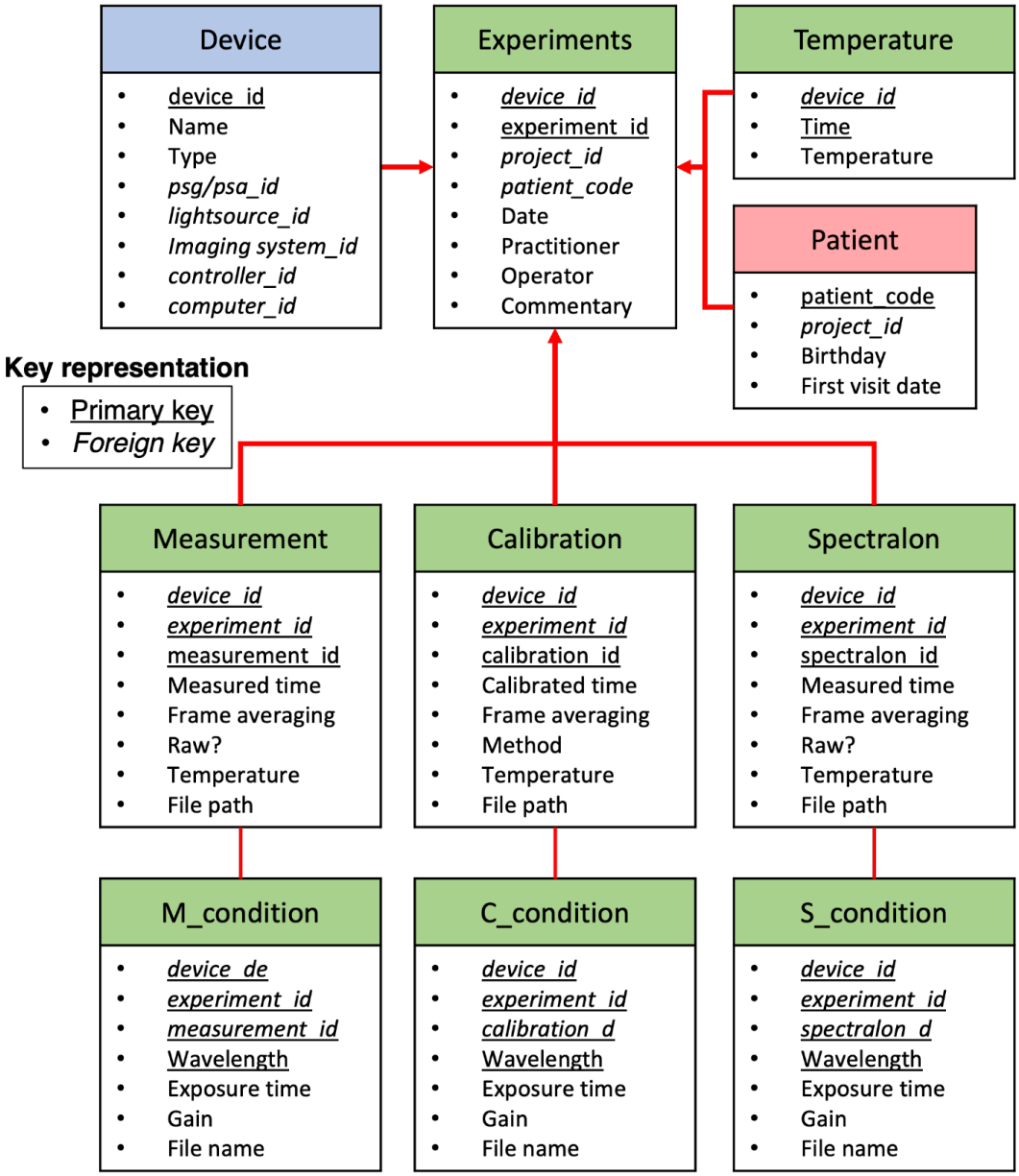

Figure 6.17 The simplified ER diagram of the operation entity. The red arrows represent references by foreign keys.

6.11 LabVIEW program for image acquisition

The User Interface (UI) of the MPC is the backbone of the system as it is directly related to the usability and physical ergonomics of the medical device. As the MPC is intended to be operated by hospital practitioners (physicians, midwives, etc.) who are not necessarily familiar with the technological aspects, the UI must be intuitive and easy to use. Moreover, it should also improve the quality of research outcomes and should guide the user to carry out the various steps in the proper order and way.

The MPC is managed by an in-house software that we developed in LabVIEW, a graphical programming language widely used in scientific research. This software controls the electronics of the MPC and enables the user to set all the parameters in experiment (exposure time of the 3-CMOS camera, the number of frame averaging, etc.) for its accurate calibration and for the acquisition of reliable images *in vivo*. The values of the parameters used in each experiment are automatically saved in the local database installed on the MPC's

workstation. In addition, the program is used to store useful information (patient code, date of birth, etc.) in the local database. This program can be easily used by the user without a detailed knowledge of all its parts thanks to a very intuitive and user-friendly Graphical User Interface (GUI) that we developed together with the hospital practitioners involved in the project.

The software is composed of several blocks. Each of these blocks is associated with a graphical interface or panel that allows a quick parametrization and an easy use of the MPC as explained in the following section.

Implementation in the clinical environment

The MPC, installed in the hospital environment, remains off-line for security reasons. Thus, the real-time update from the MPC to the server is not possible, so the acquired experimental data have to be transferred, after encryption, from the MPC storage to the Ecole Polytechnique server, using a portable SSD. Therefore, the data are first stored in the storage of the local MPC workstation and then transferred to the Ecole Polytechnique server. Data acquisition and storage on the MPC are governed by in-house LabVIEW software which will be described more in detail later in the manuscript.

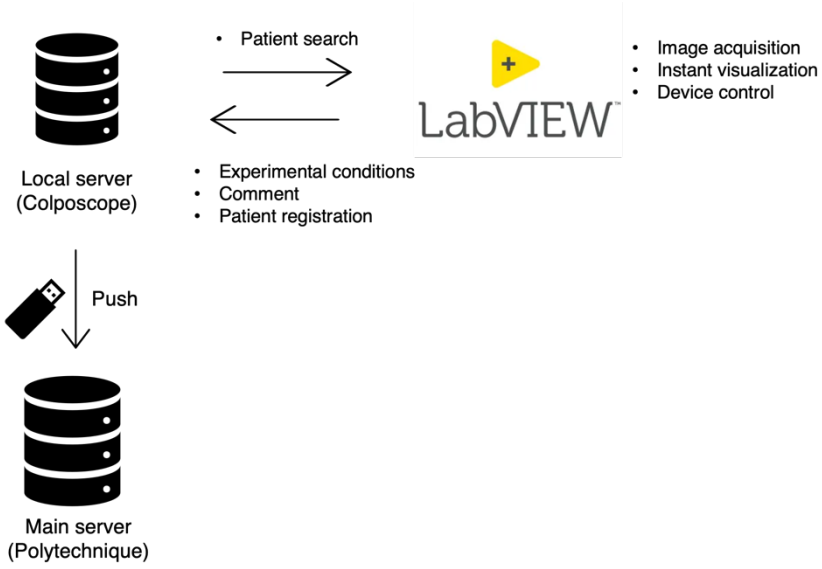

Figure 6.18 The connectivity scheme of the LabVIEW program. The data accumulated through LabVIEW are transferred to the main server in Ecole Polytechnique. The LabVIEW program is used to control the polarimetric acquisitions in the trial.

Although the database was designed for the COLPOTERME project, its structure has been generalized as much as possible to be applicable for future clinical studies on other applications of Mueller polarimetric imaging. The concept of this new database system arose from the centralization of data from multicenter clinical trials, as well as from multiple clinical projects using various polarimetric devices. It is expected to significantly increase the efficiency in data management and analysis in forward-looking collaborations with data scientists, in comparison to the previous primitive database composed with a bunch of text files.

Main panel

The detail of the LabVIEW program used for image acquisition is shown in Figure 6.19. Firstly, the long bar, placed in the purple box (marked by a) at the top of the main panel, indicates the main steps to be followed by the user during the experimental procedure. These main steps are in order: 1) registration of patient information, 2) calibration of the MPC, 3) measurement of albedo (spectralon), 4) start of a video recording, 5) acquisition of Mueller polarimetric images, 6) stop of the video recording. Each step is represented by a white circle on the long bar. Each circle turns green when the corresponding task is completed and red when it is skipped. All these main steps are performed through the dedicated buttons placed in the dotted red box (marked by c) on the left of the main panel. These buttons are activated (interactable) when the corresponding steps still need to be executed. Therefore, the user can only execute the procedure in the indicated sequence. The successful completion of each step is necessary to proceed to the next. The described workflow has been designed and developed to prevent the user from omitting any key steps.

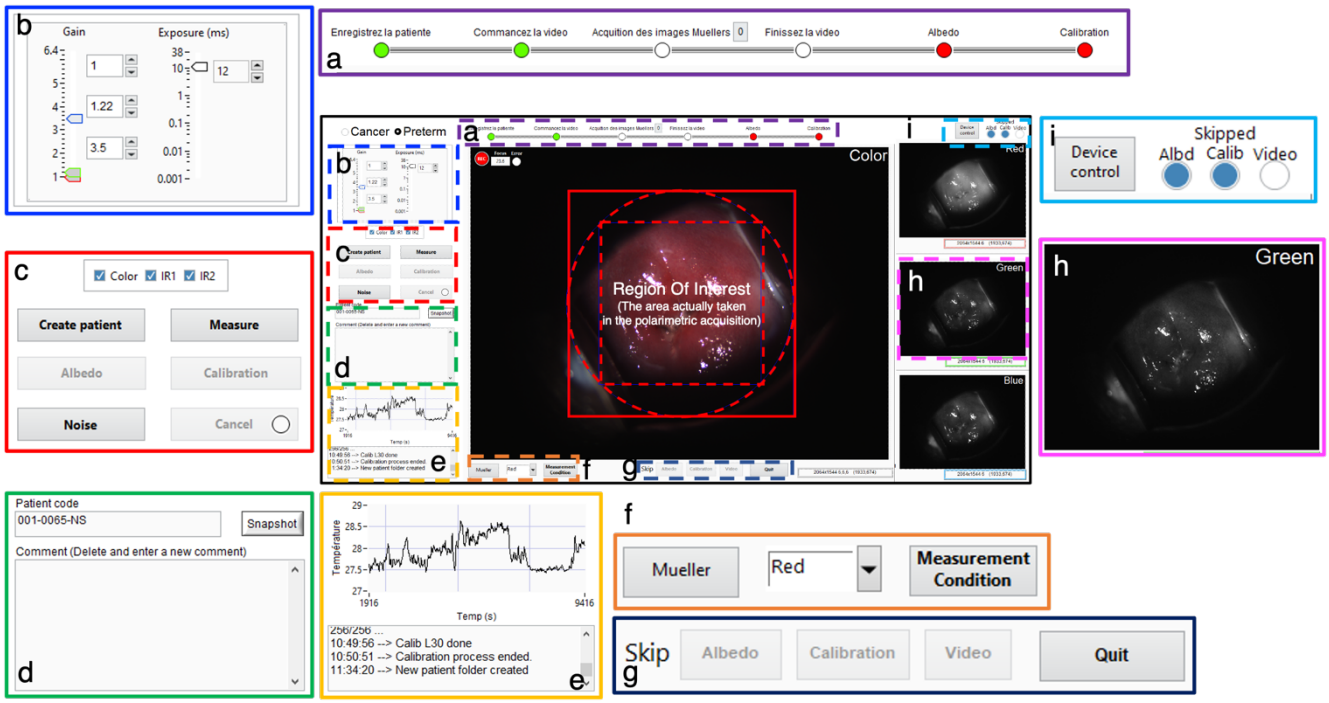

Figure 6.19 The main panel of the program used to acquire polarimetric images using the MPC.

Nevertheless, the calibration and albedo measurement steps can be skipped by touching the "Calibration" and "Albedo" buttons located next to the "Skip" text in the blue box (marked with a g) below the central panel. In this case, the user has the option to perform the calibration and albedo measurement immediately after the image acquisition is made. This option allowed us to define, together with the practitioners, the optimal and fastest procedure for *in vivo* cervical analysis. In particular, we found that calibrating the MPC and measuring the albedo after cervical inspection significantly reduces the waiting time for a patient, especially in cases where several patients are visited in a row. Skipped steps are marked by the three circles in the blue box (marked by i). The sub-panel for patient registration will be described in the following section.

The brightness and the color of the real-time image are adjusted using the sub-panel in the blue dotted box (marked by b), changing the exposure time or the gain of the three sensors. With this panel, the user can only give one value for the exposure time of the 3-CMOS camera's three sensors, while the gain can be adjusted separately. We have set the gain value for all three sensors to obtain a white balance capable of providing a real-time image close to what the practitioner sees with the naked eye through the binocular system of the colposcope. Therefore, the gains of the three sensors are adjusted to have the same intensity values for the three channels with respect to a white reference target, i.e., the spectralon. We have found empirically the red, green and blue channels with optimal gain values of 1, 1.22 and 3.5 respectively to achieve optimal white balance. In addition, the exposure time required to achieve optimal brightness is 12 ms for cervical imaging and 1 ms for metal plate and spectralon imaging. The user can easily press the 'F2' and 'F3' buttons on the keyboard to set the exposure time to 12ms and 1ms, respectively. The photographic conditions for calibration, polarimetric imaging of the spectralon, and polarimetric imaging of the cervix are defined individually in another sub-panel.

The checkbox with three options, 'Color,' 'IR1', and 'IR2', allows the user to select the color filters for acquisition. The 'Color' option corresponds to the 3-band filter, and 'IR1' and 'IR2' correspond to the 650 nm and 700 nm filters, respectively. The filters used for measurements, calibrations, and spectralons are determined depending on the options checked. In case of multiple filter selection, images are acquired by rotating the camera adapter's filter wheel.

The user can record any additional descriptive information about the current experiment in the text box surrounded by the green dotted line (marked by d). The texts written in this area are uploaded to the "Comment" attribute of the "Experiments" relation every 10 seconds in the database. The current temperature of the PSG is constantly monitored, and the temperature versus time curve displayed in the panel surrounded by the orange dotted line (marked by e) is updated every 30 seconds. The time and temperature are also automatically recorded in the "Temperature" relation of the "Operation" entity of the database.

A square of 1120×1120 pixels, indicated by Q1 in Figure 6.20, is selected in the center of the real-time image. If the colposcope is used at a working distance of 30 cm with the minimum zoom condition (×1), this square has a lateral dimension of about 3.8 centimeters, slightly larger than the typical diameter of the cervix which can vary between 2.5 and 3.5 cm. Although the real-time image is in full resolution (2064×1544 pixels), Mueller polarimetric imaging is only performed for the Q1 region. This is due to the fact that the 3-CMOS camera uses the camera link interface which limits the number of FPS to 26 for each sensor at the full resolution. By selecting the Q1 window, it is possible to increase the FPS to 64 FPS, which is the minimum required to obtain reliable polarimetric images as explained earlier in the specifications. For this reason, we have chosen an objective lens for the 3-CMOS camera able to provide an image of the cervix that fits perfectly into Q1.

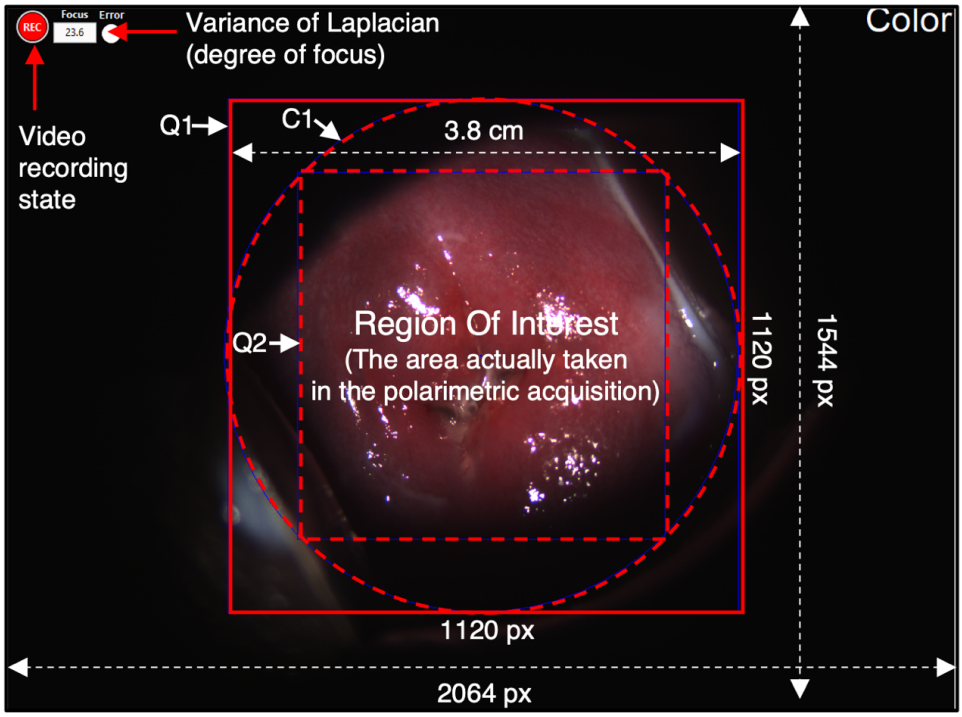

Figure 6.20 The real-time color video in the real practice with the MPC. The outer rectangle Q1 corresponds to the effective ROI where polarimetric acquisition is actually performed. The outer circle C1 corresponds to the beam size at a working distance of 300 millimeters. The inner rectangle Q2 represents the optimal position where the cervix has to be placed.

The circle marked by C1, which corresponds to the beam size (a diameter of 3.8 cm) at a working distance of 30 cm, is selected within Q1. Therefore, polarimetric analysis of the cervix is only possible for the pixels contained in C1. In addition, the smaller box marked by Q2 within C1 represents the area where the image quality is guaranteed due to the non-uniform illumination which becomes significantly weaker at the edges of the beam. For this reason, the user should place the cervix inside Q2.

The number inside the small rectangle in the upper left corner of the central sub-panel represents the variance of the Laplacian, which is used to evaluate the image sharpness in real time. The Laplacian refers to the Laplacian image filter, which is a high pass filter used for detecting the edges. The variance of the filtered image represents the contrast of the image. In other words, the high variance of the Laplacian indicates the presence of high spatial frequency terms in the image, i.e. the edges. Herein, it is worthwhile to note that the imaging optics is equivalent to the Fourier formation of its PSF. Thus, the variance of Laplacian in imaging is related whether the PSF allows to capture the high frequency part of the object. Consequently, the variance of Laplacian can be used for the quantification of sharpness of images which also represents the degree of focus [124]. Using the variance of the Laplacian, the user can search for the sharpest possible image of the cervix with a procedure that will be explained in more detail later.

The three small sub-panels to the right of the large panel within the pink dotted box (indicated by i) show separate real-time monochromatic images of the cervix in the red, green and blue parts of the visible spectrum with the same resolution as the central image. By clicking on one of the three sub-panels, the corresponding image is displayed in the

central sub-panel for better visualization. Automatically, the image that was originally in the central sub-panel is displayed in the sub-panel that was clicked on. In this way, the user can examine the intensity image for each selected color in more detail, if necessary.

Instant image visualization

After each acquisition is complete, 4 polarimetric images, obtained from the Mueller matrix measured for a selected wavelength after applying the Lu-Chipman decomposition, are displayed in the main panel, as shown in Figure 6.21, replacing the intensity images (including the color image and the monochromatic images in the three spectral regions of interest). In particular, the displayed polarimetric images are the total depolarization, the linear phase retardance, the azimuth of the linear phase retardance and the diattenuation. By clicking on one of the small panels on the right, the corresponding image is transferred to the large central panel. In this way the user can choose to look in more detail at a particular polarimetric parameter. Automatically, the image that was originally in the central panel is transferred to the side panel that was clicked on. A small panel at the bottom (in the green box) of the central image allows the selection of the wavelength at which to display the resulting polarimetric images.

The range of values for each parameter can also be adjusted by the slider at the top, which appears only for the polarimetric parameters. The user can exit this function at any time and return to the real-time intensity image by pressing the "Mueller" button at the bottom left of the central image panel. The ability to display polarimetric images immediately after intensity image acquisition is an entirely new functionality that did not exist in the dual-wavelength version of the MPC. This feature is crucial for checking the quality of the measurements in real time and repeating the measurements if necessary.

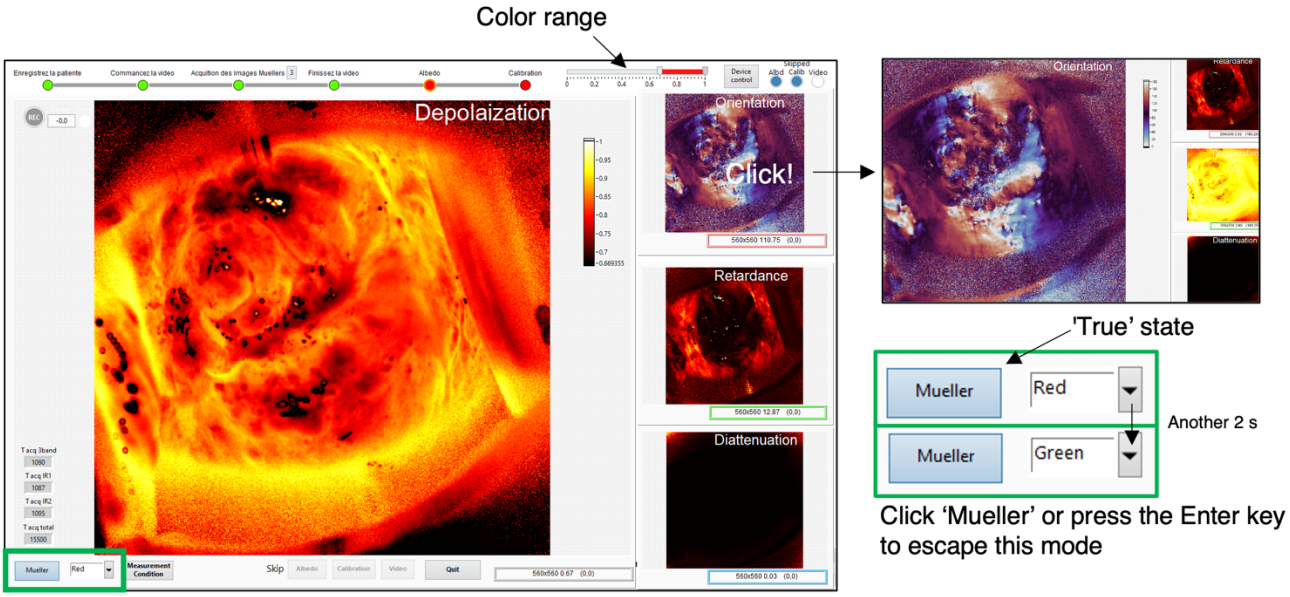

Figure 6.21 After each acquisition, 4 polarimetric images from Lu-Chipman decomposition are shown directly in the interface of the main. The color range is adjustable by the range bar on the top. The 3 small images can be moved to the biggest panel by left click.

Setting and determining an exposure time for polarimetric imaging

While the exposure time for real-time color imaging can be changed by the user simultaneously for all three sensors of the 3-CMOS camera directly on the "Main" panel, this is not the case for the photographic conditions required for polarimetric imaging.

The procedure for each patient consists of three main steps: MPC calibration, polarimetric imaging of the albedo imaging, and polarimetric imaging of the cervix. For each of these steps, the optimal settings for the exposure time, gain, and the number of averaged frames are made separately using the pop-up window shown in Figure 6.22, which is opened by clicking on the "Measurement condition" button in the sub-panel located inside the orange box (indicated by f) under the central sub-panel shown in Figure 6.19. The user can change the exposure time of the three sensors separately, which is not the case for the gain. Indeed, we found that increasing the gain has no impact on the signal-to-noise ratio, as shown in Chapter 3. For this reason, we decided to work with the gain fixed at the minimum value for all three sensors.

Nevertheless, the user can always adjust the gain of each sensor separately for any exceptional situation. The acquisition number (frame-averaging) of the intensity images is also defined here. This number is set to 16 (corresponding to the acquisition of 16×16 intensity images in total) for the calibration and polarimetric albedo (spectralon) imaging phases. In contrast, it is set to 4 (corresponding to the acquisition of 16×4 intensity images in total) for polarimetric cervical imaging. The optimal parameters for the three main steps of an entire procedure in terms of exposure time, gain, and the number of the averaged frame are fixed beforehand. Thus, the operator does not need to change them when moving from one step to the next.

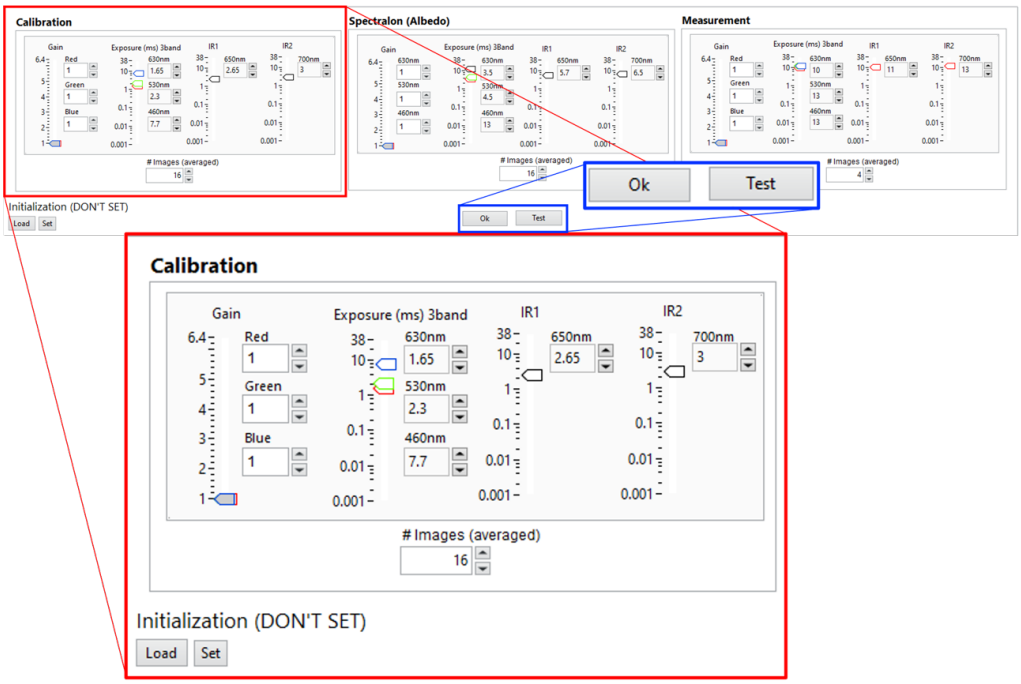

Figure 6.22 The sub-panel for setting gain and exposure times for calibration, spectralon, and (sample) measurement. Each parameter can be tested in another sub-panel called up by the 'Test' button.

The "Initialization" sub-panel at the bottom left of the pop-up window allows the gain and exposure time to be reset to the initial values. The current settings can be saved as initial settings by touching the "Set" button. In general, the same optimal settings are defined for all patients. However, these settings should be adjusted if the illumination of the Xenon lamp decreases after a certain period of use or if a new one replaces it.

The optimal exposure time can be determined using another pop-up window called "Tune param," shown in Figure 6.23Figure 6.23 The sub-panel for setting gain and exposure times for calibration, spectralon, and samples. The photographic conditions for three targets can be set individually. The parameters can be tested with the button ‘Evaluate’. When an image is acquired, an intensity distribution is shown in the ‘Histogram’ panel. Saturated pixels appear red as shown in the inset., which appears when the user clicks on the "Test" button in the blue box. The operator can optimize the exposure time separately for each wavelength range used. As a reminder, polarimetric measurements are performed simultaneously at 460 nm, 530 nm, and 630 nm through the 3-band filter (indicated by RGB). This filter also allows the acquisition of the color image of the cervix. To further explore the red/near-infrared portion of the visible spectrum, we have added two spectral filters that allow the acquisition of polarimetric images at 650 nm (indicated as IR1) and 700 nm (indicated as IR2). For each step of a patient procedure (calibration, polarimetric spectralon measurement, polarimetric cervical measurement) and each explored wavelength range, the exposure time can be optimized separately. Each step of the procedure can be selected by clicking on one of the buttons in the green box, and each filter can be selected using the sub-panel in the blue box. Once the type of filter is selected, the operator can click on the "Change" button to activate the motor that turns the mechanical gear system, described in detail in Chapter 3, which allows the selected filter to be positioned correctly in front of the 3-CMOS camera.

Once the procedure step and filter are selected, the operator presses the "Evaluate" button, which allows the acquisition of 16 intensity images, each corresponding to a particular combination between the possible PSG and PSA configurations. Depending on the properties of the target, the 16-intensity images acquired are different. On the two sub-panels on the left of the "Tune param" pop-up window are displayed the highest (top) and lowest (bottom) intensity images. The green square on these two images allows selecting the area of interest whose histogram is displayed on the right sub-panel. This way, the operator can select an exposure time and immediately check if it is optimal. Because the surface of the cervix is very smooth, some pixels in the image may be completely saturated because they receive specularly reflected light.

The optimal condition for the exposure time is when the histogram of the highest intensity image is as close as possible to the upper limit of each sensor's dynamic range, and the number of saturated pixels remains limited (less than 5% of all pixels in the image). We found that this condition is usually achieved if the exposure time is set so that the peak of the histogram relative to the highest intensity image is around 3400~3600 (in 12-bit), where the signal-to-noise ratio is maximized.

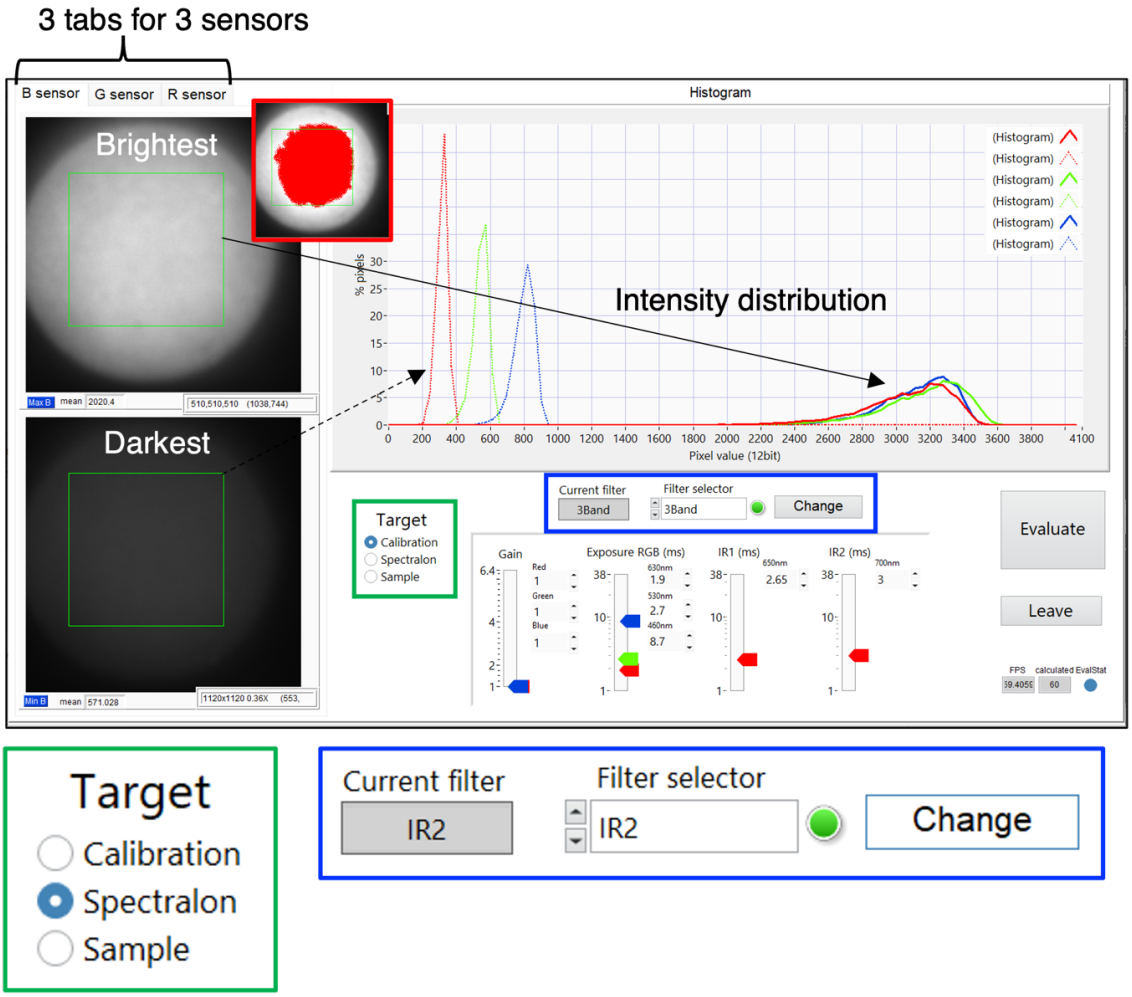

Figure 6.23 The sub-panel for setting gain and exposure times for calibration, spectralon, and samples. The photographic conditions for three targets can be set individually. The parameters can be tested with the button 'Evaluate'. When an image is acquired, an intensity distribution is shown in the 'Histogram' panel. Saturated pixels appear red as shown in the inset.

On the other hand, the user does not need to find and set the exposure time for every acquisition. If the acquisitions are performed in the same manner and with a similar (or same) target, the variations in intensities are small and do not need to be updated each time. Therefore, the users, especially medical practitioners, can perform their experiments without considering the exposure time setting. Especially for the measurement, the exposure time is fixed to be 13 ms which is the maximum exposure time for 64 FPS.

Patient registration

During the study, which has a total duration of 36 months, 650 patients will be analyzed on average three times for a total of about 2000 colposcopies. Each patient is registered before the start of the whole procedure (calibration, polarimetric imaging of the spectralon, polarimetric imaging of the cervix). For this purpose, the operator has to click on the "Create patient" button, which opens a pop-up window where the patient's information can be inserted. The operator can choose the type of project in the scrolling window at the top ("Preterm birth" corresponds to the COLPOTERME study). Furthermore, the operator has to insert the number of the center where the data collection is performed in the "# Centre" text field (001 corresponds to the University Hospital of Kremlin Bicêtre),

the inclusion number of the patient in the "# Patient" text field and the date of the beginning of pregnancy in the "DDG" text field. An algorithm automatically calculates the patient's gestational age displayed in the "Weeks of amenorrhea + Days" text field. The operator has to check the "High Risk" box if the patient is at risk of preterm birth. Finally, the operator can add additional comments in the large text box "Last comment." The "# Patient" text field is pre-filled with the new inclusion number calculated automatically.

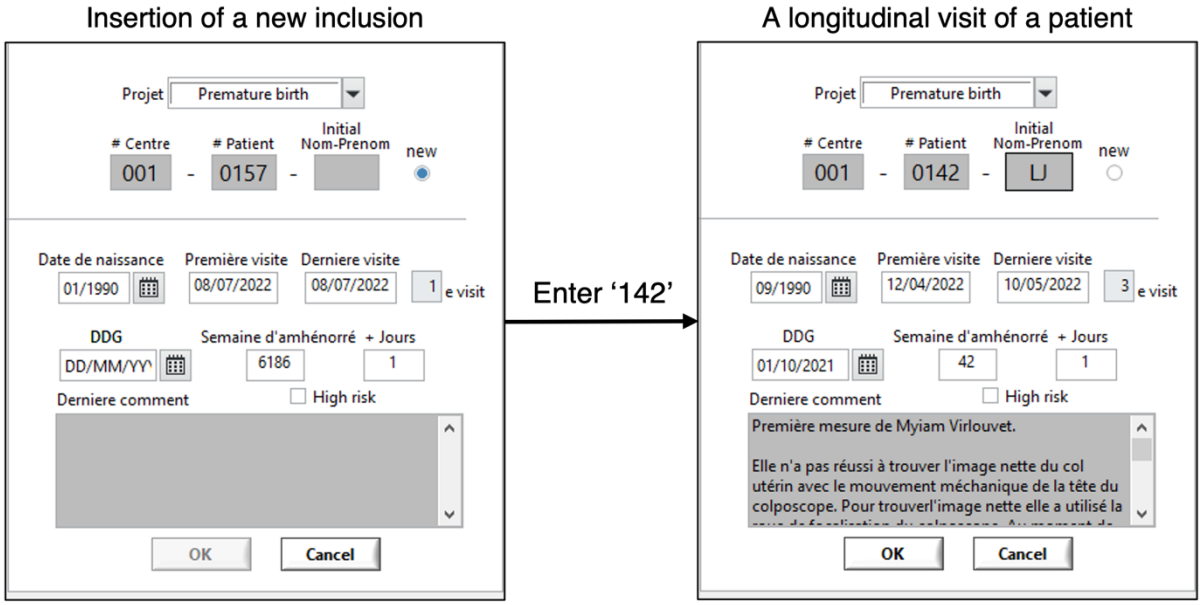

Figure 6.24 The sub-panel for registration of a patient. Each patient has a unique patient number (inclusion number). When the user enters a number, patient information appears in the panel if the patient was already registered.

By clicking on the "OK" button, a new tuple containing all the patient's information, is inserted in the "Hospital" entity and the "Experiments" relationship of the "Operation" entity of the database. During the experiment, it is expected that each patient will be examined several times to follow longitudinal changes of the cervix during pregnancy. If a patient has already been included in a previous session, the operator inserts her inclusion number in the '# Patient' text field. The number of visits made by the patient is then automatically displayed in the 'e visit' text field. The software retrieves, from the local database, all the information about the patient already inserted at the time of her inclusion. This allows the user to check that the patient information is correct, thus reducing registration errors on visits subsequent to the inclusion.

Device functionality check

Considering the MPC must keep functioning for three years in the OB/Bicetre, the maintenance of the device is important. The user needs to be able to check if all the MPC functionalities are normal and react to encountered problems and errors. The device status check can be done in the pop-up window in Figure 6.25, and it appears when the 'Device control' button in i. The states of the main components, the FPGA (controller), filter slider, camera, database, and filter wheel, are represented in the five circles. They turn green if the components are normal and turn red when there is an error.

The user can set several options for polarimetric acquisitions in this feature. The 'Save raw data' check box allows the user to choose whether the images are stored after or before the frame averaging. By choosing 'on,' each frame of the *n*-frame averaging method can be stored. The 'Direct calibration' and 'Mueller view' check boxes are to choose whether we compute the ECM and Mueller image processes ($A^{-1}BW^{-1}$, decomposition) after each calibration and measurement. These functions will be described below in more detail.

The user can initialize the filter wheel, FPGA, and slider in this window when they cause an error. These components can fall into consistent malfunction when an error occurs during polarimetric acquisition. The filter wheel and slider can be stuck in the wrong position, and the liquid crystals can keep transitioning even after the end of the acquisition. The user can initialize and test them through these buttons in these cases.

The 'session setting' button is used to change the initial setting of the experiment. It calls another pop-up window which, in fact, once appeared when the main program was launched. It lets the user choose the operator and the practitioner participating in the current experiment. The lamp usage time is also recorded through this window. The lamp usage time is related to the intensity decrease of the light source, though this value is not being used in the current analysis. A new operator and practitioner can also be registered into the database when a new member participates in the project.

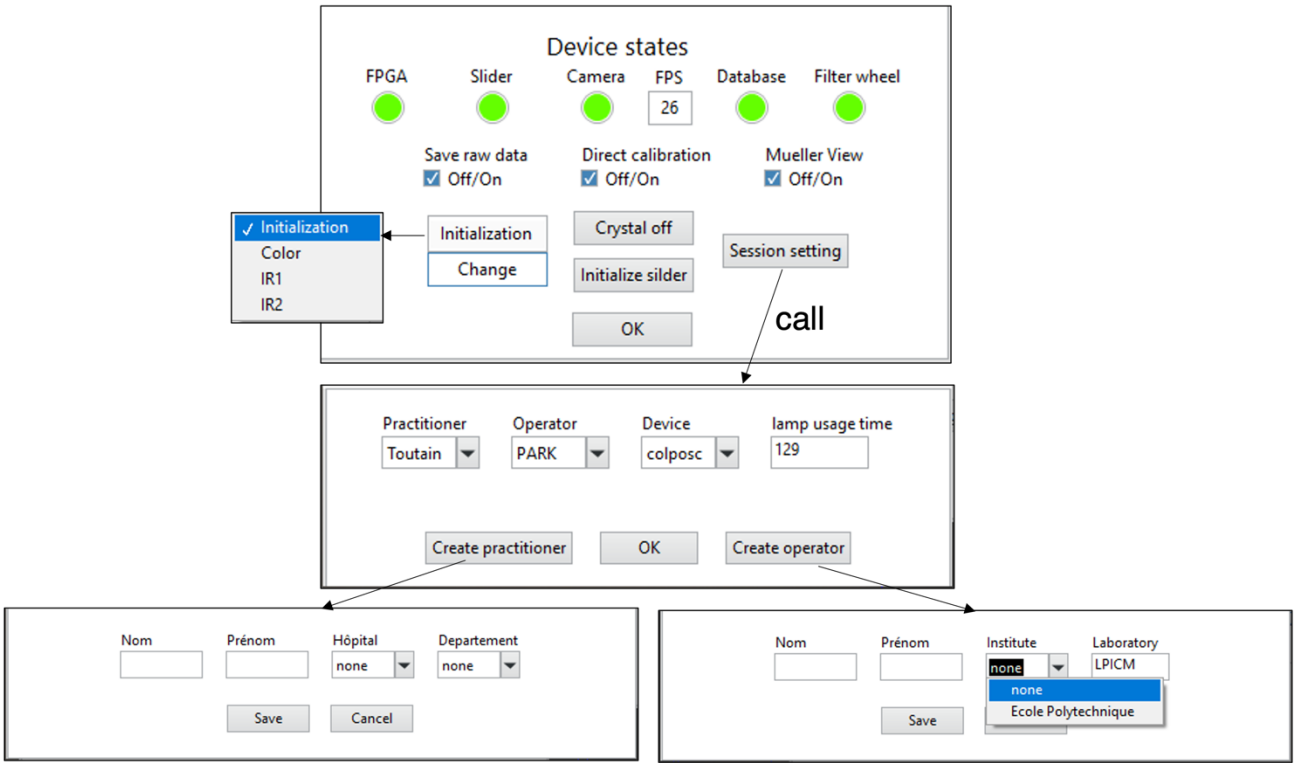

Figure 6.25 The sub-panel for checking the device status. The green circles at the top represent the status of each component. The user can set complementary options for polarimetric acquisition. The filter wheel and slider can be manually controlled from this panel. The 'Session setting' button calls up another sub-panel for registering a medical practitioner and operator.

Instant validation of the Eigenvalue Calibration Method (ECM)

The ECM might be the heaviest operation in Mueller polarimetry. Not only it requires the image acquisitions of the four reference samples (air, P0, P90, R30 (or L30 in French)), but also the optimization of the loss function H (kernel H) also has to be performed. Especially, the eigenvalue decomposition and singular value decomposition for an array of matrices are not vectorizable; their computational cost is then proportional to the number of pixels ($O(n)$ for n-pixels in the big-o notation). The former MATLAB ECM code performed the ECM with the non-vectorized codes, which took 1 minute for each wavelength. Therefore, it was supposed to take more than 5 minutes in the new MPC because the new MPC generates polarimetric images at five wavelengths and with more pixels.

However, validating the polarimetric functionality through the ECM is essential because only the ECM provides the full description of the functionality, such as accuracy and precision with respect to the reference samples. Thanks to the optimization of the codes described above, the new system can perform the ECM in 3 minutes, including image acquisitions and computation. The acquisitions of the reference samples take 2 minutes, and the computation takes 10 s for each wavelength in 660×660 resolution. After the computation, the histograms of the three matrices of the reference samples appear, as shown in Figure 6.26.

The 4×4 histogram array represents the distributions of the corresponding matrix elements of the chosen reference sample. The means and standard deviations of the distributions at five wavelengths are also charted in the 16 histogram panels as shown in the inset in the orange box (630 nm, 530 nm, 460 nm, 650 nm, and 700 nm from the top).

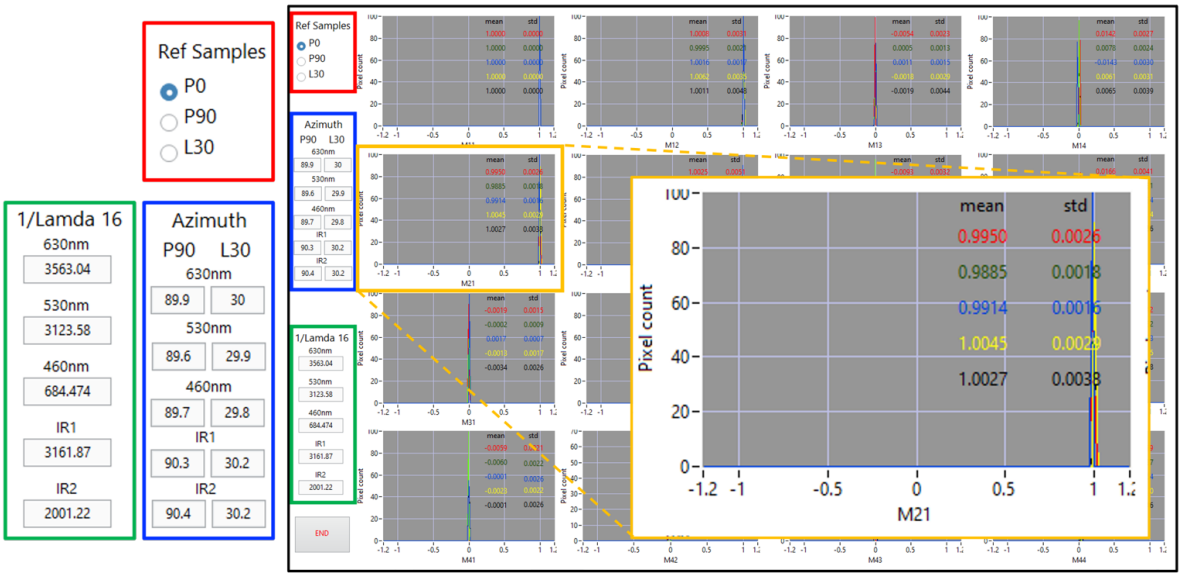

Figure 6.26 The sub-panel for validating calibration quality. The histograms of 4×4 matrix elements are shown. The quality can be verified in terms of the mean and standard deviation of each element. The three reference samples can be individually visualized (the red box.) The azimuth angle of each sample can be also verified (the blue box.) The value $1/\lambda_{16}$ for each wavelength represents a goodness-of-fit of the ECM (the green box.)

The user can choose one reference sample to visualize in the radio box in the red box on the left. The azimuth angles of P90 and L30 in 5 wavelengths are also shown in the text boxes in the blue rectangle. The reciprocal of λ_{16} represents the residue in optimizing the loss function H, which is related to the global precision of the W and A matrices.

In this feature, the user can check if the calibration results correspond to the theoretical matrix of the P0, P90, and L30. In case of bad calibrations, NaN values can appear with a broad distribution. The reciprocal of λ_{16} also converges to zero in case of a malfunctioning of the system.

6.12 Stray light subtraction

Although we have eliminated critical specular reflection by tilting the PSG as described in the hardware section, some light beams scattered by the components of the PSG can still cause stray light. The MPC is characterized by a background light signal that can strongly affect the quality of the acquired polarimetric images, especially when the cervix is highly absorbent and returns low levels of light intensity. This background signal has to be correctly estimated and subtracted from the main signal. It is composed of several contributions, firstly the signal related to the thermal noise of the 3-CMOS camera. The image I_{th} produced by the thermal noise is obtained for the three sensors simply by closing the 3-CMOS camera with a shutter. Usually, the thermal noise is proportional to exposure time. However, the contribution of the thermal noise in the modern CMOS sensors is negligible in milliseconds scale thanks to advanced dark noise compensation techniques (such as the double-sampling noise subtraction). Therefore, they remain the same regardless of the exposure time. Let I_{dark} be the constant background signal. In the case of the AP3200, I_{dark} is 98.

The second contribution is represented by the stray reflections of the polarimetric box components. Despite the great effort we put into designing the new polarimetric box, which allowed us to significantly reduce these stray reflections, as explained in detail in the hardware section, they were not completely eliminated. These stray reflections can significantly increase the background signal in a spatially inhomogeneous way. One method to estimate the signal related to the stray reflections is to acquire with the MPC the image of a strongly absorbing target for the three sensors of the 3-CMOS camera. For this reason, we placed the MPC in a dark room to acquire, for each sensor, the image of a black screen (BK5, THORLABS) placed on a wall 10 meters away from the polarimetric head. However, we found that the black screen does not have a perfect zero reflection coefficient and produces a spatially inhomogeneous image I_{wall} for each sensor.

In order to determine the contribution of the stray reflections, we acquired the black screen image in two steps. First, we measured I_{wall} for each wavelength with a fixed exposure time t_{exp} by removing the polarimetric box except for the PSG polarizer which has no impact on the stray reflections. Meanwhile, it does determine the amount of light that reaches the screen. We reasonably assumed that the attenuation coefficient of the FLCs and the WPs, which are the main sources of stray reflections, is negligible and therefore can be removed for this first part of the measurement.

In the second step, we reassembled the polarimetric box, taking care not to modify the position of the colposcope head. It allowed us to measure I_{box} for each wavelength (maintaining the same exposure time used in the first step), where $I_{box} = I_{wall} + I_{stray}$. I_{stray} denotes the contribution of the stray reflections. In this way, the I_{stray} image, measured by setting a fixed exposure time for each detector of the 3-CMOS camera, can be obtained by the following expression:

$$I_{stray} = I_{box} - I_{wall} \tag{6-29}$$

Because the stray light signal is proportional to the exposure time, the signal is normalized by the exposure time (signals per ms).

$$i_{stray} = \frac{I_{stray}}{t_{exp}} \tag{6-30}$$

Then, the stray light image can be subtracted from measured images.

$$I = I_{\text{measured}} - i_{stray} \times t_{exp} - I_{dark} \tag{6-31}$$

t_{exp} denotes the exposure time used in the measurement and I_{dark} is the image without illumination.

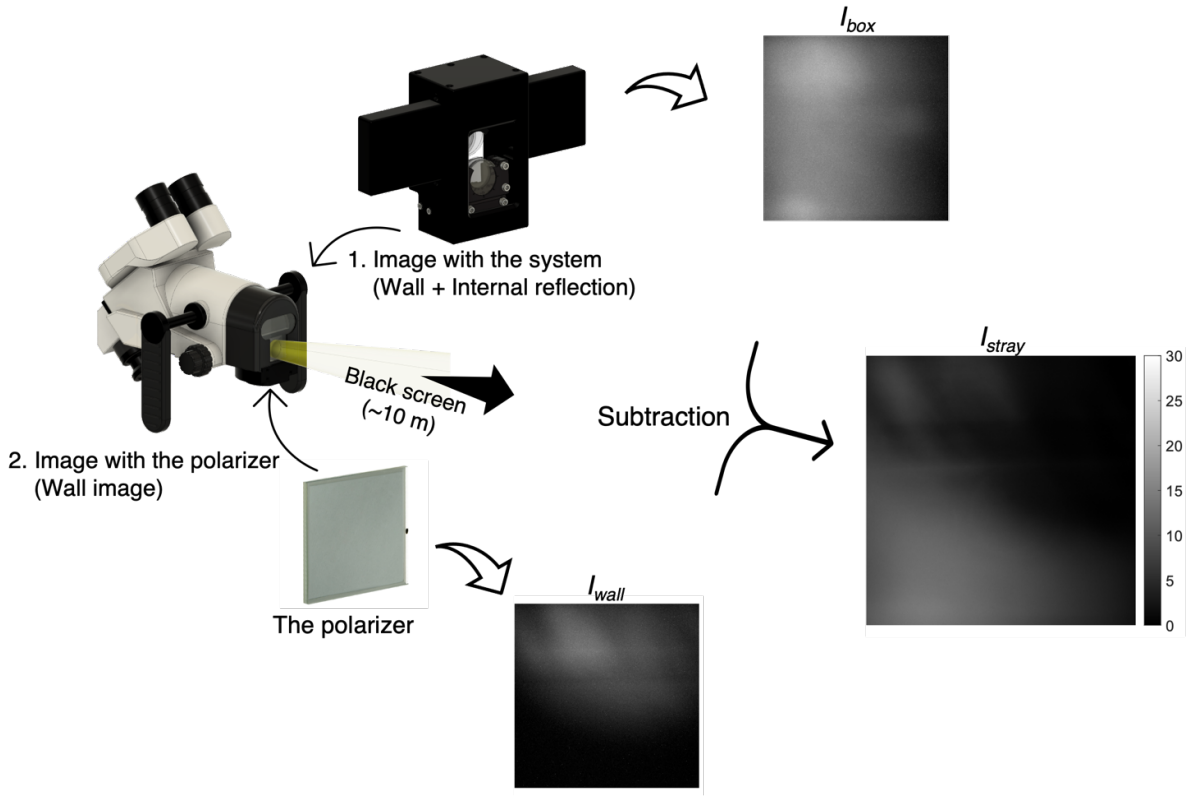

Figure 6.27 In order to extract internal stray light, 2 images of a black wall are taken in 2 different configurations, with the polarimetric system and only with the polarizer. The image from the second configuration is subtracted from the image from the first configuration.

The black wall images in both configurations, with the polarimetric system and with the polarizer only, taken with an exposure time of 38 ms are shown in the inset in Figure 6.27. Note that 38 ms are nearly 3 times longer than the exposure time in the actual use (13 ms). The subtraction of the wall image represents the actual stray reflections within the system. Consequently, the stray light has a level of less than 1 digital unit per ms. The stray light patterns acquired in the 3 sensors were identical in shape but different in intensity.

The image produced by the stray reflections is assumed not to vary if the polarimetric box is fixed and its position remains the same for all measurements, which is our case. Indeed, from the beginning of the study the polarimetric box was never dismounted and it always kept the same position. For this reason, I_{stray} was measured only once before starting the clinical study. The same I_{stray} image was always subtracted from the cervical intensity images acquired so far.

6.13 Motion blur correction: digital image stabilization

One of the most critical vulnerabilities of Mueller polarimetric imaging as a medical application is the long integration time for the 16 acquisitions (n×16 in the case of n-frame averaging). Even though improved liquid crystal technology has enabled to acquire the 16 images in a very short time of less than 1 s, which was impossible in the mechanical rotator polarimeters, Mueller imaging still requires 16 fold longer integration time than the conventional photography. In clinics where the target is a living human being, this long integration time is one of the predominant causes of poor image quality [125], [126]. The inevitable movements of the body and organs are the cause of motion blur in medical imaging. In the case of conventional photography, only movements within exposure time are responsible for the degradation of the PSF[127]. As illustrated in the first image in Figure 6.28, the superposition of translated PSFs will lead to a slightly wider PSF than the original PSF. However, Mueller polarimetry requires 16 consecutive image acquisitions to form a $\boldsymbol{B}$ matrix image, and it results in a 16-fold degradation of the PSF as shown in the middle image of Figure 6.28. The B_1~B_2 in 4 different colors denote the first 4 element images of the B matrix image, and the sum of the 16 PSFs from the 16 consecutive acquisitions will form the highly degenerated (spread) PSF in Mueller imaging. Therefore, naïve integration of the 16 intensity images will lead to critical motion blur in Mueller imaging. In photography, motion blur in a single image taken within exposure time is hardly corrected because of the loss of time domain (but not impossible[128]). However, fortunately, spatial misalignments caused by patient movement among the 16 individual images can be realigned by image registration algorithms[129].

$$f:(x,y)\rightarrow(x+a,y+b)$$
$$(\hat{a},\hat{b})=\underset{a,b\in\mathbb{N}}{\operatorname{argmin}}\,loss\left(I_{ref},f\left(I_{target}\right)\right) \tag{6-32}$$

Where f is a translation function of an image, which shift the coordinate of the input image in x and y direction by a and b. The optimization is done to find the optimal translation $\hat{a}$ and $\hat{b}$ that minimizes the loss function (difference) between the reference image I_{ref} and the target image I_{target}. 2 common loss functions in image registration are the mean square error and mutual information[130]. I_{ref} denotes a fixed image used as a

reference frame, while I_{target} is the target image to be transformed to minimize the loss with respect to I_{ref}. Finally, one can find an optimal rigid translation of the image I_{target}, which performs the vertical and horizontal translations that maximize overlaps between the 2 images.

In the case of Mueller polarimetric imaging, the first image among n×16 consecutive images (n-frame averaging) can be set as I_{ref}, and then the spatial misalignmnets in the rest of the images with respect to the first image can be corrected by the equation (6-32), which will return an enhanced PSF as shown in the 3rd image in Figure 6.28.

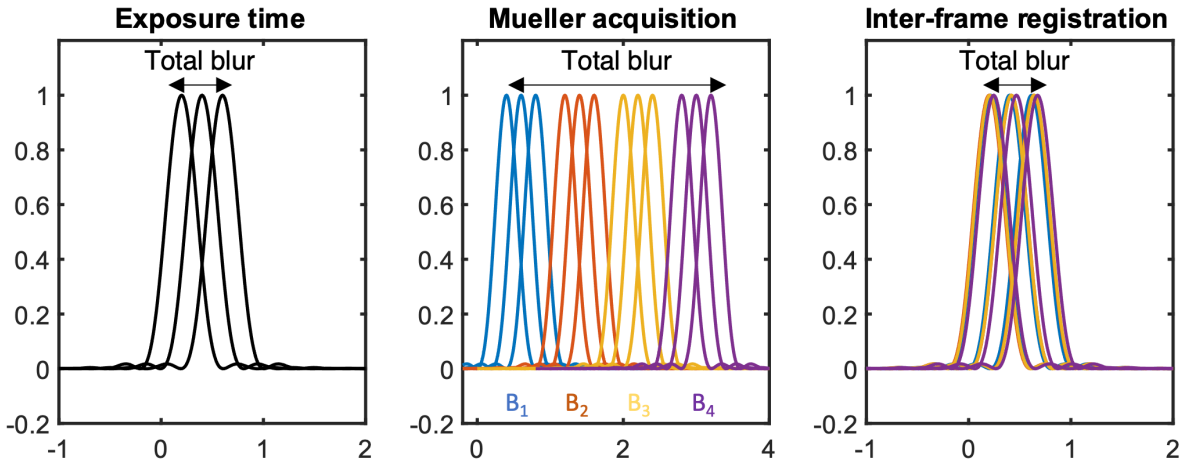

Figure 6.28 A movement of the target within exposure time widens the PSF of an imaging system (left), which appears as blurring. In the case of Muller imaging, the total integration time is equal to the time consumed for 16 acquisitions (middle). Image registration on the 16 images can recover the degenerated PSF (right).

In actual practice of Mueller colposcopy, the average of 4 frames is applied for 1 Mueller image acquisition, thus, in total, 64 intensity acquisitions are performed in a row with 64 FPS. Therefore, the image registration of the 64 images is performed to correct for patient movements that occurred for 1 s (=64 acquisitions / 64 FPS). Figure 6.29 shows the effect of this motion blur correction algorithm. The left image was created by naive averaging of 64 intensity images, while the right image was created by the inter-frame movement correction through image registration. The 'imregcorr' function in MATLAB with an option 'translation' was used to find the $\hat{a}$ and $\hat{b}$ values. The 'imwarp' function was then used to transform the target images. The effect is clearly visible around the areas saturated by specular reflection around the red arrows. The blurred image has become sharp after the application of this algorithm. This algorithm is the most important development that enabled us not only to capture details of cervical tissue in high resolution despite the movements of pregnant women, but also to increase the reproducibility and repeatability of polarimetric acquisition.

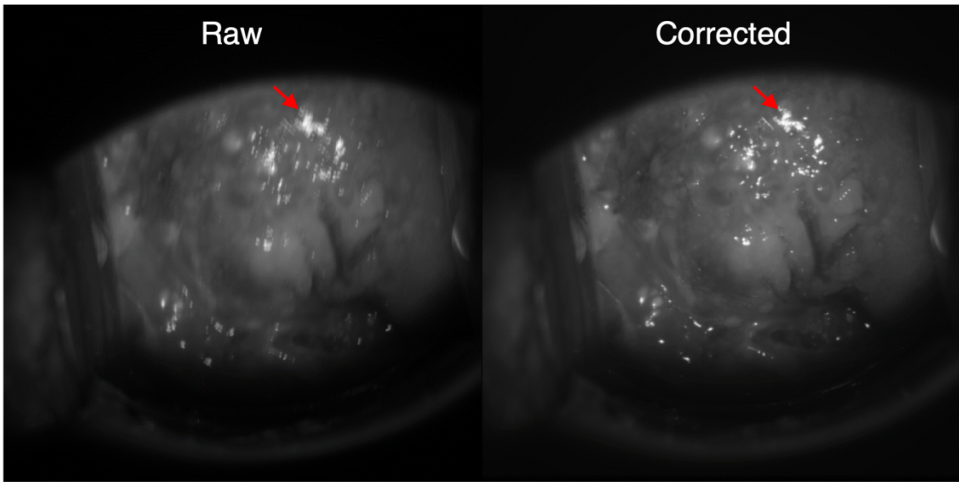

Figure 6.29 The comparison of the raw image without image registration (left) and with image registration (right). The pattern at the red arrow has become sharper after registration.

6.14 Color and beam profile correction

Color is a translation of the spectral information of light in human vision. In the human vision system, the tri-stimulus from the different spectral sensitivities of the L-, M-, and S-cone cells of the retina is decoded into the color such as red, orange, or cyan that we perceive[131], [132]. What play the role of the 3 cone cells in computer vision are the RGB channels of sensor arrays. The ratio between the 3 signals in the red, green, and blue channels corresponds to the tri-stimulus of the human vision system[132], and the RGB signals are mapped into a standard color space such as sRGB. However, a problem arises here: how to make the mapping of the RGB signals to their true colors identical or at least similar to that of human vision? As the spectral sensitivities of imaging sensors and the spectral power of illumination systems vary, each imaging system may exhibit different RGB signals for the same target. Figure 6.30 depicts a scheme of the linear color sensing process. A lighting system illuminates a target with a spectral power distribution $I(\lambda)$. Then the target (apple) reflects and absorbs the shined light with a spectral attenuation function $C(\lambda)$, resulting in $I^*C(\lambda)$. Usually, under white light, $C(\lambda)$ determines the color of the target. Let the 3 channels of a color image sensor have 3 different spectral sensitivities, $S_R(\lambda)$, $S_G(\lambda)$, and $S_R(\lambda)$. They are sensitive to red, green, and blue colors respectively. Then, the signals detected in the sensors are determined by $S^*I^*C(\lambda)$. This RGB value is not correctly mapped to the actual color of the target in the standard color space. Therefore, a signal amplifier in the camera adjusts the RGB ratio to translate the raw RGB to the standard RGB. Herein, the aim of the color correction is to find the amplifier function g that converts the incoming sensor signals to the standard RGB signals with respect to a given imaging system S and I with regardless of the target.

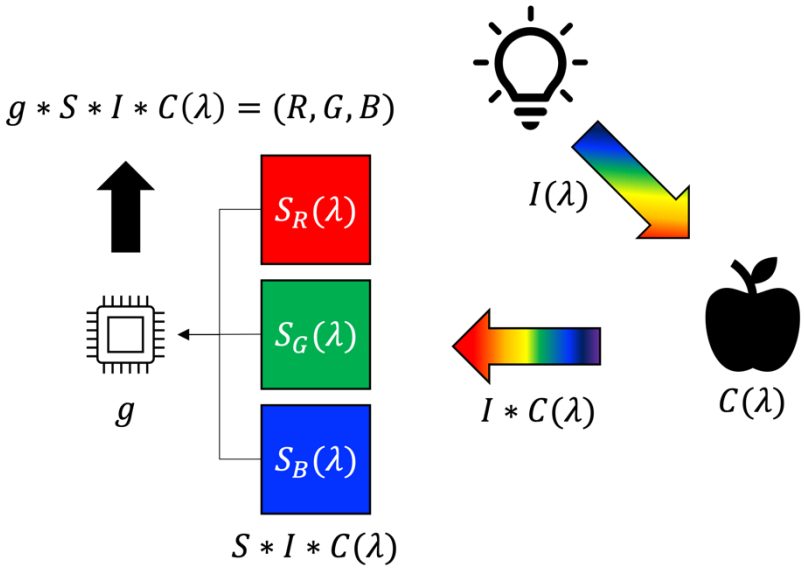

Figure 6.30 The scheme of color capturing system with 3 R, G, and B sensors. The color is determined by the spectral power *I* of the light source, spectral attenuation *C* of the target, spectral sensitivities *S* of the 3 sensors, the gain function *g* of the image processor.

If we assume the system is linear, the function g can be found by taking an image of a reference target with a well-defined color, such as white or grey. If the raw intensity values measured by a RGB color imaging system are x, y, and z, while the true RGB values of a target are a, b, and c, the function g can be found by:

$$\begin{aligned} S \times I \times C &= (x, y, z) \\ g \times (x, y, z) &= (a, b, c) \end{aligned} \tag{6-33}$$

$$g = \left(\frac{a}{x}, \frac{b}{y}, \frac{c}{z}\right) \tag{6-34}$$

The most well-known reference target is the 18% gray card in photography. The gray card gives useful information not only about the correct color but also about an optimal exposure time for an appropriate image brightness[133], [134]. However, it is not the appropriate brightness that we are interested, but the color and beam profile normalization. Thus, Spectralon® can be used as a reference target for our measurements, which has a reflectance >99% over the visible range[112]. Because the spectralon is highly diffusive over the visible spectrum, it exhibits a uniform and definitive white color. Therefore, the spatial intensity variation of the beam and the RGB intensity ratio can be corrected by dividing the acquired images by the image of the spectralon[135].

Where I_{sp} denotes the 3-channel intensity measured on the spectralon and the white color corresponds to (1,1,1) in the RGB color space:

$$g = \left(\frac{1}{I_{sp,R}}, \frac{1}{I_{sp,G}}, \frac{1}{I_{sp,B}}\right) \tag{6-35}$$

$I_{sp,X}$ denotes the intensity in the X channel. Thus, g can be found by the reciprocal of the RGB intensity on the spectralon. Consequently, the correct color of the target (the cervix) can be obtained by:

$$I_{\text{normalized}} = \left(\frac{I_{cvx,R}}{I_{sp,R}}, \frac{I_{cvx,R}}{I_{sp,G}}, \frac{I_{cvx,R}}{I_{sp,B}} \right) \tag{6-36}$$

Note that the cervical intensity images I_{cvx} and spectralon I_{sp} are normalized by their used exposure time before this correction. The images normalized by the exposure time is referred to as 'absolute intensity' while the images normalized by the spectralon are referred to as 'normalized intensity' in this manuscript. The normalized intensity represents the standardized color coordinate of the target. In addition, this property represents the diffusive reflectance, the albedo, because the spectralon is considered a perfect albedo = 1[111].

6.15 Rapid image processing for Mueller polarimetric imaging

The near-instantaneous visualization (approximately 2 seconds) of acquired polarimetric images is another significant improvement of the MPC's software compared to the previous prototype. Indeed, the previous version of the software required processing of the acquired image into a MATLAB script. The user had to execute some scripts in a particular order and sometimes manually modify them for each acquisition, which was too time-consuming for clinical use in the consulting room and unsuitable for practitioner with no knowledge of MATLAB. In addition, calculating the main polarimetric parameters from the measured Mueller matrix (which involves the calculation of its eigenvalues) was time-consuming and unsuitable for real-time verification of acquired image quality.

Two factors can briefly describe the problems of the previous image visualization system—first, the interface between LabVIEW and MATLAB. As described in the previous chapter, LabVIEW and MATLAB do not have any shared memory, and it causes critical delays in data transfer. To prevent these delays, the user can process the acquired images directly in MATLAB; however, it requires a good knowledge of MATLAB. Second, even the MATLAB codes for Mueller polarimetry are not optimized. The codes were designed to process the input images pixel-by-pixel, as shown in Figure 6.31. A single pixel data is plugged into the given function, such as the decomposition or calibration, and it is repeated until all the pixels are plugged in. This pixel-wise operation is said to be a non-vectorized operation that forms a single instruction, single data (SISD) pipeline. In this architecture, the instruction (an operation like sum) stored in the instruction register is replaced many times for each atomic data (single pixel).

On the other hand, in the single instruction, multi-data (SIMD) processing in Flynn's taxonomy[136], data are stored in the form of a "vector" in the memory. In the vector form, the data are not randomly distributed in the memory space but form a long sequence in the memory space. Therefore, the elements in a vector can be rapidly searched and plugged in. Based on these vectorized data, data-level parallelism can be exploited in the SIMD. The vectorized operations are usually faster than primitive loop operations in most cases[137].

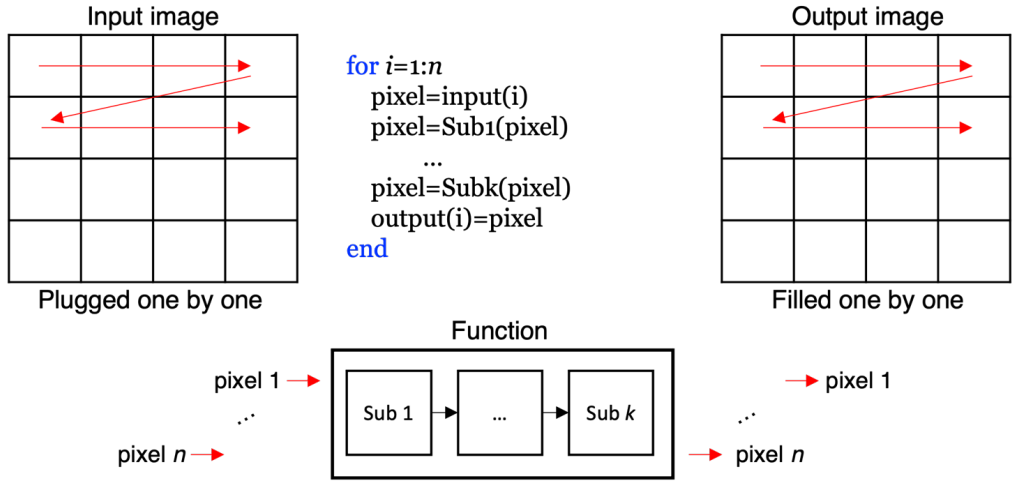

Figure 6.31 The scheme of pixel-by-pixel operation. Each pixel is processed one by one for a series of instructions (sub*1*~sub*k*.) It results in slow image processing.

Unlike compiled languages such as C and C++, which have a vectorizing compiler that transforms such for loops into sequences of vector operations [137], MATLAB is an interpreted language that compiles and executes the scripts line by line in runtime. Although MATLAB's just-in-time (JIT) compiler can optimize some simple loop operations[138], the decomposition and calibration in Muller polarimetry are composed of many sub-operations, so the JIT compiler cannot optimize these complex functions. Because MATLAB is an array programming language, the codes can be vectorized using the array data format and vectorized operations of MATLAB. The vectorized forms, the page-by-page operations, will be seen in Figure 6.32.

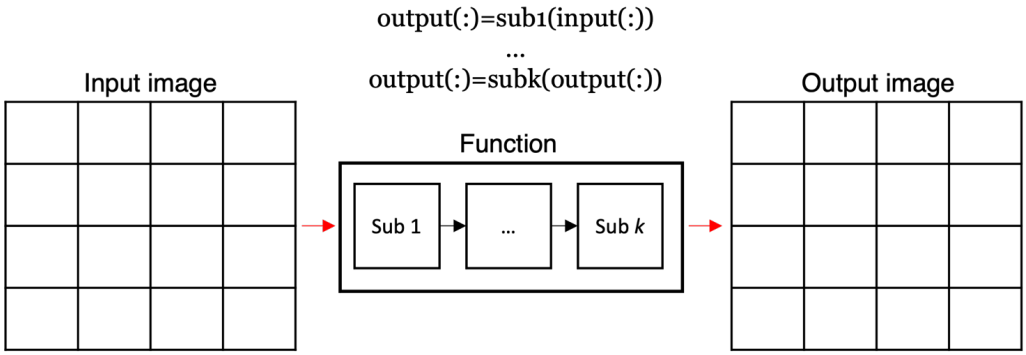

Figure 6.32 The scheme of vectorized processing. All pixels are processed at once for each instruction (sub*1*~sub*k*.) The pixel data are processed by the SIMD processing.

A simple comparison of the non-vectorized and vectorized operations in the matrix image process revealed that the vectorized matrix multiplication is 5.7 times faster (0.7 s vs 4.0 s), and the vectorized matrix inversion is 4.4 times faster (1.5s vs 6.6s). 1120×1120 image arrays of 4×4 matrices were used for the test with the Intel(R) Xeon(R) E3-1270 CPU. Thus, one can conclude that the non-vectorized codes of the previous system made the computations slow.

We first translated the MATLAB codes into LabVIEW codes to accelerate the operations for Mueller polarimetry. Second, we optimized the LabVIEW codes. On the other hand, LabVIEW is a compiled language, and the manually vectorized LabVIEW codes, as we did in MATLAB, resulted in a slightly slower processing speed than the simple loop

operations. It means LabVIEW's compiler has an automatic vectorization function. However, a complex function that consists of many sub-operations, such as the matrix multiplication and inversion, has been decomposed, as shown in Figure 6.33. Thus, each sub-operation is processed by a loop, and the compiler can vectorize the individual loops effectively.

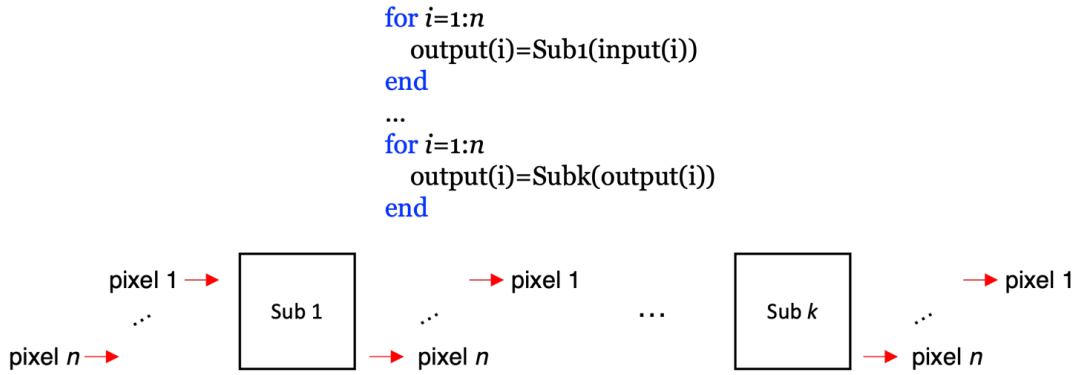

Figure 6.33 The scheme of individual loops. Although an image is processed pixel-by-pixel, all pixels are processed by a single instruction for each loop. In this case, the compiler can manage the vectorization.

As a result of these translations and optimizations, the Lu-Chipman decomposition for a single wavelength can be computed in 2 s, and the ECM for a single wavelength can be computed in 10 s. Because 1120×1120 resolution cannot be fully displayed on the full-HD monitor (1920×1080), the images are compressed to have 660×660 resolution for faster processing speed. Note that the images stored in the storage drive are still in 1120×1120 resolution. Considering the previous system took minutes to get the decomposed images and calibration in 800×600 resolution, this is a significant improvement and enables instant visualization of the results in the clinical environment.

6.16 Image visualization & analysis

As the development of the new MPC enables us to acquire thousands of polarimetric images of the cervix technically, efficient analysis tools must also be prepared and provided to promise outstanding research outputs. The previous research framework in Mueller polarimetry in LPICM was established based on MATLAB scripts, and they were effective for visualization and analysis of the former research scales, which handled ~30 samples. Analysis was done by generating MATLAB figures for each sample or a sub-group. In the project COLPOTERME, however, we are planning to analyze thousands of polarimetric images of hundreds of samples, which means a number of MATLAB figure windows are required to visualize these images. The MATLAB figure object provides some interactive features and might be good for inspecting a few images. However, it is not convenient obviously to inspect hundreds of images across hundreds of figure windows, and it will lead us to certain difficulties in having an overview of a group of collective samples.

Therefore, the necessity for a more efficient visualization method arose. The idea for image visualization was inspired by a friendly real-life application: social network services (SNS). In the SNS, people look around mass images very quickly and interact with their friends without any lack of computing resources or delay. The SNS is serviced in the web browsers such as Google's Chrome and Microsoft's Edge. In web browsers, the contexts of a

website are shown to the user in the form of the hypertext markup language (HTML). An example of an image context in HTML is:

```
<img class="image" src="cervix.png" wavelength="530">
```
(6-37)

This tag exhibits image content that has the class name 'image.' The image in the 'cervix.png' will appear for this tag. An additional attribute 'wavelength' can be referred to in JavaScript (JS), and the value '530' can be transferred to JS. The HTML contents' properties, such as size, position, and color, can be set by the cascading style sheets (CSS). An example of CSS to set the size of the 'image' class in HTML is:

```
.image {width: 100px;
        height: 100px;}
```
(6-38)

By this line, the width and height of the tags referred to as the class name 'image' in HTML are set to be 100 pixels. Complex user-website interactions and website behaviors are managed by JavaScript (JS) and the browser's dedicated JS engine. Such parts of the web concerning the appearance of websites are referred to as the front end of the website. These JS/HTML/CSS are serviced to the users (the clients) by the hosting server, such as the hypertext transfer protocol secure (HTTPS) and application programming interface (API) server.

Developing a web application for image analysis might return the best performance for our purpose. Nevertheless, considering the development cost, especially time, of such a web service and our lack of experience in web development, developing a proper web application was not a feasible option; months of development time would be needed. Inspired by web applications, the concept of the combination of JS/HTML/CSS was brought to the familiar platform – MATLAB.

Visualization of polarimetric images

The Mueller image viewer is designed to look many samples up and down. The program is written with the App designer, a MATLAB application, to build a GUI program, shown in Figure 6.34. The dotted black box marks the HTML panel. In this panel, an HTML file can be loaded, and the contexts in the file can be shown in the panel as if it is a web browser. Each image in the panel can be enlarged with a left click, as in the large color image in Figure 6.34. A color bar appears when a polarimetric image is enlarged.

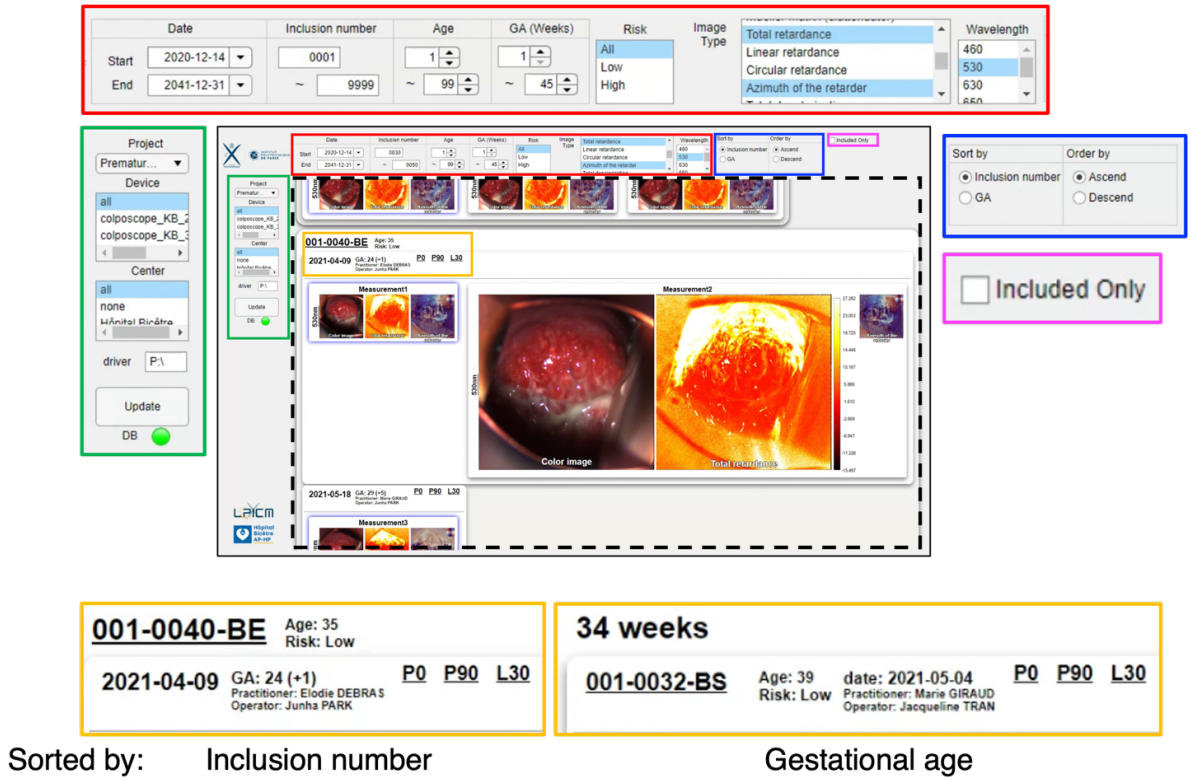

Figure 6.34 The appearance of the Mueller image viewer. Cervical images of participants appear in the black dotted box. The images shown in the panel can be filtered by the options in the colored boxes. Dependent on the 'Sort by' option in the blue box, the images are grouped by the inclusion numbers gestational ages, as shown in the orange boxes.

The objects in the red box on the top of the program provide several interactable features. The user can specify search conditions to inspect the patients in interest selectively. Five features concerning the patients' profiles are available: visit date, inclusion number, age, gestational age, and risk group. The image type and wavelength list boxes allow the user to choose multiple image types (retardance, depolarization…) and multiple wavelengths simultaneously.

The objects in the green box on the left of the program allow the user to choose project-related search conditions, such as projects, used devices, and clinic centers. Although there is only one clinical research project in our group, this feature is added for future clinical projects. The 'driver' text box is used to specify the driver of the image storage server. The circle marked by the 'DB' denotes the connection state to the database. Pushing the 'Update' button triggers the application of the search conditions.

The two radio button boxes in the blue box on the top provide two sorting options. The user can choose one of the 'inclusion number' and 'GA' (gestational age) options. It determines how the images are grouped and sorted by when they are shown on the screen. If the user chooses the inclusion number, the images are grouped by their inclusion numbers, as shown in the orange box (left). It is used to inspect patient-specific longitudinal changes in polarimetric images. On the other hand, if the 'GA' is chosen, the images are grouped by their gestational age at acquisition, as shown in the orange box (right). It is used to inspect GA-specific observations among patients.

The 'Included Only' check box in the magenta box is used to filter out the images which are not included in the final dataset of the project. Only one image is chosen for each visit by considering the images' quality in terms of sharpness and visibility of the cervix. The included images are marked by a blue border in the HTML panel.

As shown in the orange boxes, the user can easily find supplementary information for each patient and experiment, such as date, age, risk group, gestational age, and the name of the practitioner and operator. Herein, the texts with the underline provide more detailed information about the experiment by hovering the mouse cursor on the texts, as shown in Figure 6.35 by hovering over the P0, P90, and L30 texts, an image of 4×4 histograms of the Mueller matrix image of the corresponding reference sample. The mean and standard deviation of each matrix element is also shown in the colored texts. It enables the user to validate the calibration state performed in the corresponding experiment. The parameters used for calibration, such as gain, exposure time, and the number of averaged frames, also appear in the black rectangle on the top of the histogram.

Hovering the wavelength texts, the photographic conditions – used device, gain, exposure time, and the number of frame averaging – appear in a black rectangle, as shown in the wavelength box in Figure 6.35. In the case of the patient code texts, a commentary about the corresponding patient appears in a black rectangle. The commentary can be written in the image inspection app, which will be described below. The members participating in the analysis can write comments and share them with all the users, allowing text-based communication.

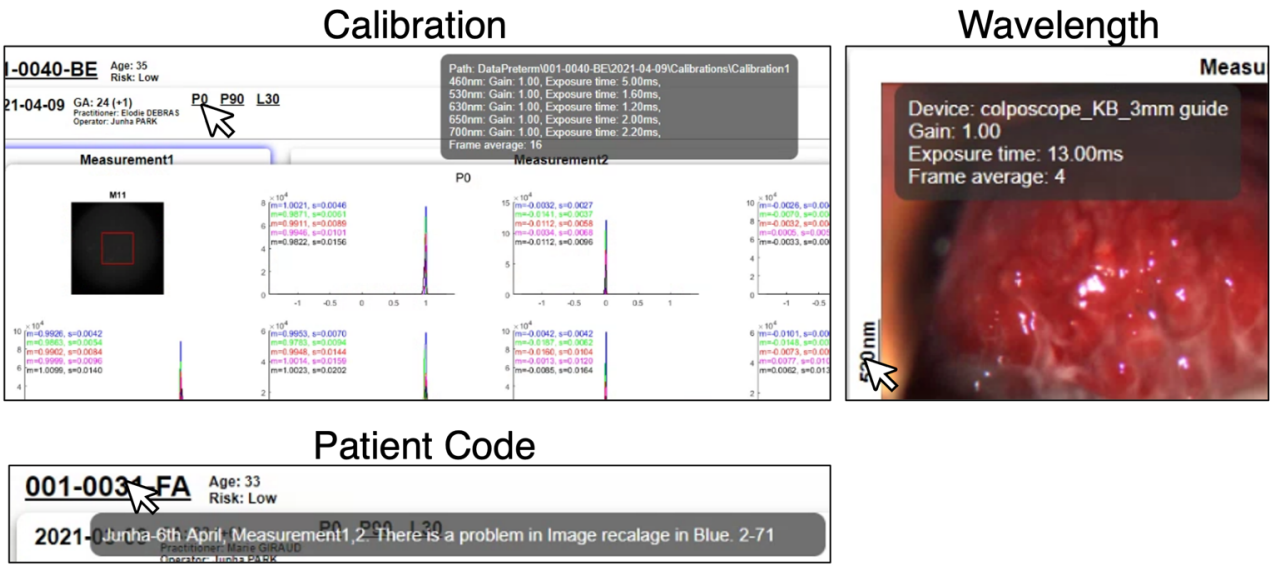

Figure 6.35 Experiment logbooks appear when the cursor is placed on the texts with underlining. The histogram of the corresponding Mueller matrix appears for the 3 reference samples in calibration (P0, P90, and L30.)

After the user sets the search conditions, the HTML panel can be updated by clicking the 'Update' button in the green box. The program sends to the SQL server a query to obtain the list of images satisfying the chosen conditions. The list is in the form of a table containing all the information describing the chosen images, such as patient information and experiment log data. Based on the list, an HTML file is written by MATLAB and exhibited in

the HTML panel. The arrangements of the contexts – the position, size, color, and alignment of the texts and images – are set by a CSS file in the server.

The HTML file is written based on the file path information of the images, which can be found in the 'file path' attribute and 'file name' attribute in the operation entity. After the HTML is shown in the panel, the images are loaded from the specified paths. The images are stored in the image data server, which uses the SMB networking protocol. The image data server appears to the user as if it is an external disk such as D:/ drive. (In this case, the server is set to P:/ drive). Therefore, no additional software or training is required to access the image data. The structure of the program is illustrated in Figure 6.36.

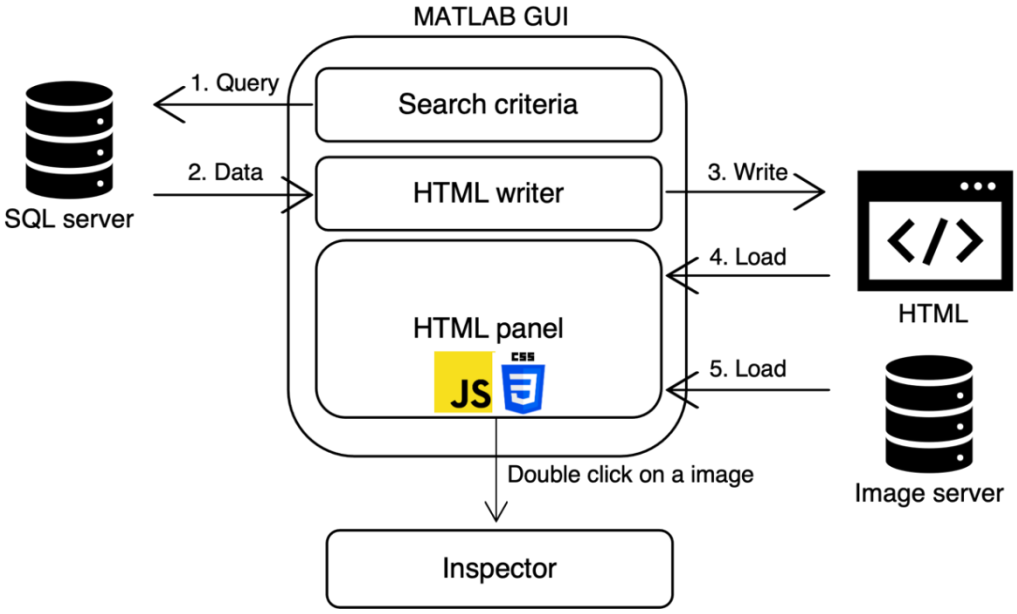

Figure 6.36 The scheme of the Mueller image viewer. It has a different server configuration from the recognized web application. There is no API server that processes image data. The preprocessed and compressed images are stored in the image server. Double-clicking an image in the viewer call up the image inspector explained below.

Therefore, this system does not have such an API server that processes and compresses the images before sending. Also, there is no HTTPS server. The HTML file is actually stored in the image data server (P:/) with a CSS file. The program loads the HTML server as if it is stored in a local drive, here, 'P:/main.html.' Obviously, this is the standard form of web service. However, it works similarly to web applications and is much easier to develop and maintain in a research environment unfamiliar with IT.

Because of the absence of the API server, the raw images have to be pretreated and stored to be shown. These pretreated images indicate the ready-to-show images, which are the captured images of the MATLAB figures with a colormap and color bar. They are captured from the MATLAB figures and compressed to be ~200 KB in size. Thus, ~50 images can be loaded per second in the 10 MB/s of the network speed.

Image inspector

A crucial problem arises in this architecture. Although the user can explore hundreds of images quickly and efficiently, detailed inspections of the images are not feasible because

they are pretreated and compressed images in low resolution and are not modifiable. Therefore, another MATLAB GUI program has been introduced for detailed inspections and analysis. The program is named 'Mueller inspector.'

If the user wants to inspect more details of the images of a patient, the Mueller inspector can be called by a double click on an image of the patient. Here, what triggers the execution of the inspector and transfers the information of the targeted image from the HTML is the JS. The Mueller inspector is described in Figure 6.37. In the inspector, the raw image data are loaded rather than the compressed images, and the user has more degrees of freedom in the image visualization. However, only one image can be shown simultaneously, contrary to the Mueller image viewer above. The user can choose an image to inspect through the list boxes in the green box. In the 'Wavelength' list box, the user can choose one of the five wavelengths. In the 'Image Type' list box, an image type as a physical property, such as intensity, retardance, and depolarization, can be chosen. In the 'Measurements' list box, the user can choose one measurement among the measurements acquired during the session (during the experiment of the day for the chosen patient).

The four checkboxes in the black rectangle on the right side of the 'Wavelength' list box are used to categorize the images in terms of the image's quality and the cervix's visibility. The 'Included' check box categorizes one 'best' measurement among several measurements within a session. Only the included images will be considered in the future analysis and the creation of the final dataset. The 'Image quality' check box can only be checked when the quality of the image in terms of sharpness and visibility of the cervix is acceptable. Good sharpness denotes the correct degree of focus and the absence of the motion blur, while good visibility denotes the presence of cervical tissue in the field of view. However, there are no quantified criteria for these classifications; therefore, the images are qualitatively discriminated by the investigators. The 'Polarimetric quality' denotes the validity of the Mueller matrix acquisition. Any malfunctioning of the polarimetric system (the PSG and PSA) and the filter sliders can cause an invalid polarimetric measurement, which appears as abnormal values in polarimetric properties. The 'Frontal image' denotes whether the cervix is completely seen or not. 'complete' refers to the presence of the posterior and anterior lips of the cervix with the presence of the cervical os in the field of view.

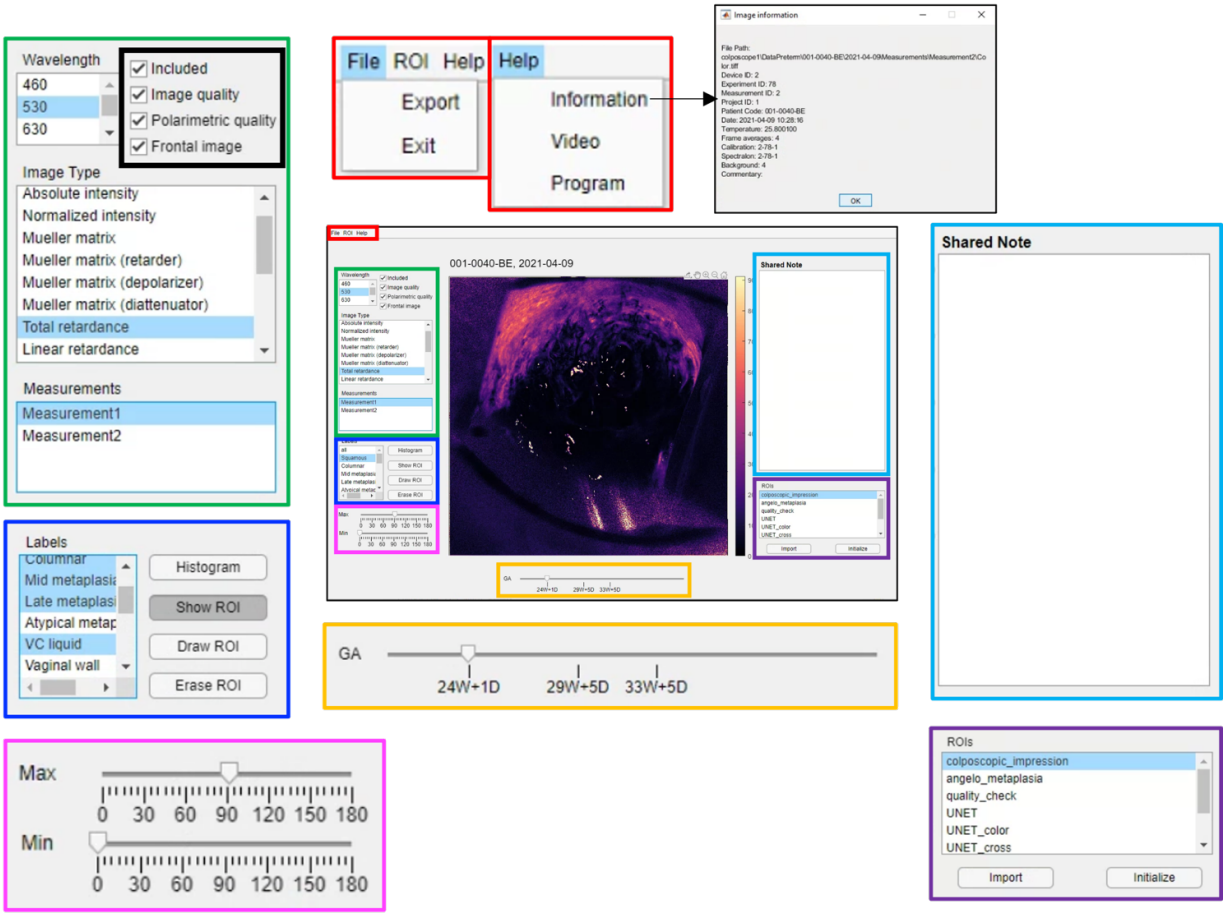

Figure 6.37 The appearance of the program for detailed inspection. It can be called by a double click of any image in the Muller viewer. It is used for detailed analysis and labeling.

The two sliders are placed in the magenta box at the bottom-left of the inspector to choose the maximum and minimum limits in the color map. The user can adjust the color contrast by dragging the sliders.

The slider in the orange box at the bottom of the inspector allows the user to move to another session performed along the longitudinal monitoring of the patient. The corresponding gestational ages are denoted on the pregnancy timeline in the form of 24W+1D (24 weeks and one day of amenorrhea). The images taken at different gestational ages can be shown by moving this slider.

The blue box at the right shows the shared commentary for the patient. All the members using this program share this note and can write and share their opinions about the patient and images. This shared note can also be shown by the mouse cursor hovering over the patient code texts shown in Figure 6.35.

The three menus are found in the red box on the top. In the 'File' menu, the user can export the current image as shown in a PNG file. The 'ROI' menu is currently empty. In the 'Help' menu, the user can call for supplementary information about the image and the recorded video. The 'Program' shows the version release information of the program.

The most important feature of the program is the ROI feature. In the blue box, there are five objects for the creation/visualization of ROI polygons. First, the user can call the 'drawfreehand' function of MATLAB. It allows the user to draw a polygon over the image by

drag & drop, as shown on the left of Figure 6.38. After drawing a polygon, a pop-up window appears. The user can choose the label (annotation) of the drawn polygon through the drop-down box. The user can choose one object usually seen on the cervix, such as:

$$\text{Labels}=\{\text{None, Squamous, Columnar, Late metaplasia, Middle metaplasia, mucus, Cervical os, Speculum, Shadow, Vaginal wall}\} \tag{6-39}$$

Each class in the set Labels is mapped to an integer number ranging from 0~255. Then, the drawn polygons and their labels form a 2D map over the cervical image. This hand-drawn segmentation will form a training dataset for the application of supervised learning (machine learning) in future analysis. This segment map is stored in an 8-bit PNG file; however, multiple segment maps can be created for one image dependent on various criteria of segmentation. Herein, the 'ROIs' list box in the violet box in Figure 6.37 allows the user to form multiple maps (ROIs) for each image. The drawn polygons are stored in the PNG file corresponding to the chosen ROI in the list box. The 'Import' button allows the user to overwrite the chosen ROI with another, and the 'Initialize' button sets the current map to all 'None.'

Pushing the 'Hist' button in this pop-up window creates a histogram of the chosen area, as shown on the right of Figure 6.38. Using this function, the user can investigate the distribution of the polarimetric properties in a selected area without storing the polygon in the map.

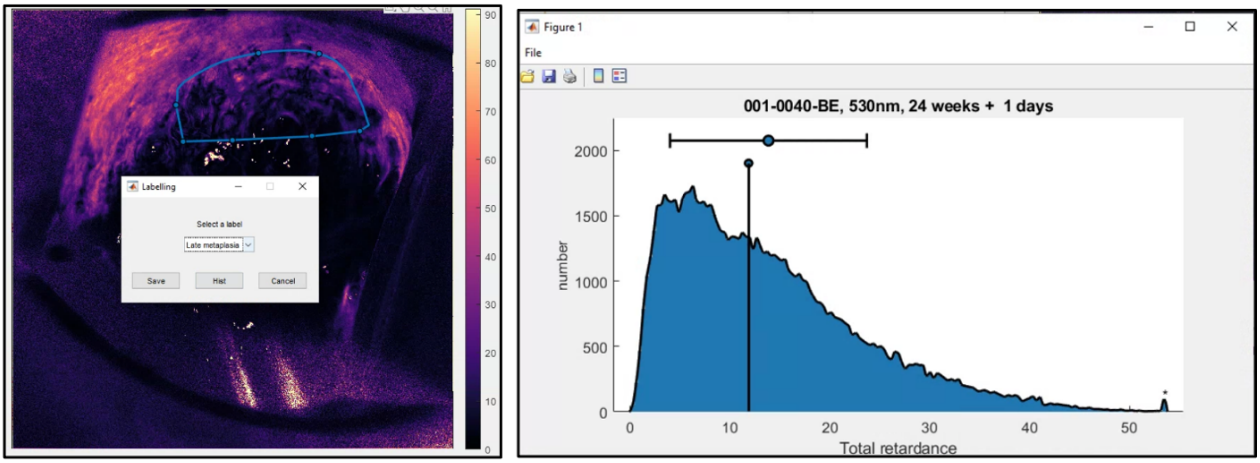

Figure 6.38 An image can be segmented as shwon on the left by hand. The label of each segement can be chosen after hand-drawing. The histogram of the chosen area can be obtained by the 'Hist' button, as shown on the right.

The map drawn by a repetition of the process above can be shown in the inspector by enabling the 'Show ROI' button in the blue box in Figure 6.37. The polygons are overlayed on the chosen polarimetric image with different colors, as shown on the left in Figure 6.39. The user can select multiple labels in the 'Labels' list box, then the polygons corresponding to the chosen labels are overlayed.

In this feature, pushing the 'Histogram' button creates the histograms of the chosen polygons, as shown in Figure 6.39.The 'Erase ROI' button sets an area to be the 'None' label.

The user is asked to draw an ROI after pushing the button, and the area of the drawn polygon can be set to be the 'None' label.

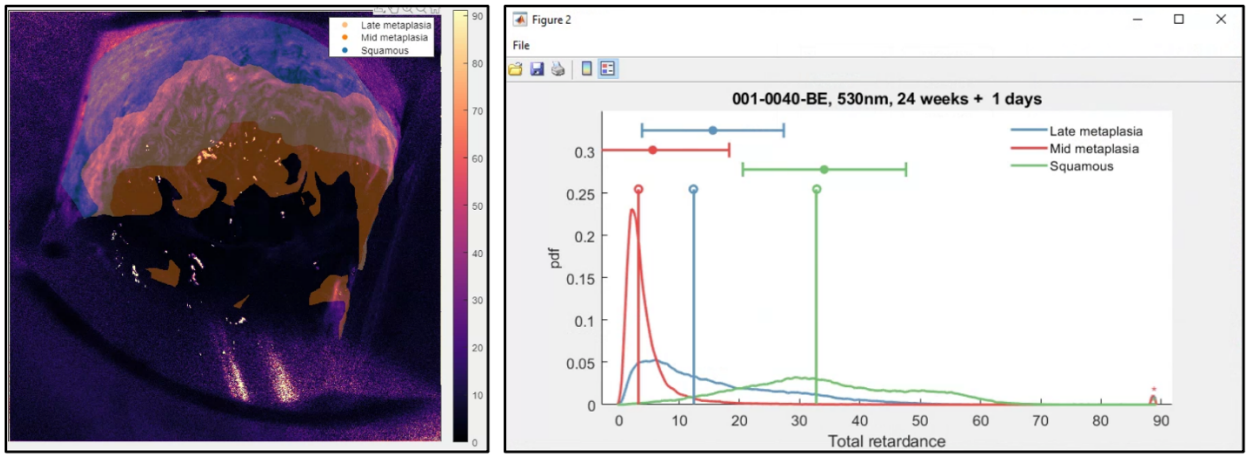

Figure 6.39 Multiple segments can be drawn in an image. They can be overlaped for visualization by the 'Show ROI' button. The histogram of segmented areas can be obtained as shown on the right by the 'Histogram' button.

Consequently, these polygons and annotations form a 2D map over the cervical image. The size of the map is identical to the polarimetric images; therefore, each pixel in the polarimetric images is mapped to the annotation of the corresponding pixel in the map. This feature enables histology-specific or label-specific image analysis.

6.17 Clinical trial

Although the new MPC has been designed with the convenience for a single user, the actual trial is carried out by 1 practitioner and 1 technical operator. The practitioner is responsible for patient-related missions; the practitioner performs consultations related to the trial, takes the consent and questionaries, interacts with the participants, and perform colposcopy. Meanwhile, the operator is responsible for technical tasks such as handling the machine-user interfaces, placing the device in the correct position, and improving the practitioner's technical accuracy. The operator is in charge of assisting the practitioner for an efficient and rapid trial.

The actual trial procedure in COLPOTERME is described in the following. If a patient accepts the trial, the required paperwork such as the consent form is completed before the polarimetric examination, and the participant is assigned an inclusion number. The trial finally begins when the operator enters the room. While the participant is lying on the colposcopy chair, the practitioner prepares a vaginal speculum, and the operator sets up the machine so that it is prepared for image acquisition. According to the established protocol, the image acquisition must be completed in 2 minutes. All the participants are asked to come to the hospital for routine obstetric examinations.

Preparation of the speculum

For cervical imaging, insertion of a vaginal speculum is essential to open the vagina and to obtain a clear view to the cervix. For this reason, the light is illuminated along the longitudinal path created by the speculum and internal reflection on the surface of the

speculum is unavoidable. This internal reflection creates strong artifacts in polarimetric imaging and can interrupt the accurate estimation of the polarimetric properties of the cervix. To this end, black specula were specially ordered as shown in Figure 6.40a.

Another problem was that the vagina tended to shrink while the speculum is inserted. The shrunken vagina covers the cervix from view as shown in Figure 6.40b. Because this is a critical obstacle to acquiring proper images of the cervix, the intrusion of the vagina was prevented by covering the speculum with latex as shown in Figure 6.40c. 2 fingers of a sterile latex glove are cut and put on the speculum. There must be slight overlay between 2 parts, otherwise there can be a gap when they are stretched. The latex layer covering the speculum effectively extrudes the vagina from the sight as shown in Figure 6.40d.

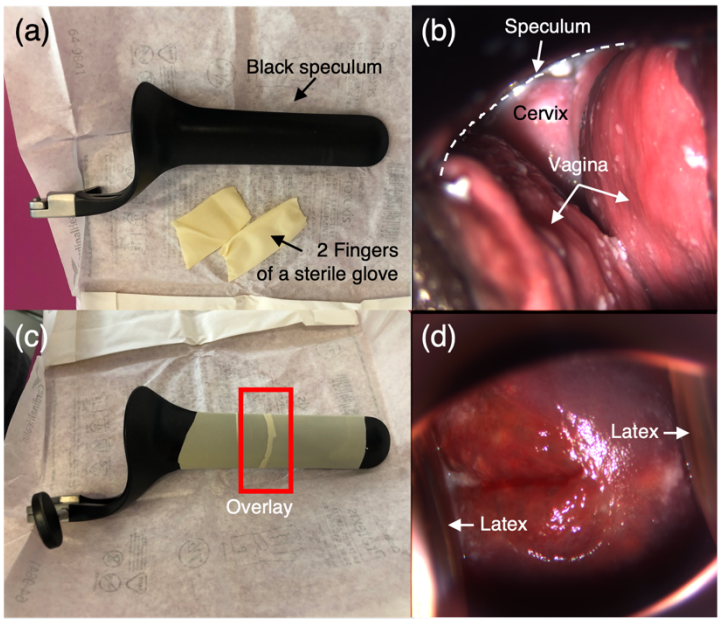

Figure 6.40 (a) A black speculum and two finger of a sterile glove. (b) An example of colposcopic images with shrunken vagina. The cervix is not completely visible. (c) The black speculum has to be covered with a silicon cover otherwise the vaginal wall can disturb the field of observation. (d) The latex cover (the fingers of the glove) prevents from the vaginal shrinkage.

Positioning of the colposcope head

After the practitioner inserts the black speculum, polarimetric images of the cervix are to be taken. Herein, it is important to acquire the images under similar conditions for 36 months for better reproducibility. For better consistency and reproducibility, the distance between the colposcope head and the cervix should remain similar for every experiment. The focus knob is set to the reference distance (the white line), and the magnification is set to 1. Because the physical distance between the colposcope head and the cervix can be implied by the focal distance written on the knob, all the images will be taken at a similar distance if the focus is around this white line.

The colposcope, now, can target the cervix though the speculum. The cervix has to be placed in the small square of the 3 guidelines as shown in as explained in the previous section. The small square represents where the cervix has to be placed. After finding the best position where the cervix stays within the small square, the practitioner moves the colposcope head

laterally to put the colposcope near the reference distance. After find the right distance that makes the image sharp, the sharpness can be maximized by maximizing the variance of Laplacian by slightly tuning the focus knob.

Image acquisition

If all the parameters, the position and sharpness, are optimized, the operator executes an acquisition by stepping the pedal. 2 beeps alert the patient before and after the acquisition to indicate that she must not move between the beeps. After an acquisition, the operator verifies the acquired image then decides what to do to obtain a better image quality. There can be a maximum of 3 acquisitions in a row, depending on the time consumption in the positioning process.

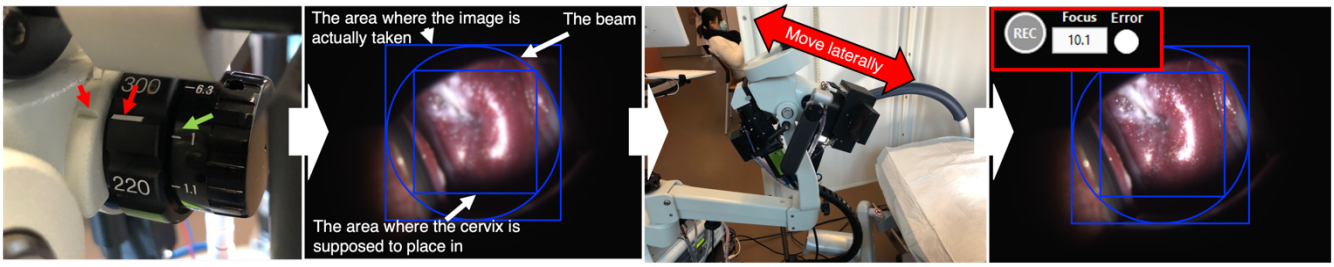

Figure 6.41 At first, the focus and magnification knobs have to be set as shown in the picture as an initialization process. The white line is corresponding to the reference focal distance. Then, the sharpness of the image has to be adjusted by moving the colposcope rather than the focus knob. However, the knob can be adjusted for micro-optimization of image sharpness.

When 2 or 3 images are taken successfully, the operator leaves the room. The practitioner ends up the examination and schedules the next visit with additional questionaries about the patient's experience. After the patient leaves the room, the operator begins the calibration process.

Calibration of the MPC

For the calibration procedure, the colposcope head is placed in front of the calibration stage attached on the pivot of the monitor arms as shown in Figure 6.42. For consistency of the calibration procedure during the repeated trials, 3 properties - distance, azimuth, and zenith – of the colposcope head are systematically constrained. The distance between the colposcope and the reflector is set to the same distance that the images of the cervix were acquired. The distance during cervical image acquisition can be determined by the position of the focus knob, if the knob is not modified after the acquisition. Thus, the variance of Laplacian is maximized when the distance between the colposcope and the reflector becomes the same as the distance between the colposcope and the cervix.

The azimuth and zenith angle of the colposcope head are determined by 2 guiding lines shown in Figure 6.43. The azimuth is set as the position where the front face of the polarimeter and hood are parallel to each other (the red solid lines). The water level on the top of the head enables the user to find the horizontal zenith of the head. In this way, a

consistent distance, azimuth, and zenith of the colposcope can be set intuitively, and the reproducibility can effectively increase.

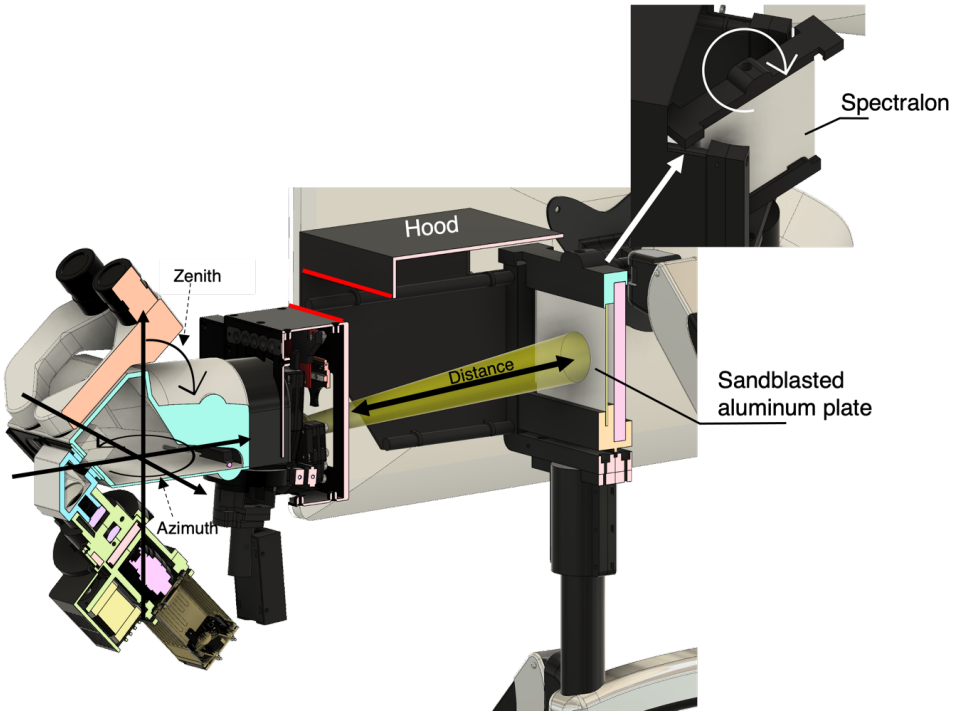

Figure 6.42 The scheme of the calibration of the colposcope. For a consistent calibration, the distance, azimuth and zenith have to be set in the same manner for repeated experiments. The reflector (the sandblasted aluminum plate) can be exchanged to the spectralon by rotation (insertion).

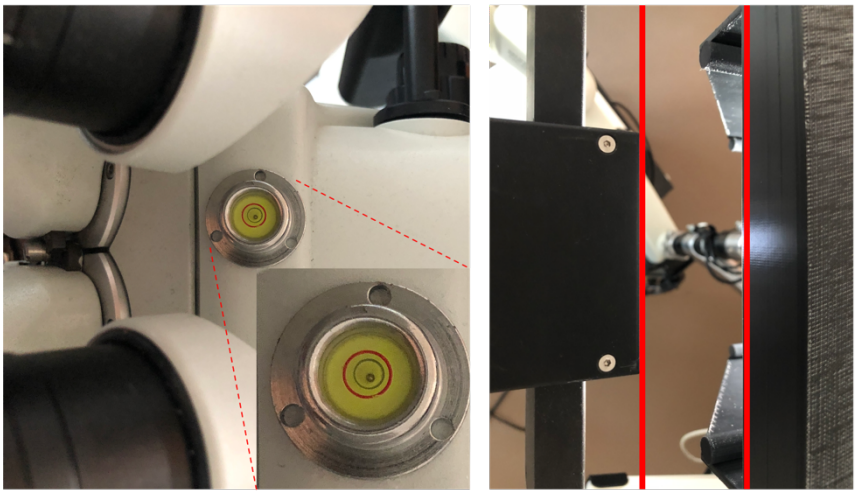

Figure 6.43 the 2 guidelines for the alignment. The water level is used to make horizontal zenith while the face of the polarimetric system and hood (2 red lines) is used for the azimuthal alignment.

The calibration process has been automatized as explained in the hardware section. A single calibration for 5 wavelengths takes 2 minutes, and the calculation takes another 1 minute. The ECM codes are implemented in LabVIEW. The results of the ECM in terms of the histograms of Mueller matrices of P0, P90, and L30 are displayed after the calculation. The user can therefore instantly judge the quality of the calibration and can decide whether an additional calibration is required or not.

6.18 Progression of the trial

The development of the MPC was completed in mid-December 2020. Accordingly, the MPC was installed in the Gynecology and Obstetrics Department of the Paris-Sud University Hospital at Kremlin-Bicêtre on 15th December, and the first inclusion took place on 22nd December as the preclinical trial began. The trial was conducted every Tuesday, and the project investigator organized additional sessions when appropriate patients appear. In this section, preliminary progress of the data collections carried out between December 2020 and April 2022 is reported.

Patient enrolment rate

Between 22nd December 2020 and 8th April 2022, 141 inclusions (141 individual patients) participated to the trial, in total, 271 sessions (visits) were established. Their participations over the timeline are charted in Figure 6.44. The patient enrollment rate in this period was found to be 4.3 sessions and 2.2 inclusions per trial-day. Maximally 9 sessions could be performed a day and 7 patients newly registered.

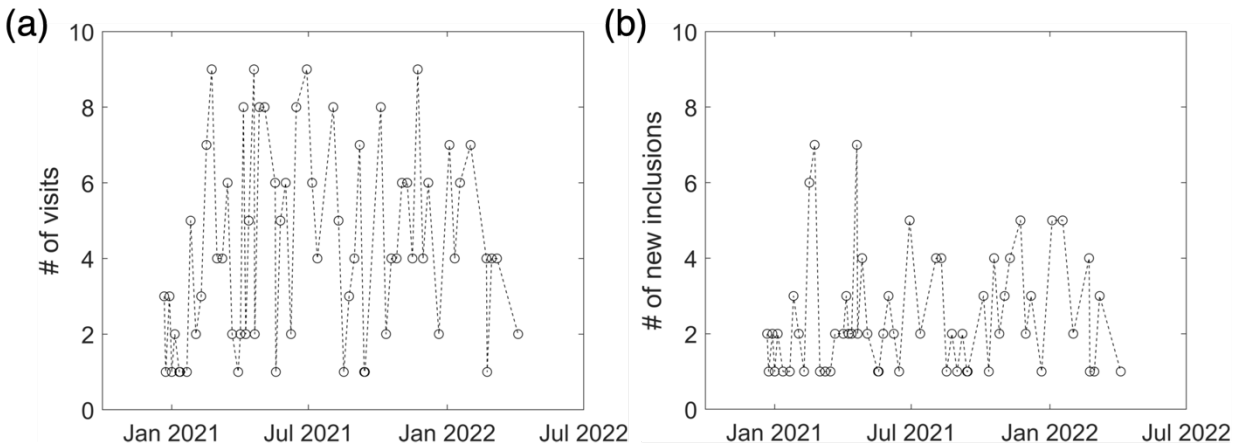

Figure 6.44(a) The number of performed experiment per day over the timeline. (b) The number of patient enrollments per day over the timeline.

However, supposing that the goal of the trial was set to recruit of 650 pregnant women, we only reached the half of the goal with respect to the recruitment timeline. To the end that we increase the patient enrollment rate, the trial started to be conducted 2 days per week, Tuesday and Friday, since the middle of April 2022.

Trial execution failures

Figure 6.45 depicts the number of patients for each accumulated number of visits. More than 50% of patients visited more than 2 times during their pregnancy. However, only 1/3 patients were visited more than 3 times, which can be analyzed longitudinally. Figure 6.45a shows all the sessions performed in the period, while Figure 6.45b shows only the effective sessions that we could acquire at least 1 proper cervix image. Even though 271 sessions were established, 21 sessions failed to acquire a proper cervix image. Accordingly, 7.7% of sessions failed, and we failed to acquire even a single polarimetric image from 11 (7.8%) of patients. These failures were attributed to 2 factors, the technical mishandling and the patients' conditions.

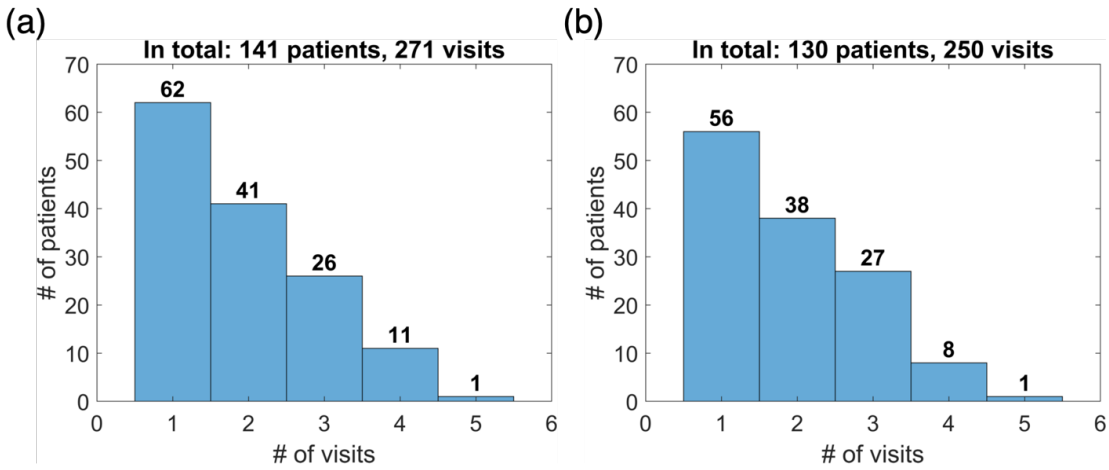

Figure 6.45(a) The number of patients who visited *x*-times for the trial. (b) The number of patients who provided *x*-times effective measurements.

3 representative failures are shown in Figure 6.46. The technical mishandling leads to the failure in visualization of the cervix (blue box). The technical mishandling predominantly happened in the early phase of the trial. It is attributed to inexperienced handling of the colposcope and speculum. The first (top) image shows an out-of-focus image, where the focal plane is not coincident to the object (cervix) plane. The second (bottom) image was taken with misalignment between the optical path of the colposcope and the speculum. Although the cervix is partially seen through the speculum, the tissue is not properly analyzable. The Shrunken vaginal wall (Orange box) was also one of the factors caused failures at the early phase. It happens as the vaginal wall is pressed out between the gap of the 2 blades of the speculum. It often appears in obese patients, and this is the reason why the latex cover is introduced as shown in Figure 6.40. In the red box in Figure 6.46, any technical failure or vaginal wall does not appear. However, the cervix is not seen because the speculum was not able to be fully inserted. What we captured in this situation was the closed vagina rather than the cervix. It happens when the vagina is too firm to insert the speculum or when the patient feels too much pain. Most of the cases when a patient repeatedly expresses pain, the session is stopped and no cervical image can be acquired.

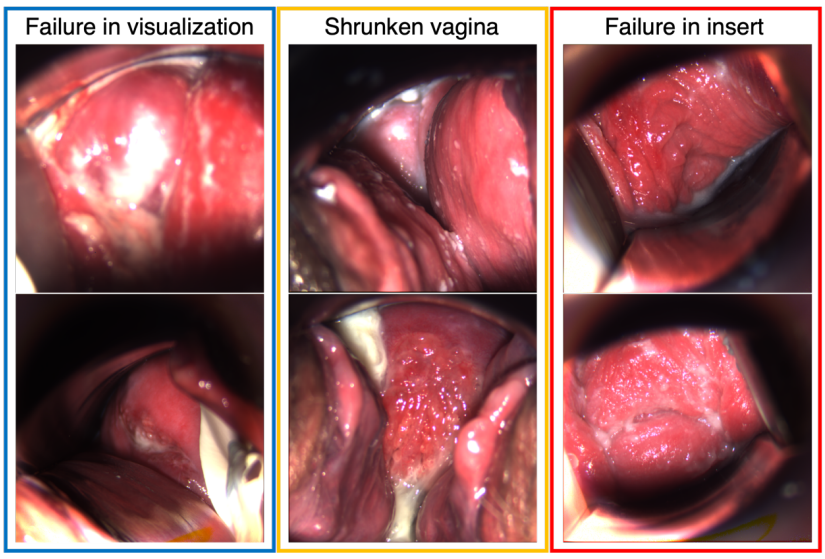

Figure 6.46 6 examples of failures in cervical image acquisitions.

Table 6.2 The numbers of 3 types of failures over 271 sessions.

	Mishandling	Shrunken vagina	Insertion failure
Number	3	5	13
Percent	1.1%	1.8%	4.8%

List of publications and conference contributions

Publications in peer-reviewed journals:

Chashchina, O., Mezouar, H., Vizet, J., Raoux, C., *Park, J.*, Ramón-Lozano, C., Schanne-Klein, M.-C., Barakat, A. I., & Pierangelo, A. "Mueller polarimetric imaging for fast macroscopic mapping of microscopic collagen matrix remodeling by smooth muscle cells," *Scientific Reports*, *11*(1), 5901, (2021).

Rehbinder, J., Vizet, J., *Park, J.*, Ossikovski, R., Vanel, J.-C., Nazac, A., & Pierangelo, A. "Depolarization imaging for fast and non-invasive monitoring of cervical microstructure remodeling in vivo during pregnancy," *Scientific Reports*, *12*(1), 12321, (2022).

Liu, B., *Park, J.*, Duchesne, C., Honnorat, B., Vizet, J., Rousseau, A., & Pierangelo A. "Mueller Polarimetric Imaging as a new tool for detecting the effect of Non-Thermal Plasma treatment on the skin," *Biomedical Optics Express* (submitted)

Park, J., Debras, E., & Pierangelo, A., *"In-vivo Mueller polarimetric imaging of subepithelial connective tissue microstructural remodeling during metaplastic transformations"*. (to be submitted)

Park, J., & Pierangelo, A., "*High-performance color Mueller polarimetric colposcope for exploring cervical tissue microstructure in vivo."* (to be submitted)

Park, J., Débras, E., & Pierangelo, A., "Accurate segmentation of the cervix of Mueller polarimetric images." (In progress)

Park J., Débras, E., & Pierangelo, A. "Evolution of polarimetric properties of the cervix during pregnancy: a longitudinal study." (In progress)

Proceedings at peer-reviewed scientific conferences:

Park, J., Lindberg, A., Vizet, J., Rehbinder, J., Gennet, C., Vanel, J.-C., Nazac, A., Debras, E., Capmas, P., Fernandez, H., & Pierangelo, A. "Cervical cancer diagnostics with a multispectral Mueller polarimetric colposcope," *Clinical and Preclinical Optical Diagnostics II,* Proc. SPIE 11073-9. (2019)

Park, J., Rehbinder, J., Vizet, J., Vanel, J.-C., Nazac, A., & Pierangelo, A. "Mueller polarimetric imaging of cervical tissue for pregnant women," *Frontiers in Optics + Laser Science*, FM5E.7. (2021)

Pierangelo, A., Rehbinder, J., Vizet, J., *Park, J.*, Ossikovski, R., Vanel, J.-C., & Nazac, A. "Polarized light: a promising tool to probe the cervical microstructure of pregnant women," *Unconventional Optical Imaging III*, Proc. SPIE PC12136. (2022)

Oral presentations at peer-reviewed scientific conferences:

Park, J. (speaker), Lindberg, A., Vizet, J., Rehbinder, J., Gennet, C., Vanel, J.-C., Nazac, A., Debras, E., Capmas, P., Fernandez, H., & Pierangelo, A. "Cervical cancer diagnostics with a multispectral Mueller polarimetric colposcope." *European Conferences on Biomedical Optics (ECBO)* (2019)

Park, J. (speaker), Rehbinder, J., Vizet, J., Vanel, J.-C., Nazac, A., & Pierangelo, A. "Mueller polarimetric imaging of cervical tissue for pregnant women," *Frontiers in Optics + Laser Science* (2021)

Poster presentations:

Lindberg, A. (speaker), *Park, J.*, Lee, H., Vizet, J., Rehbinder, J., Genet, C., Garcia-Caurel, E., Novikova, T., Ossikovski, R., & Pierangelo, A., "Imagerie polarimétrique de Mueller pour le diagnostic précoce des cancer épithéliaux," *Les Rencontres de la Cancerologie Française (RCFr)* (2018)

Lindberg, A. (speaker), *Park, J.* (speaker), Mezouar, M. H., Lee, H., Vizet, J., Rehbinder, J., Novikova, T., Ossikovski, R., & Pierangelo, A., "Imagerie polarimétrique de Mueller pour le diagnostic précoce des cancer épithéliaux," *Les Rencontres de la Cancerologie Française (RCFr)* (2019)

Park, J. (speaker), & Pierangelo, A., "A sophisticated Mueller polarimetric colposcope: potential as a diagnostic tool in gynecology," *IP Paris Science Forum* (2021)

Park, J. (speaker), Rehbinder, J., Vizet , J., Ossikovski, R., Vanel, J.C., Nazac, A., Debras, E, & Pierangelo, A., "Mueller polarimetric imaging for fast and non-invasive monitoring of cervical microstructure remodeling in vivo during pregnancy," *Engineering for Health (E4H) symposium*, École Polytechnique (2022)

Patents:

Pierangelo, A. & *Park, J.*, "Système d'observation à deux ports d'entrée équipé d'un système polarimétrique." (FR2213891, submitted)

Pierangelo, A. & *Park, J.*, "Imagerie multispectrale polarimétrique." (FR2213889, submitted)

Pierangelo, A. & *Park, J.*, "Procédé d'imagerie en temps réel." (FR2213890, submitted)

ECOLE DOCTORALE

Titre : Colposcopie de Mueller numérique multispectrale pour explorer la microstructure du col utérin *in vivo*

Mots clés : Imagerie optique, Imagerie polarimétrique de Mueller, Imagerie médicale, Colposcopie polarimétrique numérique, Col utérin, Etude clinique

Résumé : La prématurité est la première cause de mortalité périnatale dans le monde. Elle est généralement associée à des modifications structurelles anormales du col utérin.
Lors d'une grossesse à terme, le col utérin se ramollit progressivement tout en restant fermé pour maintenir le fœtus dans l'utérus pendant la majeure partie de la gestation. Après 37 semaines d'aménorrhée, il commence à se raccourcir et à se dilater (maturation cervicale) en vue de l'accouchement, qui a lieu vers 41 semaines d'aménorrhée. Lors d'une naissance prématurée, la maturation cervicale se produit avant la 37ème semaine d'aménorrhée. La pratique clinique recommande de mesurer la longueur du col utérin par échographie transvaginale pour diagnostiquer la prématurité. Cependant, cette méthode n'est pas fiable et une approche plus efficace est nécessaire.
De nombreuses études ont montré que la modification du col utérin pendant la grossesse est un processus complexe impliquant le collagène, principal composant microscopique du tissu conjonctif.
L'imagerie polarimétrique de Mueller s'est révélée très prometteuse pour caractériser la structure du collagène cervical. Les travaux développés au cours de cette thèse ont été une étape clé pour le démarrage du projet COLPOTERME en collaboration avec le CHU du Kremlin Bicêtre (France), qui a permis le lancement du premier essai clinique au monde visant à tester la pertinence de l'imagerie polarimétrique de Mueller pour le suivi du remodelage de la microstructure cervicale pendant la grossesse. A cette fin, un colposcope polarimétrique de Mueller aux performances inégalées a été développé. Ce système permet d'acquérir des images de haute qualité in vivo tout en répondant aux exigences d'un essai clinique en termes de rapidité, de convivialité et d'ergonomie. Les résultats de cette étude ont montré que l'imagerie polarimétrique de Mueller fournit des informations uniques sur les changements microstructuraux du col utérin pendant la grossesse.

Title : Digital multispectral Mueller colposcopy for exploring cervical microstructure *in vivo*

Keywords : Optical imaging, Mueller polarimetric imaging, Medical imaging, Digital polarimetric colposcopy, Uterine cervix, Clinical trial

Abstract : Prematurity is the leading cause of perinatal mortality worldwide. It is usually associated with abnormal structural changes in the cervix.
In a full-term pregnancy, the cervix gradually softens while remaining closed to hold the fetus in the uterus throughout most of gestation. After 37 weeks of amenorrhea, it begins to shorten and dilate (cervical ripening) in preparation for delivery, which occurs at around 41 weeks of amenorrhea. In preterm birth, cervical ripening occurs before 37 weeks of amenorrhea. Clinical practice recommends measuring cervical length by transvaginal ultrasound to diagnose prematurity. However, this method is not reliable and a more effective approach is needed.
Numerous studies have shown that cervical change during pregnancy is a complex process involving collagen, the main microscopic component of connective tissue.
Mueller polarimetric imaging has shown great promise in characterizing the structure of cervical collagen. The work developed during this thesis was a key step for the start of the COLPOTERME project in collaboration with the Kremlin Bicêtre University Hospital (France), which allowed the launch of the first clinical trial in the world aiming at assessing the relevance of Mueller polarimetric imaging for the monitoring of the cervical microstructure remodeling during pregnancy. For this purpose, a Mueller polarimetric colposcope with unparalleled performance was developed. This system allows the acquisition of high quality images in vivo while meeting the requirements of a clinical trial in terms of speed, usability and ergonomics. The results of this study showed that Mueller polarimetric imaging provides unique information on the microstructural changes of the cervix during pregnancy.

Institut Polytechnique de Paris
91120 Palaiseau, France